DISSERTATION

Advanced Electrical Characterization of Defects in Silicon Photodiodes

ZUR ERLANGUNG DES AKADEMISCHEN GRADES
Doktor der technischen Wissenschaften

EINGEREICHT AN DER
Technischen Universität Wien
Fakultät für Elektrotechnik und Informationstechnik

VON
Dipl.-Ing. **Paul Stampfer**
Matr. Nr. 01432009
[redacted]

UNTER BETREUUNG VON
Univ.Prof. Dipl.-Ing. Dr.techn. **Michael Waltl**

Wien, 8. April 2024

Acknowledgements

Many people accompanied me on my journey to the PhD, and this thesis would not have been possible without their guidance, help and contributions. It is a pleasure to express my gratitude and to thank all the people supporting me.

First, I am very grateful to my academic supervisor Professor Michael Waltl for his guidance, advices and continuous support. I was always welcomed at the institute in Vienna and Michael made sure, that I got the resources required for productive working. I would also like to thank Professor Tibor Grasser for his contributions and reviews of my publications, his expertise and inputs helped a lot, to improve the quality of my manuscripts. Generally, a big thanks to the whole staff at the Institute for Microelectronics for valuable discussions and including me also in non-scientific activities. Specifically, I want to thank Bernhard Stampfer for spending endless hours with me in the laboratory and helping me a lot with his expertise on measurements.

This work was done in collaboration with the ams OSRAM group. A special thanks to all the colleagues from my team, Anderson, Dinh, Fernando, Filip, Fred, Georg, Hubert, Ingrid, Jong Mun and Olesia, for fruitful discussions. Particularly, I want to express my gratitude to my managers Ingrid and Hubert as well as Rainer for supporting me and ensuring financing for my position, despite harsh economic times. Furthermore, I want to thank my supervisors Gerald and Rainer for their guidance and valuable inputs.

Pursuing a PhD is not only about working and studying, one also needs a free mind after work, to be ready for the next day. Therefore, I want to thank my friends Boris, Christof, Dinh and Mario, not only for reviewing my thesis, but also for spending spare time and vacations together and doing various after-work activities.

Finally, I really appreciate the support of my family. Mom, Dad, Anna, Gerli, Peter thanks for your support and making family gatherings always a great time.
Lena, love of my life, thank you for your unconditional support and understanding throughout this journey. Your love, encouragement and patience have been my greatest strength.

Abstract

Photodiodes made of silicon, the predominant material in the semiconductor-based sensor industry, are so pure, that already spurious amounts of contamination or a tiny fractional amount of crystallographic mismatch may cause detrimental effects on the device performance. The fundamental reason for this device degradation is, that electronic trap states within the band-gap are created, and charge carriers may interact with these states disturbing the nominal operation. Therefore, the characterization of such defects in photodiodes is essential to understand, identify and eradicate trap-related performance degradation, as well as to design trap-resistant devices.

An important parameter for opto-electronic devices, that is directly related to trap states, is the minority carrier lifetime. However, the extraction of lifetimes in photodetectors poses a formidable challenge, since state-of-the-art devices often consist of pn-junctions embedded in epitaxial layers grown on a substrate. In this work, the extraction of lifetimes on such structures has been reviewed and compared among different selected methods. It was found that the ratio of diffusion length to the thickness of the epitaxial layer is a critical parameter resulting in effective lifetimes possibly much lower than the trap related minority carrier lifetimes. The reverse recovery and open circuit voltage decay methods are excellent candidates to extract these effective carrier lifetimes. With the combined current-voltage and capacitance voltage method, however, lifetimes corresponding to diffusion lengths much larger than the layer thickness can be extracted, because the main signal investigated by this method originates from the junction depletion zone.

Another state-of-the-art concept in nowadays photodiodes is the utilization of deep trenches filled with an insulating material as terminator or separator between individual devices. However, by means of measurements and simulations it is shown that trap-related injection-dependent interface recombination at the sidewalls of the trenches may lead to non-linear responsivities with respect to the radiant flux. Different concepts to mitigate this issue are proposed and discussed, which is supported by simulation results. To draw conclusions about the nature of the trap states located at the sidewalls, a deep level transient spectroscopy study has been performed on dedicated test samples. Based on these results, it is shown that silicon dangling bonds at the silicon to silicon-dioxide interface may be the root cause of the observed injection-dependent recombination rates.

Contents

List of Figures

List of Abbreviations

C-V capacitance-voltage

I-V current-voltage

APD avalanche photodiode

BJT bipolar junction transistor

CCD charge-coupled device

cIVCV combined I-V and C-V

CMOS complementary metal-oxide-semiconductor

DFT density-functional theory

DLTS deep-level transient spectroscopy

DOE design of experiment

DT deep-trench

DTI deep-trench isolation

DTMOSCAP deep-trench metal-oxide-semiconductor capacitor

DUT device under test

EHP electron-hole pair

EQE external quantum efficiency

fcc face-centered cubic

FM forward method

FOM figure of merit

IDR injection-dependent responsivity

IQE internal quantum efficiency

IR infrared

MOS	metal–oxide–semiconductor
MOSCAP	metal–oxide–semiconductor capacitor
MOSFET	metal–oxide–semiconductor field-effect transistor
MPE	multi-phonon emission
NEP	noise-equivalent power
NIR	near-infrared
NMP	non-radiative multi-phonon
NWG	n-well guard
OCVD	open circuit voltage decay
PES	potential energy surface
PV	photovoltaic
PWG	p-well guard
QE	quantum efficiency
QNR	quasi-neutral region
RM	reverse method
RMS	root mean square
RR	reverse recovery
RTN	random telegraph noise
SNR	signal-to-noise ratio
SNS	Sah-Noyce-Shockley
SPAD	single-photon avalanche diode
SRH	Shockley-Read-Hall
STI	shallow-trench isolation
TCAD	technology computer-aided design
TDM	two-diode model
UV	ultra-violet
VIS	visible

Chapter 1

Introduction

Silicon-based photodetectors are used as sensors in a wide range of applications. Over the last decades such sensors have become an inseparable part of our modern world, permeating many aspects of our daily lives. The performance of these devices is affected by the quality of the employed materials and interfaces which are investigated by electrical measurements and simulations in this thesis. To provide a contextual framework, this chapter briefly explores the significance of sensors, in particular light sensors, as well as current challenges in that field. Finally, the thesis objectives as well as an outline will be given.

1.1 The Empowering Role of Light Sensors: Past, Presence and Future

Similar to how our own body is equipped with senses that allow us to perceive the world around us, sensors may be considered the senses, i.e. eyes and ears, of devices bestowing them with the ability to sense and interact with the environment. Among these senses, optical sensing stands out with its historical precedence, as the oldest lens artefacts are over 3000 years old and acted as a technological upgrade to the human eye [1]. On the way to the first electrical light sensors, the field of engineered optical sensing systems passed several milestones such as the telescope or the microscope. It was then in 1839, by the unveiling of the photovoltaic effect by Alexandre-Edmond Becquerel [2], that a new era in the field of light sensing was initiated. Some important milestones from that discovery to the first semiconductor photodiodes are shown in Fig. 1.1. After the foundational breakthrough of the first semiconductor photodiodes, the field of electronic photodetectors continued to witness remarkable advancements that revolutionized imaging and light sensing technologies. These innovations spanned across various types of sensors, each contributing to our ability to capture and interpret light signals with unprecedented precision:

- **Charge-Coupled Device (CCD) Image Sensors:** One milestone emerged with the invention of CCD image sensors in 1969 by Willard Boyle and George E.

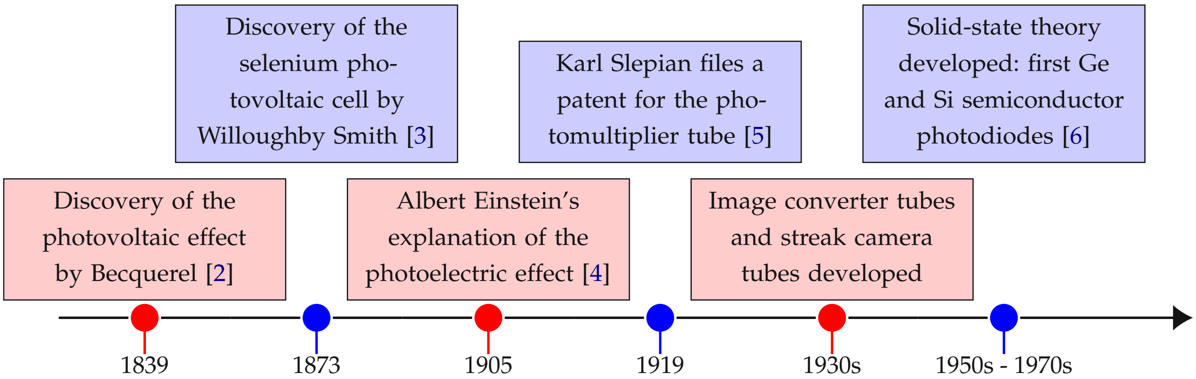

Figure 1.1. Important milestones in the history of electronic photodetectors and towards semiconductor photodiodes. Adopted from [7].

Smith [8], for which they were awarded the Nobel Prize in Physics in 2009. CCDs revolutionized imaging in fields such as photography and astronomy. These sensors utilize an array of capacitors to store and transfer charge generated by incoming photons via the photoelectric effect. This enables high-quality image capture and efficient signal processing.

- **Complementary Metal-Oxide-Semiconductor (CMOS) Image Sensors:** In the 1990s, combined efforts of different institutions and companies have led to the resurgence and breakthrough of the CMOS Image sensor [9]. A technology that, compared to the CCD, offers lower power consumption, lower voltage operation, on-chip functionality (integrated circuitry), and reduced production costs [10]. CMOS sensors quickly gained popularity, becoming a cornerstone in modern imaging devices, from digital cameras and smartphones to medical imaging, security systems and drones [11].

- **Avalanche Photodiodes (APDs) and Single-Photon Avalanche Photodiodes (SPADs):** The advancement of avalanche photodiodes brought enhanced sensitivity and signal amplification to light detection applications. APDs exploit the avalanche effect to amplify the generated charge, making them suitable for low-light scenarios such as photon counting, high-energy particle detection or optical communication systems [12]. SPADs, a specialized type of APD, enable single-photon detection and have become pivotal in quantum optics and photonics research. These devices operate in a regime where the absorption of a single photon triggers an avalanche of electron-hole pairs (EHPs), resulting in a detectable electrical signal [13]. The development of SPADs has opened up new possibilities for applications in quantum cryptography and other emerging technologies that rely on single-photon interactions [14].

- **Photomultiplier Tubes (PMTs) and Multi-Pixel Photon Counters (MPPCs):** PMTs, initially invented by Karl Slepian (see Fig. 1.1), and MPPCs, a solid-state advanced derivative, excel in applications requiring extreme sensitivity and single-photon detection, such as nuclear physics experiments [15] and medical imaging techniques like positron emission tomography (PET) [16].

- **Nanotechnology and Quantum Photodetectors:** The convergence of nanotechnology and quantum mechanics led to the development of cutting-edge photodetectors. Nanoscale structures, such as quantum dots, quanum wells or nanowires, exhibit quantum confinement effects that enable precise control over their electronic and optical properties [17, 18, 19]. These structures can be engineered, e.g. by adjusting the quantum confinement dimensions or by stacking thin layers of semiconductors in a cascade like configurations [20], to absorb specific wavelengths of light with high efficiency.

- **Extending the Detectable Spectrum:** While silicon, as the predominant material within the semiconductor industry, mainly covers the visible (VIS) and near-infrared (NIR) spectrum for optical applications, different approaches evolved to extend the applicability of sensors to a wider optical bandwidth. The bandgap of a semiconductor material indeed sets a fundamental limit on the range of wavelengths which can be absorbed and thus detected. In the case of silicon, its bandgap restricts its sensitivity to longer wavelengths such as infrared (IR), preventing efficient detection of IR light. For the extension of the detectable range into the infrared, two common approaches are nano-scaled quantum detectors [21] as mentioned in the above point or compound semicondcutors. Compound semiconductor alloys allow the bandgap of the semiconductor to be custom tailored for specific wavelenghts, where HgCdTe is the most widely used variable gap alloy for IR photodetectors [22].
  On the other side of the spectrum, i.e. in the ultra-violet (UV) regime, despite being well-established, the UV-enhanced silicon technology has critical limiations [23]. Therefore, wide-bandgap materials (such as GaN, SiC or InGaN), semiconductor thin films, organic semiconductors and quantum confined structures are frequently employed to achieve highest performing detectors [23, 24].

While the above listing discusses state-of-the-art approaches and devices in the field of light sensing also the future of light sensor technology holds exciting and promising possibilities across diverse fields. As of 2022, light sensors hold a strong position in modern technology, capturing a substantial 68 % of the sensor market [25]. This emphasizes their vital role in various applications.

1.2 Defects and Their Influence on Photodiode Performance

In many cases the properties of semiconductors depend on the types and densities of impurities they contain. Remarkably, defects in semiconductors serve a dual role, as they can be deliberately introduced to achieve specific material properties or operational conditions, yet they can also disrupt proper operation and performance (”Some Fatal, Some Vital” [26]). It is, for example, known that defects may mediate dopant diffusion, and therefore serve an essential role for certain microelectronic devices [27, 28]. On the other hand it is clear, that defects may cause several undesired effects in semiconductor devices such as enhanced noise levels [29], lower lifetime and degraded quantum efficiency in optoelectronic devices [30] or reliability and variability issues in MOS transistors [31, 32]. Therefore, the concept of ”defect engineering” has emerged, involving the deliberate utilization of the positive aspects of defects to tailor semiconductor properties for enhanced device performance, while also encompassing strategies to mitigate and minimize the negative effects of defects [33, 34].

As mentioned in the previous section, photodiodes have emerged as fundamental components across a wide spectrum of applications. Their ability to convert light into electrical signals is utilized by technologies such as the CCD or CMOS image sensor. Photodiodes are minority-carrier based devices and the performance is strongly influenced by recombination and generation processes. In silicon, the process of generation and recombination may be dominated by defects, as discovered by Shockley, Read [35] and Hall [36] in 1952. These defects may create localized traps that impact carrier lifetimes and compromise the quantum efficiency [37, 38] or contribute to excess noise [39]. Moreover, defects within photodiodes can induce dynamic phenomena, such as carrier trapping and detrapping processes, giving rise to effects that influence the device’s transient response and temporal characteristics [40]. These dynamics play a crucial role in the photodiode’s behavior during rapid changes in incident light intensity and affects its applicability for dynamic applications. Another important aspect is the temperature-dependent behavior of photodiodes, where very often applications require a stable detector output with minimal variation over a wide temperature range. However, it is known that trap-mediated recombination is strongly temperature dependent, which may strongly impact the temperature coefficient of a pn-junctions output [41].

On the other hand, defect states in photodiodes can lead to enhanced light absorption potentially improving the photodiodes response at long wavelengths. The silicon divacancy, for example, is known to mediate photodetection for wavelengths around 1.5 µm and may therefore be introduced into the material on purpose by low-dose inert ion implantation [42, 43].

To optimize photodiode performance, an understanding of defects and their influence is essential. Employing defect engineering techniques allows researchers to capitalize on positive defect effects while mitigating negative impacts. By carefully controlling defect concentrations and distributions, researchers can fine-tune photodiode properties to meet specific application needs, enhancing sensitivity, precision, and dependability.

In summary, the effects of defects on photodiode behavior are integral to their practical functionality, driving enhancements and challenges that researchers strategically address to unleash the full potential of photodiodes in various light sensing applications. As was described in this section, defects may affect the static, dynamic and temperature-dependent performance of photodetectors. While a substantial amount of research has been devoted to investigate radiation-induced defects in silicon photodiodes, the emphasis on conventional, un-irradiated photodiodes has been comparatively limited. This is partly attributed to the inherently low defect densities found in modern silicon-based devices, which present challenges in their precise measurement. This thesis addresses the challenges of defect characterization in state-of-the-art photodiodes, where the thesis outline is discussed in the next section.

1.3 Thesis Outline

This section provides a brief overview of the thesis objectives and outlines the main topics covered in each chapter. The primary aim of this research is to investigate the interplay between defects and the performance of state-of-the-art silicon-based photodiodes, as well as to contribute in the field of defect-characterization methods and techniques.

Chapter 2 explores the essential properties and behaviors of photodiodes, laying the groundwork for subsequent discussions. It delves into their operational principles, response to different wavelengths of light and the evaluation of performance through key parameters.

In the following chapter 3, defects within photodetectors and their consequential effects on device functionality are examined. Different defect types, including bulk and interface defects, are investigated in terms of their interactions with charge carriers, with particular emphasis on the prominent Shockley-Read-Hall recombination mechanism.

Chapter 4 focuses on the practical aspects of electrical characterization of defects in photodiodes. It covers various measurement techniques applied in this work, including current-voltage (I-V) and capacitance-voltage (C-V) characteristics, as well as methods like open circuit voltage decay (OCVD), reverse recovery (RR), deep level transient spectroscopy (DLTS), and intensity-dependent responsivity measurements (IRM).

In Chapter 5, the methods introduced in Chapter 4 are applied to investigate defects in dedicated test samples. First, combined I-V and C-V (cIVCV) measurements as well as OCVD and RR measurements are employed on epitaxial layer test devices to extract minority carrier lifetimes. The extraction of lifetimes on this samples, especially the importance to consider the epitaxial layer thickness, is discussed. Second, IRM and DLTS measurements on deep trench (DT) test samples are presented and the extracted parameters are discussed.

Finally, in Chapter 6 the major findings of this thesis are summarized.

Chapter 2

Properties and Characteristics of Photodiodes

Photodiodes are essential devices in the field of light sensing, playing a crucial role in converting light into electrical signals. Such devices are made from semiconductors and are widely used in various applications, ranging from ambient light detection to more complex imaging and communication systems. Their fundamental operation relies on the photovoltaic effect, where incident photons generate electron-hole pairs (EHPs) within a semiconductor material. The generated charge carriers may then be ”harvested” to generate an electrical signal, which is the photodetector output signal. In this chapter the foundational properties and behavior of photodiodes are reviewed. An examination of essential photodiode parameters and their significance as figures of merit is also conducted. As the process of light absorption in a semiconductor is wavelength-dependent, it will be discussed what fundamental physical limits materials, such as silicon, are exposed to and how a detector responses to light of different wavelengths. Furthermore, the dynamic response of photodiodes to light pulses is discussed, which is an important parameter in the field of optical communication. This parameter is getting more and more importance with modern society’s needs for lightwave based data transmission [44].

As the fundamental understanding is established, it will be examined how defects may interfere with the photodiode operation. Different types of defects, such as bulk defects and interface defects, are discussed in detail, along with their potential interactions with carriers. The chapter also delves into the modeling and simulation of these defect-carrier interactions in optoelectronic devices, utilizing both analytical and numerical approaches.

2.1 Fundamentals of Photodiodes

In the upcoming section the fundamental properties of photodiodes are reviewed. The basic structure, main parameters as well as dynamic characteristics are discussed.

2.1.1 Operating Principles and Basic Structure

A photodiode, just like a conventional pn-junction, exhibits a depletion zone between an n-type and p-type doped semiconductor region where a strong electric field is present. Due to this electric field, photo-generated EHPs are separated by the electromagnetic forces acting in opposite directions. These carriers lead to a terminal current between the anode (contact on the p-doped side) and cathode (contact on the n-doped side). A schematic of the basic photodiode structure is shown in Fig. 2.1. Also carriers generated outside the depletion region may contribute to the terminal anode to cathode current, if they manage to diffuse to the depletion region. However, unlike the directed movement of EHPs within the depletion region because of the electric field (drift), the paths of minority carriers generated outside the depletion region, that is in the quasi-neutral region (QNR) of the semiconductor, are undirected (diffusion). The average distance a minority carrier diffuses before it recombines is given by the diffusion length L_d, which is proportional to the minority carrier lifetime τ. That means, on average carriers generated within one diffusion length from the depletion zone can contribute to the current. As will be discussed in Chapter 3, defects within the semiconductor may significantly influence the minority carrier lifetime and consequently also affect the maximal achievable terminal currents. This has important consequences on static photodiode parameters such as the responsivity and quantum efficiency that will be introduced in the next subsection.

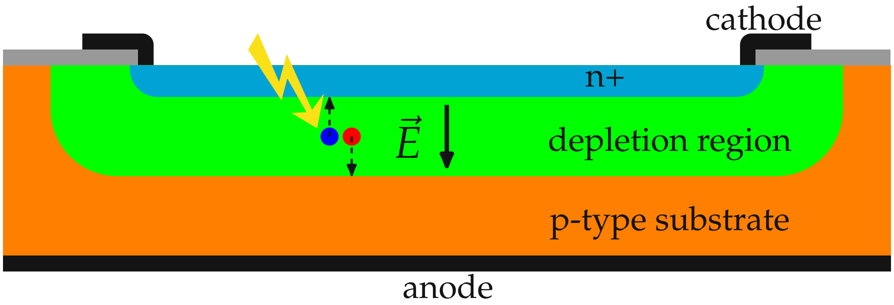

Figure 2.1. Basic photodiode structure. Electron-hole pairs created within the depletion region get separated by the electric field $\vec{E}$ leading to a terminal current between the anode (contact on the p-doped region) and the cathode (contact on the n-doped region).

2.1.2 Photogenerated Current and Output Characteristics

Photodiode Dark Current

The current voltage (I-V) characteristics of an unilluminated pn-junction (”*dark current*”, Fig. 2.2: black line) were described by Shockley in 1949 [45]. This model considers diffusion of charge carriers in the QNR of either side of the pn-junction and is often referred to as *diffusion model*. Shockley’s model of the pn-junction terminal currents was then, in 1957, complemented to account for the generation and recombination of carriers from generation-recombination centers in the diode space charge region [46]. The complemented model is at times named after their inventors, **S**ah, **N**oyce and **S**hockley: SNS model. Characteristic for the diffusion model and SNS model is an exponential dependency of the pn-junction anode-to-cathode dark current $I_{\mathrm{ac,dark}}$ on the anode to cathode voltage V_{ac} of the form

$$I_{\mathrm{ac,dark}} = I_{\mathrm{S}} \left(\exp\left(\frac{V_{\mathrm{ac}}}{n V_{\mathrm{th}}} \right) - 1 \right), \tag{2.1}$$

where I_{S} is reverse-bias saturation current, n the diode ideality factor and V_{th} the thermal voltage. For the ideal diffusion model $n = 1$, and for the *SNS* model $1 \leq n \leq 2$. However, diodes with sub-unity ideality factors [47, 48], as well as, ideality factors higher than 2 [49] have been reported in the literature. In general, for silicon diodes the ideality factor may be considered an index of crystal purity, as $n \approx 1$ indicates a diffusion dominated device with apparently few recombination centres in the depletion zone, whereas a value of n close to 2 indicates a domination of the recombination current component [50]. The relation of crystal quality and lifetime to the current voltage characteristics will be discussed in detail in Section 4.1.2.

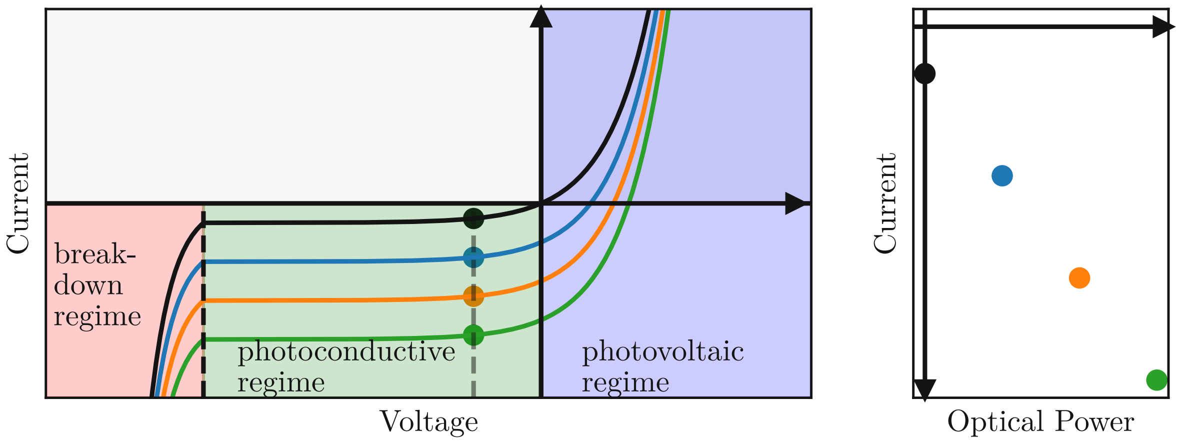

Figure 2.2. Schematics of the (illuminated) pn-junction output characteristics. (**left**) The current voltage characteristics and the different operating regimes. (**right**) The variation of diode current as function of optical power at a fixed working point in the photoconductive regime (dashed vertical line in left side plot).

The Illuminated PN-Junction

Upon illumination the diode's I-V characteristics change, as an additional source of generation modifies charge carrier densities. As indicated in Fig. 2.1 an electron-hole pair is created once a photon of a certain wavelength is absorbed in the semiconductor. This phenomena is called the photoelectric effect, and was first described by Einstein in 1905 [4]. The generated charge carriers may then either recombine within the semiconductor or drift/diffuse to a collecting electrode and generate a terminal current. The created amount of EHPs is proportional to the flux of absorbed photons and the corresponding photocurrent I_{phot} is a reverse current component that is added to the dark current ($I_{\mathrm{ac,dark}}$, Equation (2.1))

$$I_{\mathrm{ac,illum}} = I_{\mathrm{ac,dark}} - I_{\mathrm{phot}}. \tag{2.2}$$

The illuminated pn-junction characteristics are schematically drawn in Fig. 2.2 as colored lines. Operating the diode in the so called *photoconductive regime*, that is at an reverse to zero anode-to-cathode bias, the diode can be considered a current source, that depends linearly on the optical power (see Fig. 2.2, right plot). The photocurrent of silicon photodiodes is known to be highly linear with respect to the incident optical power [51, 52], however, deviations, that are, non-linearities, may arise because of injection dependent carrier-defect interactions [PSC1]. Detailed investigations and modeling of diode linearity measurements even allow for a determination of defect and interface parameters, as will be discussed in Section 4.2.2. While in the *photoconductive regime* electrical power has to be applied to the diode to make it sensitive for measuring and detecting optical signals, electrical power is delivered from the diode to a load in the *photovoltaic regime*. The main application for pn-junctions operated in the *photovoltaic regime* is, as the name indicates, photovoltaics. In that case, the main goal is to convert the most possible amount of optical power impinging on the pn-junction into usable electrical energy. Therefore, the direct current (DC) output of the junction needs to be converted into utility frequency alternating current (AC), which is achieved by so called *solar inverters*. The best optical to electrical energy conversion efficiency is achieved at a single operating point, the so called maximum power point, and different techniques have been developed to ensure a solar inverter operation closest to this point [53].

The very left regime in Fig. 2.2 is the *breakdown regime*. The high electric field strengths in the depletion region of the junction lead to breakdown phenomena such as Zener breakdown or avalanche breakdown [54, 55]. The breakdown regime has applications in the dark as well as the illuminated regime. For non-illuminated conditions, pn-junctions operated at or close to the reverse breakdown regime (*"Zener diodes"*) can utilize the very steep current-voltage characteristics in that region and act as voltage reference or regulators. However, the breakdown regime is also a very important regime in illuminated conditions, due to its application in avalanche photodiodes (APDs) and single-photon avalanche diodes (SPADs). In these devices optically generated carriers are accelerated to velocities high enough to overcome the ionization energy of bulk atoms and therefore a large avalanche of further carriers can be triggered (*impact ionization*). For SPADs even single EHPs may trigger an avalanche, allowing such a device to operate as a photon counter [56].

2.2 Light Absorption in Photodiodes

2.2.1 The Photoelectric Effect and Absorption Coefficient

As mentioned in the previous section, light is absorbed in a semiconductor based on the *photoelectric effect*. Before the explanation of the photoelectric effect by Einstein in 1905 , scientists were puzzled by the phenomena observed, when shining electromagnetic radiation on a metal plate. The kinetic energy of electrons emitted from the metal plate was independent of the intensity of the used light, as was expected from wave theory, it was rather dependent on the wavelength of the used light source. Additionally, there appeared to be a critical wavelength where there was a transition from observing electrons emitted from the metal surface to the opposite. These phenomena were successfully explained by treating light as being composed of particles, called *photons*, with energy E_{phot}

$$E_{\text{phot}} = hf = h\frac{c}{\lambda}, \tag{2.3}$$

where h is Planck's constant, f the frequency of the light, c the speed of light and λ the wavelength. For an electron to emit the metal surface it's energy must exceed the metal work function W

$$h\frac{c}{\lambda} \geq W. \tag{2.4}$$

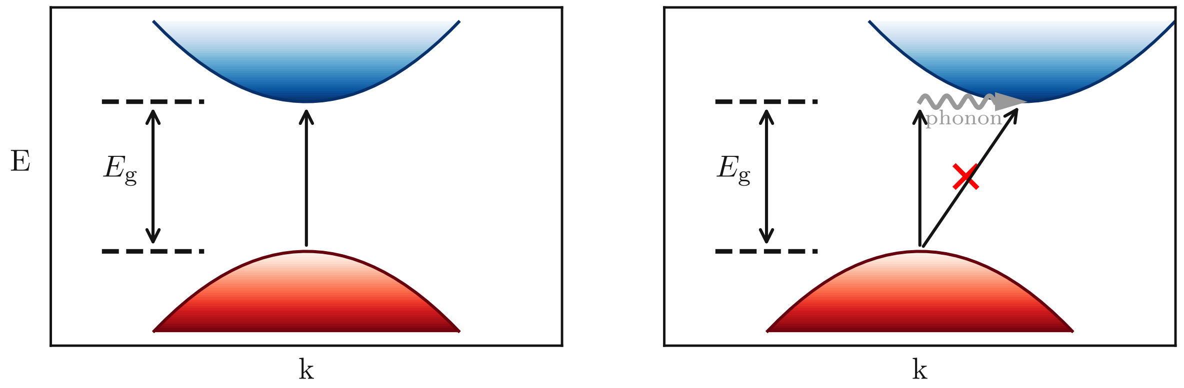

Figure 2.3. Light absorption in semiconductors with bandgap E_g: an electron is "lifted" from the valence band (red) to the conduction band (blue). In the band diagram (energy E versus wavevector k) optical transitions can be considered vertical. (**left**) Light absorption in a direct bandgap semicondutor. (**right**) Light absorption in an indirect bandgap semicondutor involving a phonon transition. A direct (no-phonon) "diagonal" absorption is not allowed, since this violates the conservation of momentum.

Similarly, for the interaction of light with a bulk semiconductor there is an energetic barrier that the energy of the light needs to exceed for absorption. The absorption of light within the bulk of a material is called *internal photoelectric effect*. For semiconductors the energetic barrier for photon absorption is determined by the bandgap energy. This means, the energy supplied must exceed the energy required to energetically ”lift” an electron from the valence band to the conduction band. Therefore, by replacing the metal work function W with the bandgap E_g in Equation (2.4) a first condition for light absorption in semiconductors can be formulated. However, there is another requirement for photon absorption in semiconductors, that is the conservation of moment. Therefore, direct and indirect bandgap semiconductors need to be considered separately. Fig. 2.3 schematically shows the absorption of light in an indirect as well as a direct semiconductor. The momentum carried by the photon, given by $|\vec{q}| = \frac{2\pi}{\lambda}$, is typically negligible small, compared to the momentum associated to the electronic quantum states of the semiconductor bands. Therefore, optical transitions can be considered vertical, as drawn in Fig. 2.3. For direct bandgap semiconductors (left plot) this means photons can be absorbed without the need of any additional process to preserve momentum. For indirect bandgap semiconductors, like silicon, however, additional momentum-conserving agents are needed. Emission or absorption of quantized lattice vibrations, called *phonons*, can preserve momentum in that case. This is indicated in the right-hand side plot in Fig. 2.3, by the gray wavy arrow. The difference between direct and indirect bandgap semiconductors on the absorption of light has important consequences for the probability or efficiency of light absorption. For indirect bandgap semiconductors the transition or absorption probability is typically lower than the absorption probability for direct bandgap semiconductors, since an additional phonon transition is involved which lowers the probability of this mechanism [57]. For direct bandgap semiconductors the rate of absorption can be computed by quantum-mechanically calculating the probability of the transition from the valence to the conduction band using Fermi’s Golden Rule [58]. Main approaches to this problem involve a classical treatment of electromagnetic radiation and describing electrons quantum-mechanically as Bloch waves [59] or the consideration of the electromagnetic stimulation by means of creation, annihilation and number operators [60, 61]. For indirect bandgap semiconductors the transition rates can be computed using second order perturbation theory [62]. Typically, the efficiencies of the second order processes involved in optical absorption in indirect bandgap semiconductors are lower compared to their first order process counterparts in direct bandgap semiconductors [62]. For practical applications this has important consequences, as for efficient absorption indirect bandgap materials need to be made thicker, prolonging the optical absorption part to get the same efficiency as in direct bandgap materials. Thus photovoltaic (PV) units made of silicon, which is the dominating material in the PV industry (mainly because of its cost efficiency [63]), are made thicker than PV units made of direct bandgap materials. On the other hand, indirect bandgap also means inefficiency for the reverse process of generation, which is recombination. This will be discussed in more detail in Section 4.1.1.

Low recombination rates are desired in PV and optical sensing applications since recombining carriers are "lost" and can not contribute to the harvested signal or energy. The absorption coefficient α describes how the power P of electromagnetic radiation is absorbed as function of the material thickness x via

$$\frac{P(x)}{P(x=0)} = e^{-\alpha x}. \tag{2.5}$$

It is directly related to a materials extinction coefficient κ, which constitutes the imaginary part of the complex refractive index $\underline{n}$, via

$$\alpha = \frac{4\pi\kappa}{\lambda}, \tag{2.6}$$

where λ is the wavelength of the corresponding radiation. The absorption coefficient for selected semiconductor materials used in optoelectronics is shown in Fig. 2.4. As can be seen, the materials have a critical wavelength λ_{crit}, where electromagnetic radiation with wavelengths larger than this critical wavelength is not absorbed. As mentioned above, this critical wavelength can be simply calculated with Equation 2.4 and the bandgap value of the corresponding material. Furthermore, it can be seen, that silicon

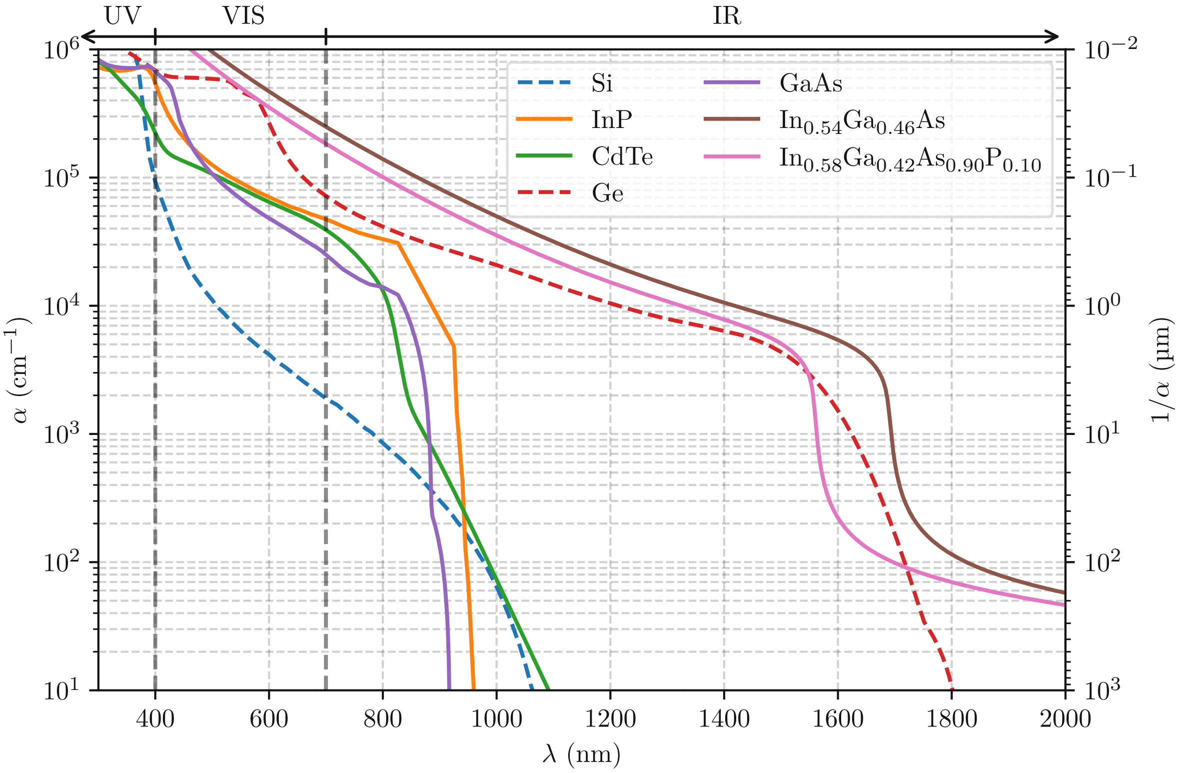

Figure 2.4. Absorption coefficient of selected direct (solid line) and indirect (dashed line) bandgap semiconductors. The right hand side axis indicates the corresponding absorption depth $1/\alpha$. The upper axis indicates the ultra-violet (UV), visible (VIS) and infrared (IR) spectral regions. Data sources: Si: [64], Ge: [65], InP: [66], CdTe: [67], GaAs: [68], $In_{0.54}Ga_{0.46}As$ [69, 70], $In_{0.58}Ga_{0.42}As_{0.90}P_{0.10}$ [69, 70].

as indirect bandgap semiconductor has a rather low value of α compared to the direct bandgap materials shown in the plot. The high absorption coefficient values for Ge, also an indirect bandgap semiconductor, are exceptional and related to its band-structure, since the indirect gap energy is only ≈ 0.1 eV below the lowest direct optical transition for this material. Comparing, e.g. the absorption efficiency at 800 nm between Si and Ge by considering Equation 2.5 and the data associated to Fig. 2.4, it turns out that to absorb 90 % of the incident power it takes a thickness of 0.6 µm for Ge, whilst it takes about 29 µm of material thickness for Si to absorb the same.
Practically, the above mentioned implies that for different applications with corresponding target spectra, different materials may come into consideration. Efficient absorption, however, is not the only important aspect when defining the material for an optical application, as there are more aspects such as long-term stability, suitability for mass production, toxicity or availability of the material, that need to be considered [71]. This is the apparent reason, why silicon is still the dominating material in the PV as well as light sensing industry despite its materialistic disadvantages.

2.2.2 The Law of Lambert Beer and Optical Generation

The law of Lambert Beer describes the absorption of light as function of the distance into the absorber material as described with Equation 2.5. In that case, it is formulated in terms of the incident optical power, but it can also be formulated in terms of the incident photon irradiance E_p. The relations, Equations (2.5) and (2.6) can be derived, considering a plane electromagnetic wave with (vacuum) wavelength λ, traveling through a medium with complex refractive index $\underline{n} = n + \mathrm{i}\kappa$. The electric field as function of position x and time t, $\mathbf{E}(x,t)$ can be written as

$$\mathbf{E}(x,t) = \mathbf{E}_0 \mathrm{e}^{\mathrm{i}(2\pi \underline{n} x/\lambda - \omega t)} = \mathbf{E}_0 \mathrm{e}^{-2\pi\kappa x/\lambda} e^{\mathrm{i}(2\pi n x/\lambda - \omega t)}, \tag{2.7}$$

and the intensity $I(x)$ which is proportional to the square of the electric field

$$\mathbf{E}(x,t)^2 \propto I(x) = I_0 \mathrm{e}^{-4\pi\kappa x/\lambda} = I_0 \mathrm{e}^{-\alpha x}. \tag{2.8}$$

In the last relation the absorption coefficient was introduced as described in Equation (2.6). Considering that any loss in light intensity is associated with light absorption, Equation (2.8) can be utilized to calculate a position dependent generation rate G, that is defined as the number of EHPs that are generated per unit volume per second. In general, when discussing light absorption in semiconductor devices such as photodiodes, energy and number of particles may be used analogously according to the important fact that each photon in a beam of monochromatic light with wavelength λ carries the energy $E_\mathrm{phot} = hf = h\frac{c}{\lambda}$, as introduced in Equation (2.3). Therefore the total number of EHPs generated by the absorption of monochromatic light may be simply omitted by dividing the absorbed radiant energy Q_e by E_phot. Considering the absorbed EHPs per unit time one has to consider the radian flux Φ_e rather than the radiant energy

Table 2.1. Important radiometric quantities

symbol	quantity	unit	description
Q_e	radiant energy	J	received energy
Φ_e	radiant flux	W	Q_e per unit time
E_e	irradiance	$\mathrm{W/m^2}$	Φ_e per unit area
$I_{\mathrm{e},\Omega}$	radiant intensity	W/sr	Φ_e per solid angle
$L_{\mathrm{e},\Omega}$	radiance	$\mathrm{W/sr/m^2}$	E_e per unit solid angle

Q_e as can be seen in Tab. 2.1, where some important radiometric quantities are listed. Since the light intensity decays exponentially with the absorption depth according to Lambert-Beers law and considering that the light is ”composed” of photons that excite EHPs upon absorption, also the generation rate follows an exponential dependency

$$G(x) = G_0 \mathrm{e}^{-\alpha x} = (1 - R^*)\,\alpha N_0 \mathrm{e}^{-\alpha x}. \tag{2.9}$$

The pre-factor G_0 was omitted in the above equation considering that the photon flux at the surface N_0, i.e. the number of photons per unit area per second impinging on the sample surface is given by $N_0 = E_\mathrm{e}/hf$ and by assuming that in a sample with infinite thickness all carriers must be absorbed

$$N_0 \overset{!}{=} \int_0^\infty G(x)\,\mathrm{d}x\,. \tag{2.10}$$

Additionally, it was considered that photons hitting the sample surface may be partially reflected, which is described by the reflectance R^*. The photon flux N_0 is sometimes also denoted E_p in analogy to the irradiance E_e.

2.2.3 Spectral Responsivity of a Photodetector

As discussed in the above sections the absorption of light leads to the generation of EHPs within a semiconductor. Assuming absorption between depth x_1 and x_2 the absorbed photon flux N_abs can be calculated as:

$$N_\mathrm{abs} = (1 - R^*) \int_{x_1}^{x_2} G(x)\,\mathrm{d}x = (1 - R)E_\mathrm{p}\left(\mathrm{e}^{-\alpha x_1} - \mathrm{e}^{-\alpha x_2}\right) \tag{2.11}$$

As mentioned in Section 2.1.1, generated carriers can lead to a terminal current by means of drift or diffusion. Depending on the presence of an electric field their movement is either directed (drift) or random (diffusion). Either way, excess carrier may lead to a current if they do not recombine before reaching an electrode. Assuming, each photon creates on average ζ EHPs the corresponding current density may be calculated as

$$j_\mathrm{PD} = \zeta N_\mathrm{abs} q. \tag{2.12}$$

The quantum efficiency (QE) of a photodiode describes which fraction of the generated carriers finally contribute to the terminal current

$$\mathrm{QE} = \frac{\zeta N_{\mathrm{abs}}}{E_{\mathrm{p}}} = \zeta(1 - R^*)\left(\mathrm{e}^{-\alpha x_1} - \mathrm{e}^{-\alpha x_2}\right). \tag{2.13}$$

In this work, the quantum efficiency will be either referred to by QE or η_{Q}. To distinguish between losses entirely within the active semiconductor and losses including reflectance in the stack above the device under investigation, the internal quantum efficiency (IQE) has been established, in that case the reflectance is $R^* = 0$. In the same context the quantum efficiency according to Equation (2.13) is referred to as external quantum efficiency (EQE). Finally, the responsivity R of a photodiode is defined as the measured photocurrent I_{PD} divided by the absorbed radiant flux

$$R = \frac{I_{\mathrm{PD}}}{\Phi_{\mathrm{e}}} = \frac{j_{\mathrm{PD}}}{E_{\mathrm{e}}} = \frac{\zeta q \lambda}{hc}(1 - R^*)\left(\mathrm{e}^{-\alpha x_1} - \mathrm{e}^{-\alpha x_2}\right). \tag{2.14}$$

Comparing Equation (2.13) and (2.14) the fundamental relation between QE and R can be easily seen

$$R = \frac{\lambda q}{hc}\mathrm{QE}. \tag{2.15}$$

The core assumption of the relations presented in this section is that a single photon may excite at maximum a single EHP. It is, however, well known that this limit can be overcome by impact ionization [72], where the excess energy of the EHP is high enough to create further EHPs. In that case, a quantum efficiency larger than one may be observed and it can be described with gain $\zeta > 1$ in Equation 2.14. $QE > 1$ for photodiodes have first been explained by Antocik in 1957 [73] and were observed in the following in many semiconducting materials, such as in Si and Ge [74]. However, while above unity QEs have been reported for IQEs, there are still fundamental obstacles to achieve very high values for EQEs [75]. For silicon, EHPs with energies high enough for impact ionization are mainly stemming from ultra-violet (UV) light, which also implies that they are mainly absorbed very close to the surface and surface recombination effects play an important role [76]. Figure 2.5 shows the calculated (with Equation (2.11) to (2.14)) responsivity R for some commonly used optoelectronic semiconductors. In that case absorption between $x_1 = 100\,\mathrm{nm}$ and $x_2 = 20\,\mu\mathrm{m}$ was considered. As can be seen in this plot, the absorption of silicon is mainly in the visible (≈ 400 nm to 700 nm) and partially in the near-infrared (NIR) (≈ 800 nm to 2500 nm) [77] region. Other semiconductors, like the alloys $\mathrm{In_{0.54}Ga_{0.46}As}$ or $\mathrm{In_{0.58}Ga_{0.42}As_{0.90}P_{0.10}}$ are mainly active in the NIR region. It should be noted that with the chosen parameters there is hardly any absorption for light in the UV region. This is, however, not related to the materials themselves, but to the lower absorption depth x_1 chosen to construct the plot. Nonetheless, silicon is still suitable for UV applications, because silicon photodetectors may outperform detectors made of other materials with respect to performance, reliability and cost [78]. A more fundamental limit to silicon is the long-wavelength region, where,

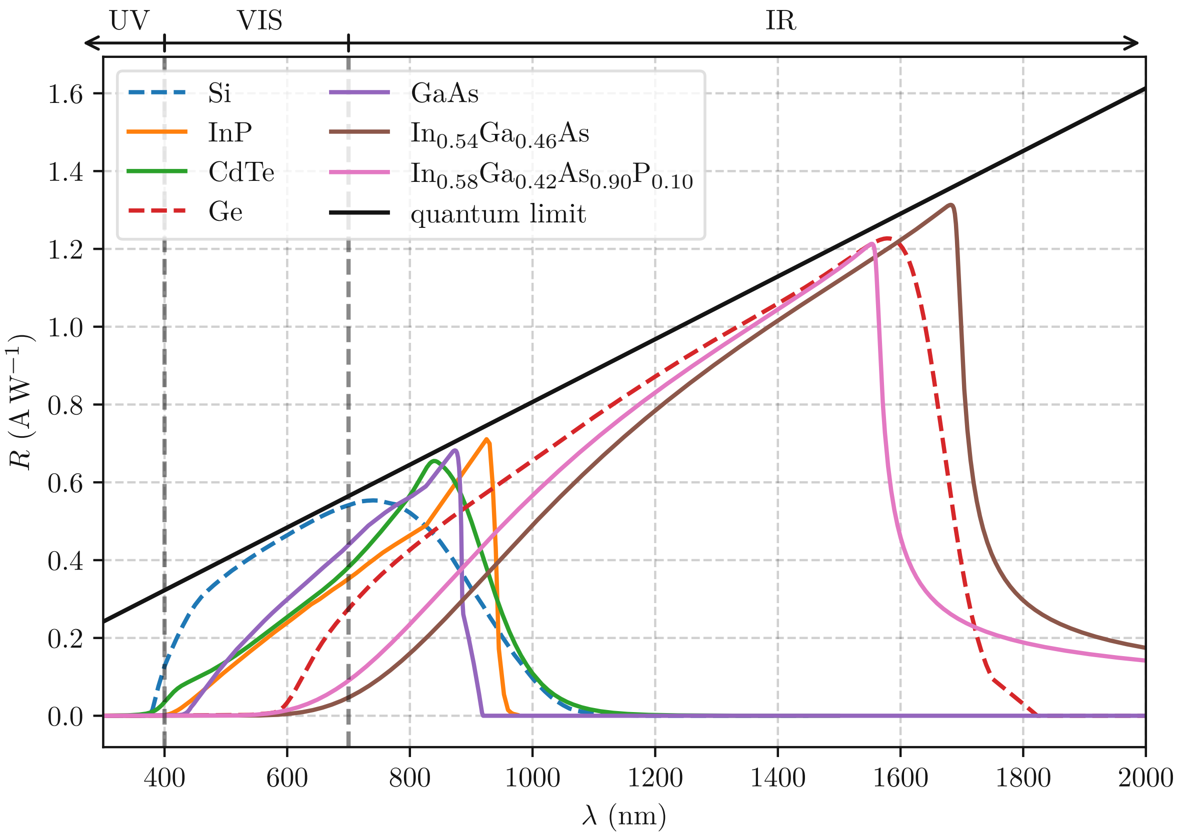

Figure 2.5. Responsivity R of selected direct (solid line) and indirect (dashed line) bandgap semiconductors versus wavelength λ computed using Equation (2.11) to (2.14) with $\zeta = 1$, $R = 0$, $x_1 = 100\,\text{nm}$, $x_2 = 20\,\mu\text{m}$. The upper axis indicates the ultra-violet (UV), visible (VIS) and infrared (IR) spectral regions. Data sources for the used absorption coefficients α according to Fig. 2.4.

as discussed in Sec. 2.2.1, a critical wavelength λ_{crit} can be assigned to a material. Light absorption for wavelengths larger than λ_{crit} is very inefficient. Therefore, for infrared (IR) detection commonly compound materials are employed, where the bandgap can be tailored by varying the individual compound's fractions. In Fig. 2.6 the bandgaps and lattice constants for different III-V and II-IV compounds are depicted. As was mentioned in Section 1.1, for IR applications HgCdTe is a commonly used ternary II-IV compound. It is competing with III-V compounds which are also frequently used for IR applications [79].

In Fig. 2.5 also the quantum limit is indicated, which is the responsivity according to Equation 2.15 with a quantum efficiency of one. As discussed above, this limit may be overcome in the case of impact ionization. The quantum efficiency may also be defined, as the ratio of responsivity to the maximal achievable (considering a gain of $\zeta = 1$) responsivity. Similarly, to the quantum limit for the efficiency of photodiodes, the Shockley Queisser efficiency limit defines a fundamental limit for the efficiency of solar cells [81]. In that case, the maximal efficiency of solar cells is calculated based on the assumption that radiative recombination is the only loss mechanism.

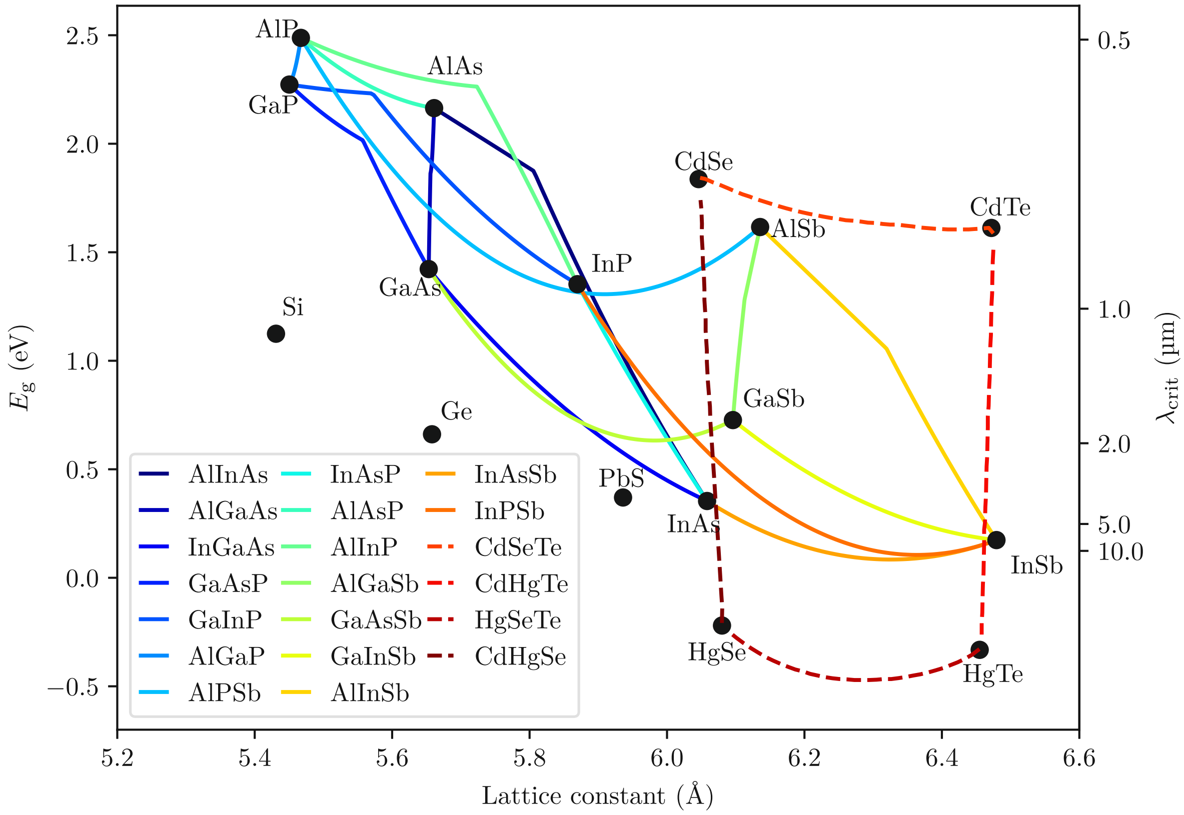

Figure 2.6. Optical bandgap engineering: commonly used compound semiconductors. Bandgap E_g and lattice constants for different materials and compounds. The right hand side axis shows the corresponding critical wavelength λ_{crit} according to Equation (2.4). Solid lines: III-V compounds, dashed lines: II-IV compounds. This graph was created using the *solcore* python package [80]. HgSe and HgTe are semimetals and therefore have a negative bandgap.

2.2.4 Dynamic Response: Rise and Fall Times

Besides the detection efficiency described by either the quantum efficiency or responsivity described in the previous section another important photodiode parameter is the dynamic performance. That is, essentially, the time it takes to reach the maximum current level if a light pulse hits the sample. And, on the other side, the time it takes to return to the dark current after a light pulse turns off. Practically, the *rise* and *fall* times of a photodetecting device are mostly defined as the time between the 10 % photocurrent and 90 % photocurrent levels (rise time) and vice versa for the fall time the time between the 90 % photocurrent and 10 % photocurrent levels. Alternatively, rise and fall times are sometimes defined referring to exponential functions as time to reach $1 - 1/e$ and $1/e$ photocurrent levels. The rise and fall times (τ_r and τ_f, respectively) according to the 10 % to 90 % definition are shown in Fig. 2.7. Whilst for an ideal photodiode the photocurrent follows the light pulse without delays, in real devices τ_r and τ_f arise because of different mechanisms, which may be listed as follows [82]:

1. τ_{RC}: the time associated with the circuitry: $\tau_{RC} = R_{eq}C_{eq}$, where R_{eq} is the equivalent resistance and, similarly, C_{eq} is the equivalent capacitance associated to the

photodiode and the load.

2. τ_{drift}: the average time associated to carriers drifting through the pn-junction depletion zone.
3. τ_{diff}: the average time associated to carriers diffusing till reaching the depletion zone.

The total rise and fall times can then be described as [82]

$$\tau_{\mathrm{r,f}} = \sqrt{(2.2\tau_{\mathrm{RC}})^2 + \tau_{\mathrm{drift}}^2 + \tau_{\mathrm{diff}}^2}, \tag{2.16}$$

where the prefactor 2.2 for τ_{RC} accounts for the fact, that τ_{RC} defined as an exponential time constant for the relaxation process [83]. In many cases, the diffusion component is the slowest component and as such dominating Equation (2.16). Therefore, for high-speed applications one approach is to use intrinsic materials, where the depletion zones are very wide, such that either carriers are entirely generated within the space charge region or that their distance to diffuse to the space charge region is minimized. As will be shown in Section 3.3 also interaction with defects, i.e. trapping and detrapping events, may affect the rise and fall times discussed in this section. However, for the definition of rise and fall times according to Equation (2.16) the impact of transients associated to trapping and detrapping is in many cases negligible, i.e. the (de-)trapping currents are less than 10 % of the total photocurrent.

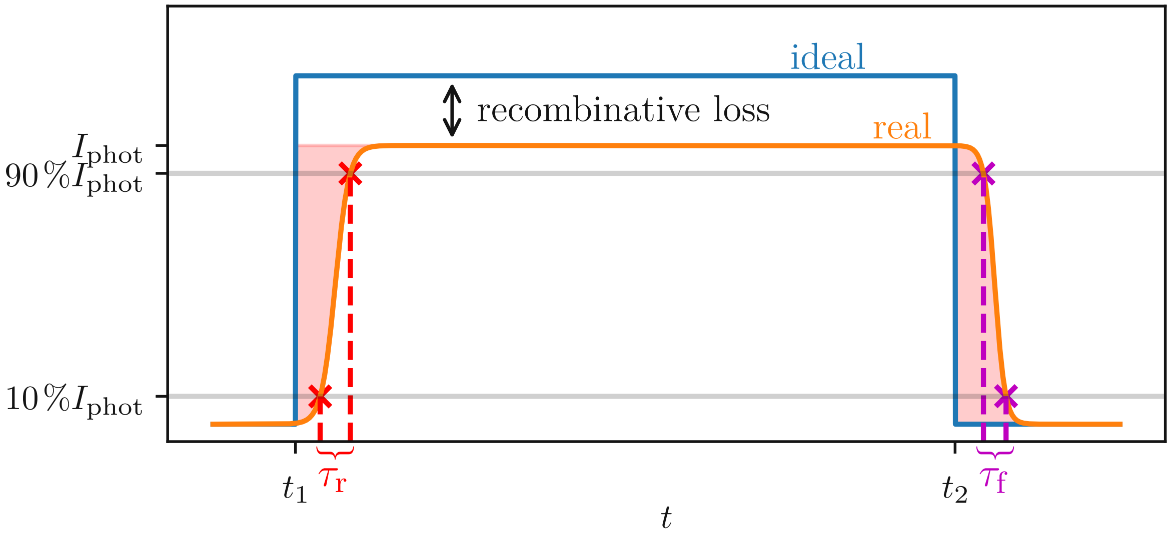

Figure 2.7. Schematics of rise and fall times of a photodiode. Photocurrent I_{phot} versus time t upon excitation with a rectangular light pulse between t_1 and t_2. In an ideal device the photocurrent follows the light pulse without any delays, in real devices non-zero rise and fall times arise. Because of recombination the real photocurrent is less than the maximal achievable ideal photocurrent.

2.2.5 Photodiode Parameters and Figure of Merit

For the development of photodetectors based on pn-junctions it is important to consider its parameters. In the preceding sections some parameters, such as the dark current (reverse bias current under no illumination conditions), responsivity or rise and fall times have been introduced. Depending on the target applications certain parameters may be more or less important and more or less in the focus of optimization. As a consequence, it is difficult to define a single figure of merit for photo detectors. One important consideration is, if an optical signal can be detected, i.e. if the electric current associated to the optical signal is larger than the noise floor. The corresponding figure of merit is called the noise-equivalent power (NEP), and defined as the optical input power P_{op} required to create a detector signal-to-noise ratio (SNR) of one [84]

$$\mathrm{NEP} = \frac{I_{\mathrm{noise}} h f}{\eta_{\mathrm{Q}} e}, \tag{2.17}$$

where different sources may contribute to the root mean square (RMS) noise current I_{noise}. In general for semiconductors, and also specifically for detectors, these contributions may be listed as follows [84, 85]:

- **Shot Noise $I_{\mathrm{noise,shot}} = \sqrt{2qI_{\mathrm{PD}}B}$:** This is due to the random arrival of photons at the photodiode's surface. It is a fundamental noise source associated with the discrete nature of light and can be described using Poisson statistics. This noise component can be calculated considering the total photodiode current I_{PD} as well as the frequency measurement bandwidth B.

- **Thermal Noise $I_{\mathrm{noise,thermal}} = \sqrt{4k_{\mathrm{B}}TB/R_{\mathrm{L}}}$:** This noise source is inevitably associated to the load resistance R_{L} of the photodiode and can be explained by the statistics and distribution of velocities of charge carriers. It is furthermore related to the temperature T of the photodiode as well as the frequency bandwidth B.

- **1/f Noise (Flicker Noise):** This low-frequency noise source can be caused by defects or impurities in the photodiode material. It becomes more significant at lower frequencies. Defect related generation-recombination associated noise will be discussed in more detail in Section 3.3.

Additionally, circuitry, like a co-integrated analog amplifier or integrator, or environmental factors such as vibrations or temperature fluctuations may act as noise sources. Another performance metric for a photodetector is its *detectivity* D, which is defined as the inverse of the NEP

$$D = \frac{1}{NEP}. \tag{2.18}$$

To normalize D to parameters that are not intrinsic to the system, i.e. the device area A and the frequency measurement bandwidth B, the specific detectivtiy D^* can be introduced as [86]

$$D^* = \frac{D}{\sqrt{AB}} \tag{2.19}$$

Finally, the following list shall give a brief summary of some of the most important photodiode parameters introduced in this as well as the preceding sections

- **Dark Current:** Dark current is the current that flows through a photodiode when no light is incident on it. It represents the inherent noise in the absence of light and should be minimized for improved performance.
- **Capacitance:** The capacitance of a pn-junction can be considered as the parameter describing how much charge per voltage is stored and separated by the depletion zone (model of a parallel plate capacitor). Generally, low values for the photodiode capacitance are desired as it acts negatively on the device' noise performance as well as RC time constant in terms of the temporal behavior.
- **Spectral Responsivity and Quantum Efficiency:** Spectral responsivity quantifies a photodiodes sensitivity to light at different wavelengths. It describes how well the photodiode converts incident photons into electrical current, and it can vary across the electromagnetic spectrum. It is directly related to the quantum efficiency via Equation 2.15.
- **Rise/Fall Times:** Rise time and fall times are measures of a photodiodes response speed. Depending on the application very short rise and or fall times may be required.
- **Detectivity:** Detectivity is a figure of merit that combines the sensitivity and noise characteristics of a photodiode. It quantifies the ability of a photodiode to detect weak optical signals while accounting for its noise sources.
- **Fill Factor:** The Fill Factor is given by the percentage of the photoactive area to the total device area, including read-out circuitry. If, for example, 3/4 of a photodiode's total area are covered by the actual photosensitive region and the rest is covered by readout circuitry and metal lines blocking light, the diode has a fill factor of 75 %.

While the above list considers some of the most common photodiode parameters for certain applications it should be noted, that additional factors, such as cost-efficiency or producibility, are inevitably very important as well. There are also recent attempts to incorporate multiple of the above parameters into a single figure of merit (FOM) [87]. However, due to the versatile applications for photodetectors no single FOM for all possible applications can be established.

Chapter 3

Defects in Photodetectors

While in theory semiconductors are often considered as perfect crystals, real structures contain imperfections. As mentioned in Section 2.1.1 the basic photodiode structures are rather simple pn-junctions in semiconducting materials. The dopants in the p-doped and n-doped regions in these materials are nothing less than defect states that strongly alter and influence the electrical and optical parameters of the basis material. Stunningly, for semiconductors already a very small amount of defect states compared to the total amount of host atoms is able to completely control and influence parameters, such as the resistivity. While these defect states are purposely introduced into the semiconductor, a certain amount of defects are also unavoidably present and may strongly impact the material parameters. While some of the defects may be introduced or created during processing of the device, some defects may be present already in the host material, i.e. in the unprocessed semiconductor wafers. Actually, from a thermodynamic point of view, following the second law of thermodynamics, some defects *must* be present in any semiconductor at finite temperatures [88].

In a broad definition, defects are referred to as any perturbation of the elsewhere perfect crystal. More specifically defects may be distinguished by their electrical parameters, such as energy levels and cross sections, as well as their nature (impurity, intrinsic, line defect, areal defect...). In this section this specification and description of defects is reviewed, for the specific case of photodiodes. While in principle the presence and nature of defects in a processed semiconductor, i.e. in any device (metal–oxide–semiconductor field-effect transistor (MOSFET), bipolar junction transistor (BJT), resistor, diode, ..), of a CMOS process, does not depend on the device itself, the way the defects may interfere with the device operation well does.

3.1 Defect Classification

Defects may be classified by their dimensionality. In the following subsections this classification will be discussed starting from zero-dimensional point defects to two-dimensional surface and interface defects. Apart from this classification based on dimensionality, they may also be divided into *intrinsic* (also *native*) defects and *extrinsic* defects. Intrinsic defects only involve atoms that are present and form the crystals whereas extrinsic defects consist of impurities, i.e. elements foreign to the crystal. For the intrinsic case, there are two versions: either a host atom is missing at its supposed place, which is called a *vacancy*, or an additional host atom is sitting at a side where it is not supposed to be, which is called an *self-interstitial*. Extrinsic defects, on the other hand, may also come in two versions: either a foreign atom is taking one of the host sides, which is called a *substitutional* defect or a foreign atoms is sitting at an interside, which is then called *interstitial*.

3.1.1 Bulk Defects: Point and Line imperfections

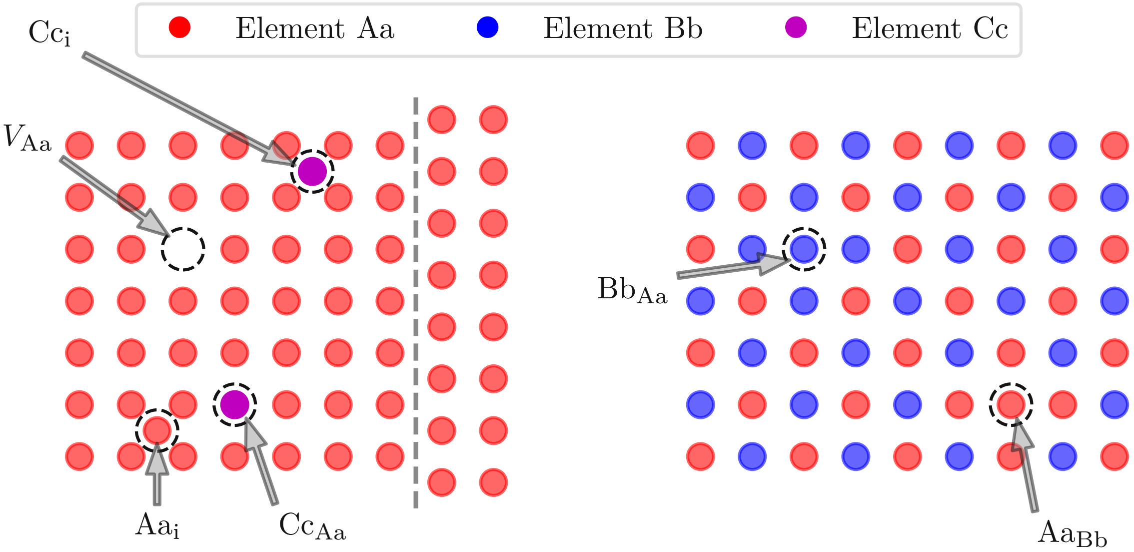

Figure 3.1. Schematics of different defect types in elemental **(left)** and compound **(right)** crystals. **(left)** Elemental crystal (element Aa) with intrinsic defects, i.e. lattice vacancy V_{Aa} and self-interstitial $\mathrm{Aa_i}$, and extrinsic defects, i.e. substitutional element Cc on an Aa side $\mathrm{Cc_{Aa}}$ and interstitial $\mathrm{Cc_i}$. The dashed vertical line marks an edge dislocation. **(right)** Compound crystal (elements Aa and Bb) with antisite defects $\mathrm{Bb_{Aa}}$ and $\mathrm{Aa_{Bb}}$.

Defects in the bulk of a semiconducting material may be point-like, i.e. zero-dimensional crystallographic errors or one-dimensional crystallographic mismatch, called dislocation. Fig. 3.1 shows bulk defects in elemental as well as compound crystals. The self-interstitial and vacancies may be formed in pairs, i.e. these defects may be formed if a host element leaves its supposed place (creating a vacancy) and moves to an unsupposed place, thereby forming an interstitial. These defect pairs are then

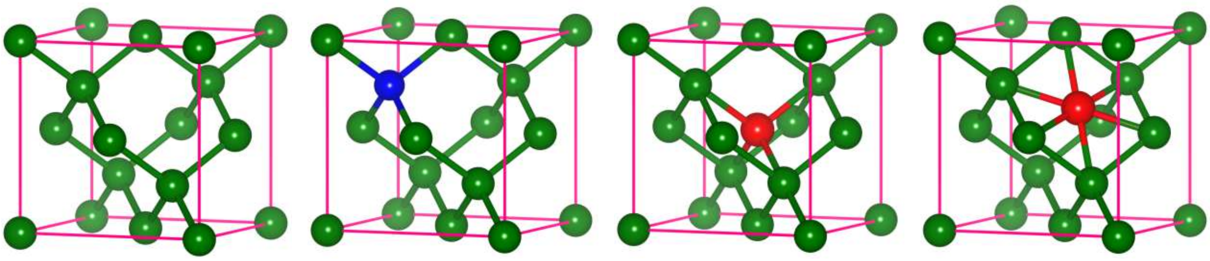

Figure 3.2. Example of point defects in the silicon crystal (diamond crystal structure). **(outer left)** Perfect silicon crystal as reference. **(left)** Substitutional atom, i.e. the blue atom replacing one of the green host atoms. **(right)** Interstitial atom (red) in the tetrahedral configuration. **(outer right)** Interstitial atom (red) in the hexagonal configuration. This plot was created using the VESTA software [89].

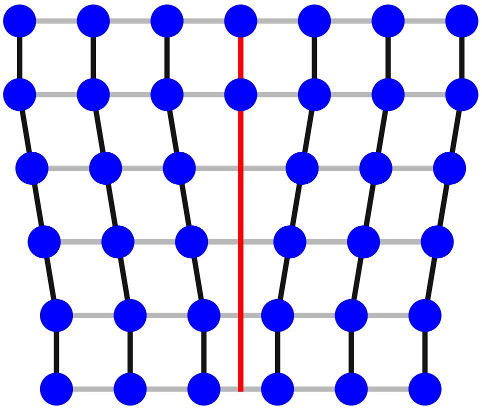

Figure 3.3. Schematics of a dislocation (edge) defect in cubic crystal shown in a 2D-plane. The deformation may be imaginary thought as caused by adding an extra plane (red line) of atoms in the upper half of the structure. The defect will cause atoms in the upper planes to be compressed whereas defects in the lower planes will be extended [90].

called **Frenkel defects**, named after their discoverer Yakov Frenkel [91]. Another way these defects are created is by leaving the host place and moving to the surface, which means creating the vacancy without becoming an interstitial. This defect is called a **Schottky defect**. For silicon, as well as many other important materials for semiconductor research and industry, point-like defects are well studied, and a lot of studies have amassed showing experimentally extracted defect parameters [92, 93, 94, 95] or simulation-wise extracted defect parameters [96, 97]. In Fig. 3.2 different point-like defects for the silicon crystal structure (diamond) are shown. As can be seen in the plots of this figure, interstitial atoms may take different positions within the 3-dimensional crystal structure. The two configurations shown in this figure are not complete and are shown exemplarily. Other well-known interstitial defect configurations include the bond-centered interstitial (one Si-Si is broken by an interstitial in the middle of the breaking line), the dumbbell interstitial or the $\langle 1\,1\,1 \rangle$-split interstitial [98]. It should be noted that typically the presence of a defect will also cause the positions of the remaining host atoms to be shifted, which, out of simplicity, was not considered in these plots. These equilibrium positions can be calculated by means of first principle calculations like density-functional theory (DFT).

Next to zero-dimensional point-like defects line imperfections, so called dislocations, might occur in the bulk of a crystal. One schematic example of a dislocation is shown in Fig. 3.3. The defect shown there is the simplest form of a dislocation and is called an

edge dislocation. Next to this type of dislocation there is the so called screw dislocation where successive atom planes are transformed into the surface of a helix [90]. More complicated forms of dislocations can be formed by combining segments of edge and screw dislocations. In silicon different forms of edge dislocations have been observed and described [99] where an example is shown in Fig. 3.4. The dangling bonds associated to the dislocations as drawn in this figure might be electrically active, i.e. interact with the free charge carriers of the crystal [100, 101].
It should be noted, that the defects discussed above are not limited to crystalline structures only. Actually, they may as well occur in amorphous materials like the amorphous silicon dioxide used as gate insulators in most CMOS processes. Defects in gate oxides are indeed also very important for transistor reliability issues where they can cause breakdowns or shift the gate threshold voltage. A structural plot of amorphous SiO_2 can be seen in Fig. 3.5 in the next section. A common defect in this insulating material is the E' center, which is an unpaired electron bond of one silicon atom, where several variants of these defects exist [102]. Another important defect is the oxygen vacancy where an oxygen atom is missing between the two silicon atoms.

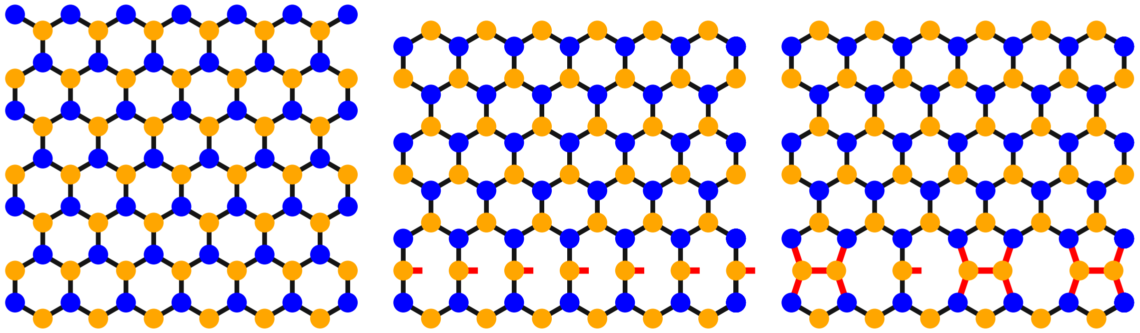

Figure 3.4. Example of a dislocation in the silicon $(1\,1\,1)$ plane. The blue and orange circles mark the Si atoms of the two face-centered cubic (fcc) sub-lattices forming the diamond crystal structure [103]. The perfect crystal structure **(left)** is disturbed by the so called 30° partial dislocation. The unreconstructed structure **(middle)** tends to change to the reconstructed structure **(right)** since this phase is energetically preferred [104]. Still in the reconstructed structure unpaired dangling bonds are present. This figure is recreated after [99].

3.1.2 Interface Defects

The bulk of a material can be considered as individual mono-layers on top of each other with the very same structure, i.e. atomic spacings etc. This however, is quite different for interfaces, where there might be a sudden structural mismatch between the top layer of the first material and the bottom layer of the second material forming the interface. This makes interfaces very prone to large defect densities and defines challenges to grow dielectrics with low interface defect densities on semiconductors in semiconductor processes. Infact, one of the main reasons for silicon being the predominant material in the semiconductor industry is the ability to grow silicon-dioxide as insulating material on top of silicon with very low defect densities. This is quite remarkable considering an about 30 % larger Si to Si atomic distance in the amorphous SiO_2 compared to the Si crystal [105]. In Fig. 3.5 the structure of amorphous SiO_2 is shown. It consists of tetrahedral SiO_4 basis units linked together by "sharing" oxygen atoms with various bonding angles leading to the amorphous phase with a stoichiometry of SiO_2. Additionally, passivation techniques have been developed that allow to passivate defects present at this interface, by minimizing the interaction capability of defects with charge carriers. In Fig. 3.6 a 3-dimensional plot of a Si-SiO_2 interface is shown. As can be seen, some of the Si atoms bond to hydrogen atoms (colored white in this plot). The passivation of otherwise dangling Si bonds with hydrogen (hydrogenation) is one major factor that leads to the high-quality interfaces achieved in nowadays SiO_2 gates oxides. This is typically done in annealing treatments after the oxide growth, where the source of hydrogen may be the annealing ambient like H_2 or a forming gas [106]. By doing so, interfacial trap densities for dangling bonds can be successfully reduced from about $10^{12}\,\mathrm{cm}^{-2}$ before annealing treatment to about $10^{9}\,\mathrm{cm}^{-2}$ to $10^{10}\,\mathrm{cm}^{-2}$ after annealing in CMOS processes [107].

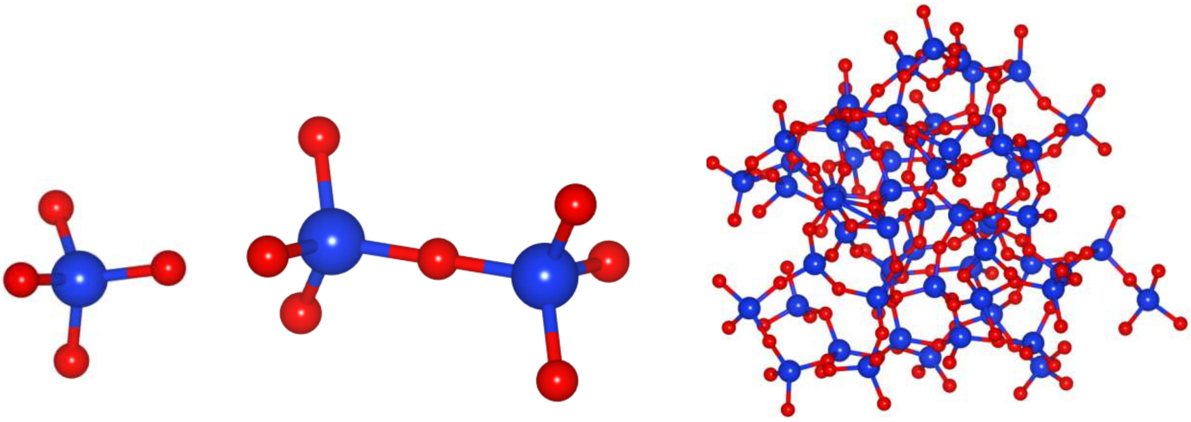

Figure 3.5. 3-dimensional structure of silicon dioxide. **(left)** Tetrahedral basis unit consisting of a silicon atom (blue) bonded to 4 oxygen atoms (red). **(middle)** Amorphous silicon dioxide (a-SiO_2) is formed by linking the SiO_4 tetrahedra with varied Si-O-Si bond angles (here 180°). One oxygen atom is "shared" between two silicon atoms leading to a 1:2-Si:O stoichiometry. **(right)** Amorphous silicon dioxide structure with atomic coordinates taken from [108]. This plot was created using the VESTA software [89].

Specifically, the defects at the Si-SiO_2 interface have been investigated with great detail since this interface is crucial for the operation of silicon metal–oxide–semiconductor (MOS) devices. Not only defects at this interface affect and degrade the nominal performance of these devices but they also impose severe drawbacks in terms of reliability [31, 109]. The main electronically active defects at this interface are Si dangling bonds, called P_b-type centers, with three subtypes referred to as P_b, P_{b1}, P_{b2}. All of these defects have been identified as unsaturated Si dangling bonds back-bonded by three other Si atoms without bonding to oxygen atoms[110]. A schematic for the P_{b1} and P_{b2} defects at the Si(1 0 0)-SiO_2 interface is shown in Fig. 3.7. As can be seen, some of the dangling bonds at this interface are passivated by hydrogen atoms. However, high energetic (and thus very fast) carriers in transistor channels may have enough kinetic energy to break these passivated bonds which can lead to reliability issues (called hot carrier degradation) [111].

As mentioned above, the defect landscape at the semiconductor to oxide interfaces poses severe drawbacks and challenges to the operation of transistors, however, it is well known that defects at the Si-SiO_2 also play an important role in minority carrier based devices such as photodiodes or BJTs. The interaction of minority carriers with defects at the Si-SiO_2 interface might be different to the interaction of majority carriers in the transistor channel and these defects. While in devices relying on the field-effect, trapped carriers might influence the electrostatics and electro-dynamics, another important point adds up in minority carrier based devices, which is defect-mediated recombination. As will be explained in more detail in Section 3.2 interface defects, as well as bulk defects discussed in the previous section, can act as recombination centers which can reduce the performance of minority carrier based devices. It should be noted, that this is not only limited to the defects at the Si-SiO_2 interface but actually to any interface minority carrier might diffuse to. This is also a very important difference when considering and comparing the physics in field-effect based majority carrier devices and e.g. photodiodes. While for the operation of the transistor the main region of interest regarding carrier trapping is the channel and semiconductor-to-oxide interface at the channel, minority carriers responsible for the main signal in photodiodes might diffuse to any other interface, such as the interface between an epitaxial layer and a below laying substrate or the interface between the semiconductor and an above deposited low-quality interlevel dielectricum.

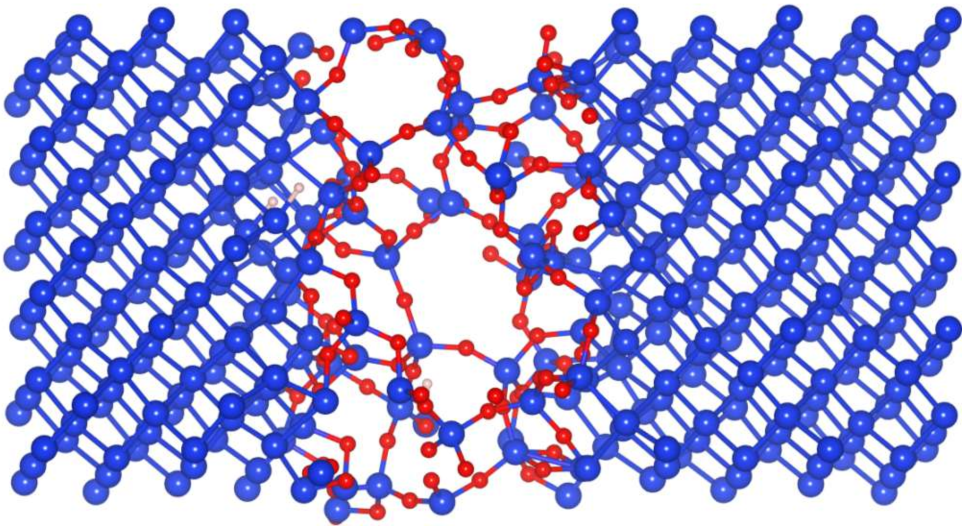

Figure 3.6. The silicon to silicon dioxide interface. Supercell of a Si-SiO_2-Si interface structure after molecular dynamics simulation of the atomic configuration. Si atoms are colored blue, oxygen atoms are colored red and hydrogen atoms are colored white. The structural data was provided as supplemental material of reference [112]. This plot was created using the VESTA software [89].

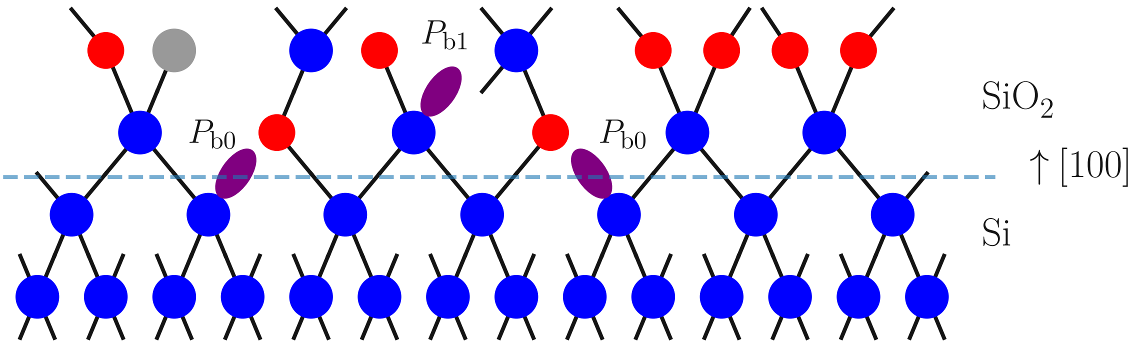

Figure 3.7. Dangling bonds (violet) at the Si(1 0 0)-SiO_2 interface. Silicon atoms are colored blue, oxygen atoms are colored red and hydrogen atoms are colored gray. Recreated after [113].

3.2 Defect-Carrier Interaction

While the previous section focused on how to classify crystallographic mismatch and where it may occur within a material system, this section aims at providing a basic understanding of how defects can interact with charge carriers. Basically the interaction of defects with carriers involves a change in the charge state of the defect. Therefore this section focuses on defects that are able to change their charge state by capturing or emitting charge carriers. Defects that are not able to do so, i.e. defects that always have the same charge state, are still important as they may affect the electrostatics or equilibrium carrier concentrations of the device. An example of this kind of defects are fixed oxide charges within the gate oxide of a transistor, that will lead to a persistent shift of the devices threshold voltage. Similarly, the doping of semiconductors can be seen as deliberate introduction of defect states into the crystal structure. These defects, however, are energetically so close to the bands, that in normal operation they will not change the ionization state. This way, donors can always be considered positively ionized (since they ”lost” an electron) and acceptors can always be considered negatively ionized (since they ”gathered” an additional electron). As will be discussed in this section, donors and acceptors are the very same crystalline defects as impurity atoms like iron in silicon, only their electrical defect parameters are different in the sense that under normal operational conditions the Fermi level will not cross their energetic position within the bandgap.

3.2.1 Defect parameter: Energy, Density and Cross-section

The physical presence of defects in a semiconductor crystal has important consequences for its electronic states. Generally, in semiconductors electronic states are described by the band diagram where the energy of charge carriers is considered as a function of the electron wave vector. Considering semiconducting materials it turns

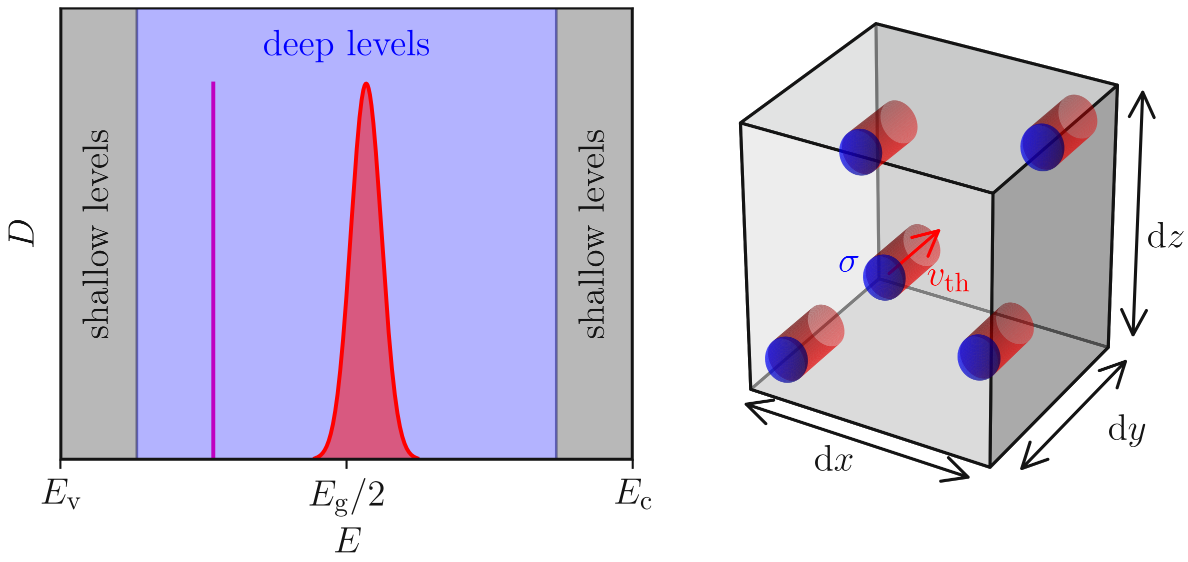

Figure 3.8. Electrical defect parameters. **(left)** Defect density D versus energy for two deep levels: one discrete (violet) and one continuously distributed (red). The trap density can be calculated by integration along the bandgap. **(right)** Schematic illustration of the capture cross section σ considering the volume $\mathrm{d}V = \mathrm{d}x\mathrm{d}y\mathrm{d}z$. Recreated after [114].

out that there are continua of allowed states (bands), as well as energies with no corresponding states (bandgap). However, the presence of defects in the crystal introduces additional states that may be populated by charge carriers. In principle, anything that interrupts a crystals periodicity will create localized states that are not part of the semiconductor band structure. It should be noted that the activation energy of defects does not necessarily have to be within the bandgap [115]. If the activation energy is within the bandgap, it depends on the ionization energy of these states, if they can act as traps. For example, considering hydrogen like impurities, such as phosphorous in silicon, the ionization energy may be estimated with the Rydberg constant corrected for the carrier effective mass and the dielectric constant of the semiconductor. The ionization energy estimated with this approach is 25 meV compared to measured values of 45 meV, below the conduction band, respectively [116]. States that are so close to the silicon band edges will always be ionized at room temperature and are called *shallow levels*. There is no formal definition of a concrete energy to divide between *shallow levels* and *deep levels*, however, levels can be considered shallow when the separation of the ground state energy to the relevant band edge is comparable to the thermal energy $k_\mathrm{B}T$ at room temperature [117][1]. In the left hand side plot of Fig. 3.8 defect regions (shallow, deep) are plotted schematically against the energy E. Next to the activation energy of defects another important parameter is the density of defects. For bulk defects this density is typically calculated with respect to the unit volume (units of cm^{-3}) whereas for interface or surface defects with respect to the unit area (units of cm^{-2}). Another distinction can be made in terms of the energetic distribution, i.e. between discrete

---

[1] It should be mentioned, that there is still some ambiguity in the terminology of shallow and deep levels [118], in this work however, a distinction corresponding to the above description is made.

(violet peak in Fig. 3.8) and continuously distributed defect energies (red distribution in Fig. 3.8). A continuous distribution of traps is typically seen at interfaces, therefore trap distributions at interfaces are typically described with a interface trap density D_{it} in units of $\mathrm{cm}^{-2}\,\mathrm{eV}^{-1}$. A more detailed analysis reveals, that also the ionization state of a defect, i.e. if an defect state is occupied or not by an electron, will affect the neighboring atoms by attractive and repulsive forces leading to different equilibrated relaxation positions and energy levels, depending on whether the trap is occupied or not. This phenomena are not included in the basic Shockley-Read-Hall (SRH) theory discussed in the next section but they will be discussed in Section 3.2.3. Apart from energetic trap levels and trap densities, a parameter that describes how effectively charge carriers interact with defect states is the defect capture cross section. It should be mentioned, that the concept of defect capture cross section is phenomenological and agnostic about the physics of carrier trapping, still the great utility of this parameter and the SRH recombination model in general lies in its general applicability [119]. The concepts of capture cross section and capture rates can be understood as depicted in the right hand side plot in Fig. 3.8. Considering the infinitesimal volume $\mathrm{d}V$ containing $N_{\mathrm{VT}}\mathrm{d}V$ defects, where each defect is represented by its cross sectional area $\sigma = a^2\pi$, i.e. a circle with radius a, and furthermore that an electron is traveling through the crystal with thermal velocity v_{th}. This defines a cylindrical volume within which an electron is captured by the defect for certain. Consequently, the rate for capturing n electrons in the volume $\mathrm{d}V$ is given by the product of n, σ_n, v_{th} and the number of defects $N_{\mathrm{VT}}\mathrm{d}V$

$$C_{\mathrm{V,n}} = N_{\mathrm{VT}}\sigma_n v_{\mathrm{th}} n \mathrm{d}V, \tag{3.1}$$

and a capture rate normalized to the number of traps and the number of electrons can be defined as

$$c_n = \sigma_n v_{\mathrm{th}}. \tag{3.2}$$

The above capture rate is a macroscopic capture coefficient that should be generalized by averaging over all the electrons with respect to their energies[2]. An intuitive estimation for the order of magnitude for σ can be made considering the definition of the cross section as circle with radius a [114]. Taking, for example, the lattice constant of silicon $a \approx 5.43\,\text{Å}$, yields a result of $\sigma \approx 10^{-14}\,\mathrm{cm}^2$, which is a typical order of magnitude for cross sections of point defects in silicon [120]. Capture cross sections are most often determined experimentally, however, there are approaches in computing these values by first-principle-methods such as DFT [121]. Together with the energetic trap position/distribution, capture cross sections are important defect parameters affecting the carrier lifetimes via SRH recombination which is discussed next.

---

[2] This is discussed in further detail in Section 3.2.2 and given by Equation (3.10).

3.2.2 Shockley-Read-Hall (SRH) Recombination Model

The Shockley-Read-Hall (SRH) model describes trap-mediated recombination and generation in a statistical manner. It was first proposed by its eponyms Shockley, Read [35] and Hall in 1952 [36]. This model considers the rates of transitions from a trap state being occupied or empty (filled or not filled circle in Fig. 3.9) and the defects are described by the parameters as introduced in the previous Section 3.2.1. The model is based on four basic defect-carrier interaction processes as indicated in Fig. 3.9:

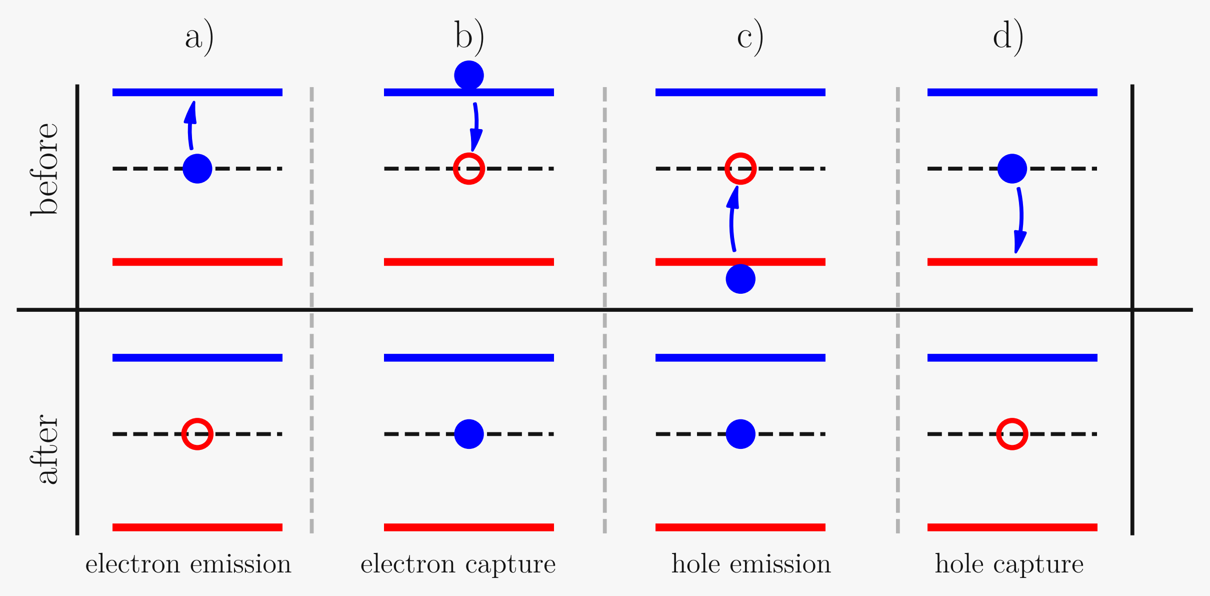

Figure 3.9. Shockley-Read-Hall recombination processes. A trap level (dashed horizontal line), energetically between the valence band (red) and conduction band (blue), may act as recombination center. The model consists of 4 basic processes: a) to d). Recombination and generation is occuring with a combination of process a) and c) or b) and d).

a) *Electron emission:* An electron is excited from the trap level to the conduction band.

b) *Electron capture:* An electron is released from the conduction band to the trap level.

c) *Hole emission:* An electron is excited from the valence band to the trap level, which is equivalent to an hole being released from the trap level to the valence band.

d) *Hole capture*: An electron is released from the trap level to the valence band, which is equivalent to an hole being excited from the valence band to the trap level.

To derive the SRH recombination rate, N_T traps are considered where n_T traps are filled with electron and p_T traps are not filled with electrons such that

$$N_\mathrm{T} = n_\mathrm{T} + p_\mathrm{T}. \tag{3.3}$$

This can be also expressed in terms of a trap occupation function $f_{(\mathrm{p})\mathrm{t}}$ for electrons (holes)

$$n_\mathrm{T} = N_\mathrm{T} f_\mathrm{t} \tag{3.4a}$$

$$p_{\mathrm{T}} = N_{\mathrm{T}} f_{\mathrm{pt}} \tag{3.4b}$$

$$1 = f_{\mathrm{t}} + f_{\mathrm{pt}}. \tag{3.4c}$$

In the following the rates for the processes as indicated in Fig. 3.9 will be introduced with reference to their name in that figure, i.e. k_{a} for the rate of process a), k_{b} for the rate of process b) and so forth. The rate for electron emission k_{a} can be calculated considering that the trap has to be occupied and the state in the conduction has to be free [35]

$$k_{\mathrm{a}} = \int_{E_{\mathrm{c}}}^{\infty} e_n(E) N_{\mathrm{t}} f_{\mathrm{t}}(E)(1 - f(E)) N_{\mathrm{c}}(E) \mathrm{d}E, \tag{3.5}$$

where e_{n} is an a-priori unknown emission rate in analogy to the capture rate, Equation (3.2) introduced in Section 3.2.1 and $f(E)$ and $N_{\mathrm{c}}(E)$ are the Fermi function and density of states in the conduction band, respectively. Similarly, the rate for process b), i.e. electron emission, k_{b} is given by

$$k_{\mathrm{b}} = \int_{E_{\mathrm{c}}}^{\infty} N_{\mathrm{t}}(1 - f_{\mathrm{t}}) c_n f(E) N_{\mathrm{c}}(E) \mathrm{d}E. \tag{3.6}$$

Considering that the net rate of electron capture $k_{\mathrm{ab}} = k_{\mathrm{b}} - k_{\mathrm{a}}$ in thermal equilibrium has to be 0 for any energy interval dE (principle of *detailed balance*) allows to relate e_n to c_n via balancing the integrands of Equation (3.5) and Equation (3.6) [35]

$$e_n = c_n \mathrm{e}^{(E_{\mathrm{T}} - E)/(k_{\mathrm{B}} T)}, \tag{3.7}$$

where the useful relation for the Fermi function was used

$$\frac{f(E)}{1 - f(E)} = \mathrm{e}^{(E - E_{\mathrm{f}})/(k_{\mathrm{B}} T)}. \tag{3.8}$$

Therefore Equation (3.5) can be rewritten as

$$k_{\mathrm{a}} = \int_{E_{\mathrm{c}}}^{\infty} c_{\mathrm{n}} \mathrm{e}^{(E_{\mathrm{T}} - E)/(k_{\mathrm{B}} T)} N_{\mathrm{t}} f_{\mathrm{t}}(1 - f(E)) N_{\mathrm{c}}(E) \mathrm{d}E. \tag{3.9}$$

For solving the integrals, Equation (3.6) and Equation (3.9), an averaged capture cross section $\overline{c_n}$ is introduced

$$\overline{c_{\mathrm{n}}} = \frac{\int_{E_{\mathrm{c}}}^{\infty} c_n(E) \mathrm{e}^{(E_{\mathrm{c}} - E)/(k_{\mathrm{B}} T)} N_{\mathrm{c}}(E) \mathrm{d}E}{\int_{E_{\mathrm{c}}}^{\infty} \mathrm{e}^{(E_{\mathrm{c}} - E)/(k_{\mathrm{B}} T)} N_{\mathrm{c}}(E) \mathrm{d}E} \tag{3.10}$$

and Boltzmann statistics are applied, i.e. the Fermi function $f(E)$ is approximated by

$$f(E) = \frac{1}{\mathrm{e}^{(E - E_{\mathrm{f}})/(k_{\mathrm{B}} T)} + 1} \approx \mathrm{e}^{(E_{\mathrm{f}} - E)/(k_{\mathrm{B}} T)}. \tag{3.11}$$

Then Equation (3.6) and Equation (3.9) can be further simplified to

$$k_\mathrm{a} = N_\mathrm{T}\overline{c_\mathrm{n}} f_\mathrm{t} n_1 \tag{3.12}$$

$$k_\mathrm{b} = N_\mathrm{T}\overline{c_\mathrm{n}} f_\mathrm{pt} n. \tag{3.13}$$

In Equation (3.12) n_1 is introduced as auxiliary variable that corresponds to the carrier concentration computed with Boltzmann statistics if the Fermi level E_f would coincide with the trap energy level E_T

$$n_1 = N_\mathrm{c}\mathrm{e}^{(E_\mathrm{T}-E_\mathrm{c})/(k_\mathrm{B}T)}. \tag{3.14}$$

Now the net rate of electron capture from the conduction band, that is the rate of electron emission (process b) in Fig. 3.9) minus the rate of electron capture (process a) in Fig. 3.9) can be calculated as

$$k_\mathrm{ba} = k_\mathrm{b} - k_\mathrm{a} = N_\mathrm{T}\overline{c_\mathrm{n}} f_\mathrm{pt} n - N_\mathrm{T}\overline{c_\mathrm{n}} f_\mathrm{t} n_1. \tag{3.15}$$

In analogy to the derived net rate for electron capture the net rate for hole capture, that is k_dc can be derived

$$k_\mathrm{dc} = \overbrace{N_\mathrm{T}\overline{c_\mathrm{p}} f_\mathrm{t} p}^{k_\mathrm{d}} - \overbrace{N_\mathrm{T}\overline{c_\mathrm{p}} f_\mathrm{pt} p_1}^{k_\mathrm{c}}, \tag{3.16}$$

where p_1 is given in analogy to n_1

$$p_1 = N_\mathrm{v}\mathrm{e}^{(E_\mathrm{v}-E_\mathrm{T})/(k_\mathrm{B}T)}, \tag{3.17}$$

with N_v being the density of states in the valence band. Finally, to derive an expression for the net rate of recombination, it has to be considered that in steady-state conditions k_ba must be equal to k_dc leading to the well known result for the SRH recombination rate

$$k_\mathrm{ba} \overset{!}{=} k_\mathrm{dc} \implies U_\mathrm{SRH} = \frac{pn - n_\mathrm{i}^2}{\tau_{p0}(n+n_1) + \tau_{n0}(p+p_1)}, \tag{3.18}$$

with the lifetime parameters

$$\tau_{n0} = \frac{1}{N_\mathrm{T}\overline{c_\mathrm{n}}} \tag{3.19a}$$

$$\tau_{p0} = \frac{1}{N_\mathrm{T}\overline{c_\mathrm{p}}}. \tag{3.19b}$$

To derive Equation (3.18) the identity $n_1 p_1 = n_\mathrm{i}^2$, with the intrinsic carrier concentration n_i was utilized. A parametrization with the lifetime parameters τ_{n0} and τ_{p0}, Equations (3.19a) and (3.19b), is useful, since a SRH carrier lifetime τ_SRH can be defined with respect to the recombination rate U according to [3]

$$\tau_{\mathrm{SRH}} = \frac{\Delta n}{U_{\mathrm{SRH}}}, \tag{3.20}$$

and this equation reduces to the parameters τ_{n0} and τ_{p0} in some cases as will be shown in Section 3.2.2. In Fig. 3.10 the individual rates as well as the total SRH recombination rate for n-type, intrinsic and p-type silicon as a function of the trap energy E_{T} is shown. Despite the same doping levels for the n-type and p-type silicon in these plots the symmetry is slightly broken because of different values for thermal velocities and effective density of states for electrons and holes. As can be seen in this figure, the recombination rate is largest for "midgap" traps. In the case of traps energetically located close to the band edges, the interaction of one type of carrier with the traps dominates and recombination becomes therefore inefficient. For example, considering intrinsic silicon (**center**), close to the valence band there is hardly electron emission since this requires lifting an electron energetically a wide distance, leading to low rates

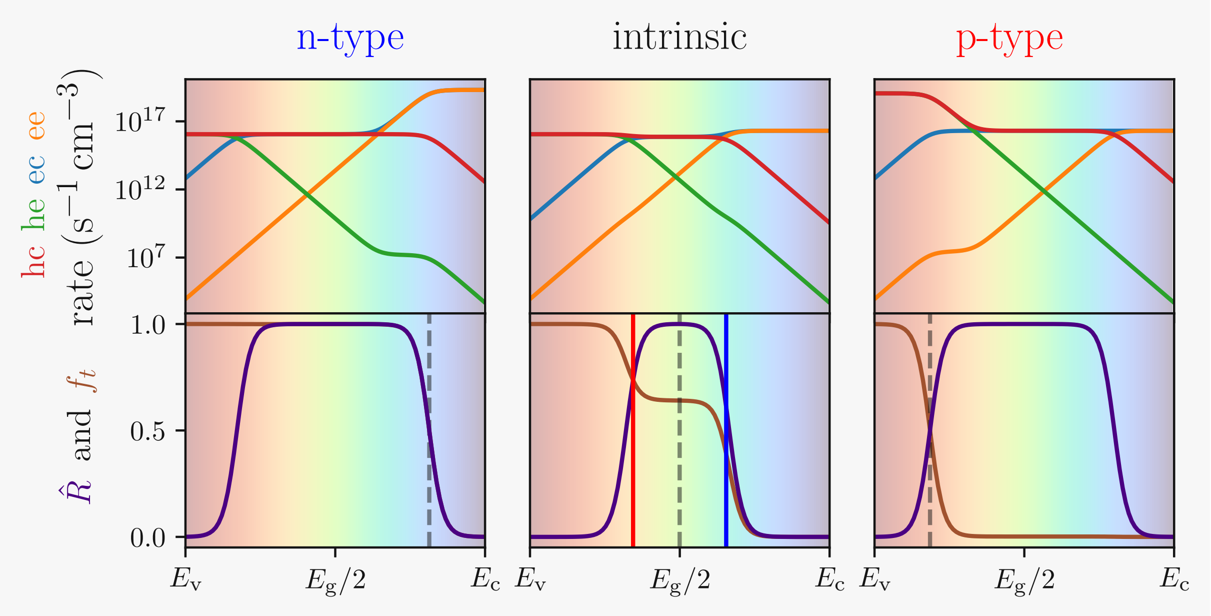

Figure 3.10. Shockley-Read-Hall recombination rates as function of trap energy E_{T}: **left** n-type doped silicon ($N_{\mathrm{D}} = 10^{16}\,\mathrm{cm}^{-3}$), **center** intrinsic silicon, **right** p-type doped silicon ($N_{\mathrm{A}} = 10^{16}\,\mathrm{cm}^{-3}$) for an excess carrier density of $\Delta n = 10^{13}\,\mathrm{cm}^{-3}$ and cross sections $\sigma_n = \sigma_p = 10^{-14}\,\mathrm{cm}^2$. **Upper plots:** recombination rates for the different processes according to Fig. 3.9 and Equations (3.16) and (3.15): hole capture (hc): k_{d}; hole emission (he): k_{c}; electron capture (ec): k_{b}; electron emission (ee): k_{a} **Lower plots:** Trap occupation f_{t} and normalized recombination rate $\hat{R} = R(E_{\mathrm{T}})/\max(R(E_{\mathrm{T}}))$. The vertical dashed line marks the Fermi level, the vertical red and blue line in the central plot mark the quasi-Fermi levels for holes and electrons, respectively. Recombination is most effective for traps close to the center of the bandgap.

---

[3] The concept of carrier lifetimes will be discussed with more detail and in a more global context in Section 4.1.

for this transition, which is incorporated in the definition of n_1 appearing in Equation (3.12). The process of electron capture is also by magnitudes smaller than hole capture or emission since electron capture requires the traps to be empty. However, looking at the lower plots it becomes apparent that almost all traps are filled by electrons in that case ($f_\mathrm{t} \approx 1$). Consequently, the rate of hole capture is quite high in this case. However, also the hole emission rates become quite high since the energetic barriers for this rate are low. Therefore, the dominant processes in this regime are hole capture and emission, whereas recombination is less important. An analog conclusion can be drawn for the other side of the bandgap, i.e. energetically close to the conduction band. The same principles also apply for the case of doped silicon. Considering the trap occupation probability f_t it can be seen, that this factor follows a Fermi-like distribution centered at the Fermi level (being approx. equal to the quasi-Fermi level for the majority carriers in the doped case). For the intrinsic case there are two distinct transition regions in f_t at the location of the quasi-Fermi levels for holes and electrons. Apparently, in the case of intrinsic silicon the two quasi-Fermi levels define the region of efficient recombination. This is the basic idea of an approximation formulated by Simmons and Taylor [122], where the SRH processes are simplified based on this assessment. This approximation may be applied whenever $n \approx p$, which means either in the case of intrinsically doped semiconductors or if the excess carrier concentration is much larger than the doping concentration.

Injection Dependency

It is well known, that the SRH processes might be strongly dependent on the amount of excess carriers Δn. In 1952 Hall already considered the injection dependency of SRH processes in his publication [36]. Δn is implicitly taken into account in the SRH recombination rate, Equation (3.18), considering that the total electron and hole concentrations are given by

$$n = n_0 + \Delta n \tag{3.21a}$$

$$p = p_0 + \Delta n, \tag{3.21b}$$

where n_0 and p_0 are the equilibrium carrier concentration. In that case it is assumed that the amount of excess electrons equals the amount of excess holes, i.e. $\Delta n = \Delta p$, which is an assumption that holds in case of negligible carrier trapping effects [123]. It is worth noting, that in the case of presence of excess carriers, the law of mass action is not satisfied any longer, that means $np \neq n_\mathrm{i}^2$ but rather

$$np = n_0 p_0 + \Delta n(n_0 + p_0) + \Delta n^2 = n_\mathrm{i}^2 + \Delta n(n_0 + p_0) + \Delta n^2 \tag{3.22}$$

Assuming a p-type doped semiconductor[4] (with acceptor concentration N_A) and complete dopant ionization the equilibrium carrier densities can be estimated as follows

---

[4] In this section a p-type doped semiconductor is considered, the very same conclusions can, however, be drawn considering n-type doping.

$$p_0 \approx N_\mathrm{A} \tag{3.23a}$$

$$n_0 = n_\mathrm{i}^2 / N_\mathrm{A}. \tag{3.23b}$$

In that case $p_0 \gg n_0$ which allows to simplify the SRH recombination rate for the minority carriers (electrons) as follows

$$U_{\mathrm{SRH},n} = \frac{\Delta n N_\mathrm{A} + \Delta n^2}{\tau_{p0} n_1 + \tau_{n0} N_\mathrm{A} + \tau_{n0} \Delta n + \tau_{n0} p_1} \tag{3.24}$$

Two important limits for the carrier lifetimes according to Equation (3.20) can be investigated now. First, the low injection limit, i.e. $\Delta n \ll N_\mathrm{A}$, where the excess carrier concentration is negligible small compared to the bulk doping, is considered. In that case the minority carrier lifetime reduces to [124]

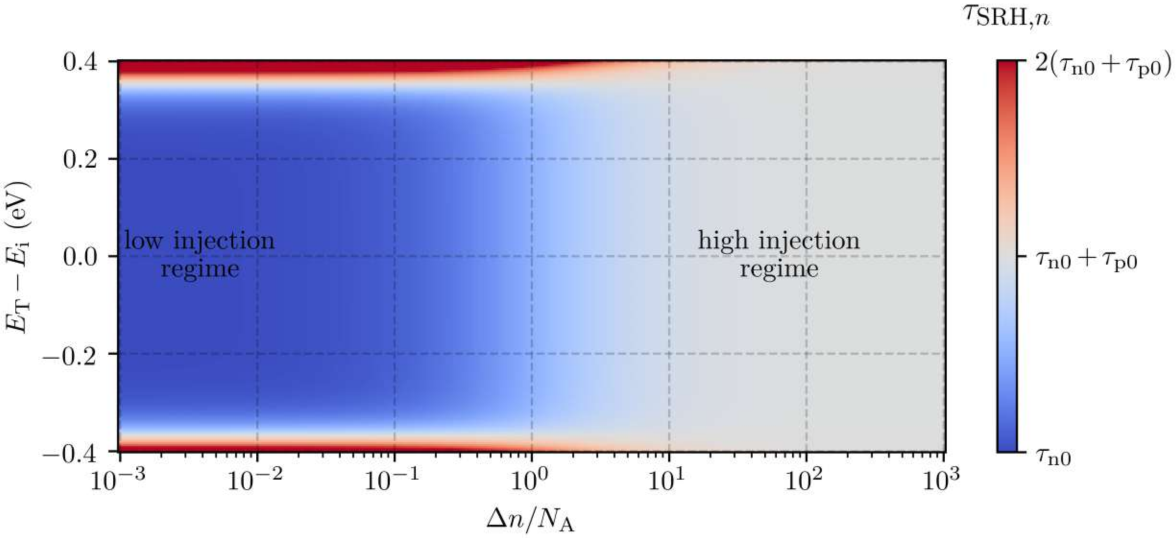

Figure 3.11. Injection-dependency of the SRH lifetime $\tau_{\mathrm{SRH},n}$ for p-type silicon (with acceptor doping concentration N_A) as function of excess carrier density Δn and energetic trap level E_T with respect to the intrinsic energy E_i. The capture cross sections were chosen identical $\sigma_n = \sigma_p$.

$$\tau_{\mathrm{SRH},n}^{\mathrm{low}} = \frac{\Delta n}{U_{\mathrm{SRH},p}^{\mathrm{low}}} = \tau_{n0} \left(1 + \frac{K n_1 + p_1}{N_\mathrm{A}} \right), \tag{3.25}$$

where K is the ratio of lifetime parameters τ_{p0} / τ_{n0}. As can be seen, τ_{n0} can be considered a lower barrier for minority carrier lifetime in p-type doped silicon and a higher acceptor concentration leads to lower achievable lifetimes in the low injection limit.

The limit on the other side, i.e. the high injection limit, can be derived similarly considering that $\Delta n \gg n, p, n_1, p_1$ which yields

$$\tau_{\mathrm{SRH},n}^{\mathrm{high}} = \tau_{n0} + \tau_{p0}. \tag{3.26}$$

The minority carrier lifetime is plotted as a function of injection level and trap energy in Fig. 3.11. Considering the low injection regime, in many cases the term in the brackets in Equation (3.25) can be considered 1 and the lifetime reduces to $\tau_{\mathrm{SRH},n} = \tau_{n0}$. This happens if the trap is near the midgap region, since then the carrier concentrations n_1 and p_1 become rather small. Contrary, for traps located near the bandgap edges, the low injection lifetime can become quite high, even higher than the high-injection lifetime. A higher lifetime for traps towards the band edges is in agreement with the plots in Fig. 3.10, where the recombination rate was investigated as function of trap energy, and midgap traps were identified as being the most recombination-active. Additionally, it can be seen in Fig. 3.11, that the lifetime approaches the high injection limit $\tau_{n0} + \tau_{p0}$ independent of the trap's energetic position within the bandgap, according to Equation (3.26).

Dynamics

The SRH recombination rate, given by Equation (3.18), is a steady-state recombination rate. It is based on the condition of very same net electron capture and hole capture, which is not necessarily true in non-steady-state conditions. The kinetics are described with the rates for the SRH processes yielding the following system of coupled differential equations

$$\left(\frac{\mathrm{d}n}{\mathrm{d}t}\right)_{\mathrm{SRH}} = N_{\mathrm{T}}\overline{c_{\mathrm{n}}}f_{\mathrm{t}}n_1 - N_{\mathrm{T}}\overline{c_{\mathrm{n}}}(1-f_{\mathrm{t}})n \tag{3.27a}$$

$$\left(\frac{\mathrm{d}p}{\mathrm{d}t}\right)_{\mathrm{SRH}} = N_{\mathrm{T}}\overline{c_{\mathrm{p}}}(1-f_{\mathrm{t}})p_1 - N_{\mathrm{T}}\overline{c_{\mathrm{p}}}f_{\mathrm{t}}p \tag{3.27b}$$

$$\left(\frac{\mathrm{d}f_{\mathrm{t}}}{\mathrm{d}t}\right)_{\mathrm{SRH}} = \overline{c_{\mathrm{p}}}(1-f_{\mathrm{t}})p_1 - \overline{c_{\mathrm{p}}}f_{\mathrm{t}}p - \overline{c_{\mathrm{n}}}f_{\mathrm{t}}n_1 + \overline{c_{\mathrm{n}}}(1-f_{\mathrm{t}})n \tag{3.27c}$$

This system of equations can then be coupled to the basic system of equations, e.g. to the drift-diffusion equations, to model transient trapping and recombination effects via single defect levels. The model can be easily extended to more defects if transitions between the individual levels are ignored [125], but inter-level transitions may also be included, as for example shown for a two-level system in reference [126].

Surface Recombination

Defect-mediated surface recombination is in principle described in analogy to SRH bulk recombination. Brattain and Bardeen were the first to apply the SRH theory to recombination at surfaces by introducing a surface recombination velocity S [127, 128]. The recombination velocity can be seen as the surface lifetime equivalent. As the name indicates it has the dimensions of a velocity and is typically stated in units of $\mathrm{cm\,s^{-1}}$. A recombination rate at the surface can be defined as [129]

$$U_\mathrm{s} = \frac{n_\mathrm{s} p_\mathrm{s} - n_\mathrm{i}^2}{\frac{n_\mathrm{s}+n_1}{\sigma_p v_\mathrm{th} N_\mathrm{st}} + \frac{p_\mathrm{s}+p_1}{\sigma_n v_\mathrm{th} N_\mathrm{st}}}, \tag{3.28}$$

where the subscript s refers to the quantity at the interface. It should be considered that n_s and p_s have units of cm^{-3} (they are the bulk carrier concentrations at the interface) and the interface trap density N_st has units of cm^{-2}. Comparing the form of Equation (3.28) to Equation (3.18) one can see that instead of the lifetime parameters $\tau_{n0,p0}$, velocity parameters $S_{n0,p0}$ can be defined for the surface case

$$S_{n0} = \frac{1}{N_\mathrm{st}\overline{c_\mathrm{n}}} \tag{3.29a}$$

$$S_{p0} = \frac{1}{N_\mathrm{st}\overline{c_\mathrm{p}}}. \tag{3.29b}$$

Considering interface recombination an equivalent to the carrier lifetime can now be defined as surface recombination velocity

$$S = \frac{U_\mathrm{s}}{\Delta n}. \tag{3.30}$$

The generation/recombination of carriers at any surface or interface can be considered a source or sink for charge carriers. Therefore, a corresponding surface current density j_s normal to the considered surface can be defined as

$$j_\mathrm{s} = qU_\mathrm{s} = q\frac{S}{\Delta n}. \tag{3.31}$$

which imposes a boundary condition in the drift-diffusion system as

$$\boldsymbol{nj} = -qS\Delta n, \tag{3.32}$$

where $\boldsymbol{n}$ is the normal vector to the surface under consideration. It should be noted that a definition of the surface recombination velocity as in Equation (3.30) is meaningful in the case of flatband conditions towards the surface, where the surface carrier concentrations are equal to those in the bulk and there is no depletion or accumulation layer towards the interface. In the case of non-flatband conditions typically an effective surface recombination velocity S_eff is defined, which relates the surface recombination rate U_s to the excess carrier density at the edge of depletion-region [130]. S_eff will be further introduced in in Section 4.2.2. It should be noted, that in literature both metrics, i.e. S_eff as well as the surface current density j_s, are used to quantify recombination at interfaces, where a discussion of the observed phenomena can have subtle advantages in one or the other quantity [131]. It is worth mentioning that the interface traps (as well as bulk traps) may have a continuous energetic distribution within the bandgap, instead of being discrete levels. In that case, for the calculation of the recombination rate one needs to integrate over the defect distribution within the bandgap

$$U_\mathrm{s} = \int_{E_\mathrm{v}}^{E_\mathrm{c}} D_\mathrm{it}(E) \frac{n_\mathrm{s} p_\mathrm{s} - n_i^2}{\frac{n_\mathrm{s}+n_1(E)}{v_{\mathrm{th},p}\sigma_p(E)} + \frac{p_\mathrm{s}+p_1(E)}{v_{\mathrm{th},n}\sigma_n(E)}} \mathrm{d}E, \tag{3.33}$$

where the interface trap density $D_\mathrm{it}(E)$ was introduced, such that the total interface trap density (withing the bandgap) is given by

$$N_\mathrm{st} = \int_{E_\mathrm{v}}^{E_\mathrm{c}} D_\mathrm{it}(E) \mathrm{d}E. \tag{3.34}$$

In that case n_1 and p_1 are calculated according to Equations (3.14) and (3.14) with E_T becoming the integration variable E and the dependency of capture cross sections $\sigma_{n(p)}$ on energy will be discussed with more detail in Section 4.2.2.

3.2.3 Non-Radiative Multi-Phonon Model

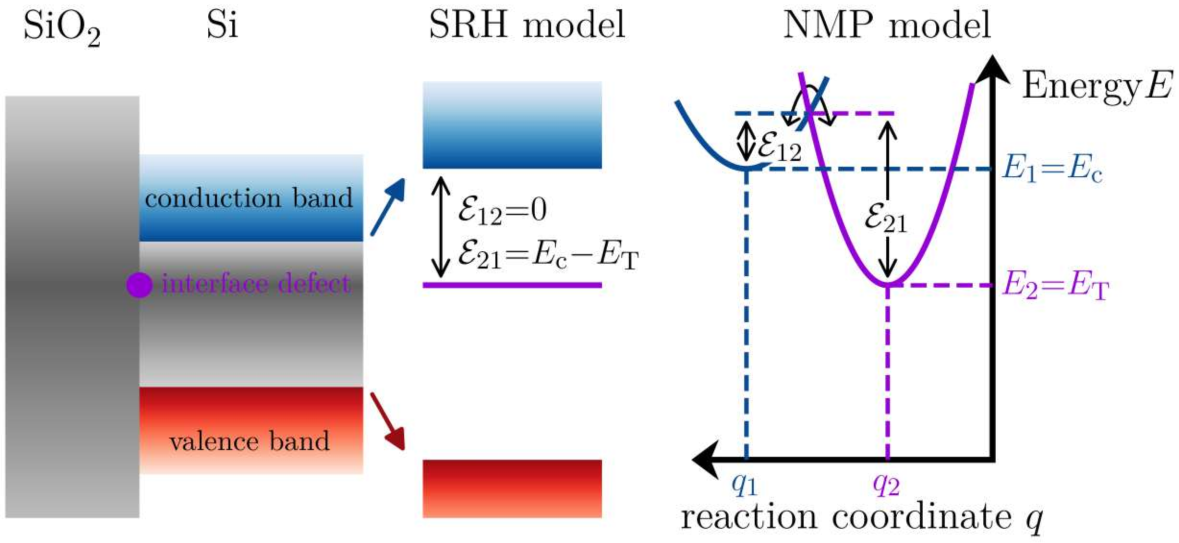

Figure 3.12. Defect-carrier interaction at the Si-SiO$_2$ interface: Shockley-Read-Hall (SRH) model versus non-radiative multi-phonon (NMP) model considering the capture/emission of an electron from/to the conduction band to/from the trap level. **(left)** Schematics of the Si-SiO$_2$ interface with an interface trap level. **(center)** The SRH model considers no energetic barrier for the capture of an electron ($\mathcal{E}_{12}^{SRH} = 0$) and the barrier for the emission of an trapped electron to the conduction band is given by the trap ionization energy with respect to the conduction band energy ($\mathcal{E}_{21}^{SRH} = E_\mathrm{c} - E_\mathrm{T}$). **(right)** The non-radiative multi-phonon (NMP) model considers the structural relaxation of the nuclei in the vicinity of the defect site. Originally published in [PSJ1].

The SRH model as introduced in the previous section considers defects by the parameters of capture cross sections and trap energies. However, the model is reluctant against including the structural relaxation of the atoms in the vicinity of the defect upon changing its charge state. However, it is well known that structural relaxations may impact the transition rates of carriers from a reservoir (i.e. conduction or valence band) to the defect state. Historically, the non-radiative multi-phonon (NMP) theory in the context of defects was first introduced by Huang and Rhys in 1950 [132] and subsequently complemented by Gummel and Lax [133], Henry and Lang [119] and others. Nowadays, the NMP model is discussed a lot in terms of transistor physics, where transition times of emission and capture events leading to reliability issues can be explained and accurately modeled with it [134, 31, 135, 136]. A comparison between the SRH and NMP model to describe carrier interactions with an interface defect is schematically shown in Fig. 3.12. To describe the physical phenomena the nomenclature is adapted compared to the formalism introduced in Section 3.2.2 to describe SRH recombination. The electron being trapped by the defect, is referred to as state 2 and the defect not being occupied and the electron being in the conduction band is referred to as state 1. A transition from state 1 to state 2 is described by the rate k_{12} and vice versa as k_{21}. For the SRH case, these rates, considering a single trap, where already introduced as

$$k_{12}^{SRH} = n v_{\mathrm{th}} \sigma_n \tag{3.35a}$$

$$k_{21}^{SRH} = N_{\mathrm{c}} v_{\mathrm{th}} \sigma \mathrm{e}^{\frac{E_{\mathrm{T}}-E_{\mathrm{C}}}{k_{\mathrm{B}}T}} . \tag{3.35b}$$

One can see that the SRH model has an energetic barrier for the electron emission whereas for the electron capture the electron simply "falls" from the conduction band to the trap level, i.e. there is no energetic barrier that has to be overcome. In the NMP model, however, there is an energetic barrier also for the capture of an electron. Despite the fact that the trap level is energetically favoured for the electron from the conduction band, it is considered by this model, that a structural change has to take place, which requires the energy $\mathcal{E}_{12}$. The structural change is typically described with a reaction coordinate q. This coordinate describes the configuration, i.e. position of the nuclei , in a simplified 1-dimensional fashion. The configuration landscape can be calculated by a separation of the total problem into a part for the much heavier nuclei and a part for the much lighter electrons, known as Born-Oppenheimer approximation [137]. Concretely, the electronic part is solved on top of the potential energy surface (PES) for the nuclei, where the energetic landscape in the vicinity of a local minima is approximated by second order series expansions [31]

$$V_{\mathrm{i}} = \frac{1}{2} M \omega_{\mathrm{i}} \left(q - q_{\mathrm{i}}\right)^2 + E_{\mathrm{i}}, \tag{3.36}$$

In Equation (3.36) the subscript refers to the state i, V_{i} is the total potential energy, M an effective mass of the defect, ω_{i} the vibrational frequency in the minimum of the corresponding state, and E_{i} the potential energy in the minimum. A transition from one state to the other happens at the intersection of the parabolas where the energy is supplied in form of quantized lattice vibrations, called phonons, hence the name of the model. A common simplification, allowing the solution of the NMP transitions to be formulated in a very compact manner, is to assume the same curvature of the two parabolas considered, i.e. $\omega_1 = \omega_2 = \omega$. This simplification is called *linear electron-phonon coupling* and in that case the energies for the transitions are given by [31]

$$\mathcal{E}_{12} = \frac{\left(\mathcal{E}_\mathrm{R} + E_{21}\right)^2}{4\mathcal{E}_\mathrm{R}} \tag{3.37a}$$

$$\mathcal{E}_{21} = \mathcal{E}_{12} - E_{21} = \frac{\left(\mathcal{E}_\mathrm{R} - E_{21}\right)^2}{4\mathcal{E}_\mathrm{R}}, \tag{3.37b}$$

where $E_{21} = E_2 - E_1$ (where $E_2 = E_\mathrm{T}$ and $E_1 = E_\mathrm{c}$, see Fig. 3.12) denotes the total energy difference between the two states, and $\mathcal{E}_\mathrm{R}$ is the relaxation energy given by

$$\mathcal{E}_\mathrm{R} = S\hbar\omega, \tag{3.38}$$

with S being the Huang-Rhys factor which is a measure for the average number of phonons required for the particular transition [132]. With the above introduced formalism, the capture and emission rate for the NMP model can be written as

$$k_{12}^{NMP} = n v_\mathrm{th} \sigma_n \mathrm{e}^{\frac{-\mathcal{E}_{12}}{k_\mathrm{B}T}} \tag{3.39a}$$

$$k_{21}^{NMP} = N_\mathrm{c} v_\mathrm{th} \sigma_n \mathrm{e}^{\frac{-\mathcal{E}_{21}}{k_\mathrm{B}T}}. \tag{3.39b}$$

Comparing the SRH rates to the NMP rates on fundamental difference is the energetic barrier for the electron capture. This has important consequences for the modeling of time-dependent phenomena, such as random telegraph noise (RTN), observed in MOSFET devices. In that case, a modeling according to the SRH model will fail since the bias and temperature dependency of the capture times are wrongly incorporated by the model (which is linked to the lack of an energetic barrier for the capture process, and a too small barrier for the emission process).

3.3 Impact of Defects on the Performance of Photodiodes

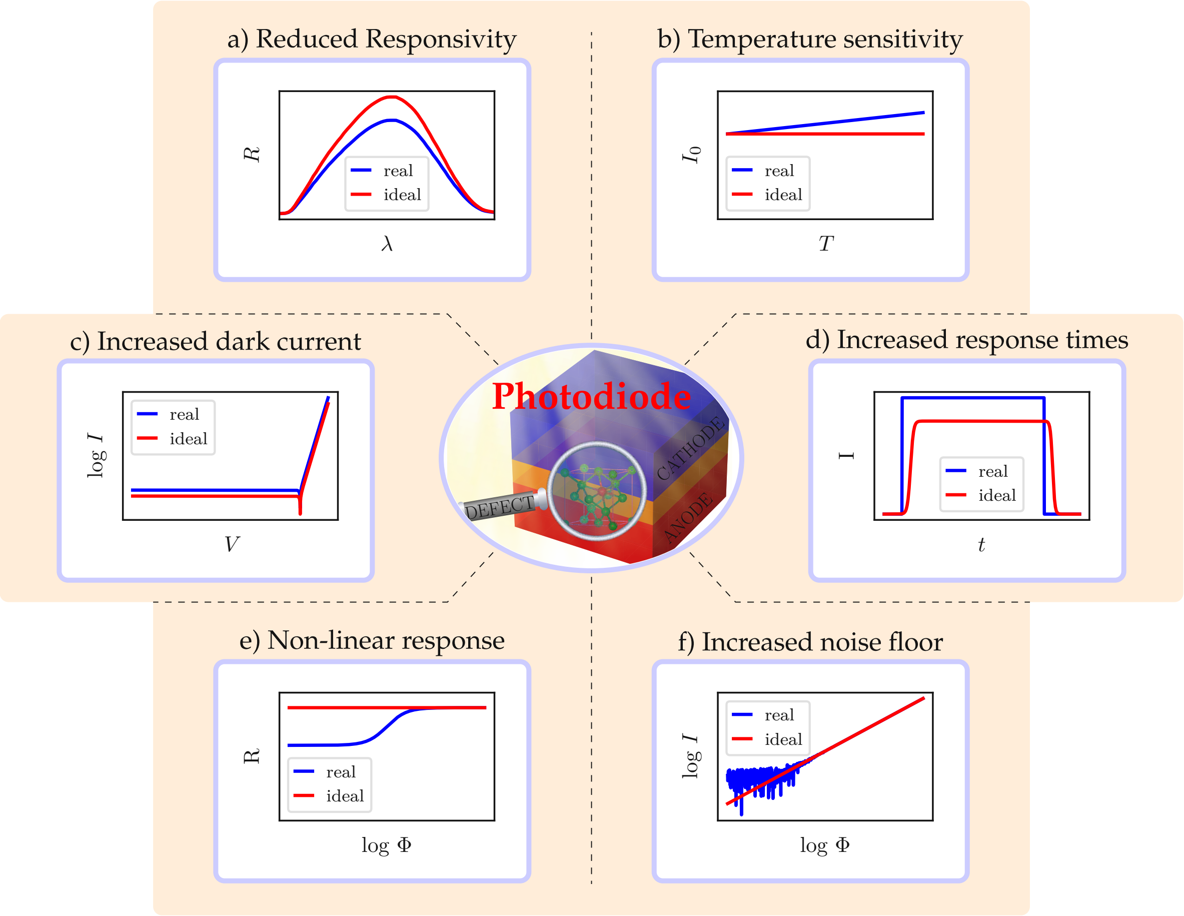

Figure 3.13. Selected examples of how defects may impact the performance of photodiodes.

Having introduced and classified defects as well as described how they interact with charge carriers in semiconductors this section aims at looking specifically how defects interfere with the operation and nominal parameters of photodiodes. In Figure 3.13 a selection of these interferences is schematically drawn:

(a) **Reduced Responsivity**
In Equation (2.14) the responsivity R of a photodiode was introduced as a function of the parameter ξ describing the collection efficiency, that is the fraction of collected to generated carriers within the diode active area. This parameter strongly depends on the carrier lifetimes, and therefore ultimately on the density of defect states in the material as is shown below. In general to calculate the terminal currents of an illuminated pn-junction the drift diffusion equations need to be solved for each QNR. Considering the recombination rate R in terms of the minority carrier lifetime τ the drift diffusion equations in each QNR of the junction read

$$D_n \frac{\mathrm{d}^2 n_p}{\mathrm{d}x^2} = \frac{n_p - n_{p0}}{\tau_n} - G(x) \tag{3.40a}$$

$$D_p \frac{\mathrm{d}^2 p_n}{\mathrm{d}x^2} = \frac{p_n - p_{n0}}{\tau_p} - G(x), \tag{3.40b}$$

where the subscript n, p refers to the n-type and p-type doped region of the junction, D is the diffusion constant and $G(x)$ the generation rate. If furthermore it is assumed, that the generation rate is constant (this corresponds to the case where the absorption length $1/\alpha$ is much longer than the domain under investigation)[5] then general solutions to Equation (3.40) can be formulated as follows

$$\Delta p(x) = p(x) - p_{n0} = A\mathrm{e}^{x/L_p} + B\mathrm{e}^{-x/L_p} + G\tau_p \tag{3.41a}$$

$$\Delta n(x) = n(x) - n_{p0} = C\mathrm{e}^{x/L_n} + D\mathrm{e}^{-x/L_n} + G\tau_n, \tag{3.41b}$$

with $L_{n(p)} = \sqrt{D_{n(p)}\tau_{n(p)}}$ and the constants A to D that are determined by the boundary conditions. Except for the term containing the generation rate G these solutions are identical to the un-illuminated pn-junction. Considering finite device dimensions (width of anode QNR region W_p and width of cathode QNR region W_n) one needs to define the boundary conditions. At the edges of the depletion region the boundary conditions are determined by the Shockley relation whereas at the outer boundaries the surface recombination velocities S_n and S_p need to be considered

$$\left.\frac{\partial \Delta p(x')}{\partial x'}\right|_{x'=W_n} = \Delta p(x' = W_n) * S_p/D_p \tag{3.42a}$$

$$\left.\frac{\partial \Delta n(x'')}{\partial x''}\right|_{x''=W_p} = \Delta n(x'' = W_p) * S_n/D_n, \tag{3.42b}$$

where x' and x'' denote positions in the QNR regions in coordinate systems with the origins at the corresponding edge of the depletion zone. In the wide base approximation the surface recombination velocities are assumed zero ($S_n = S_p = 0$) since the anode and cathode widths W_n and W_p are much larger than the diffusion lengths L_p and L_n, respectively. In that case, and assuming recombination within the depletion zone to be neglectable, solutions for the overall current density j may be written as

$$j = j_{\mathrm{dark}} - \overbrace{qG(L_n \tanh\frac{W_p}{L_n} + L_p \tanh\frac{W_n}{L_p} + W_{\mathrm{depl}})}^{j_{\mathrm{phot}}}, \tag{3.43}$$

where j_{dark} is the dark current density, j_{phot} the current density related to the illumination and W_{depl} the depletion width. It should be noted that a solution of the illuminated case as sum of an un-illuminated current density and an additional term is an inherent property of the governing linear differential equation, where a

---

[5] This simplification is used to demonstrate the influence of lifetime on the collection efficiency of generated charge carriers in a compact manner. However, similar conclusions can be drawn when solving the equations with an exponentially decaying generation rate [138, 139].

solution to the general problem (with external perturbation) can always be written as sum of a solution to the homogeneous system plus a particular solution to the inhomogeneous system. The internal collection efficiency may now be calculated as function of diffusion length (and therefore carrier lifetime) by comparing j_{phot} to the maximal current $qG(W_p + W_n + W_{\mathrm{depl}})$. The terms $L_{n(p)} \tanh \frac{W_{p(n)}}{L_n(p)}$ have two important limits that are

$$\lim_{L_{n(p)} \gg W_{p(n)}} L_{n(p)} \tanh \frac{W_{p(n)}}{L_{n(p)}} = W_{p(n)} \tag{3.44a}$$

$$\lim_{L_{n(p)} \ll W_{p(n)}} L_{n(p)} \tanh \frac{W_{p(n)}}{L_{n(p)}} = 0 \tag{3.44b}$$

These limits indicate the importance of diffusion length (and therefore lifetime) on the collection efficiency and ultimately quantum efficiency of photodiodes. If the diffusion length is small compared to the device dimension (i.e. the distance of carrier generation to the next collecting terminal) a large fraction of carriers recombines instead of contributing to the photocurrent, else if the diffusion length is large compared to the device dimension then high quantum efficiencies close to unity can be achieved. The knowledge of carrier lifetimes and correspondingly diffusion lengths may therefore be crucial in photodiode design and layout considerations.

(b) **Temperature Sensitivity**

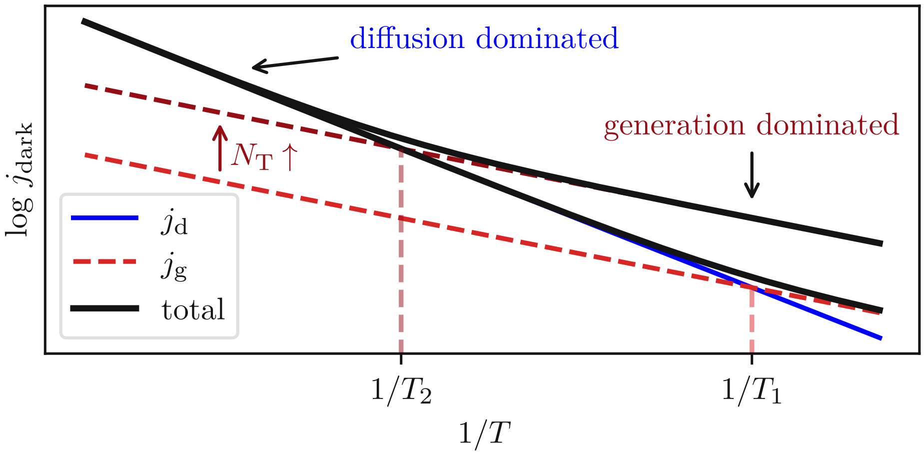

Figure 3.14. Temperature dependency of dark current. In the high temperature regime the dark current is dominated by the diffusion component whereas in the low temperature regime the generation term dominates. A higher trap density $N_2 > N_1$ leads to a shift of the transition from a lower temperature T_1 to a higher temperatures T_2. To achieve a small dark current, the generation component should be minimized and therefore a low trap density is desirable.

The reverse bias dark current of a pn-junction is given by a diffusion and generation component[6]

$$|j_{\mathrm{dark}}| = j_{\mathrm{d}} + j_{\mathrm{g}} \tag{3.45}$$

where j_{g} is the result of trap-mediated generation (described with the SRH formalism) in the depletion region, where carrier concentration are below their equilibrium values and hence a net generation rate sets in to re-establish the equilibrium. The governing temperature dependency of Equation (3.45) is given by the dependencies of the two components on the intrinsic carrier density n_{i}, since this quantity strongly depends on temperature

$$j_{\mathrm{d}} \propto n_{\mathrm{i}}^2 \propto T^3 \mathrm{e}^{-\frac{E_{\mathrm{g}}}{k_{\mathrm{B}}T}} \tag{3.46a}$$

$$j_{\mathrm{g}} \propto n_{\mathrm{i}} \propto T^{3/2} \mathrm{e}^{-\frac{E_{\mathrm{g}}}{2k_{\mathrm{B}}T}}. \tag{3.46b}$$

As a function of temperature, the total dark current density may thus be modeled as

$$j_{\mathrm{dark}} = C_{\mathrm{diff}} T^3 \mathrm{e}^{-\frac{E_{\mathrm{g}}}{k_{\mathrm{B}}T}} + C_{\mathrm{gen}} T^{3/2} \mathrm{e}^{-\frac{E_{\mathrm{g}}}{2k_{\mathrm{B}}T}}, \tag{3.47}$$

with temperature-independent coefficients C_{diff} and C_{gen}. Considering the influence of trap states on the temperature dependency it should be considered that j_{g} is related to the SRH generation and hence j_{g} and C_{gen} are proportional to the amount of trap states N_{T}. This dependency is schematically drawn in Fig. 3.14. Generally low dark currents are desired as this current component competes with the photo-current and therefore low trap densities are generally desired. A measurement of dark current can therefore also be utilized to get information about the presence of traps in single devices. Comparing different sites on a wafer in a statistical fashion even allows for an identification defects as well as an estimation of the corresponding trap energy as was shown for charge-coupled device (CCD) image sensors [140].

(c) **Increased Dark Current**

An trap-related increased dark current is strongly related to the above point, where the temperature dependency of the dark current is discussed. In Equation (3.45) a diffusion and generation component of the dark current is stated. The generation component appears because of net SRH generation in the depletion zone and the formula will be derived explicitly in Section 4.1.2. Similar to the responsivity degradation because of defect-mediated recombination of photo-generated charge carriers, the dark current degradation is worst for midgap traps. In that case the generation process is most efficient since the two processes (generation and recombination) have very same characteristics as a function of the trap energy level (see Fig. 3.10 for recombination).

---

[6] This formula will be derived and investigated in more detail in Section 4.1.2

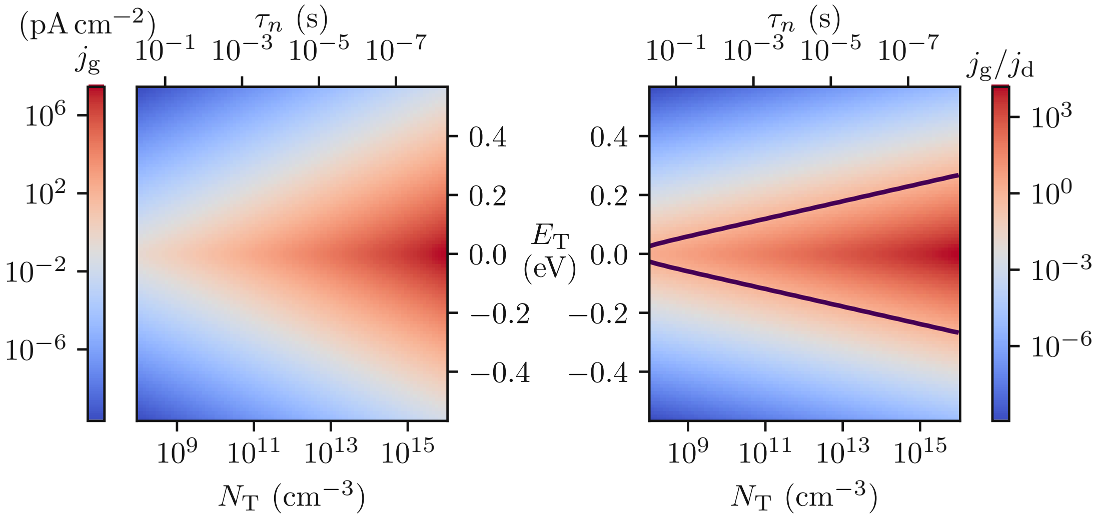

Figure 3.15. Generation dark current density component j_g as function of trap parameters at room temperature $T = 300\,\mathrm{K}$. j_g is modeled after Equation (4.22), j_d after Equation (4.17) with $F = 1$, assuming an n+/p junction ($N_A = 10^{15}\,\mathrm{cm}^{-3}$, $N_D = 10^{20}\,\mathrm{cm}^{-3} \gg N_A$), such that the current density is dominated by the component from the lower doped p-side. **(left)** j_g as function of trap density N_T (related to carrier lifetime τ on the upper axis via Equation (3.19)) and trap energy E_T. **(right)** Ratio of diffusion current density j_d to generation current density j_g as function of trap parameters. The contour lines mark a ratio of 1.

In Fig. 3.15 the trap-related dark current component j_g is plotted as function of trap parameters. As mentioned above j_g is largest for midgap traps and the plots are symmetric about $E_T = E_i$. It should be noted that, j_g depends linearly on N_T. Furthermore, in the right hand side plot of Fig. 3.15 the $j_d = j_g$ contour-lines are indicated. These diagonals mark the transitions from a diffusion to a generation dominated pn-junction, which also strongly affects the temperature dependency as was discussed above.

(d) **Increased Response Times**

The SRH dynamics, i.e. time dependent differential equations, were introduced by Equation (3.27). They add an additional component to the semiconductor transport equations (e.g. drift-diffusion), and may cause transient effects in the event of a change of the biasing condition (electric stress or optical stress, see for example Fig. 2.7) because of trapped carriers being released or vice versa carriers being trapped from the bands.

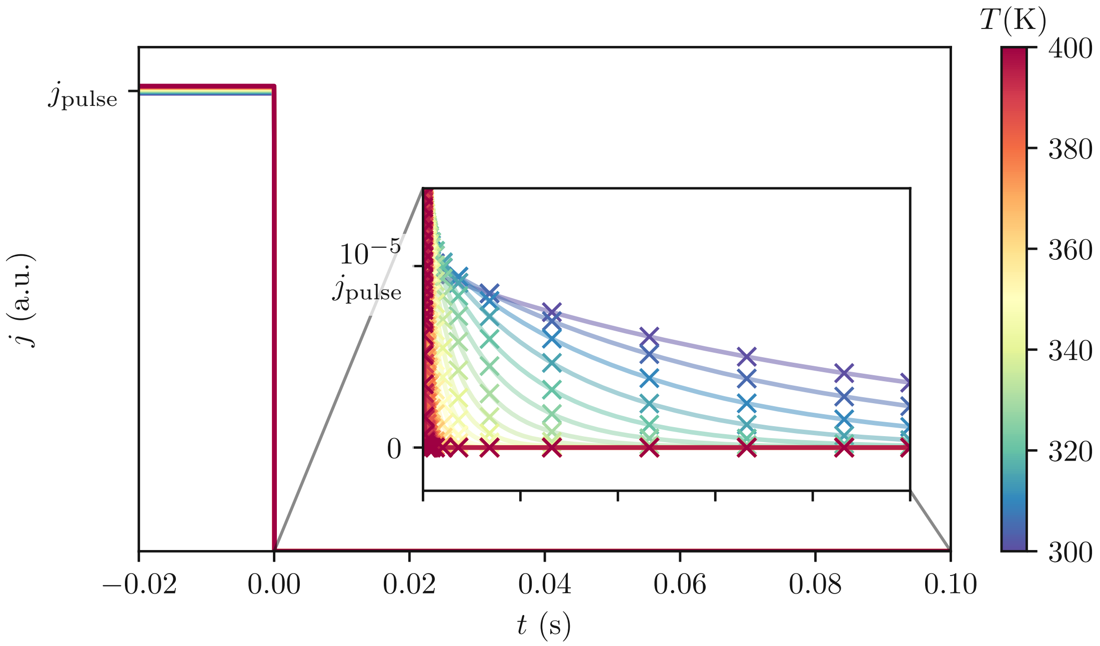

Figure 3.16. TCAD simulated current transient related to trapped carriers after optical stress at various temperatures T according to the colorbar. A quasi-1D n+/p junction is illuminated with green a light pulse (wavelength $\lambda = 530\,\text{nm}$) with a power of $P_{\text{opt}} = 10^{-5}\,\text{W}$ leading to the current density j_{pulse}. At $t_0 = 0$ the illumination is stopped and the small ($\approx 10^{-5} j_{\text{pulse}}$) current transients appear because of trap states in the device. For the simulation a single trap level is placed at $E_{\text{T}} = E_{\text{i}}$ with a trap density $N_{\text{T}} = 10^{12}\,\text{cm}^{-3}$.

In Fig. 3.16 current transients after optical excitation are shown. Trap states are filled because of higher carrier concentrations upon illumination and in the subsequent relaxation phase the carrier are re-emitted from the traps leading to this current in the ms-time regime. Characteristic for trap related emission is that the charge transition times of the defect strongly depend on temperature. These currents are in many cases (as well as in the simulation shown in Fig. 3.16) not affecting the formal rise and fall times of a device because typically their magnitude is too small to become effective on the usually defined 10 % - 90 % levels, see Section 2.2.4. However, trapping related transient currents are still undesired and should be avoided since they can disturb the operativeness of the device (photodiode plus read-out circuitry) in some applications.
Finally, it should be mentioned, that (de-)trapping transients (measured in current or capacitance) and their temperature dependencies are the foundation of the deep-level transient spectroscopy (DLTS) measurements which are introduced in Section 4.2.1.

(e) **Non-linear Response**

Trap related non-linearities with respect to the illumination intensity may be introduced since the SRH recombination rate is injection-dependent. Considering the responsivity R of a photodiode, i.e. the photocurrent divided by the optical power Φ, this quantity is expected to be constant $R(\Phi) = \text{const}$. This can be seen in the model solution of the diffusion equations in the QNR (Equations (3.40) with solution (3.41)) presented above, where apparently the ratio $j_{\text{phot}}/G \propto R$ is constant. Trap states, however, may lead to injection-dependent recombination rates (see Figure 3.11) and thus lifetimes (see Equation (4.4)), in which case the responsivity might become non-constant, i.e. R becomes a function of Φ. To demonstrate trap related non-linearity phenomena in photodiodes the system of differential Equations (3.40) can be considered. Typically the carrier lifetime τ as well as the surface recombination velocity S (introduced in the boundary conditions, Equation (3.42)) are considered constants, i.e. the low-injection limits are assumed. However, considering the p-side of the junction only, an injection-dependent boundary condition may be formulated as[7]

$$\left.\frac{\partial \Delta n(x'')}{\partial x''}\right|_{x''=W_p} = \Delta n(x'' = W_p) * S_n(\Delta n(x'' = W_p))/D_n, \tag{3.48}$$

with

$$S_n(\Delta n) = \frac{n_{\text{p0}} + N_{\text{A}} + \Delta n}{\frac{n_{\text{p0}}+n_1+\Delta n}{S_{\text{p0}}} + \frac{N_{\text{A}}+p_1+\Delta n}{S_{\text{n0}}}}, \tag{3.49}$$

which corresponds to Equation (3.30) evaluated at the p-side of the junction. In Fig. 3.17 the solution to the diffusion equation are shown. In the upper plot the excess carrier densities as well as the corresponding current densities are shown for different surface recombination velocities as depicted in the lower right plot. It should be noted that the solution for $S_n = 0$ corresponds to the one discussed above, and is given by Equation (3.43). In that case the gradient of the carrier density towards the boundary is zero and therefore also the corresponding current density. The other limit, i.e. $S_n = \infty$ corresponds to a scenario, where the minority carrier diffusion length L_n is much shorter that the device dimension W_p (short base diode approximation). In that case the excess minority carrier density is forced to zero at both boundaries and about half of the current (or generated charge carriers) is lost due to recombination (see lower left plot).

---

[7] Here an injection-dependent boundary condition is assumed, since this is the main focus of investigation in the result section of this thesis. However, solving the system with respect to an injection-dependent carrier lifetime will lead to qualitatively same results.

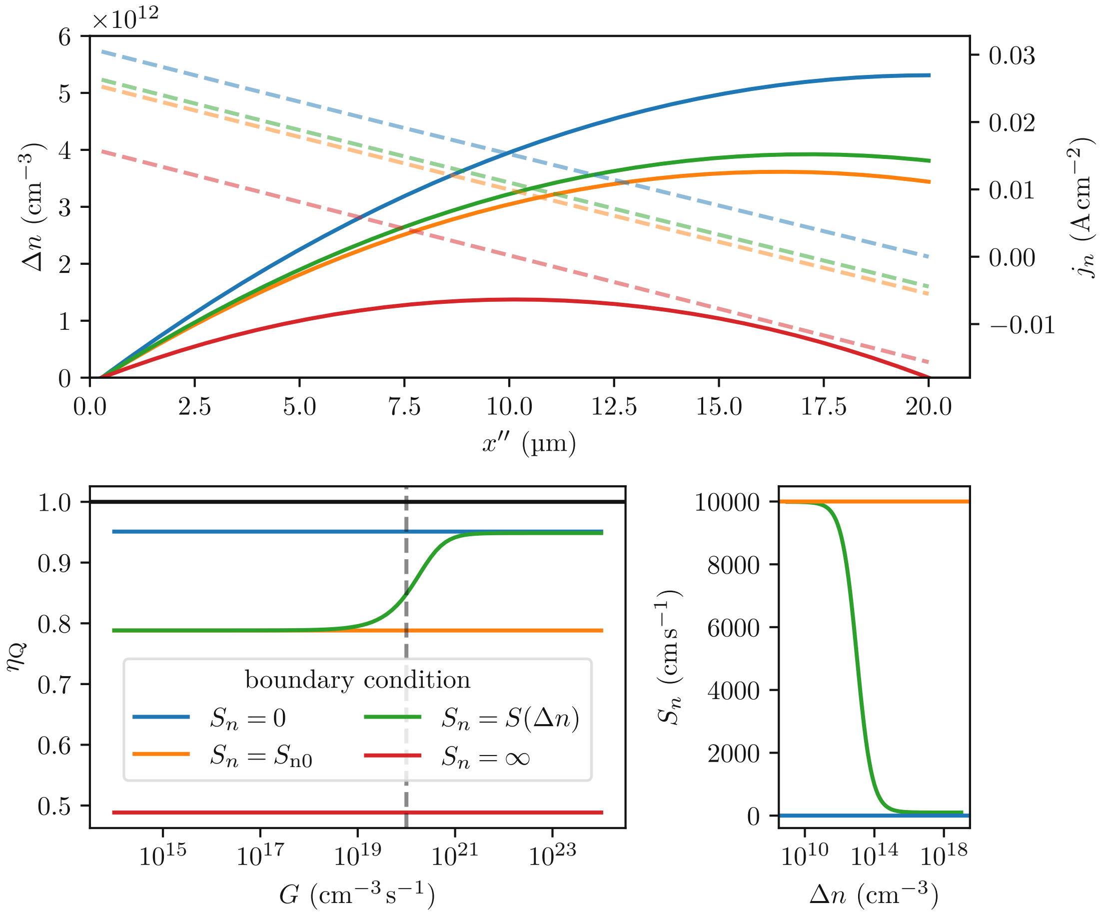

Figure 3.17. Influence of injection-dependent boundary conditions on the linearity of photocurrent. The diffusion equation in the p-side of the photodiode, Equation (3.40a), is solved analytically subjected to the boundary condition given by Equation (3.48) and Equation (3.49) using the Mathematica software [141]. The used parameters are: $D_n = 35\,\mathrm{cm}^2\,\mathrm{s}^{-1}$, $\tau_n = 1\,\mathrm{\mu s}$, $n_{p0} = \frac{n_i^2}{N_\mathrm{A}}$ with $N_\mathrm{A} = 10^{15}\,\mathrm{cm}^{-3}$ and $W_\mathrm{p} = 20\,\mathrm{\mu m}$. For the boundary conditions the parameters, $\Delta n(x'' = 0) = 0$, $S_{n0} = 10^4\,\mathrm{cm\,s}^{-1}$, $S_{p0} = 10^2\,\mathrm{cm\,s}^{-1}$ and $E_\mathrm{T} = E_\mathrm{i}$ and therefore $n_1 = p_1 = n_i$, were used. **(upper)**: excess carrier density Δn (left axis) as well as corresponding current density $j_n = qD_n \frac{\mathrm{d}\Delta n}{\mathrm{d}x''}\Big|_{x''=0}$ (right axis) versus position in the p-side x''. **(lower left)**: Quantum efficiency η_Q as function of generation rate G. The vertical dashed line marks the value for the generation rate used in the upper plot. **(lower right)**: The different boundary conditions, i.e. surface recombination velocities S_n employed for the curves shown in the other plots.

The other two solutions for the boundary conditions $S_n = S(\Delta n)$ and $S_n = S_{n0}$ are between the above discussed extreme cases in terms of carrier densities and current densities at the outer boundary. The carrier density of the solution corresponding to the $S_n = S(\Delta n)$ condition at the right boundary is slightly higher than the solution corresponding to the $S_n = S_{n0}$ because of a lower value of $S(\Delta n)$ for this particular generation rate (and excess carrier density, correspondingly). Considering the injection dependency (i.e. the boundary condition $S_n = S(\Delta n)$), non-linear effects become clearly visible when observing the quantum efficiency

η_Q, which is calculated by comparing the calculated current density $j_n(x'' = 0)$ to the maximum achievable current density $j_{n\max} = qW_pG$. The solution for $S_n = S(\Delta n)$ gives rise to a non-linear η_Q as function of generation rate G, where the S-shaped curve form reflects the inverse dependency of S_n on (Δn), as shown in the lower right graph of Figure 3.17. Comparing η_Q for $S_n = S_{n0}$ and $S_n = S(\Delta n)$ one can see, that at high injection higher values for η_Q can be achieved because of reduced surface recombination. Solutions for $S_n = 0$ show constant and almost unity η_Q (small losses because of finite liftime τ_n), while solutions for $S_n = \infty$ show $\approx 50\,\%$ η_Q since about half of the generated carriers recombines at the surface.

Experimental results of defect-related non-linearities, similar to the analytically calculated ones in this section, are presented in Section 5.

(f) Increased Noise Floor

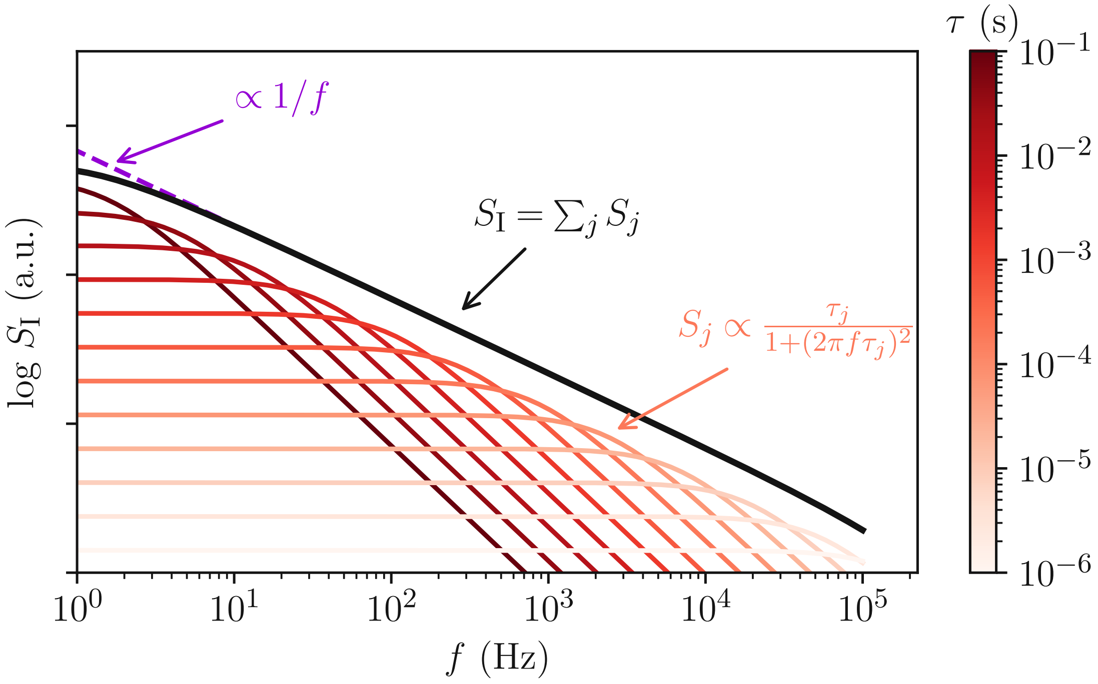

Figure 3.18. Lorentzian noise spectra of single defects S_j summing up to $1/f$ noise. The current noise spectral density S_I is plotted against the frequency f.

As discussed in Section 2.2.5 there are different components contributing to the total noise floor of a photodiode. Since in the presence of traps there are constant trapping and de-trapping events this will also lead to an increase in the noise floor of the devices. In that case these processes have to be considered in a stochastic fashion rather than describing the process by rates, as done in the SRH theory. In essence, when a carrier diffuses from one region to the other, it may ”fall” into a trap level, stay there for a characteristic time before being re-emitted (if it does not recombine) into the band, thus creating a current pulse. The times for trapping and de-trapping are then of random nature and it has been shown that a superposition of such events leads to a $1/f$-noise component [142, 143, 144, 145], which is schematically shown in Fig. 3.18. It should be mentioned, however, that despite a large pool of data and modeling approaches there is no generally accepted universal theory for the nature of $1/f$ noise [142]. Additionally, trap-related noise is just one of a few noise sources in photodiodes and typically devices under normal operating conditions are rather dominated by other noise mechanisms. However, trap related noise $1/f$ noise has been measured in pn-junctions [146]. In CMOS image sensors trap related $1/f$ noise has often been reported but it is generally rather attributed to be caused by defects in the MOSFET transistor of the source follower in the pixel read-out circuit [147]. In nano-scaled transistors the influence of single defects gets more pronounced (despite the total number of defects being lower for smaller area the increase of influence of each defect overcompensates for this effect) which allows to measure the influence of single defects, for example in terms of random-telegraph noise [148].

Finally, it should be stated that the discussion about the relation between noise and defects in photodiodes is mentioned here for completeness. However, further experimental or theoretical investigation on the correlations are out of the scope of this work.

Chapter 4

Electrical Characterization of Defects in Photodiodes

In the previous chapters the fundamentals of photodiodes and the influence of defects on the performance of photodetectors were discussed. This chapter focuses on characterization methods to explore the impact of defects on the performance parameters of optoelectronic devices. First, the determination of carrier lifetime is discussed. With the pure materials, commonly used in photodetectors, the lifetime is typically determined and dominated by defect carrier interaction [149] and therefore a measurement of lifetime allows for an estimation of the defect concentration and purity of materials. In optoelectronic applications naturally high lifetimes are desired, as they lead to improved quantum efficiency and performance of the devices. Different methods have been established to measure carrier lifetime, however, caution needs to be taken when utilizing these methods as results may be ambiguous depending on the device under test.
Secondly, methods are introduced that allow a direct extraction and examination of defect parameters. Most prominently, there is deep level transient spectroscopy (DLTS), a defect scanning technique introduced and termed by D. V. Lang in 1974 [150]. This technique has become one of the most widely applied defect characterization methods and various adoptions have been developed. A more recent developed defect characterization technique is the temperature and injection-dependent lifetime spectroscopy (TIDLS) [151]. Here the basic SRH theory is utilized to extract defect properties based on the injection and temperature dependency of the capture and emission rates. Similarly, in this work, the injection-dependent responsivity is utilized to infer defect characteristics in photodiodes. *Parts of this section are directly quoted from the publications [PSJ2, PSJ3, PSJ1].*

4.1 Determination of Minority Carrier Lifetime

Minority carrier lifetimes are essential for optical devices. High carrier lifetimes correspond to high quantum efficiencies, in e.g. photo detectors or also solar cells, because of reduced recombination losses [152, 153]. Lifetimes may not only be used to characterize the performance of a semiconductor device but also to assess the purity and quality of a semiconductor fabrication process [154]. In that case, lifetimes are measured at different stages of the fabrication process and a possible degradation at a certain processing step can be observed. A variety of methods has been established to measure carrier lifetimes [155], however, it has been observed that the methods and samples employed might affect the measurement results [156, 157]. This indicates that special care should be taken, when measuring and analysing lifetime data. Another very important aspect are interfaces and recombination at such, which becomes very present in epitaxial layer structures. Many optoelectronic devices, however, are processed on epitaxial layer since they typically have a very high quality low defect density.
In the following the concept of carrier lifetimes will be discussed in terms of different recombination mechanisms. Afterwards, methods to characterize and measure the lifetime, that were utilized in the framework of this thesis, will be presented.

4.1.1 The Concept of Carrier Lifetime

In the context of SRH recombination a lifetime was introduced in the previous section, by Equation (3.20). Considering also other sources of recombination a general recombination lifetime can be introduced as

$$\tau = \frac{\Delta n}{R_{\mathrm{tot}}} = \frac{\Delta n}{\sum_i R_i}. \tag{4.1}$$

The term *recombination lifetime* is used to clarify that this is the average time before an excess carrier *recombines*. There is a different concept called *generation lifetime* which describes the opposite process, i.e. the average time it takes until a carrier is *generated*, which happens if the carrier concentration is below the corresponding equilibrium value [156][1]. The quantity $1/\tau$ can be interpreted as the rate of recombination (unit of s^{-1}) for a single carrier and thus needs to be multiplied by the total excess carrier density to give the total recombination rate. Considering the excess electron concentration Δn in a p-type material the continuity equation (given a recombination rate R_{tot}) can be written as

$$\frac{\mathrm{d}\Delta n(t)}{\mathrm{d}t} = -R_{\mathrm{tot}}. \tag{4.2}$$

---

[1] It should be noted that recombination and generation rates are non-zero even in the case of carrier concentrations being at their equilibrium values. In the equilibrium case, recombination and generation balance each other out. What is discussed in this section are the net recombination and generation rates in excess of these equilibrium rates.

Considering furthermore that R_{tot} is simply proportional to Δn the solution to the above equation is a simple exponential function

$$\Delta n(t) = \Delta n_0 \mathrm{e}^{-\frac{t}{\tau}}, \tag{4.3}$$

and the lifetime can be interpreted as the time it takes for the excess carrier concentration to decay to a fraction of 1/e of the initial value. However, as was already discussed in the context of SRH recombination, the rate of recombination is not necessarily simply proportional to the excess carrier density, but may depend on it on a rather complicated form. A more general definition of carrier lifetime that also considers injection dependency is then given by [158]

$$\tau\left(\Delta n\right) = -\frac{\Delta n(t)}{\frac{\mathrm{d}\Delta n(t)}{\mathrm{d}t}}. \tag{4.4}$$

Carrier lifetimes are sometimes discussed in terms of an average length, that an excited carrier travels before it recombines. This length is called diffusion length L_{D} and is given by

$$L_{\text{D}} = \sqrt{D\tau}, \tag{4.5}$$

where D is the diffusion coefficient which is related to the carrier mobility μ via the Einstein relation

$$D = \frac{\mu k_{\text{B}} T}{q}. \tag{4.6}$$

The discussion of recombination phenomena in terms of the diffusion length is sometimes preferred since it allows to compare the physical device dimensions (lengths, widths, thicknesses, spacings, etc.) to this quantity, and to draw conclusions based on this comparison. For silicon a typical diffusion length is around 100 µm corresponding to about 10 µs lifetime at room temperature, but this strongly depends on the material quality.

Recombination Mechanism

To compute the total net recombination rate R_{tot} every single channel for recombination / generation has to be considered (clarify Fig. 4.1) which can be listed as:

(a) **Direct Recombination**

Direct (band-to-band) recombination is a vertical transition in the band-diagram since the momentum of the emitted photon is much smaller than the typical momentum associated to horizontal transitions in the band-diagram. It is the opposite process of light absorption as shown in Figure 2.3. Since this transition necessitates the presence of an electron as well as a hole the direct recombination rate is typically modeled according to [159]

$$R_{\text{direct}} = B(np - n_{\text{i}}^2), \tag{4.7}$$

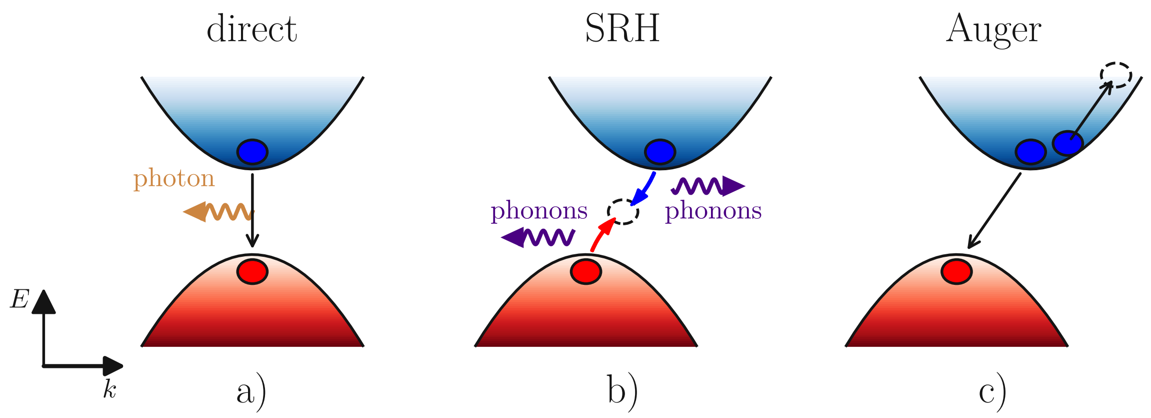

Figure 4.1. Schematics of different recombination mechanism. An electron from the conduction band (blue) may recombine with a hole in the valence band (red) via: **a) Direct recombination** is a vertical transition in the band-diagram and a photon is emitted conserving the energy. **b)** In the **SRH** theory electrons recombine with holes via trap states in the bandgap (trap-mediated recombination). **c) Auger** recombination involves three particles: Here an electron-electron-hole (eeh) process is shown, where the momentum for the transition is transferred to a second electron.

where B is the direct recombination coefficient which depends on the temperature T. For indirect bandgap semiconductors, like silicon, the direct recombination rate is typically low compared to the other two. This can be seen in Fig. 4.2, where this rate is lowest at any bulk doping. The corresponding direct recombination carrier lifetime τ_{direct} is highest, however, the overall lifetime is dominated by the lowest lifetime component.

(b) **Defect-mediated SRH Recombination**
This was already discussed in Section 3.2 and is given by Equation (3.18).

(c) **Auger Recombination**
Auger recombination is a non-radiative process where an electron from the conduction band annihilates a hole from the valence band and the conservation of momentum is provided by a transfer of moment to a third particle (electron or hole). The process is then either referred to as *eeh* (two electrons, one hole) or *ehh* (one electron, two holes) process, and the recombination probability is therefore dependent on the carrier concentrations according to n^2p or p^2n, respectively [160]. Typically it is computed with the Auger coefficients C_n and C_p according to [161]

$$R_{\text{Auger}} = C_n(n^2p - n_0^2p_0) + C_p(np^2 - n_0p_0^2). \tag{4.8}$$

It should be mentioned, that combinations of these mechanism might also occur, e.g. Auger transitions can also be assisted by carrier-scattering mechanisms such as electron-phonon coupling [162] or involve impurities [163]. The conventional modeling of Auger recombination, i.e. Equation (4.8), is found to fail at low free carrier densities, which can be attributed to Coulomb interactions of the mobile charge carriers [164]. An often employed modeling approach by Richter et al. includes this effect by Coulomb enhancement factors for the *eeh* and *ehh* processes [165].

In Fig. 4.1 schematics in the band-diagram for the individual recombination channels are shown. Radiative recombination is drawn for a direct bandgap material in that figure, since it is typically a negigible component in indirect bandgap semiconductors. The other two mechanisms, i.e. SRH and Auger recombination, in Fig. 4.1 drawn for an indirect bandgap material are, however, also well present in direct bandgap materials and compete with radiative recombination.

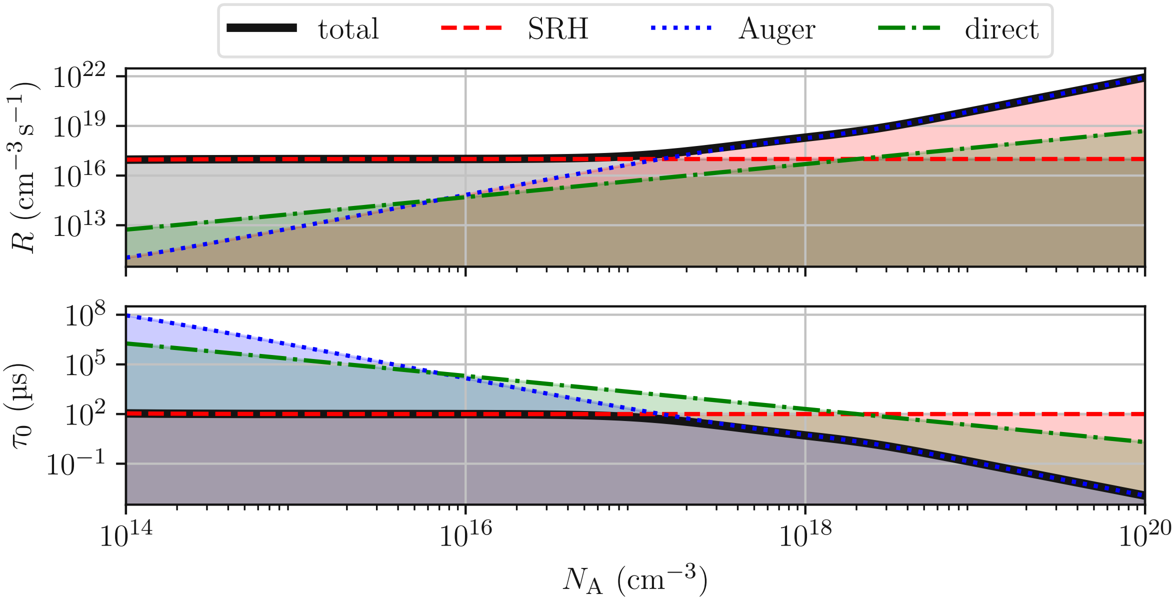

Figure 4.2. Recombination rates and corresponding lifetimes in p-type silicon. The combined recombination rate R and the minority carrier lifetime τ_0 ($\Delta n = 10^{13}\,\mathrm{cm}^{-3}$) is depicted versus the bulk acceptor concentration N_A. Auger recombination is modeled after [160], and direct recombination after [166]. SRH recombination is modeled after Equation (3.18) with $\tau_{n0} = \tau_{p0} = 100\,\mu\mathrm{s}$, which are typical values for high-purity silicon layers [167]. The trap is assumed to be mid-gap $E_\mathrm{T} = E_\mathrm{i}$. Originally published in [PSJ2].

It should be noted that the discussed recombination rates (Equations (3.18), (4.7) and (4.8)) account for net recombination, that is the rate of recombination or generation toward equilibrium. At finite temperatures recombination and generation are presented even in the case of equilibrium, given by the equilibrium recombination rate R_0 and generation rate G_0, which are equal and therefore the net rate is 0 (the principle of detailed balance holds for every of the discussed sub-process). In the equilibrium case the above stated net rates will be vanishing as $R_\mathrm{X}(n{=}n_0, p{=}p_0) = 0$ for any of the three processes X, as can be easily seen by observing the stated formulas. In Fig. 4.2 the above listed recombination rates are plotted as a function of the doping concentration in p-type silicon. As can be seen, direct recombination is a negligible component for any bulk doping. This is a direct consequence of the band structure of silicon, where an indirect bandgap leads to inefficienct direct recombination because of the conservation of momentum. Due to the same reason and as discussed in Section 2.2, also the opposite process, i.e. direct absorption of light is a rather inefficient process in indirect bandgap materials. Considering SRH and Auger recombination, it can be seen that at low bulk doping the SRH component dominates whereas at high bulk doping (transition at about $10^{17}\,\mathrm{cm}^{-3}$ in Fig. 4.2) Auger recombination dominates. A distinction between the above listed recombination channels is important to correctly interpret lifetime measurement data. For example, for a measured lifetime in the high doping regime, one needs to correctly identify Auger recombination as dominant mechanism, since an estimation of trap densities according to the SRH recombination rate would lead to an overestimation in that case.

Surface Recombination and Effective Lifetimes

In addition to recombination in the bulk, recombination at surfaces can decisively influence the measured carrier lifetimes. As was already discussed in Section 3.2.2 surface and interface recombination can be described with the SRH theory. In a one-dimensional approach the effect of surface recombination at the left (front) and right (back) boundaries of the domain can be modeled by an effective lifetime [168]:

$$\frac{1}{\tau_{\mathrm{eff}}} = \frac{1}{\tau_0} + \frac{1}{\tau_{\mathrm{s}}}, \tag{4.9}$$

where τ_{s} is called the surface lifetime. Considering an initial distribution of excess carriers $\Delta n(x,t)$ according to

$$\Delta n(x, t{=}0) \propto \exp\{-x\}, \tag{4.10}$$

a front-surface recombination velocity S_1 and a back-surface recombination velocity S_2, a general solution to the continuity equation can be found (by the technique of separating the variables), which has the form of [169, 170]

$$\Delta n(x,t) = \mathrm{e}^{-\frac{t}{\tau}} \sum_{n=1}^{\infty} A_n \mathrm{e}^{-\alpha_n^2 Dt} \sin\left(\alpha_n x\right) + B_n \mathrm{e}^{-\beta_n^2 Dt} \cos\left(\beta_n x\right), \tag{4.11}$$

where the coefficients A_n and B_n are determined by the initial conditions $\Delta n(x, t = 0)$ whilst the coefficients α_n and β_n are determined by the boundary conditions S_1 and S_2. When using Equation (4.11) to calculate a position averaged carrier lifetime, odd modes (sinus terms in the sum) vanish when performing a depth integration [170] and the carrier lifetime can be calculated in terms of characteristic modes m

$$\frac{1}{\tau_{\mathrm{eff},m}} = \frac{1}{\tau} + \beta_m^2 D, \tag{4.12}$$

where typically just the first mode is considered since it is the dominating component[2] [169]

$$\frac{1}{\tau_{\text{eff}}} = \frac{1}{\tau} + \beta^2 D, \tag{4.13}$$

where $\beta \equiv \beta_1$ was used. As mentioned above, β is related to the boundary conditions and domain length t_x via [171]

$$\cot(\beta t_\text{x}) = \frac{\beta^2 D^2 - S_1 S_2}{\beta D (S_1 + S_2)}, \tag{4.14}$$

which has no explicit solution but needs to be solved numerically. It should be mentioned that the assumption of an initially exponential spacial distribution (Equation 4.10) is typically justified, since in most carrier lifetime experiments excess carriers are created via electrical (forward biasing a pn-junction) or optical injection. In both cases carrier densities in the quasi-neutral region can be assumed to exponentially decay into the material (see for example Section 2.2.2). In Fig. 4.3 the effective lifetime is plotted as function of the surface recombination velocities. The lower left and upper right regions of this plot correspond to the special cases of same and very low surface recombination velocities and same and very high surface recombination velocities. In these cases explicit solutions to the problem are known [172]

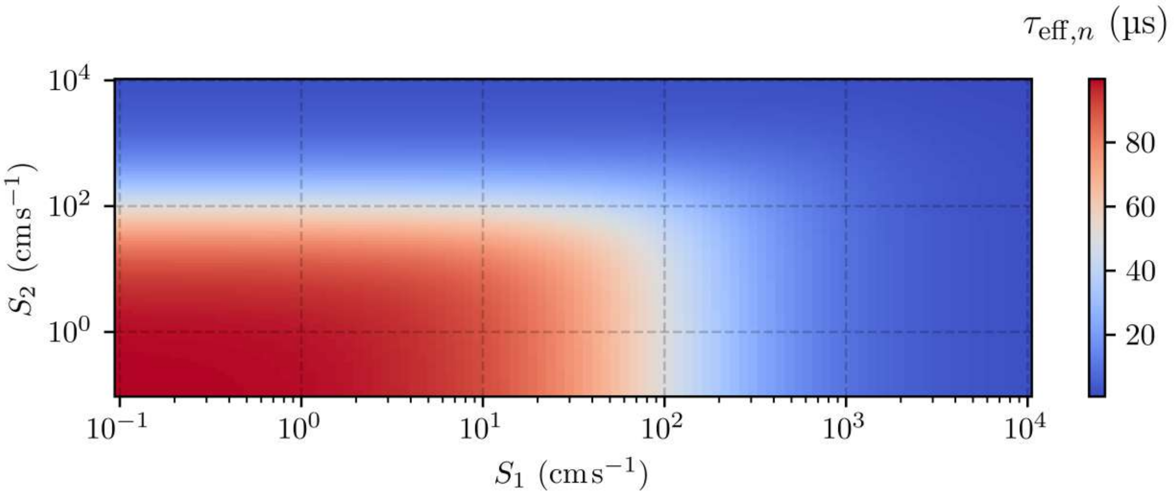

Figure 4.3. Effective electron lifetime $\tau_{\text{n,eff}}$ as function of surface recombination velocities S_1 and S_2 for a bulk lifetime of $\tau = 100\,\mu\text{s}$ according to Equation (4.13) and (4.14). The effective lifetime is maximal (max $\tau_{\text{n,eff}} = \tau$) for low surface recombination velocities (lower left corner) and the plot is symmetric with respect to the $x = y$ diagonal.

$$\lim_{S_1 = S_2 \gg \beta D} \frac{1}{\tau_\text{s}} = \frac{\pi^2}{t_\text{x}^2} D \tag{4.15a}$$

---

[2] β_1 is the smallest of the β_m and therefore $\tau_{\text{eff},1}$ the longest of the $\tau_{\text{eff},m}$. Consequently, higher order modes die out more rapidly and after some characteristic time the solution can be represented by a single exponential [169]

$$\lim_{S_1=S_2\ll\beta D} \frac{1}{\tau_\mathrm{s}} = \frac{2S}{t_\mathrm{x}} \tag{4.15b}$$

Interestingly, in the high surface recombination limit the solution becomes independent of the surface recombination velocity itself and becomes a function of the domain size only.

4.1.2 Current-Voltage and Capactiance-Voltage Characteristics

Various methods for the extraction of minority carrier lifetimes have been proposed in the literature. The majority of these methods is based on transient measurements, such as reverse recovery [173, 174, 175], open circuit voltage decay [176, 177], or the pulsed MOS capacitor technique [178, 179, 180]. Additionally, optical measurement techniques are frequently utilized to extract carrier lifetimes [155], which are often based on measured current or voltage transients after optical excitation, such as the photo-conductance decay method [181]. These methods are known to give reliable results but require additional optical tools which increase the experimental efforts. However, it is well known, that minority carrier lifetimes can also be extracted using cIVCV measurements, which do not require transient measurements or a special setup and can therefore be routinely utilized. Nonetheless, some of the proposed methods rely on approximations and simplifications that do not necessarily hold for every real device.
Therefore, the basic theory for the I-V and C-V relations in pn-junctions is reviewed, and accurate extraction procedures for the generation and recombination lifetime are discussed in detail in the subsections below. The basic equation describing a pn-junctions current-voltage characteristic was derived by Shockley in 1949 [45]. Shockley's diode model (often referred to as diffusion model) was later, in 1957, complemented by Sah, Noyce and Shockley to account for the generation and recombination of carriers from generation-recombination centers in the space charge region of a p-n junction (SNS model) [46]. Different approximations for the generation/recombination current can be found in literature, as well as lifetime extraction methods, relying on those approximations. In this section, it is shown how to accurately extract generation and recombination lifetime from cIVCV measurements. The results are benchmarked against computer simulations based on the drift-diffusion model and measurement results in Section 5.1.

PN-Junction Current Components

The total pn-junction current density j consists of a diffusion current density j_d and a generation/recombination current density j_U[3]. Neglecting the device's series

---

[3] In Section 3.3, where the influence of defects on the dark current was discussed, this quantity was introduced as j_g. In this section this quantity is more globally named j_U since it is discussed in the forward (net recombination) as well as reverse (net generation) bias regime. The net recombination rate $U = R - G$ is positive for recombination and negative for generation.

resistance the current density j can be calculated via

$$j = j_\mathrm{d} + j_\mathrm{U} = j_\mathrm{d0}\left(\exp\left(\frac{qV}{k_\mathrm{B}T}\right) - 1\right) + j_\mathrm{U}, \tag{4.16}$$

where j_d0 is the diffusion saturation current. It should be noted that the current density as introduced by Equation 4.16 scales directly with area. For devices with a non-negligible component from the perimeter (mostly surface effects) a separation between area and perimeter component should be performed [182].

(a) Diffusion Current Density j_d0

Within the depletion approximation and assuming 1D constant doping profiles (acceptor doping concentration N_A on the p-side and donor doping concentration N_D on the n-side) j_d0 is given by [45]

$$j_\mathrm{d0} = qn_\mathrm{i}^2 F\left(\frac{1}{N_\mathrm{A}}\sqrt{\frac{D_\mathrm{n}}{\tau_n}} + \frac{1}{N_\mathrm{D}}\sqrt{\frac{D_\mathrm{p}}{\tau_p}}\right), \tag{4.17}$$

where $\tau_{\mathrm{n(p)}}$ is the electron (hole) minority carrier lifetime and F a correction factor accounting for finite device lengths [183]. An important limit of Equation 4.17 is the case of strongly asymmetric doping ($N_\mathrm{A} \ll N_\mathrm{D}$ or vice versa $N_\mathrm{A} \gg N_\mathrm{D}$) where the sum gets dominated by the lower doped side.

(b) Generation / Recombination Current Density j_U

The space charge region generation/recombination current j_U can be calculated by integrating the net recombination rate along the depletion zone $W = W_2 - W_1$:

$$j_U = q\int_{W_1}^{W_2} U\,\mathrm{d}x\,, \tag{4.18}$$

where the recombination rate U can be calculated according to SRH theory, i.e. Equation 3.18 for single defect dominated recombination. Next, different analytical approximations of this integral in the forward and reverse bias regime are discussed.

PN-Junction Capacitance and Depletion Width

According to the simple model of a parallel-plate capacitor with area A the voltage dependent junction capacitance $C(V)$ is related to the depletion width W via

$$C(V) = \frac{\epsilon_\mathrm{Si} A}{W(V)}. \tag{4.19}$$

Therefore, a measurement of $C(V)$ allows for simple experimental extraction of the voltage-dependent depletion width $W(V)$. It should be noted that (4.19) neglects the diffusion capacitance, which is a valid assumption in the reverse bias and small forward bias regime but may fail at strong forward biases [184]. Commonly, the C-V measurement of the pn-junction is used to extract the voltage-dependent width of the depletion region $W(V)$, which is then used in conjunction with I-V measurements to extract lifetime parameters. In the following subsection, approximations to derive the lifetime extraction equations in the reverse and forward bias regime are discussed.

Lifetime Extraction with Combined I-V and C-V Measurements

(a) **Reverse Bias Regime**

The reverse bias extraction method (RM) [185, 186] relies on a widely used approximation of the SRH recombination rate in the reverse bias regime

$$U \approx -\frac{n_\mathrm{i}^2}{\tau_0(n_1+p_1)} = -\frac{n_\mathrm{i}}{\tau_\mathrm{g}}, \tag{4.20}$$

where τ_0 is the minority carrier recombination lifetime. In Equation (4.20) the generation lifetime τ_g was introduced as

$$\tau_\mathrm{g} = 2\tau_0 \cosh\left(\frac{E_\mathrm{T}-E_\mathrm{i}}{k_\mathrm{B}T}\right). \tag{4.21}$$

The minus sign in Equation (4.20) indicates net generation in the depletion zone. Since Equation (4.20) is independent of the integration variable x in Equation (4.18), j_U can be straightforwardly calculated by multiplying with the depletion width W

$$j_\mathrm{U} = \frac{-qn_\mathrm{i}W}{\tau_\mathrm{g}} \tag{4.22}$$

and the total current density for a larger reverse bias can then be written as

$$j = -j_\mathrm{d0} - \frac{qn_\mathrm{i}}{\tau_\mathrm{g}}W. \tag{4.23}$$

Consequently, the reverse current density $-j$ is expected to rise linearly with W, and a linear fit of $-j$ versus W allows to extract τ_g and j_d0.

As can be seen in Fig. 4.4, Equation (4.20) is indeed an accurate approximation for R. However, R is not constant along the full depletion width W but rather along some effective width W_eff. For an abrupt junction and $N_\mathrm{D} \gg N_\mathrm{A}$, W_eff can be approximated via [187, 188]

$$W_{\mathrm{eff}}(V) \approx W(V) - \sqrt{\frac{2\epsilon_{\mathrm{Si}} k_{\mathrm{B}} T}{q^2} \left(\frac{1}{N_{\mathrm{A}}} \log\left(\frac{N_{\mathrm{A}}}{n_{\mathrm{i}}} \right) \right)}. \qquad (4.24)$$

Therefore, higher accuracy can be achieved by fitting the current density j in Equation (4.23) against W_{eff} instead of W to correct for the otherwise present overestimation of the effective generation width. It should be noted that W_{eff} and W differ by a constant offset meaning the correction will only affect the extracted value of j_{d0} not τ_{g}. However, as outlined in Reference [189], a correction according to Equation 4.24 might still lack accuracy and in Reference [189] a more advanced formula for W_{eff} is presented. For the purpose of this work, however, the method is used to extract τ_{g} only, where good extraction accuracy is achieved even without any correction. Nevertheless, the correction via Equation (4.24) improves the accuracy of the extracted value for j_{d0}. For a more reliable extraction of j_{d0} a direct fit in the forward bias regime according to the two-diode model (TDM) can be performed as is presented in the following section.

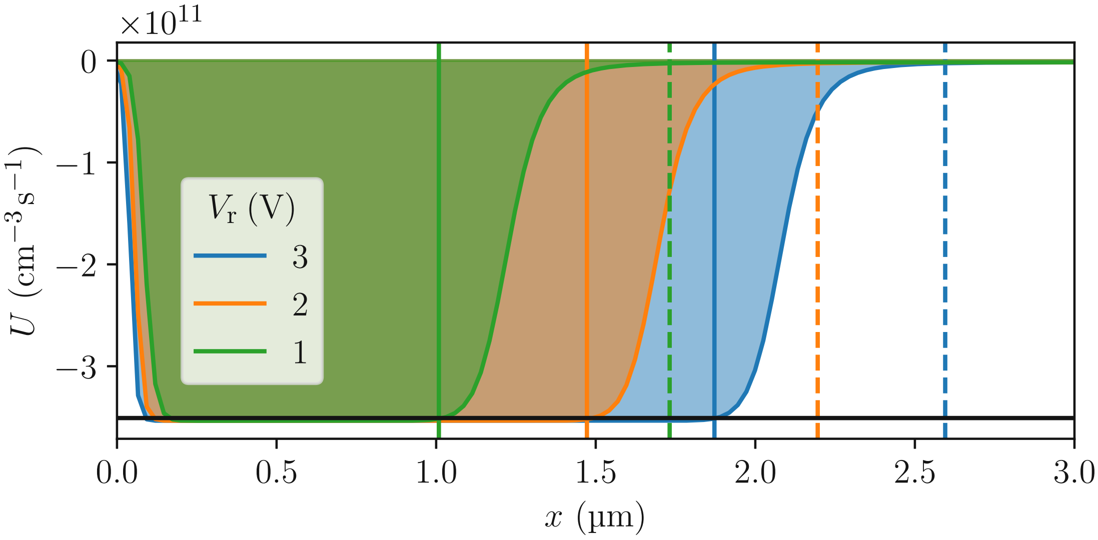

Figure 4.4. TCAD simulation results of the generation rate in the depletion zone in a reverse biased pn-junction. Details and models of the simulation are shown in Section 5.1. Plotted is the net recombination rate U versus position x for different values of the applied reverse voltage V_{r} and simulation data with lifetime $\tau_0 = 100\,\mu\mathrm{s}$ and $E_{\mathrm{T}} - E_{\mathrm{i}} = 0.15\,\mathrm{eV}$. The dashed vertical lines indicate the depletion width W, the solid vertical lines the effective width W_{eff} (Equation 4.24). The black horizontal line marks the approximation, Equation (4.20). The negative values of the net-recombination rate $U = R - G$ indicate generation. Originally published in [PSJ3].

(b) Forward Bias Regime

A lifetime extraction method in the forward bias regime, that allows for a simulatenous extraction of τ_0 and τ_g was presented in Reference [182]. However, in this work a correction scheme to get improved and more accurate results is proposed. The basic idea is to find a suitable way to accurately calculate the position dependent recombination rate $U(x)$ within the depletion zone, and then to calculate the recombination current via integrating over it with respect to the position x.

(b1) **Derivation of Lifetime Extraction Equation**

The starting point is the recombination current, Equation (4.18), with the full expression for the SRH recombination rate:

$$j_\mathrm{U} = q \int_{W_1}^{W_2} \overbrace{\frac{1}{\tau_0} \frac{n_\mathrm{i}^2 \left(\exp\left(\frac{qV}{k_\mathrm{B}T}\right) - 1\right)}{n(x) + p(x) + 2n_\mathrm{i} \cosh\left(\frac{E_\mathrm{T}-E_\mathrm{i}}{k_\mathrm{B}T}\right)}}^{U_\mathrm{SRH}(x)} \mathrm{d}x, \tag{4.25}$$

where the simplification $\tau_{n0} = \tau_{p0} = \tau_0$ was used. The exact integral in (4.25) can not be solved analytically, however, the integrand shows a maximum U_max [190]:

$$U_\mathrm{max} = \frac{1}{2n_\mathrm{i}\tau_0} \frac{n_\mathrm{i}^2 \left(\exp\left(\frac{qV}{k_\mathrm{B}T}\right) - 1\right)}{\exp\left(\frac{qV}{2k_\mathrm{B}T}\right) + \cosh\left(\frac{E_\mathrm{T}-E_\mathrm{i}}{k_\mathrm{B}T}\right)}. \tag{4.26}$$

Via Equation (4.26) an upper limit $j_\mathrm{U,max} = WU_\mathrm{max}$ can be defined, whereas the exact value of j_U is given by:

$$j_\mathrm{U} = W \overbrace{\frac{1}{W} \int_{W_1}^{W_2} U(x)\mathrm{d}x}^{U_\mathrm{avg}} = \frac{j_\mathrm{U,max}}{f_\mathrm{U}}, \tag{4.27}$$

with $U_\mathrm{avg} < U_\mathrm{max}$ and $f_\mathrm{R} > 1$. In (4.27) f_R is introduced as the ratio between j_U and $j_\mathrm{U,max}$ (or equivalently U_avg and U_max). Equation (4.25) is then given by

$$j_\mathrm{U} = \frac{qn_\mathrm{i}}{2\tau_0 f_\mathrm{R}} \frac{\left(\exp\left(\frac{qV}{k_\mathrm{B}T}\right) - 1\right) W}{\exp\left(\frac{qV}{2k_\mathrm{B}T}\right) + \cosh\left(\frac{E_\mathrm{T}-E_\mathrm{i}}{k_\mathrm{B}T}\right)}. \tag{4.28}$$

Defining the saturation bulk recombination current density j_rb0 as

$$j_\mathrm{rb0} = \frac{j}{\left(\exp\left(\frac{qV}{k_\mathrm{B}T}\right) - 1\right)} - j_\mathrm{d0}, \tag{4.29}$$

the following relation can be derived:

$$\frac{qn_\mathrm{i}W}{j_\mathrm{rb0} f_\mathrm{U}} = 2\tau_0 \exp\left(\frac{qV}{2k_\mathrm{B}T}\right) + \tau_\mathrm{g}. \tag{4.30}$$

The basic methodology to extract lifetimes based on Equation (4.30) is to plot $\frac{qn_iW}{j_{rb0}}$ against $2\exp\left(\frac{qV}{2k_BT}\right)$ and perform a linear regression to extract τ_0 (slope) as well as τ_g (intercept). It should be noted that the correction factor f_U was not considered in Reference [182] which might lead to an enormous overestimation of the extracted lifetime (see Tab. 5.3 in Section 5.1.3). Therefore, the results without correction might serve as upper bounds for the extracted lifetime parameters but can deviate from the real values. However, in the next section, it is outlined how the results can be analytically corrected for this overestimation. Fig. 4.5 shows a plot of recombination rate R versus position x within the depletion width for TCAD simulations with $\tau_{EPI} = 10\,\mu s$. One can see that $j_{U,max}$ considerably overestimates j_U.

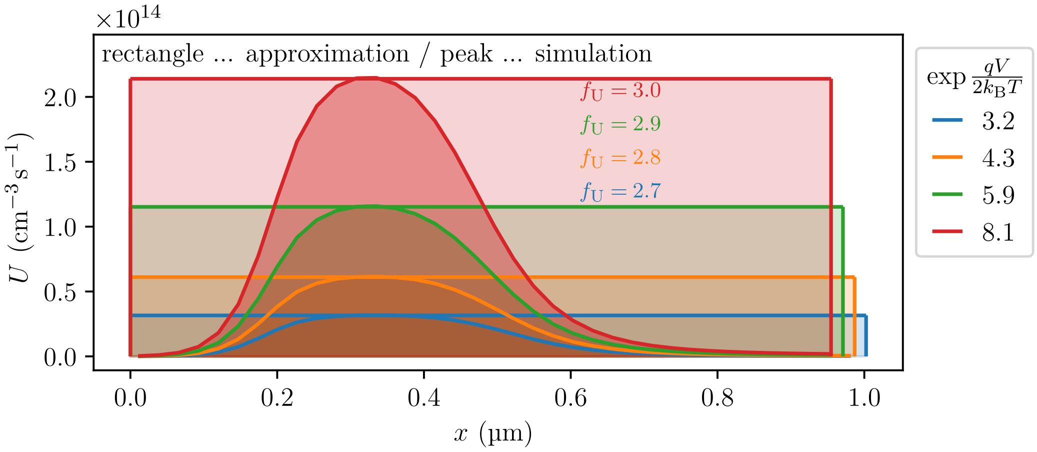

Figure 4.5. TCAD simulation results of the recombination rate in the depletion zone in a forward biased pn-junction. Details and employed models of the simulation are shown in Section 5.1. Plotted is the net recombination rate U versus position x for 4 different values of the forward bias $\exp\left(\frac{qV}{2k_BT}\right)$ of the simulation data with lifetime $\tau_0 = 100\,\mu s$ and $E_T - E_i = 0.15\,eV$. Originally published in [PSJ3].

(b2) Analytical Correction

In the forward bias regime the recombination R is peaked at the plane $x = x_0$, where $p = n$ (see also Fig. 4.5) and the electric field is at its maximal value F_0 [191]

$$F_0 = \sqrt{\frac{k_BTN_A}{\epsilon_{Si}}\left(2\log\left(\frac{N_A}{n_i}\right) - \frac{eV}{k_BT}\right)}. \tag{4.31}$$

In the vicinity of this plane, the carrier concentrations can be calculated via a first-order expansion in the electrostatic potential [191, 192]

$$n(p) = n_i \exp\left(\frac{eV}{2k_BT}\right)\exp\left(\frac{\pm qF_0(x-x_0)}{k_BT}\right), \tag{4.32}$$

where the positive sign in the exponent refers to electrons and the negative sign refers to holes. Substituting Equation (4.32) into Equation (4.25) yields:

$$j_U = \frac{qn_\mathrm{i}\left(\exp\left(\frac{qV}{k_\mathrm{B}T}\right)-1\right)}{2\tau_0\exp\left(\frac{qV}{2k_\mathrm{B}T}\right)}\int_{W_1}^{W_2}\frac{1}{\cosh\left(\frac{qF_0(x-x_0)}{k_\mathrm{B}T}\right)+\beta}\mathrm{d}x, \tag{4.33}$$

where β was introduced as

$$\beta = \cosh\left(\frac{E_\mathrm{T}-E_\mathrm{i}}{k_\mathrm{B}T}\right)\exp\left(\frac{-qV}{2k_\mathrm{B}T}\right). \tag{4.34}$$

Since the integrand in Equation (4.33) is sharply peaked and decreases towards zero rapidly (see also Fig. 4.5), the integration limits W_1 and W_2 can be extended to $\pm\infty$, allowing the integral, Equation (4.33), to be solved analytically [193]

$$j_\mathrm{U} = \frac{qn_\mathrm{i}}{2\tau_0}\frac{\left(\exp\left(\frac{qV}{k_\mathrm{B}T}\right)-1\right)V_\mathrm{t}/F_0 f_\mathrm{b}(\beta)}{\exp\left(\frac{qV}{2k_\mathrm{B}T}\right)}, \tag{4.35}$$

where V_t is the thermal voltage

$$V_\mathrm{t} = \frac{k_\mathrm{B}T}{q}, \tag{4.36}$$

and the function $f_\mathrm{b}(\beta)$ is given by

$$f_\mathrm{b}(\beta)=\int_{-\infty}^{\infty}\frac{1}{\cosh x+\beta}\mathrm{d}x=\begin{cases}\frac{2\log\left(\beta+\sqrt{\beta^2-1}\right)}{\sqrt{\beta^2-1}} & \text{if}\,\beta\geq 1\\ \frac{4\arctan\left(\frac{\beta-1}{\sqrt{1-\beta^2}}\right)}{\sqrt{1-\beta^2}} & \text{if}\,\beta<1\end{cases}. \tag{4.37}$$

Considering Equations (4.27)-(4.35) the correction factor f_R can be calculated

$$f_\mathrm{R} = \frac{WF_0}{V_\mathrm{t}f_\mathrm{b}(\beta)(1+\beta)}. \tag{4.38}$$

This correction factor accounts for the overestimation of the current density, Equation 4.33, if the actual integrand $U_\mathrm{SRH}(x)$ is approximated by U_max and is visually given by the ratio of the rectangular area to the area below the peaked curve in Fig. 4.5. Consistent with the results presented in Tab. 5.3 the correction factor does not depend on the lifetime τ_0, however, it depends on E_T via Equation (4.34).

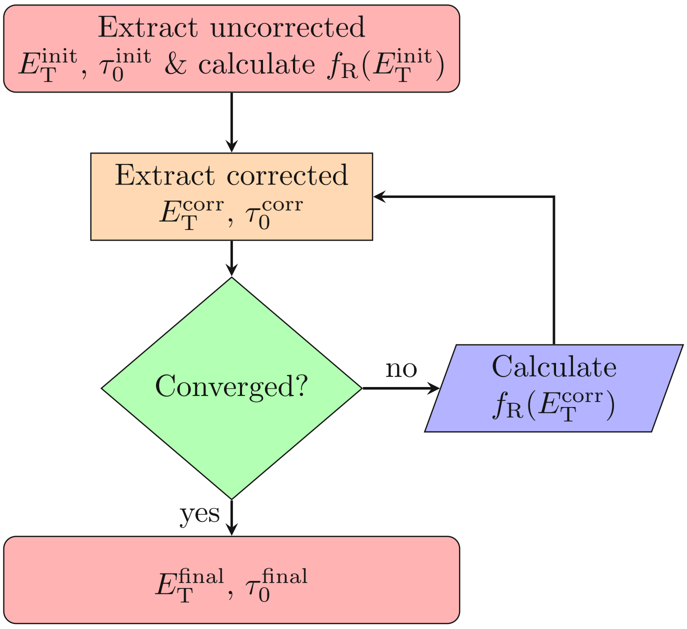

Figure 4.6. Flow-chart of the cIVCV correction scheme. Originally published in [PSJ3].

Therefore an iterative correction scheme which as shown in Fig. 4.6 is proposed. First, the linear fit, using Equation (4.30), without correction, i.e., $f_\mathrm{R} = 1$, is made to extract τ_0^init and $E_\mathrm{T}^\mathrm{init}$. Then the correction factor, given by Equation (4.38), is computed and the fit is repeated with $f_\mathrm{R} = f_\mathrm{R}(E_\mathrm{T}^\mathrm{init})$. This procedure is repeated until convergence is reached, where a convergence criterion such as $E_\mathrm{T}^i - E_\mathrm{T}^{i-1} < \delta$ can be defined, where E_T^i is the extracted trap energy of the i-th iteration and δ a small energy difference, e.g. $\delta = 1\,\mathrm{meV}$. Finally, it should be mentioned that the extracted trap energy can just be estimated as absolute distance to the intrinsic energy, i.e. $|E_\mathrm{T} - E_\mathrm{i}|$, because of the even symmetry of the $\cosh(x)$ function.

(b3) Extraction of Diffusion Current Density

In Equation (4.29) j_d0 needs to be subtracted. Therefore, the extraction of this parameter is discussed next. For a forward bias larger than $\approx 0.25\,\mathrm{V}$ and considering the diode area A and series resistance R_s the forward current of a pn-junction can be well described by a two-diode model (TDM) [194]

$$j = j_\mathrm{d0} \exp\left(\frac{q(V - jAR_\mathrm{s})}{k_\mathrm{B}T}\right) + j_\mathrm{r0} \exp\left(\frac{q(V - jAR_\mathrm{s})}{2k_\mathrm{B}T}\right). \tag{4.39}$$

The TDM consists of a diffusion-dominated diode with ideality factor 1 and a recombination-dominated diode with ideality factor 2. Equation (4.39) is implicit in j, still, it can be easily fitted to measurement/simulation data with numerical routines. Therefore, the extraction of j_d0 via minimizing residuals of measurement/simulation data to the model Equation (4.39) on a log scale is proposed. This procedure has led to the most reliable results compared to other methods such as the reverse method (fit to Equation (4.23)) presented above or the forward bias separation method [194].

4.1.3 Open Circuit Voltage Decay (OCVD)

The OCVD technique [176, 177] has been proposed to determine minority carrier lifetimes in junction devices and relies on measuring the voltage decay across the junction after excitation at forward bias. A schematic circuit drawing can be seen in Fig. 4.7, and the method works as follows: For the period $t < t_0$ the pn-junction is forward biased by a voltage V_f (leading to the forward current I_f). At t_0 the circuit is opened using a switch and the open voltage decay from $V_\mathrm{oc} = V_\mathrm{f}$ to $V_\mathrm{oc} = 0$ is recorded. It should be noted, that a high input impedance of the voltage acquisition unit is required as otherwise the leakage current into the measurement system would dominate and distort the extracted lifetimes. From the data, the first-order effective carrier lifetime $F(t)$ can be extracted using

$$F(t) = -n\frac{k_\mathrm{B}T}{q}\left(\frac{\mathrm{d}V_\mathrm{oc}}{\mathrm{d}t}\right)^{-1}, \tag{4.40}$$

where n is the ideality factor of diodes, with typical values between 1 and 2 [195]. Equation (4.40) can be derived considering that the electron concentration $n(t)$ of an n+/p junction at the edge of the depletion region on the lower doped p-side is related to the voltage across the junction $V(t)$ via the Shockley relation

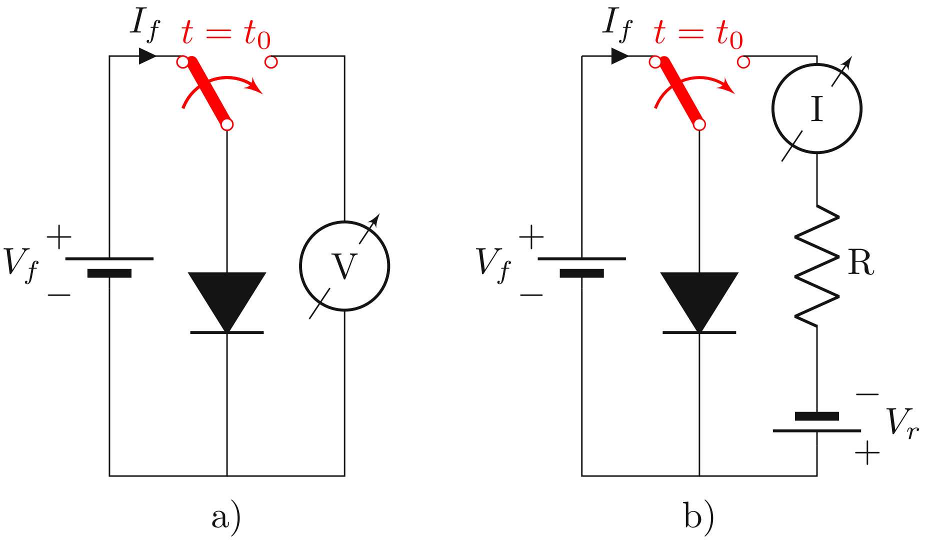

Figure 4.7. Schematic circuit diagrams for the **a)** open circuit voltage decay (**OCVD**) and **b)** reverse recovery (**RR**) measurement method. For $t < t_0$ a forward voltage V_f drives a current I_f through the device under test. At $t = t_0$ the position of the switch is changed and the voltage (OCVD) / current (RR) across / through the diode is recorded. Originally published in [PSJ2].

$$n = n_{p0} + \Delta n(t) = n_{p0}\mathrm{e}^{qV(t)/(k_\mathrm{B}T)}. \tag{4.41}$$

After excitation, i.e. at $t = 0$, the electron concentration $\Delta n(t)$ returns to equilibrium governed by an exponential time constant given by the effective carrier lifetime τ_{eff} [196] (see also Equation (4.11) and subsequent discussion)

$$\Delta n(t) = \Delta n_0 \mathrm{e}^{-t/\tau_{\mathrm{eff}}} = n_{p0}\left(\mathrm{e}^{qV_0/(k_\mathrm{B}T)} - 1\right)\mathrm{e}^{-t/\tau_{\mathrm{eff}}} \tag{4.42}$$

and hence by combining Equations (4.41) and (4.42) a relation for the open circuit voltage can be derived

$$V(t) = \frac{k_\mathrm{B}T}{q}\ln\left(1 + \left(\mathrm{e}^{qV_0/(k_\mathrm{B}T)} - 1\right)\mathrm{e}^{-t/\tau_{\mathrm{eff}}}\right). \tag{4.43}$$

Finally, for t/τ_{eff} being small and for $V_0 \gg k_\mathrm{B}T/q$ the derivative of Equation (4.43) is given by Equation (4.40), allowing for an extraction of lifetime via measuring the voltage decay [177]

$$F(t) \approx \tau_{\mathrm{eff}}. \tag{4.44}$$

Depending on the measurement period, the assumption t/τ_{eff} being small might be violated at some point during the measurement, and hence $V(t)$ might not decay linearly any more. Additionally, circuitry parasitics may lead to a deviating voltage decay [197]. However, it can be shown, that F shows a constant plateau immediately after opening the circuit which allows to extract τ_{eff} [198]. This plateau is visible in the measurement and simulation results discussed in Section 5.1.4.

4.1.4 Reverse Recovery (RR)

The reverse recovery method also allows for the extraction of carrier lifetimes by transient I-V measurements on junction devices [173, 174, 175] and a schematic of the circuitry is given on the right hand side of Fig. 4.7. For $t < t_0$ a forward voltage V_f is applied resulting in a forward current I_f. At $t = t_0$ the voltage across the pn-junction is switched from a forward to a reverse bias. Before the diode is able to block the current flux, minority carriers are still in place that must be removed. These minority carriers will result in an initial reverse current I_r, that will in the first stage remain constant until the excess carrier density at the edges of the space charge region has decreased to zero, which takes place within the storage time t_s. Afterwards, the reverse current will approach its equilibrium value I_0 [155]. The forward current I_f, reverse current I_r and storage time t_s are related to the effective minority carrier lifetime τ_{eff} via [199, 200]

$$t_\mathrm{s} = \tau_{\mathrm{eff}}\left(\ln\left(1 + \frac{I_\mathrm{f}}{I_\mathrm{r}}\right) + \mathrm{const}\right), \tag{4.45}$$

which allows for the extraction of τ_{eff}.
In theory, the reverse current after excitation I_r without any load resistor in the circuit, (i.e. with $R = 0$ according to Fig. 4.7), is infinitely high, corresponding to zero device under test (DUT) resistance, i.e. $R_{\mathrm{DUT}} = 0$ [196]. Therefore, I_r in the storage phase

$(0 < t < t_\mathrm{s})$ is governed by the parasitic and circuitry resistance and can be set with the external resistor $I_\mathrm{r} = V_\mathrm{r}/R$.

4.2 Determination of Defect Parameters

Whilst the previously presented methods of lifetime characterization and extraction allow for an indirect estimation of defect parameters, based on the assumption of SRH dominated lifetimes, direct defect spectroscopy methods are discussed in this section.

4.2.1 Deep Level Transient Spectroscopy (DLTS)

DLTS, as one of the most utilized electrical defect spectroscopy methods, was introduced and termed by Lang in 1974 [150]. The basic idea is to measure the emission of charge carriers from trap states into the bands via observing the corresponding change in capacitance of a pn-junction. The rates at which carriers are captured or emitted from trap states to the bands were discussed in terms of the SRH model in Section 3.2.2 and for the NMP model in Section 3.2.3.

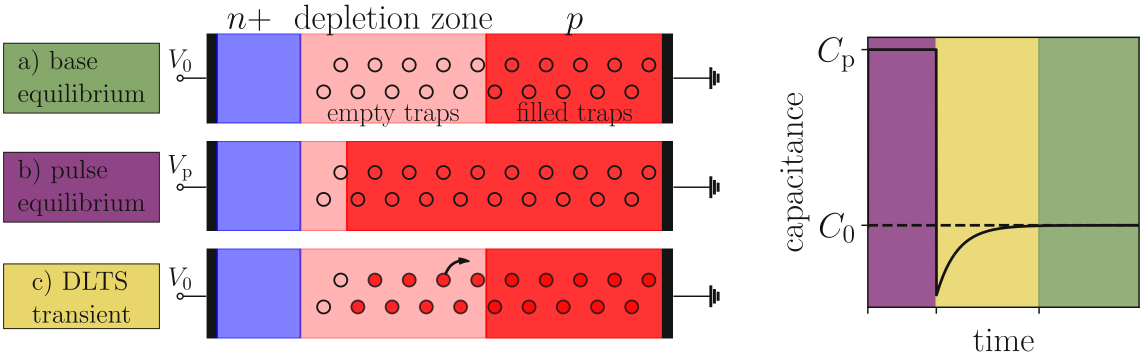

Figure 4.8. Schematics of a DLTS sequence in a pn-junction. Because of the asymmetric doping the depletion zone is almost entirely located in the lower doped p-side. In the base equilibrium state (reverse voltage V_0 applied) trap states in the depletion zone can be considered empty of holes and trap states in the QNR can be considered filled with holes. When the pulse voltage V_p is applied for a long enough time (pulse equilibrium) the depletion zone gets narrower (the capacitance gets higher, i.e. to C_p) and previously empty traps get filled. Upon returning to the base voltage, charge carriers filling the traps are re-emitted leading to a DLTS transient.

Considering an n+/p junction, as sketched in Fig. 4.8 the capacitance C is given by the net charge density on the lower doped side N_src via

$$C(t) = A\sqrt{\frac{q\epsilon}{2}}\sqrt{\frac{N_\mathrm{scr}(t)}{V_\mathrm{bi} - V}}, \tag{4.46}$$

where ϵ is the material-specific dielectric constant and V_bi the pn-junction built-in voltage. The net charge density N_src is in principle given by the density of ionized acceptor atoms N_A^-. However, in the presence of holes being in trap states it is reduced according to

$$N_\mathrm{src}(t) = N_\mathrm{A}^- - p_\mathrm{T}(t). \tag{4.47}$$

The basic idea of the DLTS is to first fill trap states by applying a filling pulse (with a zero or forward bias to the diode) such that

$$p_\mathrm{T}(t=0) \approx N_\mathrm{T}, \tag{4.48}$$

and then to return to a reverse bias while measuring the capacitance transients

$$C(t) \approx C_0 \left(1 - \frac{p_\mathrm{T}(t)}{2N_\mathrm{A}}\right). \tag{4.49}$$

To derive Equation (4.49), parameters are summarized by the constant C_0 and it is considered that the trap densities are typically much lower than the doping concentrations $N_\mathrm{T} \ll N_\mathrm{A}$ and hence a first order expansion may be used

$$\sqrt{1 - \frac{p_\mathrm{T}}{N_\mathrm{A}}} \approx 1 - \frac{p_\mathrm{T}}{2N_\mathrm{A}}. \tag{4.50}$$

Finally, for the time-dependency of the emission $p_\mathrm{T}(t)$, it has to be considered that trap-emitted holes are in the depletion zone and will be swept out fast by the strong electric field, minimizing the change of re-capturing and therefore [155]

$$p_\mathrm{T}(t) = N_\mathrm{T} \exp\{-tk_\mathrm{c}\} = N_\mathrm{T} \exp\left(-\frac{t}{\tau_\mathrm{e}}\right), \tag{4.51}$$

with the emission time constant $\tau_\mathrm{e} = 1/k_\mathrm{c}$ given by Equation (3.16), such that

$$\widehat{C} = \frac{C(t) - C_0}{C_0} = \frac{\Delta C(t)}{C_0} = -\frac{N_\mathrm{T}}{2N_\mathrm{A}} \exp\left(-\frac{t}{\tau_\mathrm{e}}\right), \tag{4.52}$$

where the normalized capacitance was introduced as $\widehat{C}$. The essence of this technique, is to extract the emission times τ_e via Equation (4.52) at multiple temperatures to exploit their strong temperature dependency in the Arrhenius relation

$$\tau_e T^2 = \frac{1}{\gamma_p \sigma_p} \exp\left(\frac{E_\mathrm{T} - E_\mathrm{v}}{k_\mathrm{B} T}\right), \tag{4.53}$$

where the temperature-independent parameters of k_c are incorporated in the material constant γ_p.

Distinction Between Trapped Majority and Minority Carriers

The DLTS relations stated above were discussed in terms of trapped majority carriers. The very same relations can be derived for minority carriers, with the one main difference, that the charge related to trapped carriers in Equation (4.47) has the opposite sign. In that case the leading sign of the exponential in Equation (4.52) changes allowing a distinction between trapped majority and minority carriers. This is schematically drawn in Fig. 4.9. It should be noted, that the curve forms for majority and minority carrier related trapping are not inherent to the n+/p configuration used to derive and demonstrate the DLTS relations in this section but are the very same for the opposite configuration, i.e. carriers being trapped in the lower doped n-type side of a pn-junction.

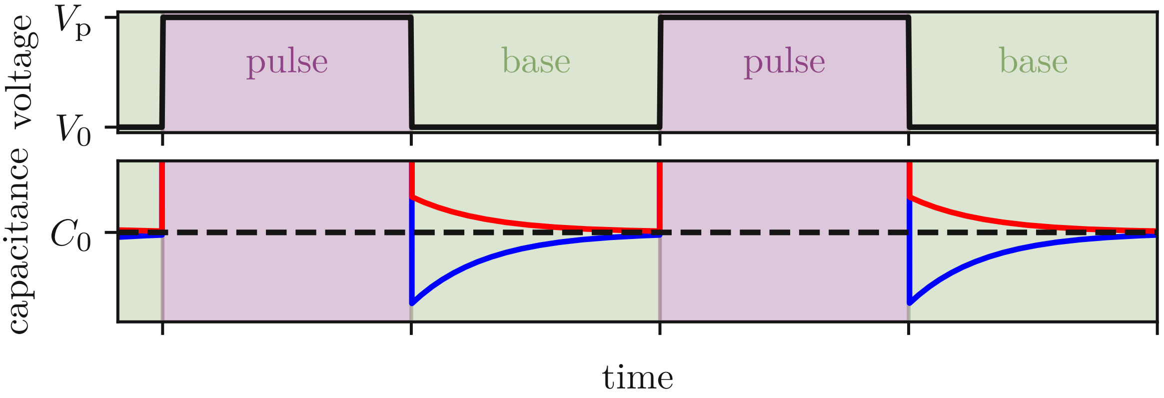

Figure 4.9. Distinction between majority (blue) and minority carrier (red) traps in a DLTS sequence. **(upper)** The voltage is varied between the levels V_0 and V_p. **(lower)** Majority (blue) and minority carrier (red) trap-related capacitance transients can be distinguished by the leading sign of the exponential.

Extraction of Time Constants

The extraction of time constant of DLTS capacitance transients, given by Equation (4.52), is a challenging task considering the measurement noise floor and that typically $N_\mathrm{T} \ll N_\mathrm{A}$ and hence $\Delta C/C_0 \ll 1$. Therefore Lang proposed the boxcar approach, where the difference in capacitance $\Delta C = C(t_2) - C(t_1)$ at two time stamps t_1, t_2 is evaluated at multiple temperatures [150]. This extraction procedure is schematically drawn in Fig. 4.10 (right side plot). The basic principle is, that $\Delta\widehat{C}(T)$ is expected to have a maximum $\widehat{C}^*$ at the temperature T^*, which relates the emission time constant at T^* to the chosen timestamps t_1 and t_2. This *rate window* formula is shown as inset in Fig. 4.10. It is important to note, that the double boxcar approach, as sketched in Fig. 4.10 was done in the early days of DLTS in an analog fashion [201]. In nowadays experimental setups, capacitance transients are mostly recorded digitally, allowing the DLTS analysis to be done in the post-processing. Furthermore, to get better resolution performance, instead of using the capacitance difference at single timestamps, different weighting functions, such as the boxcar average or square wave weighting function, may be used, that make use of the whole measurement data [202]. Another, more recent, approach to extract time constants from the measured capacitance transients is *Laplace DLTS*, where the emission time constants are extracted by applying the inverse Laplace

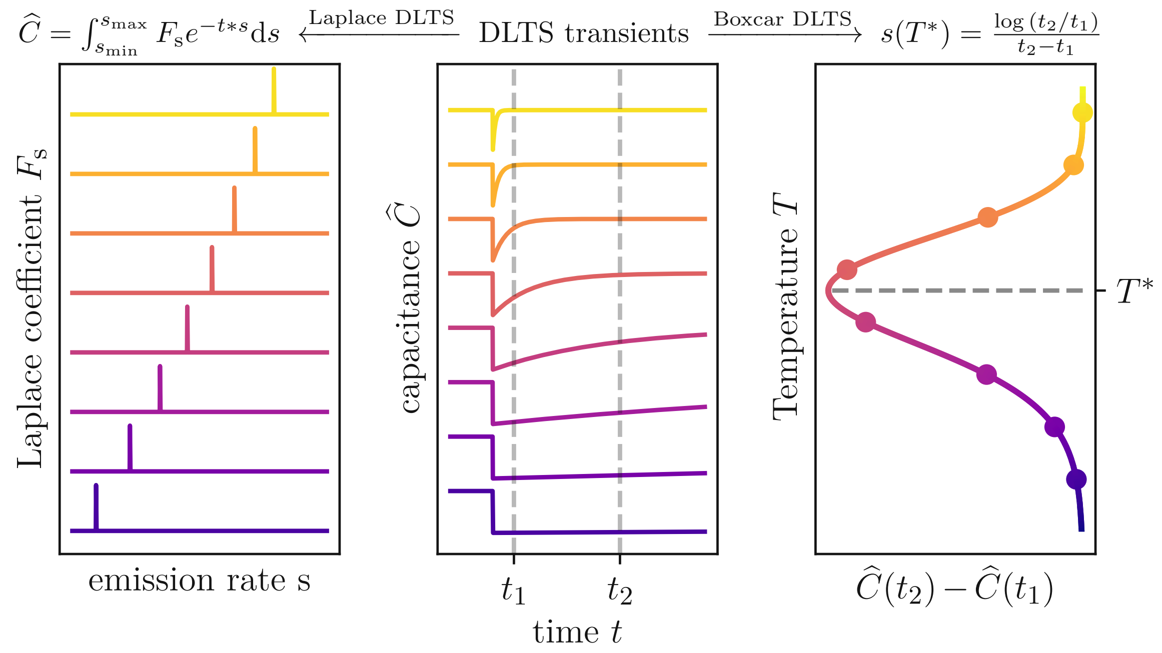

Figure 4.10. Extraction of emission time constants. The measured DLTS capacitance transients **(middle)** can be analysed by means of the Laplacian method **(left)** or the conventional boxcar approach **(right)**. For Laplace DLTS the measured capacitance transients $C(t)$ are deconvoluted into the emission spectra via the inverse Laplace transform $s(T^*) = \mathcal{L}^{-1}(\widehat{C}(T^*))$. In the double boxcar approach the capacitance difference $\Delta\widehat{C} = \widehat{C}(t_2) - \widehat{C}(t_1)$ is evaluated at multiple temperatures and the rate s, at temperature T^* where $\Delta\widehat{C}(T^*)$ is maximized, is given by $s(T^*) = \log(t_2/t_1)/(t_2 - t_1)$.

transform to the measured signal [203], as indicated in the left side plot of Fig. 4.10. However, this procedure is a mathematically ill-posed problem, and the numerical solution requires advanced computational methods [204], which is one of the reasons for the rather late breakthrough of this method compared to the conventional ones. One major difference is the fact that, with the conventional extraction procedures (boxcar or different weighting functions) capacitance transients at multiple temperatures have to be measured, whilst for the Laplace DLTS in principle emission times can be extracted out of a single temperature measurement. For an extraction of defect parameters by a linear fit in the Arrhenius relation, i.e. Equation (4.53), however, extracted emission times at multiple temperatures are needed anyway.

4.2.2 Injection-Dependent Responsivity Measurements (IDRM)

As has been mentioned previously, the SRH recombination rate is injection-dependent. The basic idea of the injection-dependent responsivity (IDR) extraction is to exploit the injection-dependency of (interface) defects to infer information about the defect parameters. Basically, defect parameters are fitted to the measured responsivity as function of radiant flux $R(\Phi)$ by means of performing technology computer-aided design (TCAD) simulations. The work-flow of the fitting procedure is shown in Fig. 4.11. After performing the measurement, defining the initial parameter set and parameter space based on the information available in literature a TCAD device simulation is performed. The simulation results are then compared to measurement results by computing the corresponding residuals, and if the targeted tolerance is not achieved, the parameter set is varied and the procedure is repeated. Different, well established, methods for finding the minimum in the multi-dimensional parameter space may be used. In this work the Nelder-Mead algorithm is employed [205]. Finally, it should be noted that the extraction of defect parameters by means of injection-dependent lifetime measurements is well established [206, 207, 208]. In this work, however, the methods are not applied on lifetimes but rather responsivities, a photodiode quantity that is directly related to lifetimes as was discussed in Section 3.3.

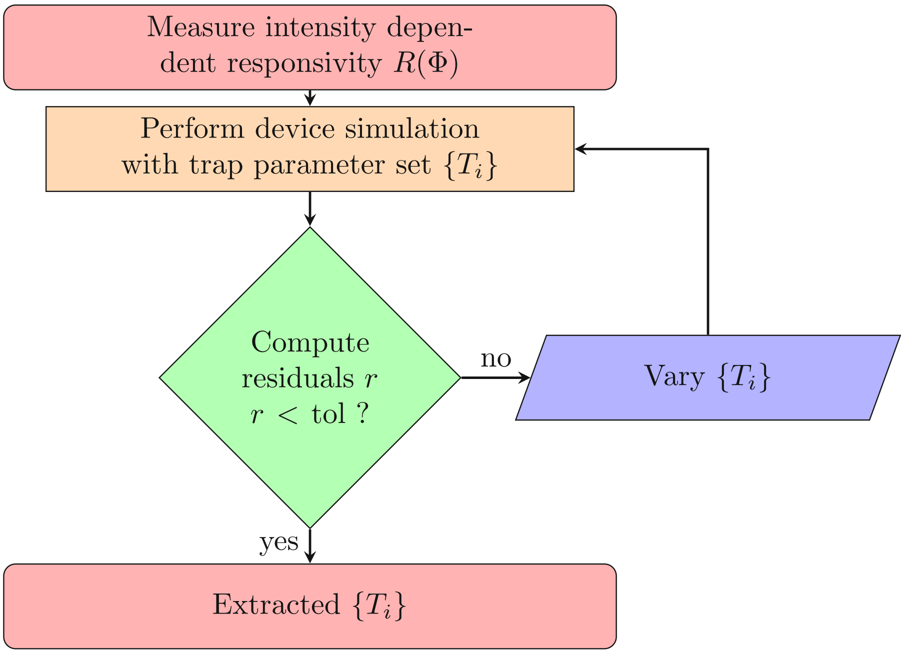

Figure 4.11. Extraction of defect parameters via minimizing simulation residuals to intensity dependent resonsivity measurements.

Chapter 5

Measurements and Simulations

In this chapter measurement and simulation results in the realm of defects within photodetectors are presented. To support the observed experimental results as well as to discuss them in further detail, measurements results are compared to TCAD simulations in the studies presented.

First the methods as introduced in Chapter 4 are utilized to extract and infer lifetime parameters in silicon epitaxial layer pn-junctions, where results have been published in [PSJ2, PSJ3] and some passages have been quoted verbatim from these sources in Section 5.1. As discussed in the previous chapters, typically the dominant lifetime-determining mechanism in silicon photodiodes is trap-related SRH recombination. Hence, a lifetime measurement allows for an estimation of trap parameters. However, when dealing with lifetime on structures with limited thicknesses, such as the epitaxial layer structures investigated in this work, special care has to be taken on the boundaries of the domain under investigation, i.e. on the surfaces/interfaces of this epitaxial layer. The results indicate a strong influence of the epitaxial layer to below-laying substrate transition and therefore the correct interpretation of measured lifetime data on such structures is not trivial, as discussed in this chapter.

Secondly defect characterization studies on deep-trench (DT) terminated epitaxial layer pn-junctions are presented, where results have been published in [PSJ4, PSJ1, PSC1, PSC2] and are partially quoted verbatim in Section 5.2. In these studies it is shown, by means of experiments as well as TCAD simulations, that injection-dependent minority carrier recombination at the DT sidewalls may lead to non-linear responsivities of the corresponding DUT. Since fixed oxide charges as well as the charge associated to trapped carriers at the DT sidewalls to silicon interfaces lead to a bending of the corresponding bands with respect to the Fermi level, it is discussed and shown which conditions favor recombination and lead to bad device performance, and inversely, which conditions lead to optimized device performance. Finally, it is discussed and shown by means of simulations as well as semi-analytical modeling, how a vertical MOSCAP structure may be utilized to mitigate the problem of DT sidewall recombination and therefore achieve improved device performance.

5.1 Lifetime Study of Silicon Epitaxial PN-Junctions

A well-defined and high minority carrier lifetime is a key enabler for high-performance optoelectronic detectors. To verify the targeted carrier lifetime various experimental methods, such as the ones presented in Chapter 4 (open circuit voltage decay (OCVD), reverse recovery (RR) and cIVCV) have been proposed in the literature. However, the extracted lifetimes can differ between the techniques, primarily due to geometric effects such as the epitaxial layer thickness. To evaluate the quality of these methods dedicated test structures, i.e., pn-junctions embedded in 20 µm epitaxial pp+ silicon wafers, are characterized and the results are presented in this section. The collected measurement results on such test structures are compared to TCAD simulations. To investigate the influence of the electric field (associated with the lowly-doped epitaxial layer to the highly doped substrate transition) on the extracted carrier lifetimes, simulations with and without substrate are compared. A strong influence of this low-high transition on the extracted parameters is observed. This effect can be modeled with an effective surface recombination velocity associated to the low-high transition region as is shown below.

5.1.1 Sample Description

The test structures used in this work have been fabricated within a 350 nm CMOS process. As a start material, 14 Ω cm epitaxial p/p^+ silicon wafers are used, and n^+ implants are made to form the pn-junction of the optical diodes. The nominal resistivity of the substrate material is 15 mΩ cm. The epitaxial layer is contacted with p^+ implants adjacent to the n^+ region. The depth of the p^+ and n^+ regions is approximately 200 nm. In Figure 5.1 the cross section of the devices is given and the corresponding parameters are listed in Table 5.1. The width W stated in Table 5.1 is the extension of the pn-junction in the direction perpendicular to the cross section in Figure 5.1.

Table 5.1. Device geometry and doping

symbol	description	value
W	device width	1720 µm
t_{sub}	substrate thickness	725 µm
t_{EPI}	epitaxial layer thickness	20 µm
L_{np}	lateral n+ to p+ distance	0.6 µm
L_{n}	n+ length	1260 µm
$N_{\text{A,EPI}}$	EPI layer boron concentration	$7 \times 10^{14}\,\text{cm}^{-3}$
$N_{\text{A,sub}}$	substrate boron concentration	$4 \times 10^{18}\,\text{cm}^{-3}$
$N_{\text{A,p+}}$	p+ boron concentration	$\approx 10^{19}\,\text{cm}^{-3}$
$N_{\text{D,n+}}$	n+ phosphorous concentration	$\approx 10^{19}\,\text{cm}^{-3}$

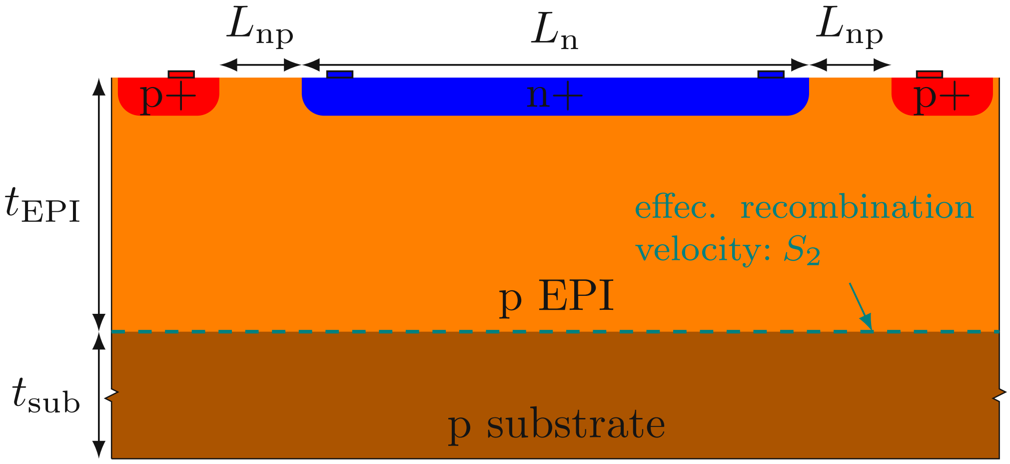

Figure 5.1. Schematic of the device cross section. The values of the parameters are summarized in Table 5.1. p^+ and n^+ regions are contacted and the top surface is passivated with an SiO_2 layer. The dashed horizontal lines marks the interface between the epitaxial layer and the substrate where interface recombination is modeled with the effective surface recombination velocities S_2. The small rectangles on top of the structure indicate the contact placement (red - anode, blue - cathode). The widths of the contacts as well as the lateral distance of the contacts to the edge of the un-implanted regions are 400 nm. Originally published in [PSJ2].

5.1.2 Computer Simulations: Setup and Models

To ensure an accurate interpretation of the measurement results, computer simulations based on the drift-diffusion model have been performed using the Sentaurus Device simulator sofware provided by Synopsis. The simulated cross section is shown in Fig. 5.1 and the placement of contacts is as described in the caption of Fig. 5.1. The employed simulation models and parameters are summarized in Table 5.2. Meshing towards the front surface is done as described in [209]. Front surface recombination (used parameters see Tab. 5.2) is considered using the SRH interface recombination model. However, a significant influence of this recombination mechanism on the extracted lifetimes was not observed. This result is not surprising as most of the front surface is covered by the n+ and p+ contact implants, and therefore the un-passivated front surface recombination area is very small (see Fig. 5.1 and compare L_{np} versus L_{n} according to Table I) in relation to the back surface. It should be noted that for the simulations the energetic trap position of the trap-mediated SRH bulk recombination in the epitaxial layer (see Equation (3.18), (3.14) and (3.17)) is fixed to $E_{\mathrm{t}} - E_{\mathrm{i}} = 0.15\,\mathrm{eV}$, as experimentally extracted on the test sample by the cIVCV method shown below. The lifetimes τ_{EPI} for the epitaxial layer are systematically varied from 1 µs to 500 µs to investigate their impact on the extraction methods. Furthermore, to investigate the influence of the back surface and the associated back surface recombination velocity S_2, the simulations are repeated for a structure without highly doped substrate, that is the lowly doped epitaxial layer covers the whole sample thickness of 745 µm.

Table 5.2. Simulation models and parameters

name	model	parameters / values
Carrier statistics	Fermi-Dirac	
SRH (EPI)	Eq. (3.18)	$\tau_{n0} = \tau_{p0} = \tau_{\mathrm{EPI}}$, $E_\mathrm{t} - E_\mathrm{i} = 0.15\,\mathrm{eV}$
SRH (substrate)	Eq. (3.18)	$\tau_{n0} = 9\,\mu\mathrm{s}$, $\tau_{p0} = 5\,\mu\mathrm{s}$, $E_\mathrm{t} - E_\mathrm{i} = 0$
Auger rec.	after [160]	$C_n = 2.8 \times 10^{-31}\,\mathrm{cm}^6/\mathrm{s}$ $C_p = 9.9 \times 10^{-32}\,\mathrm{cm}^6/\mathrm{s}$
Direct rec.	after [166]	$\mathrm{B} = 4.73 \times 10^{-15}\,\mathrm{cm}^3\,\mathrm{s}^{-1}$
Band gap narrow.	after [210]	as stated in [210]
Mobility	after [211]	as stated in [211]
Front surf. rec.	after [212, 213]	$S_{n0} = S_{p0} = 1000\,\mathrm{cm/s}$ $Q_\mathrm{f} = 6 \times 10^{10}\,\mathrm{cm}^{-2}$, $E_\mathrm{t} - E_\mathrm{i} = 0$
Boundary conditions		ideal Neumann boundary

5.1.3 Steady-State Simulations and Measurements

The *I*-*V* as well as *C*-*V* measurement and simulation data is shown in Fig. 5.2. As can be seen, the simulated, as well as measured *C*-*V* curves do not vary a lot. However, a significant dependence of the *I*-*V* characteristics on the epitaxial lifetime can be observed. An increased value of absolute current for lower lifetimes can be explained, considering that lower lifetimes (and hence increased trap densities) are associated with a higher generation current component in the reverse bias and a higher recombination component in the forward bias regime. Characteristic plots for the reverse method (RM) and forward method (FM) are shown in Fig. 5.3. First, considering the RM, indeed a linear relationship between the depletion width W_eff and the reverse current density j can be observed. The corresponding extracted values for the generation lifetime τ_g as well as the diffusion saturation current density j_d0 are presented in Tab. 5.3. The RM is a

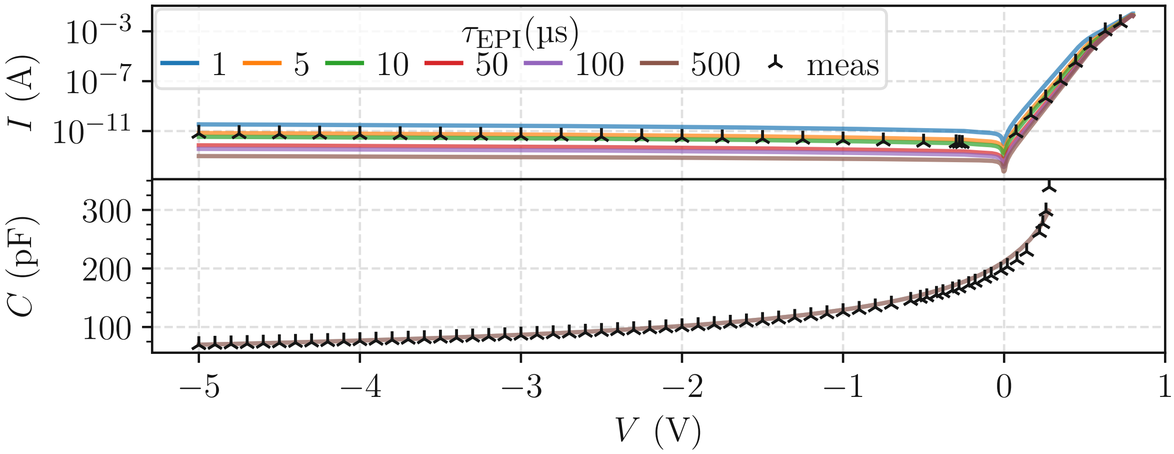

Figure 5.2. *I*-*V* and *C*-*V* measurements (symbols) and 2D TCAD simulation results (lines). Originally published in [PSJ2].

reliable approach for the extraction of generation lifetimes, where excellent accuracy is achieved without any correction. However, the extraction of the diffusion saturation current density j_{d0} with this method yields unreliable results even after a correction by Equation 4.24. Just for the high lifetime case it seems that with this correction j_{d0} might be estimated accurately. In our work we use the TDM to extract j_{d0}, which gave better results. It should be noted that there are various publications on the extraction of TDM parameters in the photovoltaic community [214, 215, 216, 217], however, the extracted parameters may differ significantly between the different formulations of the model as well as the extraction routines [218], yielding results that might be useful for the purpose of modeling pn-junction currents but suffer from being physically unsound. Typically, the accuracy of the models is measured and compared in terms of residuals. In this work, however, the extracted values of j_{d0} are validated by a comparison to the values extracted from TCAD simulations, where good agreement is achieved, see Tab. 5.3.

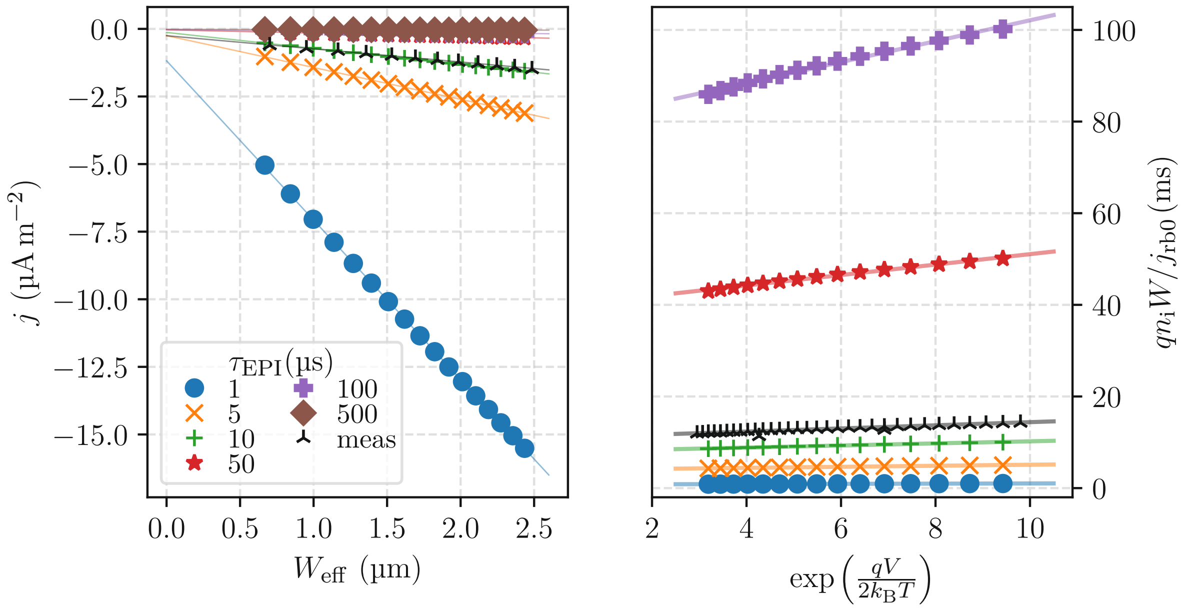

Figure 5.3. RM **(left)** and FM **(right)** method employed on the cIVCV measurement and simulation data. **(left)** The reverse current density j is plotted against the effective depletion width W_{eff} given by Equation 4.24. The markers show every 5th simulation and measurement point and straight lines are the linear fits according to Equation (4.23). **(right)** Plot of $qn_{\mathrm{i}}W/j_{\mathrm{rb0}}$ versus $\exp(qV/(2k_{\mathrm{B}}T))$ and linear fit according to Equation (4.29) without correction, i.e. $f_{\mathrm{U}} = 1$. Extracted parameters are shown in Tab. 5.3. Originally published in [PSJ2].

Comparing the results for the corrected and uncorrected FM in Tab. 5.3 it becomes evident that a correction according to the proposed scheme or simulation results should be performed to avoid erroneous results. It should be noted that, RM and FM measurements can be performed in a single sweep. A combination of these methods is beneficial because it allows comparing and verifying the extracted generation lifetimes τ_{g}. Unlike the effective lifetime, which can be extracted by the transient methods presented in the next section, the epitaxial layer lifetime extracted by the FM is not affected by the

Table 5.3. cIVCV lifetime extraction results[†]

	simulation				extracted											
					$\mathrm{RM}^{\mathrm{corr}}$		$\mathrm{RM}^{\mathrm{uncorr}}$		TDM	$\mathrm{FM}^{\mathrm{corr}}$			$\mathrm{FM}^{\mathrm{uncorr}}$		
	τ_0	τ_g	E_T	$j_{d0}{}^a$	τ_g	j_{d0}	τ_g	j_{d0}	j_{d0}	τ_0	τ_g	E_T	τ_0	τ_g	E_T
●	1	0.31	0.15	53	0.29	120	0.29	-310	60	1	0.27	0.15	13	0.82	0.11
×	5	1.5	0.15	12	1.5	26	1.5	-59	13	5	1.4	0.15	62	4.1	0.11
+	10	3.1	0.15	6.7	2.9	14	2.9	-28	7.2	10	2.7	0.15	122	8.1	0.11
★	50	15	0.15	2.4	15	4.9	15	-3.6	2.5	47	14	0.15	601	40	0.11
✚	100	31	0.15	1.9	29	3.7	29	-0.54	1.9	93	27	0.15	1187	80	0.11
◆	500	150	0.15	1.5	140	2.8	140	1.9	1.5	434	130	0.15	5645	390	0.11
⅄	measurement				3.5	25	3.5	-9.9	4.7	13	3.5	0.15	171	11	0.11

[†] Results originally published in [PSJ2]. τ_0 is given in units of µs, τ_g is given in units of ms, E_T is given in units of eV with respect to the intrinsic energy E_i and j_{d0} is given in units of $\mathrm{pA\,cm^{-2}}$.

[a] j_{d0} (simulation) is extracted out of the simulation data by a fit of $j_d = j - j_U$ to the model equation $j_d = j_{d0}(\exp(eV/(k_B T)) - 1)$ in the voltage range −5 V to 0.3 V.

epitaxial layer thickness t_{EPI}. To further investigate the (in-)dependency of the extracted epitaxial layer lifetimes on t_{EPI}, simulations without a substrate layer have been performed. In that case, the epitaxial layer width is enlarged to cover the full device and no epitaxial layer to substrate transition region is present. The results of these simulations are shown together with the lifetime results of the RR and OCVD methods in Tab. 5.4. As can be seen, the lifetimes extracted by the cIVCV method are similar for both structures (i.e. with and without substrate, as described above), which is expected since with the cIVCV method τ_{eff} is extracted, which is not affected by the interface.

5.1.4 Transient Simulations and Measurements

With the transient methods, OCVD and RR, effective lifetimes can be extracted. Hence, the modeling of effective lifetimes is first discussed, considering the test structure, as described in Section 5.1.1. Afterwards the measurement and simulation results are presented and discussed.

Modeling of Effective Carrier Lifetimes

In Section 4.1.1 the modeling of effective carrier lifetimes (as extracted by the OCVD and RR methods) in terms of surface recombination velocities was discussed (see Equations (4.13) and (4.34)). For the test structure investigated in this work, formed by heavily counterdoping the front surface region of the epitaxial layer, and for negligible recombination effects in the heavily doped region, S_1 becomes negligibly small compared to S_2

and Equation (4.34) reduces to [219, 220]

$$\cot(\beta t_{\mathrm{EPI}}) = \frac{\beta D}{S_2}. \tag{5.1}$$

For a pn-junction S_1 is determined by recombination effects in the heavily doped side (in the test structure in this work, this is the n+ region), and can be computed according to [221, 222]

$$S_1 = \frac{J_{\mathrm{E0}}}{q n_{\mathrm{i}}^2} N_{\mathrm{B}}, \tag{5.2}$$

where J_{E0} is the emitter saturation current density and N_{B} the base (in this work anode) doping. For the TCAD simulations, S_1 was extracted according to Equation (5.2) (extraction procedure according to Reference [223]) and it was found that $S_1 < 1\,\mathrm{cm\,s^{-1}}$. In that case, S_1 is much smaller than the typical values reported for S_2 (recombination velocity at the epitaxial layer to below laying substrate interface), which are in the order of $10\,\mathrm{cm\,s^{-1}}$ to $100\,\mathrm{cm\,s^{-1}}$ [168, 224, 225, 226]. In Fig. 5.4 the two modeling approaches are compared, i.e., considering the back-surface only ($S_2 = 0$) versus considering $S_1 = 1\,\mathrm{cm\,s^{-1}}$, both as a function of the back-surface associated recombination velocity S_2. In that figure, the region with typical values for S_2 is shaded gray. As can be seen, the modeling with S_2 only appears justified without appreciable error, because of the relatively small value of S_1.

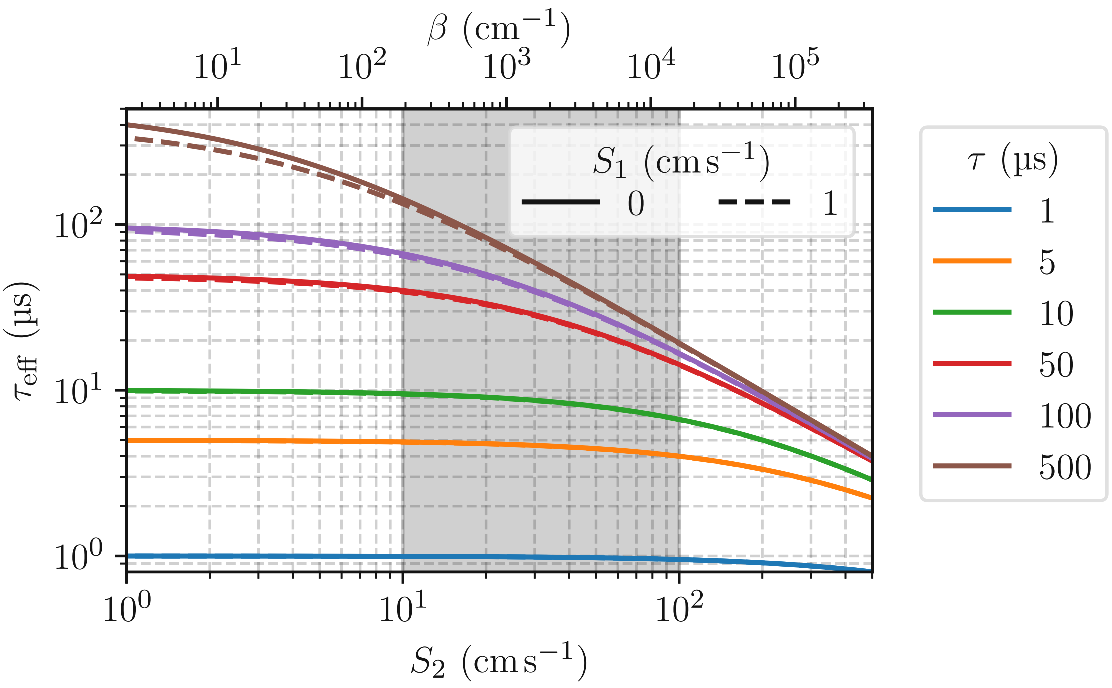

Figure 5.4. Influence of front surface recombination velocity S_1 on the effective lifetimes τ_{eff} as function of back surface recombination velocity S_2 for different lifetimes τ. The shaded region marks typical values for S_2.

Transient Methods: Measurement and Simulation Results

The test structure, as described in Section 5.1.1, is investigated in terms of transient measurements (OCVD, RR) where results are compared to TCAD simulations employing parameters and models according to Tab. 5.2. Plots for measurement results of the OCVD method can be seen in Fig. 5.5, where the ideality factor n is extracted from the I-V measurements, which are presented in Section 5.1.3. For the extraction of the lifetime, F is plotted as a function of time on a log-log scale, where plateaus become visible allowing for an extraction of the effective lifetime of τ_{eff}. For the measurement data, this procedure yields an extracted lifetime τ_{eff} of about 10 µs.
RR measurements have been performed, with the circuitry as shown in Fig. 4.7, where the series resistor R was set to 10 kΩ. A forward bias V_{f} is applied for 10 ms resulting in a current $I_{\mathrm{f}} \approx 0.6$ mA. Afterwards the diode is switched to different reverse biases leading to initial reverse currents I_{r} of approximately 0.15 mA to 0.45 mA. As can be seen in Fig. 5.6 (right plot), the varied values in the reverse bias lead to different value pairs of I_{r} and t_{s} (fixed I_{f}). Plots of the linear fit according to the RR extraction equation, i.e. Equation (4.45), can be seen in Fig. 5.6 (left plot). The extracted lifetime of the measured data is $\tau_{\mathrm{eff}} \approx 9$ µs.

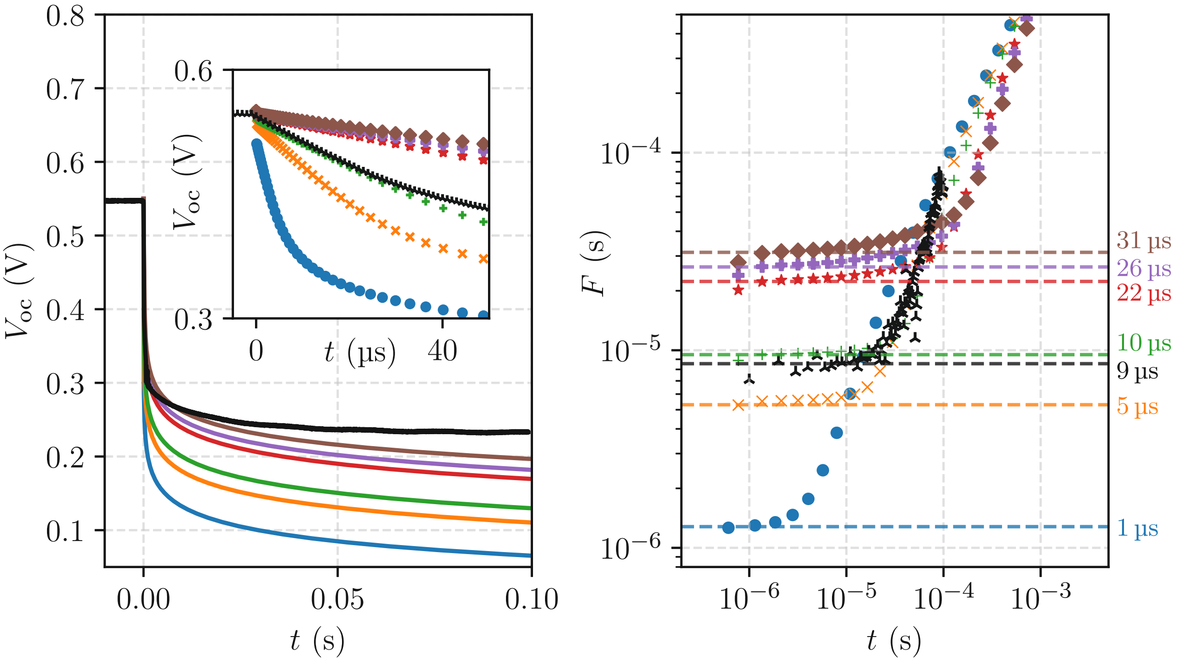

Figure 5.5. OCVD measurement and simulation result. **(left)** Open circuit voltage V_{oc} versus time t for measurements and TCAD simulations. The inset shows a zoom into the first 50 µs after the switch has been opened. The significant difference between measurements and simulations of V_{oc} at times larger than about 1 ms can be attributed to parasitic effects [197, 227, 228]. **(right)** Extracted first order lifetime F versus time t. The dashed horizontal lines indicate the extracted effective lifetime τ_{eff}. Originally published in [PSJ2].

The simulation results, as summarized in Table 5.4, indicate that for $\tau_{\mathrm{EPI}} > 10$ µs the extracted OCVD and RR effective lifetimes become much lower than τ_{EPI} and thus an

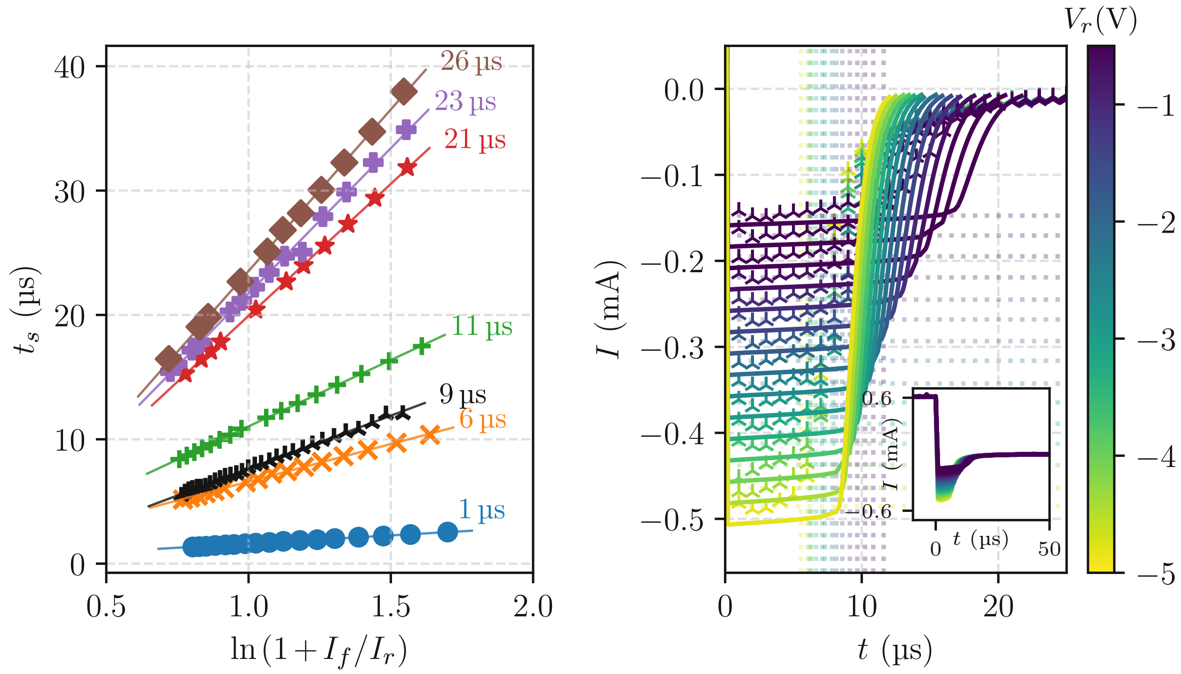

Figure 5.6. RR measurement and simulation result. **(left)** Open circuit voltage V_{oc} versus time t for measurements and TCAD simulations. The inset shows a zoom into the first 50 µs after the switch has been opened. The significant difference between measurements and simulations of V_{oc} at times larger than about 1 ms can be attributed to parasitic effects [197, 227, 228]. **(right)** Extracted first order lifetime F versus time t. The dashed horizontal lines indicate the extracted effective lifetime τ_{eff}. Originally published in [PSJ2].

extraction of τ_{EPI} via these methods becomes impractical. The reason for the considerable discrepancy at high τ_{EPI} is the fact that due to the long diffusion length at high lifetimes the influence of the epitaxial layer to substrate interface becomes more dominant. Comparing the epitaxial diffusion lengths L_{EPI} associated to the varied epitaxial layer lifetimes τ_{EPI}, shown in Tab. 5.4, to the thickness of the epitaxial layer t_{EPI}, that is $t_{\text{EPI}} = 20$ µm, one can see that lifetime deviations between τ_{EPI} and τ_{eff} start occurring once L_{EPI} is comparable or larger than t_{EPI}. Equivalently, referring to Equation (4.13), in that case $D\beta^2$ becomes smaller than $1/\tau_{\text{EPI}}$ and starts dominating the effective lifetime τ_{eff}. This explanation is supported by our simulation results for the structure without the substrate layer, where this discrepancy is less pronounced and measurement results instead give a small overestimation for τ_{EPI}. The simulation results without substrate provide a good understanding of the influence of the epitaxial layer to substrate interface. They indicate that the methods presented are suitable candidates not only to extract effective carrier lifetimes on epitaxial layer structures, but also to extract the minority carrier lifetimes in the case of non-epitaxial test structures, which can be used to assess the material quality on, e.g., pn-junctions embedded in prime wafers. A least square fit is performed for the extracted τ_{eff} versus τ_{EPI} dependence of the OCVD and RR simulations according to Equation (4.13) with the epitaxial layer to substrate interface recombination velocity S_2 being the fitting parameter (further utilizing Equation (5.1)).

Table 5.4. Lifetime extraction results[†]

	parameter		extracted τ_{eff}		fitted τ_{EPI}[a]		τ_{EPI}
	τ_{EPI}	L_{EPI}[b]	OCVD	RR	OCVD	RR	cIVCV
⅄	measurement		9	9	-	-	13
	simulations with substrate						
●	1	6	1	1	1	1	1
×	5	13	5	6	7	8	5
+	10	19	10	11	13	17	10
★	50	42	22	21	67	77	47
✚	100	59	26	23	126	120	93
◆	500	132	31	26	498	498	434
	simulations without substrate						
●	1	6	1	1	-	-	1
×	5	13	5	4	-	-	4
+	10	19	10	8	-	-	8
★	50	42	52	48	-	-	48
✚	100	59	100	120	-	-	120
◆	500	132	506	657	-	-	657

[†] Results originally published in [PSJ2]. All times are given in units of µs, L_{EPI} is given in units of µm. Green colored values are within a 50 % interval $[0.5 \times \tau_{\mathrm{EPI}}, 1.5 \times \tau_{\mathrm{EPI}}]$, red colored values are outside this interval.

[a] These columns show the results for the extracted epitaxial lifetimes after correcting by a fit of τ_{eff} and τ_{EPI} according to Equation (4.13) and (5.1). Fitting results are: $S_2(\mathrm{OCVD}) = 60\,\mathrm{cm/s}$ and $S_2(\mathrm{RR}) = 72\,\mathrm{cm/s}$.

[b] The diffusion length L_{EPI} is computed as described in Reference [229].

The extracted values of $S_2(\mathrm{OCVD}) = 60\,\mathrm{cm/s}$ and $S_2(\mathrm{RR}) = 72\,\mathrm{cm/s}$ are reasonable results for the recombination velocity of this interface, as in literature primarily values of 10 cm/s to 100 cm/s for low/high junctions are reported [168, 224, 225, 226]. A calculation back from τ_{eff} to τ_{EPI} as has been performed for the simulation results will be practically difficult, as the influence of S_2 is quite significant (see Fig. 5.4), and a precise determination of S_2 difficult. Therefore OCVD and RR are excellent methods for the extraction of τ_{eff}, however a determination of τ_{EPI} with these methods remains challenging for thin EPI layers.

To further investigate the influence of the epitaxial layer thickness and the modeling according to Equation (4.13) and (5.1) an additional set of simulations is performed, where the epitaxial layer lifetime τ_{EPI} is kept at 50 µs and the epitaxial layer thickness t_{EPI} is varied between 3 µm to 100 µm. As can be seen in Fig. 5.7, τ_{eff} varies strongly with t_{EPI} and approaches τ_{EPI} for $t_{\mathrm{EPI}} \approx 100\,\mu\mathrm{m}$. The dependency of τ_{eff} on t_{EPI} can be accurately modeled with Equation (4.13) and (5.1), where a value of $s_{r2} = 42\,\mathrm{cm\,s^{-1}}$ is extracted for the surface recombination velocity.

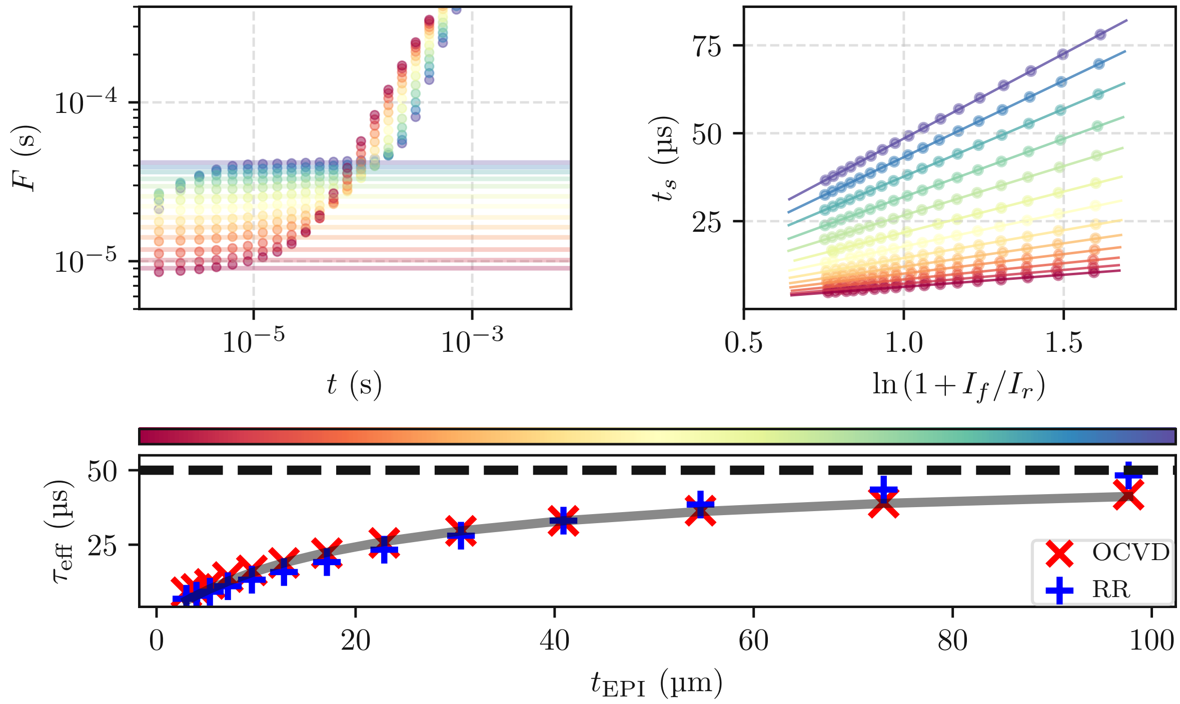

Figure 5.7. RR and OCVD effective lifetimes for a varied epitaxial layer thickness t_{EPI} and an epitaxial layer lifetime $\tau_{\mathrm{EPI}} = 50\,\mathrm{\mu s}$. **(Upper left)** OCVD first order lifetime versus time for different t_{EPI}. **(Upper right)** RR plots for different t_{EPI}. **(Lower)**: Extracted τ_{eff} for the OCVD and RR according to the upper plots. The dashed horizontal line marks the epitaxial layer lifetime and the gray line represents a fit according to Equation (4.13) and (5.1), where $S_2 = 42\,\mathrm{cm\,s^{-1}}$ was extracted. The colorbar maps the values from t_{EPI} of the lower plot x-axis to the differently colored lines in the upper plots.

5.1.5 DLTS Measurements

To further verify the lifetime results, DLTS measurements have been performed on the same test sample, i.e. the structure as shown in Fig. 5.1. A cryogenic probe station (Lakeshore CRX-4K) was used and a temperature scan from 100 K to 350 K has been performed, where 100 ms capacitance transients at a reverse bias of 2.4 V have been recorded after stressing for 100 ms at a bias point leading to a forward current of approximately 100 nA. The corresponding capacitance transients are shown in Fig. 5.8. A conventional DLTS analysis is performed on the measured data, with an rectangular weighting function of various lengths, with the results being presented in Fig. 5.9. The results indicate a trap state located 0.39 eV from the valence band and thus roughly 0.17 eV away from midgap, supporting the extracted $|E_{\mathrm{T}} - E_{\mathrm{i}}| = 0.15\,\mathrm{eV}$ of the cIVCV measurements and simulations. Furthermore, a calculation of the low-injection minority carrier lifetime, Equation (3.19a), assuming same cross section for electron and holes, i.e. that σ_n corresponds to the extracted σ_p results in a lifetime estimator of

$$\tau_{\mathrm{n0,DLTS}} = \frac{1}{N_{\mathrm{T}}\sigma_n v_{\mathrm{th,n}}} \approx \frac{1}{1.4\times10^{13}\,\mathrm{cm}^{-3}3\times10^{-16}\,\mathrm{cm}^{2}2\times10^{7}\,\mathrm{cm\,s}^{-1}} = 12\,\mathrm{\mu s}, \tag{5.3}$$

which is perfectly in line with the extracted value of 10 µs from the steady-state and transient methods above. It should be mentioned, that despite performing DLTS measurements at various stress levels and bias points, in all the measurements only the above discussed majority carrier trapping was observed.

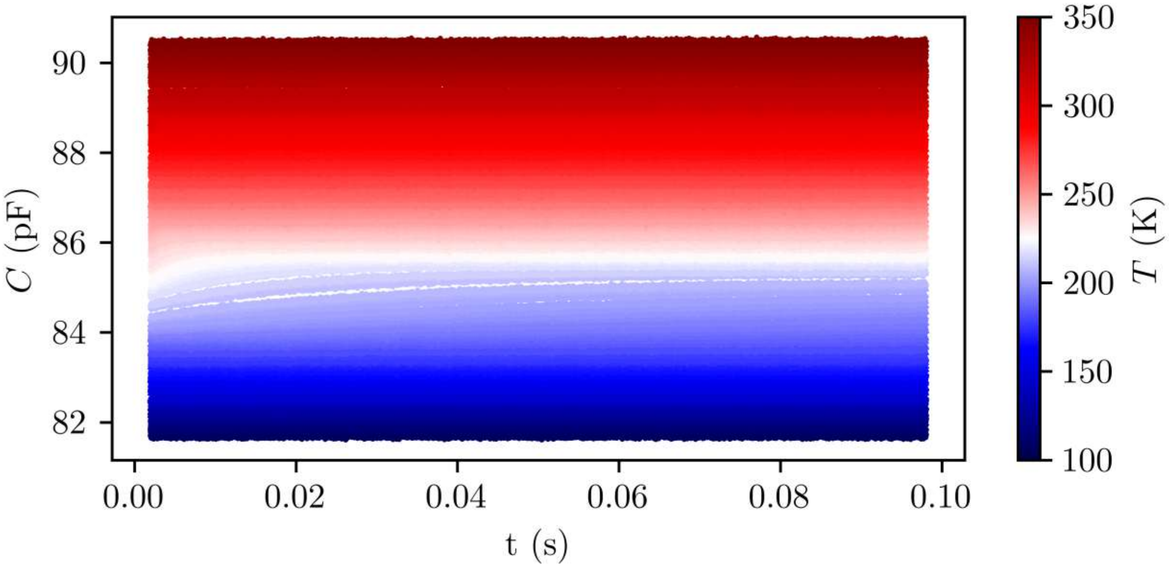

Figure 5.8. DLTS capacitance transients measured on the lifetime test samples at various temperatures. Majority carrier trapping is visible on the 100 ms timescale at temperatures of about 220 K.

5.1.6 Discussion

The characterization of carrier lifetimes is challenging and various methods to measure them have been proposed. To evaluate the suitability of the proposed methods, two transient methods, namely OCVD and RR, and the steady-state cIVCV method have been systematically studied employing dedicated test structures. The results demonstrate that the effect of the epitaxial layer to substrate interface becomes more pronounced the higher the minority carrier diffusion length L_{EPI}, resulting in an effective carrier lifetime τ_{eff} that is much lower than the epitaxial layer lifetime τ_{EPI}. OCVD and RR are well-working methods to measure this effective carrier lifetime, which is an essential parameter for opto-electronic devices and other minority carrier based applications. For larger lifetimes and thus larger diffusion lengths, the results for the transient measurements (OCVD and RR) differ significantly from the cIVCV results. As was pointed out, OCVD and RR are methods to measure effective lifetimes, whilst the main signal for the cIVCV method originates from the pn-junction depletion zone and is, therefore, less affected by the epitaxial layer to substrate transition. Therefore the forward cIVCV method is a candidate for the extraction of the epitaxial layer lifetime. This parameter is important for assessing the purity of devices or semiconductor processes. For the cIVCV method, the proposed correction scheme should be applied to avoid

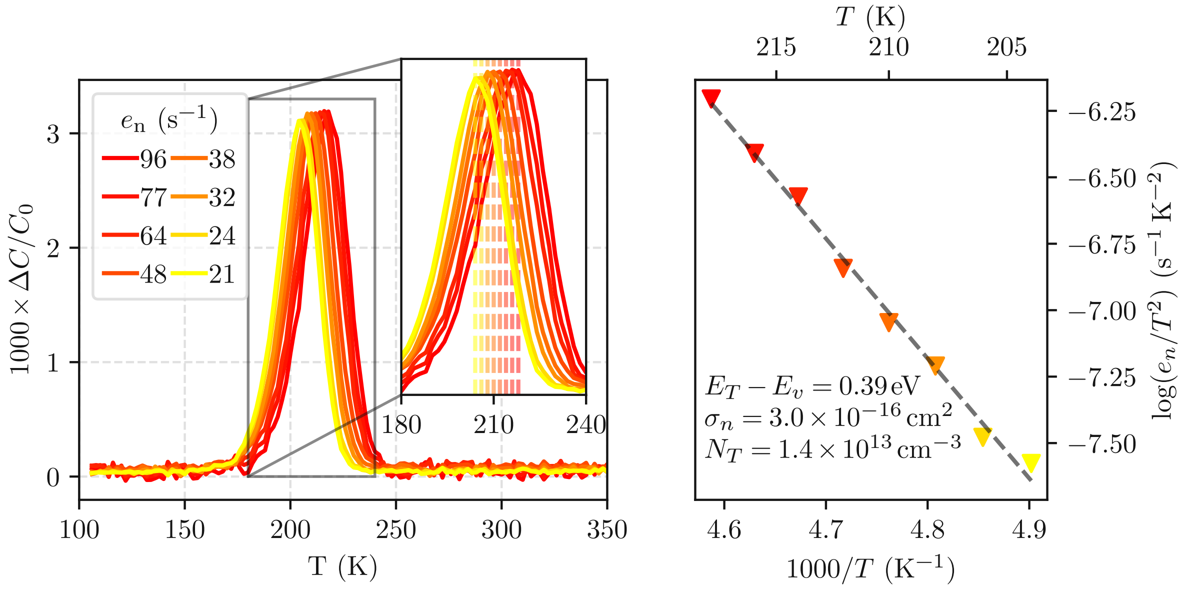

Figure 5.9. DLTS plot and Arrhenious plot of the capacitance transients shown in Fig. 5.8. **(left)** DLTS plot for different emission rates e_n showing a shift of the corresponding maximum. The inset axis shows a zoom in the region of interest, where the dashed vertical lines mark the extracted peak temperatures. **(right)** Arrhenius plot of the extracted data pairs $e_{\mathrm{n,i}}$, $T_{\mathrm{max,i}}$ confirming a linear relation. The extracted parameters (corresponding to the linear fit showing by the dashed straight line) are written as inset in the Arrhenius plot.

erroneous results because otherwise the recombination current density component is overestimated, leading to erroneous results. Finally, DLTS measurements have been performed to accomplish and support the lifetime results. A single trap level could be detected confirming the extracted value of the trap energy by the cIVCV method. Additionally, a lifetime estimator based on the extracted trap parameters by means of DLTS yields good agreement to the lifetime extracted by the cIVCV, RR and OCVD methods.

5.2 Deep Trench Processing Induced Trap States in Silicon Photodiodes

The isolation of photodetectors by DTs filled with insulating material is widely used to minimize cross-talk between devices fabricated on the same chip as well as to isolate opto-electronic blocks from other monolithically integrated electronic parts of the chip. With the constant reduction of the image sensor's pixel pitch to meet the requirements for high-resolution images in consumer applications, deep-trench isolation (DTI) turns out to be the method of choice to meet the stringent criteria for pixel-to-pixel crosstalk in small-pixel ($\approx 1\,\mu$m and below) CMOS image sensors [230, 231, 232, 233]. One main advantage of the DTI compared to other isolation techniques such as shallow-trench isolation (STI), n-well guard (NWG), or p-well guard (PWG) rings, is the ability to block diffusing minority carriers at depths far (several µm) away from the surface, and thus efficiently prohibiting their incidence into neighboring structures (termed electrical cross-talk). Minority carriers reaching the silicon-oxide interface at the DTI are partially reflected and partially recombine at this interface. In photodetectors carriers that are reflected at the DTI interface might finally reach the collecting electrode and contribute to the photocurrent thus increasing the spectral response (SR) of the detector [234]. This means, for photodetectors the DTI imposes two important improvements: reduced cross talk and improved spectral response.

At the same time, however, the interface of the DT introduces trap states that can act as recombination centers and affect the performance of silicon photodetectors. It was demonstrated in Section 3.3, that SRH recombination is injection-dependent, and hence in this work the Si to SiO_2 interface of DT-terminated photodiodes is investigated by means of injection-dependent responsivity (IDR) measurements and simulations.

To begin with, a semi-analytical modeling approach of interface recombination is utilized to compute the surface recombination rates, where the model includes the typical band-bending towards the interface because of fixed oxide charges and charges associated to trapped charge carriers. These results were published in [PSC1] and are compared to TCAD simulations. Additionally, a comparison with respect to crosstalk, between DT- and NWG- terminated structures has been performed in [PSC1] and is presented in this work.

Secondly, IDR measurements are presented on DT terminated photodiodes with different processing conditions. Essentially, photodiode test structures, that were processed with different DT sidewall implants, are compared. The actual purpose of these implants is to passivate the interface and improve the device performance. However, as is shown, the peak doping concentration is a critical parameter, where high values ($> 10^{18}\,\mathrm{cm}^{-3}$) are required for successful passivation. For lower peak doping concentrations even a degradation in terms of device performance might occur. TCAD simulations are utilized to extract and infer defect parameters, as explained in Section 4.2.2. This study was presented in the publication [PSJ4].

Finally, DLTS was utilized to extract defect parameters on dedicated DTs test structures.

Trapping of minority and majority carriers was observed allowing for the extraction of multiple trap parameters. The main results and extracted parameters were then utilized to model the interface traps in TCAD simulation and a comparison to the measurement data was performed. Results were published in reference [PSJ1].

5.2.1 Modeling and Simulating the Injection-dependent Carrier Recombination on Deep Trench Sidewalls

As mentioned above, injection-dependent interface recombination on DT sidewalls might cause undesired effects and performance degradation in DT terminated photodiodes. The purpose of (semi-) analytical modeling the interface recombination in such devices is to get an easy-to-use tool, capable of predicting the corresponding magnitude of recombination. Such an analytical tool is beneficial for gaining further insights into the physics of recombination at the sidewalls and also to investigate the influence of parameters in an easy fashion. In principle the surface recombination rate might be calculated using Equation (3.28), by assuming that the surface carrier concentrations n_s, p_s correspond to the bulk values, i.e. for a p-type semiconductor $p_\mathrm{s} \approx N_\mathrm{A}$ and $n_\mathrm{s} \approx n_\mathrm{i}^2/N_\mathrm{A}$. However, this approach assumes flat band conditions towards the surface and ignores the fact, that due to fixed oxide charges and the charges associated to trapped carriers the bands will bend towards the interface, leading to strongly modified carrier concentrations and thus recombination rates. An analytical model that does include band-bending, based on a one-dimensional charge sheet approximation, was introduced in references [235, 236], and is further utilized in this work to compute the responsivity of photodiodes and essentially the degradation due to the DT sidewall recombination.

Description of Simulation Setup and Test Vehicle

The simulated/modeled test structures are schematically drawn in Fig. 5.10. DT-terminated photodiodes are compared to NWG-terminated ones, and additionally test structures for cross-talk performance with both guard ring concepts are shown in this figure. The DT-to-DT, as well as NWG-to-NWG, pitch is fixed to $W_\mathrm{dev} = 100\,\mu\mathrm{m}$ in this study. The metal aperture t_apt as well as cathode width W_cath (see Fig. 5.10) are parameters that are varied in set of simulation experiments. The depth and doping concentration of the p-doped epitaxial layer are $t_\mathrm{EPI} = 25\,\mu\mathrm{m}$ and $N_\mathrm{A} = 5 \times 10^{15}\,\mathrm{cm}^{-3}$, respectively. The epitaxial layer is grown on a p+ ($17\,\mathrm{m}\Omega\,\mathrm{cm}$) doped substrate. Laterally the structure is either terminated by a $27\,\mu\mathrm{m}$ deep DTI exceeding the EPI layer thickness or by an n-well guard (NWG) with the same width and spacing for direct comparison. The simulation software Minimos NT [237] which is provided within the GTS framework is used to solve the drift-diffusion equations on the defined domain subjected to boundary conditions given by the DTI interface parameters as well as varied optical generation by illumination with a monochromatic light source with a wavelength of $\lambda = 670\,\mathrm{nm}$. The anode and cathode voltage is set to $0\,\mathrm{V}$. In the simulation default

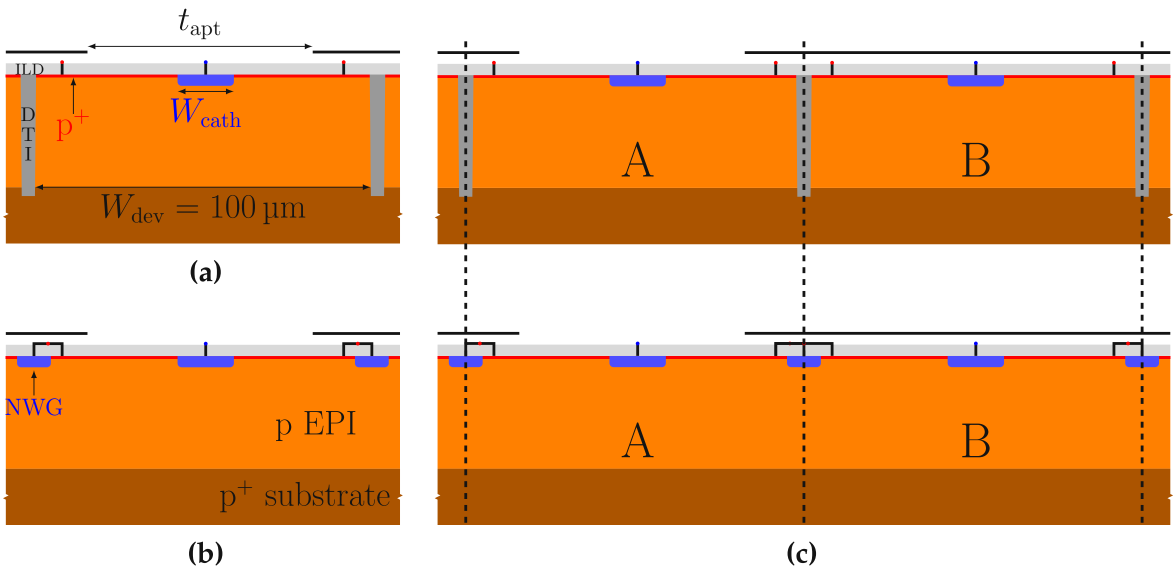

(a)

(b)

(c)

Figure 5.10. Cross sections and parameters of the simulated structures. The devices consist of p-doped epitaxial (EPI) layers grown on a p^+-substrate and pn-junctions are formed by a central n-well cathode. Devices with a DT **(a)** are compared to devices with an NWG **(b)**. The simulations are performed for a fixed device length $W_{\mathrm{dev}} = 100\,\mu\mathrm{m}$, varied optical aperture t_{apt}, and cathode length W_{cath}. **(c)** Schematic of the setup to simulate electrical cross-talk. The metal above the test structure is just open above device A and the current of the illuminated device A is compared to the current of its not illuminated neighbor device B. Originally published in [PSC1].

models for Auger and bulk SRH recombination ($\tau_{n0} = \tau_{p0} = 10\,\mu\mathrm{s}$, $E_{\mathrm{T}} = E_{\mathrm{i}}$) are utilized. Interface recombination at the two lateral DTI to Si interfaces is modeled using SRH theory with midband traps, trap density $N_{\mathrm{it}} = 10^{10}\,\mathrm{cm}^{-2}$, fixed oxide charge density $Q_0 = 10^{11}\,\mathrm{cm}^{-3}$ and electron (hole) cross section of $\sigma_n = 10^{-14}\,\mathrm{cm}^2$, $\sigma_p = 10^{-17}\,\mathrm{cm}^2$ (parameters for trap density, cross sections and fixed oxide charge density are according to reference [235]).

Influence of Geometry and Design Parameters

In Fig. 5.11, left side plot, the responsivities R (versus irradiance) for structures with DTI (with and without interface traps) and with NWG are compared. As can be seen, DTI terminated diodes show higher responsivities R compared to NWG-terminated ones, but suffer from non-linearity because of interface recombination (see simulation without interface traps in Fig. 5.11) for the same guard/DTI to aperture distance. In the following, the optical aperture t_{apt} as well as the cathode length W_{cath} are varied in a simulation design of experiment (DOE) to investigate their impact. According to Fig. 5.11 and Tab. 5.5, decreasing t_{apt} leads to a reduced non-linearity and better performance of the DTI terminated devices at low irradiance. In that case, a more significant fraction of carriers is generated closer to the cathode and thus more likely collected by the same. This is further confirmed by the simulation results from structures with a varied W_{cath}.

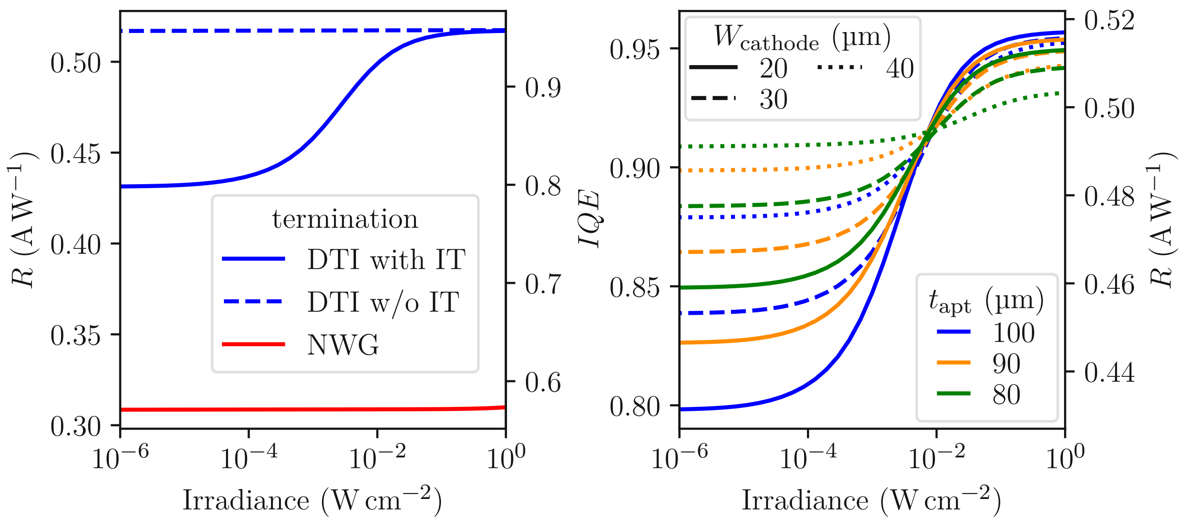

Figure 5.11. Influence of interface traps (IT) at the deep-trench-isolation (DTI) sidewalls on the performance of photodiodes: parameter study and comparison to the NWG. **(left)** Responsivity R and internal quantum efficiency (IQE) versus irradiance for a structure with DTI and NWG termination. The structure with DTI is simulated with and without interface traps. Used geometry parameters are $t_{\mathrm{apt}} = 100\,\mu\mathrm{m}$ and $W_{\mathrm{cath}} = 20\,\mu\mathrm{m}$. DTI terminated devices outperform NWG terminated ones in terms of responsivity but suffer from non-linearity because of IT recombination. **(right)** R and IQE versus irradiance for structures with DTI and varied optical aperture t_{apt} and cathode length W_{cath}. Increasing W_{cath} and reducing t_{apt} are measures to reduce non-linearity effects but at the expense of other important device parameters. Originally published in [PSC1].

Here the collection efficiency of the cathode compared to the DTI/guard increases at higher W_{cath}, which ultimately leads to better device performance. It should be noted, however, that the reduced non-linearity and improved R for these structures are at the cost of increased capacitance and reduced packaging density. Finally, as summarized in Tab. 5.5, DTI terminated devices have lower averaged electrical cross-talk by a factor of approximately 100. This is expected since the DTs impose a physical barrier for charge carriers and are thus very efficient in blocking crosstalk. The NWG on the other hand, collects carriers that might diffuse in the periphery or to the neighboring device via the electric field associated to the junction which is located directly around the NWG and is thus less efficient in blocking carriers that are further below. It should be mentioned that the p-to-p+ transition associated to the epitaxial layer to substrate border also has a built-in electric field that pushes electrons (which are the generated minority carriers) back towards the epitaxial layer and hence is also beneficial for cross-talk and improved diode efficiency.

Influence of Fixed Oxide Charges and Device Proposal

Fixed oxide charges are an important parameter affecting the recombination properties of interfaces. The DTs fixed oxide charge density might strongly depend on the pro-

Table 5.5. Impact of geometry on extracted device parameters†

parameter[a]		result			
t_{apt}	W_{cath}	R_{low} [b]	R_{high} [b]	Δ_{lin} [c]	$\overline{CT}$ [d]
µm	µm	$\mathrm{A\,W^{-1}}$	$\mathrm{A\,W^{-1}}$	%	%
100	20	0.43 / 0.31	0.52 / 0.31	17 / <1	0.02 / 2.15
	30	0.45 / 0.33	0.52 / 0.34	13 / <1	0.02 / 1.82
	40	0.46 / 0.36	0.51 / 0.36	11 / <1	0.01 / 1.51
80	20	0.45 / 0.37	0.52 / 0.37	12 / <1	0.02 / 1.67
	30	0.47 / 0.40	0.51 / 0.40	9 / <1	0.01 / 1.32
	40	0.48 / 0.42	0.51 / 0.43	6 / <1	0.01 / 1.00
60	20	0.48 / 0.42	0.51 / 0.43	8 / <1	0.01 / 0.98
	30	0.49 / 0.45	0.51 / 0.45	5 / <1	0.01 / 0.65
	40	0.49 / 0.47	0.50 / 0.48	2 / <1	0.01 / 0.38

[†] Simulation results for structures with DTI / NWG termination. Originally published in [PSC1].

[a] Parameters as defined in Fig. 5.10.

[b] Responsivities R at two irradiances, $R_{\mathrm{low}} = R(1\,\mathrm{pW\,cm^{-2}})$, $R_{\mathrm{high}} = R(1\,\mathrm{W\,cm^{-2}})$

[c] Non-linearity $\Delta_{\mathrm{lin}} = 1 - R_{\mathrm{low}}/R_{\mathrm{high}}$

[d] Averaged electrical crosstalk $\overline{CT} = \overline{I_{\mathrm{cath,B}}/I_{\mathrm{cath,A}}}$

cessing details, such as the etching/oxidation methods used or thermal treatments [238, 106]. This charge density can considerably alter the interface passivation properties by modifying the band structure towards the interface [213] (see also Fig. 5.12). Thus, in the next step, the fixed oxide charge density Q_0 is varied over several decades (with both charge polarities) to investigate the influence on the responsivity of our structure with DTI termination. The simulation results are shown in Fig. 5.13 (a). As can be seen, a fixed oxide charge density of $|Q_0| > 10^{12}\,\mathrm{cm^{-2}}$ provides good passivation properties for the DTI sidewall interfaces. However, the intrinsic fixed oxide charges for the Si-SiO$_2$ interface are known to be positive with a fixed oxide charge density of about $10^{10}\,\mathrm{cm^{-2}}$ to $10^{11}\,\mathrm{cm^{-2}}$ [238, 239], which implies poor passivation characteristics for the p-doped samples, as can be seen in Fig. 5.13.

While the quality of horizontal silicon to insulator interfaces (e.g. the silicon to interlevel-dielectric interface, or silicon to gate oxide interface in a horizontal MOS transistor) can be improved by modern semiconductor production facilities utilizing advanced insulating materials, intentional placement of fixed interface charges, or passivation implants [240], it is a challenging task to control and optimize the parameters of the vertical silicon to DTI interface. Nonetheless, the DTI offers advantages in terms of internal quantum efficiency and electrical crosstalk compared to other termination techniques, like the NWG, as was shown above. Besides processing improvements, another way to control the interface properties is a structure laterally terminated with a contacted

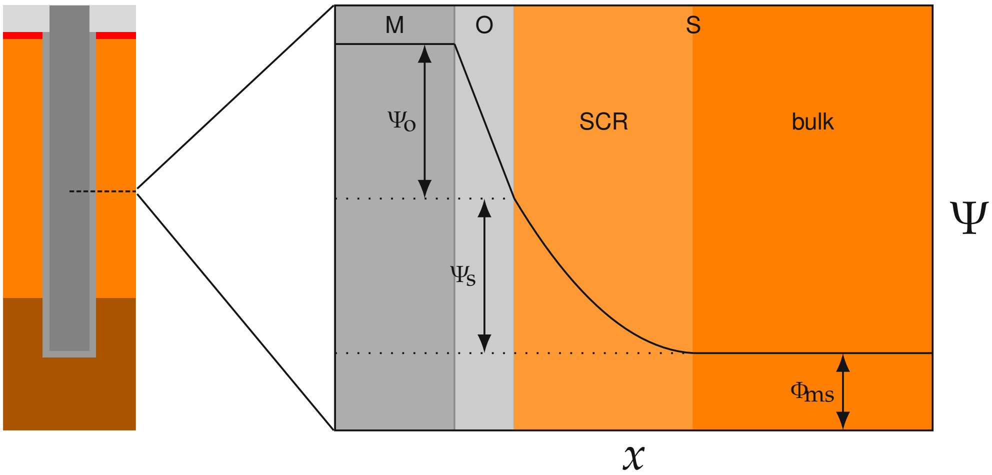

Figure 5.12. Schematics of the deep-trench metal-oxide-semiconductor capacitor (DT-MOSCAP): potential Ψ versus position x. An applied gate bias leads to a potential drop across the oxide Ψ_o as well as a surface potential Ψ_s that affects the carrier concentrations at the interface and therefore impacts the interface recombination. The system is furthermore characterized by the metal-semiconductor workfunction ϕ_{ms}. Originally published in [PSC1].

poly-Si filled DT-capacitor (DTMOSCAP). This structure exhibits all the advantages of a DTI terminated photodetector whilst, at the same time, the interface recombination and thus losses can be minimized by applying a bias at the DTMOSCAP gate. A schematic cross section, as well as a drawing of the potential in the vicinity of the DTMOSCAP, can be seen in Fig. 5.12. For such a device, the surface carrier concentration and therefore the interface recombination properties (see Equation (3.28)) can be controlled by an applied gate bias. Fig. 5.13 (c) shows the responsivity R versus applied gate bias V_G and irradiance E_e for a DTMOSCAP structure with a n-poly gate and 20 nm oxide thickness. In essence, the proposed device combines the advantages of DTI termination without the drawback of enhanced interface recombination and non-linearity, as is shown by means of TCAD simulations. Already at a gate bias of $V_G = 0\,\mathrm{V}$ the device always operates in the highly passivated regime leading to maximized responsivities without issues of non-linearity. It should be noted that the dependence on the gate voltage can be shifted by Fermi level engineering, e.g., by choosing a different gate material, which will alter the metal-semiconductor workfunction ϕ_{ms}, as indicated in Fig. 5.12.

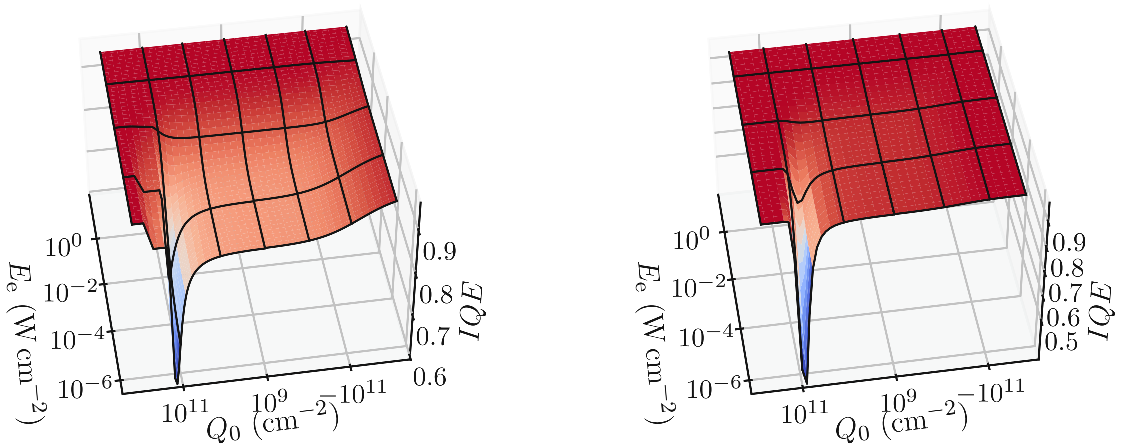

(a) TCAD simulated IQE versus Q_0 and irradiance for $t_{\mathrm{apt}} = 100\,\mu\mathrm{m}$, $W_{\mathrm{cath}} = 20\,\mu\mathrm{m}$. For $|Q_0| > 10^{12}\,\mathrm{cm}^{-2}$ the device is in the high R regime (red) for any injection level (irradiance).

(b) Modeled IQE versus Q_0 and irradiance. Agreeing to simulations the model predicts high recombination (low R) for $Q_0 \approx 10^{11}\,\mathrm{cm}^{-2}$ and low injection (irradiance).

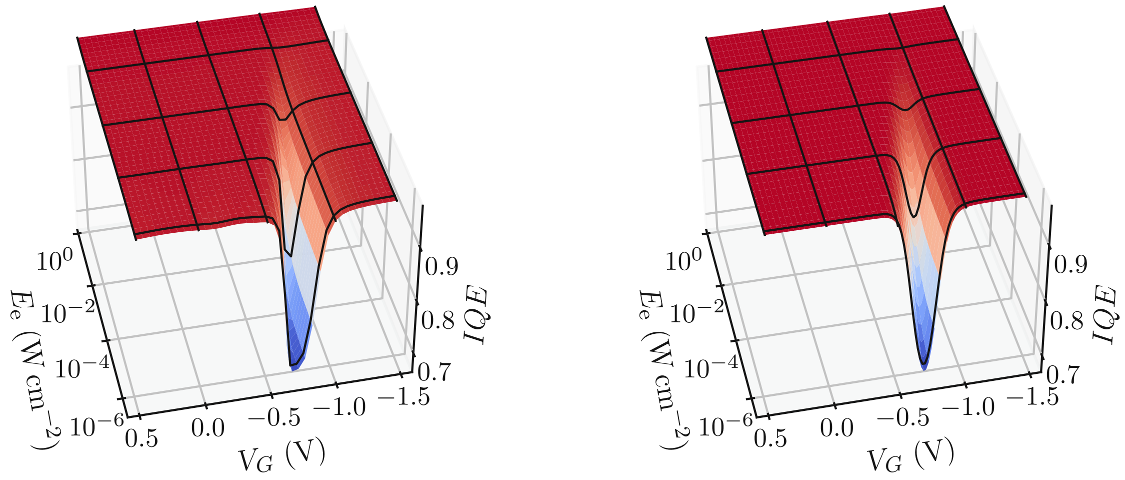

(c) TCAD simulated IQE versus applied gate voltage V_{G} and irradiance for the DTIMOSCAP with a n-poly gate and 20 nm oxide thickness. Used parameters are $t_{\mathrm{apt}} = 100\,\mu\mathrm{m}$, $W_{\mathrm{cath}} = 20\,\mu\mathrm{m}$. Operating the device at e.g. $V_{\mathrm{G}} = 0\,\mathrm{V}$ ensures maximized and linear responsivity R and quantum efficiency IQE.

(d) Modeled IQE versus applied gate voltage V_{G} and irradiance for the DTIMOSCAP with a n-poly gate and 20 nm oxide thickness. The model agrees well with the simulation data and predicts enhanced recombination for low injection and a gate bias of about $V_{\mathrm{G}} \approx -0.7\,\mathrm{V}$.

Figure 5.13. Injection dependent simulation and modeling results. Internal quantum efficiency IQE versus irradiance E_{e} and fixed oxide charge density Q_0 (**(a)** and **(b)**) / gate voltage V_{G} (**(c)** and **(d)**). Originally published in [PSC1].

Modeling

A one-dimensional charge-sheet based model [235, 236] along a horizontal cross section through the device (as indicated by the dashed line in Fig. 5.12) is utilized to compute the surface recombination rate and responsivity of DT terminated photodiodes as well as DTMOSCAP terminated photodiodes. The theoretical formulation and effective parameters of the model have been recently reviewed [131, 241, 242]. This formalism allows to compute the effective surface recombination velocity S_{eff} as a function of fixed oxide charges Q_0, gate voltage V_{G}, and excess carrier density Δn by balancing charges appearing close to the interface of investigation

$$Q_{\mathrm{Si}}(\Psi_{\mathrm{s}}, \Delta n, V_{\mathrm{G}}) + Q_{\mathrm{it}}(\Psi_{\mathrm{s}}, \Delta n, V_{\mathrm{G}}) + Q_{\mathrm{G}}(\Psi_{\mathrm{s}}, \Delta n, V_{\mathrm{G}}) + Q_0 = 0. \tag{5.4}$$

Equation (5.4) has been solved numerically for the surface potential Ψ_{s} with Δn and V_{G} as parameters. A detailed description of the extraction procedure as well as explicit formulas for the net charge in the semiconductor Q_{Si}, the gate charge Q_{G} and the interface trap charge Q_{it} are given in Reference [131]. Once Ψ_{s} is computed from (5.4) the surface carrier concentration n_{s} and p_{s} can be obtained from

$$n_{\mathrm{s}}(p_{\mathrm{s}}) = (n_0(p_0) + \Delta n) \exp\left(\frac{\pm\Psi_{\mathrm{s}}}{V_{\mathrm{th}}}\right), \tag{5.5}$$

where n_0 (p_0) is the bulk equilibrium electron (hole) concentration and the positive sign refers to electrons and the negative sign refers to holes. Finally, knowing n_{s} and p_{s}, the surface recombination rate can be computed according to Equation (3.28). In the study presented, S_{eff} is calibrated with the simulation data as a function of the irradiance. This allows to calculate R_{loss}, i.e. the lost responsivity as function of irradiance, V_{G} and Q_0 and finally the responsivity $R = R_{\mathrm{max}} - R_{\mathrm{loss}}$, where $R_{\mathrm{max}} \approx 0.52\,\mathrm{A\,W^{-1}}$ is extracted from the simulations. Considering the results shown in Fig. 5.13, it can be seen that a good agreement between simulation and modeled data is achieved. Therefore the discussed model is a valuable tool to predict the performance of DTI terminated photodiodes as a function of the aforementioned parameters.

5.2.2 Intensity Dependent Responsivity Measurements and TCAD Simulations

After discussing the modeling and simulation of recombination phenomena in DT sidewalls in Section 5.2.1, in this section an experimental study of injection-dependent responsivity measurements is presented. Measurements on photodetectors processed in a 180 nm CMOS process confirm that DTI-terminated island photodiodes show larger responsivities compared to NWG terminated island photodiodes. This superiority in terms of responsivity is more pronounced at high radiant fluxes because of reduced SRH surface recombination at the lateral DTI to silicon interface. Therefore, the responsivity of the DTI-terminated devices becomes non-linear with respect to the incoming radiant flux. For a linear photodiode the responsivity $R(\Phi)$ is constant. Thus, a non-linearity $\Delta_{\text{lin}}(\Phi)$ is defined according to:

$$\Delta_{\text{lin}}(\Phi) = 1 - \frac{R(\Phi)}{R(\Phi_{\text{max}})}. \tag{5.6}$$

Experimental findings regarding DT recombination related Δ_{lin} are well supported by TCAD simulations which are presented together with the measurement results below.

Sample description: layout and processing

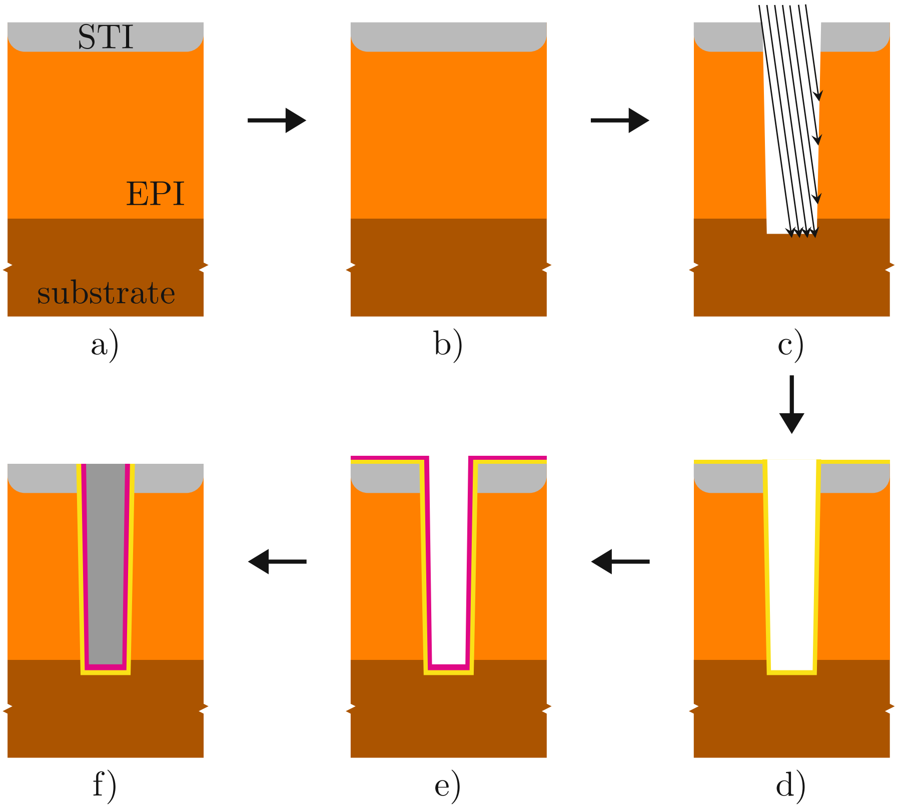

Figure 5.14. Schematic summarizing the DTI processing steps: **a)** structure after shallow trench isolation (STI) **b)** DTI lithography and etch **c)** (optional) DTI passivation implant **d)** dry liner oxidation **e)** TEOS oxidation **f)** DTI polyfill and etchback. Originally published in [PSJ4].

For this study photo-detectors fabricated within a standard 180 nm CMOS process extended by a DTI processing option are investigated. The main steps of the DTI processing are summarized in Fig. 5.14. The DTI patterning is performed after a conventional STI processing step. After the hard mask deposition, trenches are etched by the deep reactive ion etch (DRIE) technique [243]. The depth of the etch exceeds the epitaxial layer thickness of 20 µm and the width is ≈ 1 µm, yielding an aspect ratio of ≈ 20. After the trench etch an optional ion side-wall implant is performed, where different implants are compared based on their peak doping concentration. This processing step is a well-established technology, e.g. to achieve a conductive capacitor plate in

DRAM cells [244] or for lateral power devices [245]. Additionally, the sidewall implant might serve as passivation of the lateral silicon-to-silicon dioxide interface for bipolar as well as electro-optical applications [234]. To isolate the silicon from the polysilicon fill, first, a 40 nm liner oxide is grown by dry oxidation at 1000 °C which is a typical liner oxide known to have a low defect density as well as fixed oxide charge density [246]. Next, a 100 nm thick TEOS oxide is grown. This two-step oxidation process is needed because the initial dry oxide thickness is limited [247]. Finally, the trench is filled with undoped poly-Si due to its highly conformal nature and thus good filling properties. It should be noted that the DTI formation is done early in the manufacturing process, ensuring a high thermal budget to anneal out lattice defects caused by etching and sidewall implants. Test devices consist of silicon island-type photodiodes as drawn in Fig. 5.15. The structures consist of hexagonally distributed n-well cathode implants formed within a p-type epitaxial layer. The front surface is passivated with a p^+ implant and the active device area is ≈ 400 × 200 µm^2. Two different termination schemes are compared, namely the DTI and the NWG concepts.

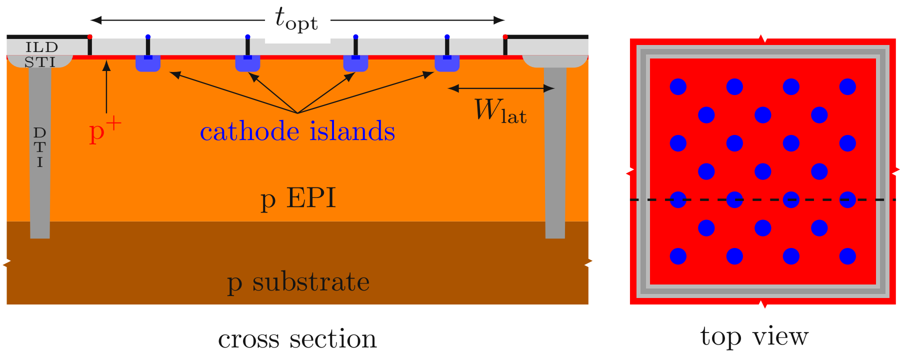

(a) DT terminated test device.

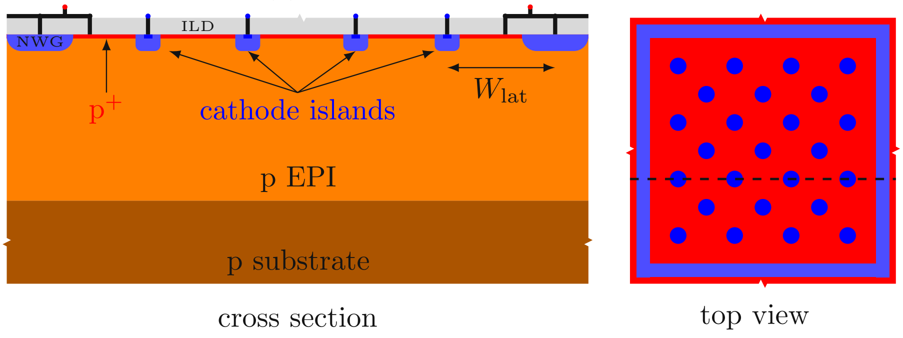

(b) NWG terminated test device.

Figure 5.15. Test structures used for IDR measurements: P-doped epitaxial layers are grown on a p-doped substrate. PN-junctions are formed by cathode island implants that are connected to form the cathode contacts (blue). The front surface is passivated with a p^+ implant that is connected to form the anode contact (red). Front surface isolation is provided by an interlevel dielectric (ILD). The pitch of the center of the DTI/NWG to the metal opening defining the optical aperture is ≈ 10 µm and the island to island spacing as well as the outer island to DTI spacing (denoted W_{lat}) is ≈ 40 µm. The islands are distributed hexagonally on the sample. Originally published in [PSJ4].

Measurement Setup

A schematic of the measurement setup is shown in Fig. 5.16a. Light from a 670 nm light emitting diode is coupled into a multi-mode optical fiber (type OM1). The incident radiant flux Φ can be varied with the attenuator ATT and is measured with a calibrated reference photodiode PD REF. The photodiode (PD DUT) is measured on wafer level and contacted using a semi-automatic probe station. No anode to cathode bias is applied, i.e. $V_{\mathrm{AC}} = 0\,\mathrm{V}$, and the photocurrent I_{phot} is measured as a function of Φ. The responsivity R and non-linearity Δ_{lin} are extracted according to (2.14) and (5.6). The core diameter of the optical fiber is 62.5 µm and the fiber is positioned $\approx$ 100 µm above PD DUT. For the illumination with a wavelength of 670 nm the optical output profile at the top of the DUT, that is $\approx$ 100 µm away from the fiber tip, can be considered not yet substantially expanded and to be within a diameter of $\approx$ 62.5 µm [248, 249], which is smaller than our DUT size. This allows to deliberately illuminate different parts of the photodiode. In the measurements, two configurations, namely central illumination and lateral illumination are compared as shown in Fig. 5.16b and 5.16c, respectively. All measurements are performed at room temperature and the LED in combination with the variable attenuator ATT is used to establish radiant fluxes of about 1 pW to 1 µW.

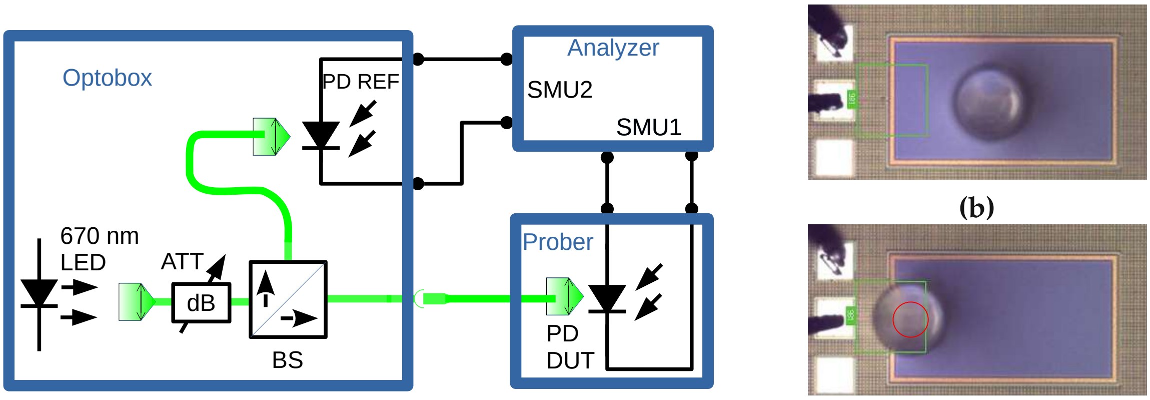

(a)

(b)

(c)

Figure 5.16. IDR measurement setup. **(a)** Measurement schematics consisting of a custom-designed optobox, the wafer prober, and an Agilent 4156A parameter analyzer. The 670 nm radiation from a light emitting diode (LED) is coupled into an optical fiber, where it is attenuated at a variable attenuator ATT. The beam is split at the beam splitter BS. One part goes to a reference photodiode PD REF that is connected to the source measurement unit SMU2. The other part from BS goes to the device under test (PD DUT) that is connected to SMU1. Electrical connections are drawn in black, and optical connections (multimode fiber, type OM1) are drawn in green. **(b)** & **(c)** Microscopic view of fiber head above the test sample. The diameter of the fiber and the lighting spots are smaller than the sample size. This allows to deliberately expose sections of the DUT to light, were a central **(b)** and lateral **(c)** illumination is compared. Additionally, the contact needles can be seen on the left side of the images. Originally published in [PSJ4].

Measurement Results

Measurement results for structures with NWG and DTI are compared in Fig. 5.17. It should be noted that the DTI in these structures is processed without a sidewall implant. As can be seen, structures with DTI show higher responsivity R compared to structures with NWG. For the highest measured radiant flux ($\Phi \approx 1\,\mu\mathrm{W}$) the increase is about 16 % for central and about 58 % for lateral illumination. However, whilst R is constant for the NWG case (within the experimental error estimation of ±1 %) a non-linearity for the DTI structures can be observed, where the spectral response is reduced at lower radiant fluxes, i.e. there is increased recombination, which qualitatively agrees with the form of the IDR results discussed in Section 5.2.1. It can be concluded, that this intensity-dependent recombination behavior is either introduced by DTI interface recombination or by recombination via DTI processing-induced bulk defects. By comparing lateral to central illumination it can be seen that R is lower for both NWG and DTI in the lateral case. This can be related to the higher excess carrier density towards the diode termination and thus increased recombination/losses at the boundaries.

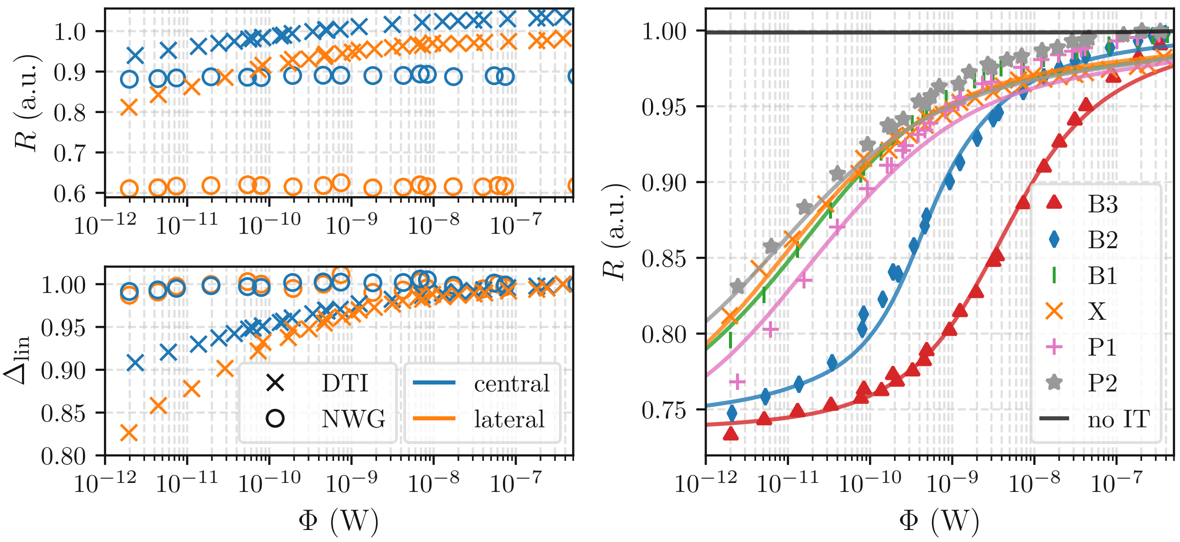

Figure 5.17. IDR measurement and simulation results. **(left)** Measurement results comparing the structure with NWG and DTI termination. Upper plot shows responsivity R, lower plot non-linearity Δ_{lin} versus radiant flux Φ. Δ_{lin} is calculated according to Equation (5.6). The DTI was processed without a sidewall implant. **(right)** Measurement (marker) and simulation (solid lines) results for different DTI passivation implants according to Table 5.7. The responsivity R is plotted versus the radiant flux Φ. The black line is the result of a simulation without interface traps. Originally published in [PSJ4].

Simulation Results and Extraction of Interface Parameters

In the right hand side plot of Fig. 5.17 TCAD simulations are shown together with the measurement results. The simulation results were obtained using the Synopsis Sentaurus package [250], where a layout-based process, as well as electro-optical device simulations were performed. The simulation domain is a 2D cross section of the island photodiode with DTI termination, as shown in Fig. 5.15 and the used simulation models and parameters are summarized in Tab. 5.7. The DTI sidewall ion implantation (see Fig. 5.14) is simulated using the Monte Carlo implant model with 100 000 particles, and the final peak doping concentrations are given in Tab. 5.7. For the device simulation, the illumination window is set to a width of 62.5 µm and is laterally aligned to the optical aperture. DTI interface recombination is implemented by the SRH surface recombination model where, as starting point for the defect landscape (energetic distribution, cross sections, fixed oxide charges), values reported in the literature were considered. At this point, it should be mentioned, that an accurate and reliable extraction of interface parameters is challenging, as a considerable variance of the model parameters (i.e. fixed oxide charge densities, trap densities, energetic trap positions/distributions, trap cross sections) has been reported [252, 253, 254, 129, 235, 213, 255, 256]. It has been shown, that despite being negligible contributors to recombination, band-tail states might have an impact on surface passivation properties as a large amount of charge may be associated with carriers occupying these states [256, 241]. Therefore, $D_{\mathrm{it}}(E)$ of the Si-SiO$_2$ interface is typically modeled assuming a constant mid-gap trap density $D_{\mathrm{it,mg}}$ plus energy-dependent band tail states $D_{\mathrm{it,bt}}(E)$ [252]:

Table 5.6. Simulation models and parameters[†]

name	model	parameters / values
Carrier statistics	Fermi-Dirac	
SRH bulk recombination	after [251]	$\tau_{\max,n} = \tau_{\max,p} = 50\,\mu\mathrm{s}$ $\tau_{\min,n} = \tau_{\min,p} = 0\,\mu\mathrm{s}$, $\gamma = 1$ $N_{\mathrm{ref},n} = N_{\mathrm{ref},p} = 10^{16}\,\mathrm{cm}^{-3}$
DTI interf. rec.	according to Fig. 5.18 and Tab. 5.7	
	Optical Generation	
Generation model	Optical Beam Absorption Method [250]	
Incident angle	0°	
Polarization	unpolarized	
Wavelength	670 nm, monochromatic	
Window	62.5 µm, left edge aligned	
Intensity	10^{-12} W to 10^{-6} W	

[†] Auger recombination, direct recombination, bandgap narrowing, mobility and front surface recombination are modeled as stated in Tab. 5.2.

$$D_{\mathrm{it}}(E) = D_{\mathrm{it,mg}} + D_{\mathrm{it,bt}}(E). \tag{5.7}$$

Therefore the values of Q_0, $D_{\mathrm{it,mg}}$ and $\sigma_{\mathrm{n,p}}$ according to reference [254] are adopted, and band tail states as proposed in [256] are added. Additionally, constant cross sections for electrons and holes over the bandgap are assumed and divided between acceptor-and donor-like traps at mid-gap, which are reasonable assumptions [257, 252]. These parameters and the trap distribution are shown in Fig. 5.18 and serve as an initial guess for the parameter extraction.

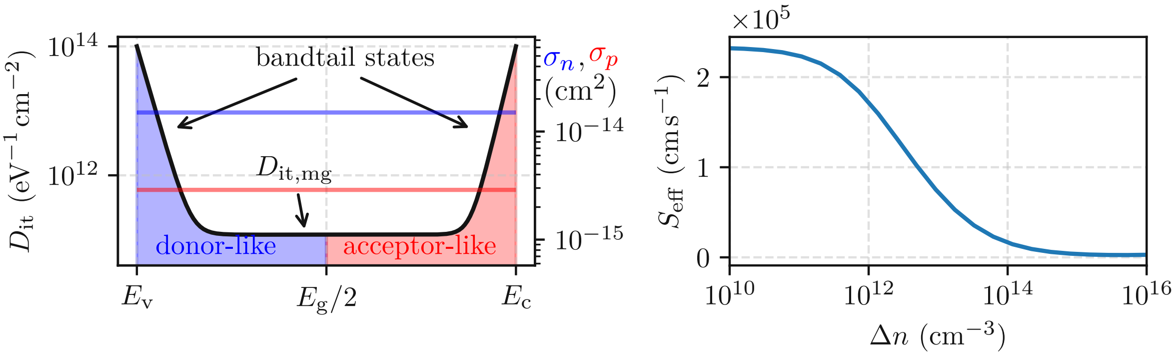

Figure 5.18. Defect landscape and corresponding surface recombination velocity at the DTI to silicon interface. **(left)** Interface trap parameters, namely interface trap density $D_{\rm it}$ (black line, left axis) consisting of mid-gap trap density $D_{\rm it,mg}$ plus bandtail states and cross sections $\sigma_{\rm n,p}$ (colored lines, right axis) versus energy in the bandgap for the values reported from [254] extended by band-tail states as reported in [256]. Traps between valence band $E_{\rm v}$ and mid-gap $E_{\rm g}/2$ are considered donor-like whilst traps between $E_{\rm g}/2$ and the conduction band are considered acceptor-like. **(right)** Effective surface recombination velocity $S_{\rm eff}$ versus excess carrier density Δn for a p-type ($N_{\rm A} = 10^{15}\,{\rm cm}^{-3}$) Si-SiO$_2$ interface with trap parameters according to the upper plot and a fixed oxide charge density $Q_0 = 2.6 \times 10^{11}\,{\rm cm}^{-2}$. Originally published in [PSJ4].

Table 5.7. Passivation implants and extracted interface trap parameters [†]

	Passivation implant		Extracted parameter		
	name[a]	peak conc. cm^{-3}	Q_0 cm^{-2}	$D_{\rm it,mg}$ cm^{-2} eV^{-1}	ξ [b]
×	X	no implant	2.7×10^{11}	1.4×10^{11}	4.7
|	B1	2×10^{16}	3.8×10^{11}	1.6×10^{11}	6.0
⬥	B2	4×10^{16}	1.1×10^{12}	1.7×10^{11}	4.6
▲	B3	6×10^{16}	1.2×10^{12}	4.2×10^{11}	2.8
+	P1	5×10^{15}	2.8×10^{11}	2.0×10^{11}	4.5
★	P2	3×10^{16}	4.9×10^{11}	1.5×10^{11}	4.7

[†] Results originally published in [PSJ4].
[a] B1, B2, and B3 are boron implants and P1 and P2 are phosphorous implants.
[b] $\xi = \sigma_n/\sigma_p$ for a fixed $\sigma_n = 1.5 \times 10^{-14}\,{\rm cm}^2$.

The aim of the simulations is to provide a physics based explanation for the measurement results and to validate the theory of SRH interface recombination at the DTI sidewalls, as well as to extract the corresponding interface parameters. The simulations do not account for external losses, i.e. reflections and absorptions in the dielectric layer/interfaces above the DUT, and therefore the simulations are scaled such that the simulation without interface traps (black flat line in Fig. 5.17) matches the highest level of measured responsivity R at high radiant fluxes. Subsequently, the interface trap parameters used in the simulation are adjusted in the following way: Starting point is the parameter set as shown in Fig. 5.18. Then $D_{\mathrm{it,mg}}$, Q_0 and σ_p are adjusted to minimize residuals (least square error) to the measurement result using the Nelder-Mead optimization algorithm. This procedure is performed individually for each passivation implant since the different passivation implants or passivation doping concentrations might affect the interface defect parameters [258, 259]. Simulation results for different passivation implants according to Table 5.7 are shown together with the measurement results in Fig. 5.17. It should be noted, that Table 5.7 also shows the extracted values for the fitted interface parameters. The fitted parameters show an increase in Q_0 and $D_{\mathrm{it,mg}}$ for the different implants which, for similar doping concentration, is less pronounced for the n-type implants than the p-type implants. Referring to the results shown in Fig. 5.17, it can be seen that the measured radiant flux-dependent responsivity can be fully modeled with interface recombination at the DTI sidewalls. Higher responsivities R are observed at high radiant fluxes because of reduced sidewall interface recombination. The simulated non-linear response can be directly attributed to recombination at the DTI sidewall since a simulation without these traps appears flat and therefore linear. Additionally, the TCAD simulations reproduce the influence of the DTI sidewall implant, namely a shift of the high response to low response transition region to higher fluxes Φ for boron implants B2 and B3 and hardly any impact by the implants B1, P1, and P2.

Influence of Bias, Sidewall Doping and Wavelength

As shown above, a moderate boron implant at the DTI sidewall does not improve the device performance and may even have a negative impact. Therefore, the simulation study is extended to high boron sidewall doping concentrations since it is known that an accumulation layer can provide good surface passivation properties [260]. For this purpose, the interface parameters are fixed to the values stated in the first row in Tab. 5.7, and the boron sidewall doping concentration is implemented analytically with a Gaussian doping profile (0.2 µm depth) with a varied peak doping concentration N_{peak}. As can be seen in Fig. 5.19, the simulations show a performance degradation at moderate ($10^{16}\,\mathrm{cm}^{-3}$ to $10^{17}\,\mathrm{cm}^{-3}$), and a performance optimization at sufficiently high ($> 10^{18}\,\mathrm{cm}^{-3}$) values of N_{peak}. Therefore, with a sufficiently high boron doping concentration at the DTI sidewalls, the effect of non-linearity on the DTI-terminated test structures can be mitigated. However, it should be mentioned that achieving such doping concentrations in regions with high aspect ratios is challenging [261]. Another equivalent way to accomplish a hole accumulation layer passivating the lateral DTI to silicon interface is the creation of DTI to silicon capacitor structures [262], which was discussed in Section 5.2.1.

It should be noted, that the experimental results presented in Fig. 5.17 are with 0 V diode bias. However, simulations up to a reverse bias of 2 V, shown in the right hand side plot of Fig. 5.19, result in responsivity degradation analogical to the ones presented in Fig. 5.17. The influence of pn-junction bias on the results presented in this study is expected to be low since the associated depletion zone is small (for both: zero as well as reverse bias) compared to the total device's active area.

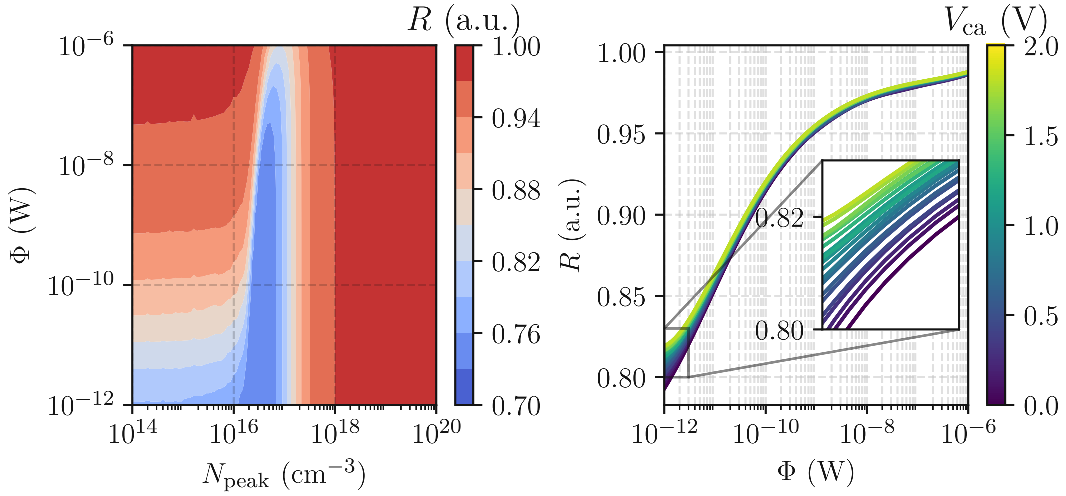

Figure 5.19. Influence of DTI sidewall peak doping concentration and anode to cathode bias on the responsivity R and non-linearity of DTI-terminated photodiodes. **(left)** Contour plot of the responsivity R as a function of radiant flux Φ and boron peak doping concentration at the DTI sidewall N_{peak}. R becomes high and linear at sufficiently high values of N_{peak}. Originally published in [PSJ4]. **(right)** Responsivity as function of cathode to anode bias V_{ca} (reverse) and radiant flux. The inset shows a zoom in the region with the highest spread, which shows small influence of the applied bias on the extracted non-linearity.

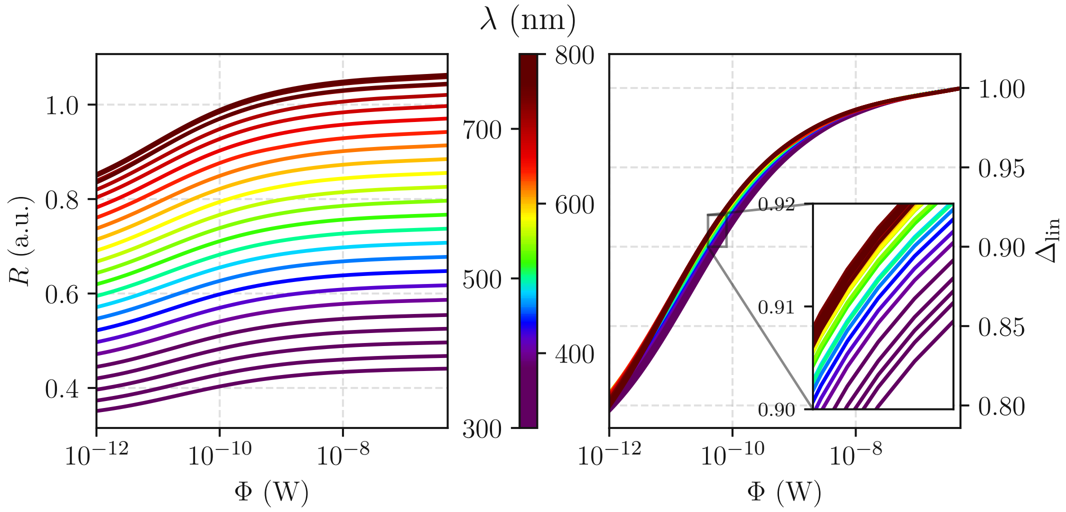

Figure 5.20. Influence of wavelength λ (according to central colorbar) on the responsivity **(left)** and non-linearity Δ_{lin} **(right)** of DTI-terminated photodiodes as function of radiant flux Φ. The inset in shows a zoom in the region with the highest spread, which is less than $\approx 2\,\%$ showing small influence of wavelength on the extracted non-linearity.

Similarly, in the experiment a wavelength of 670 nm is considered. However, simulations with an extended wavelength range from 300 nm to 800 nm, presented in Fig. 5.20, show variations of less than 2 % on the extracted non-linearity Δ_{lin}. Hence it can be concluded, that the experimental results shown are representative, and non-linear effects on the same order of magnitude may be expected for experiments at other wavelengths in the visible range.

5.2.3 DTI DLTS Measurements and Simulations

As introduced in Section 4.2.1 DLTS is a well-known characterization technique for identifying and extracting trap parameters. To further investigate the critical DTI to silicon interface associated to the trench sidewall dedicated test structures have been processed and a DLTS study has been performed on these structrues.

Sample Description and Experimental Setup

The deep trenches of the test structures are processed as described in Section 5.2.2 and as schematically drawn in Fig. 5.14. In a typical DLTS measurement sequence trap states are filled by applying a pulsed filling voltage to a pn-junction. Then, a quiescent reverse bias is applied and the trap-carrier dynamics are monitored by measuring a transient capacitance. To get a strong impact from trap states located at the DTI Si-SiO$_2$ interface on the measured DLTS capacitance, devices consisting of alternating n-well and p-well regions separated by DTs are investigated. In such a device, a large fraction of the depletion zone in the epitaxial layer covers the DTI to silicon interface leading to strong DLTS signals from the interface traps. A schematic of the test structures is shown in Fig. 5.21 and the corresponding capacitance-voltage characteristics are shown in Fig. 5.22. For the measurements a Lakeshore CRX-4K cryogenic wafer prober is used and the probed temperature range is 40 K to 330 K. The DLTS experiments consist of capacitance transients measurements (sampling time 100 ms with a time resolution of 10 µs), which are recorded with an in-house measurement instrument, i.e., defect probing instrument [263].

DLTS Results

The lower plot in Fig. 5.22 shows capacitance transients after a 100 ms forward bias pulse voltage of 100 mV at a quiescent reverse bias of 2.4 V and selected temperatures indicating no significant trapping at very low and high temperatures (flat curves) and mixed majority (increasing C) and minority carrier (decreasing C) [150] trapping at about 220 K. Fig. 5.23 shows the conventional DLTS plot of the capacitance transients presented in Fig. 5.22, which is constructed by correlating the measured capacitance transient with a square wave weighting function over a varied time window. This form of analysis has advantages over the frequently used double boxcar approach in terms of resolution [202]. In the spectrum shown in Fig. 5.23, three defects can be identified: two

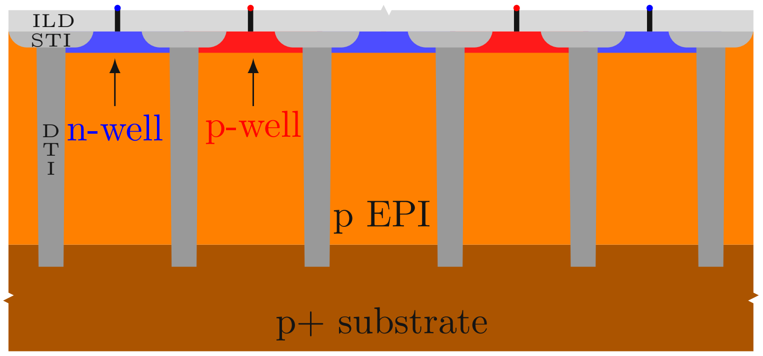

Figure 5.21. Schematics of the DLTS test structures. PN-junctions are formed by n-well and p-well implants that are separated by deep trench isolation (DTI). The DTIs are formed after shallow trench isolation (STI) and the top surface is passivated with an interlevel dielectricum (ILD). The trench to trench pitch is 4.42 µm, the length of the structure in the direction perpendicular to the drawing is ≈ 40 µm. Originally published in [PSC2].

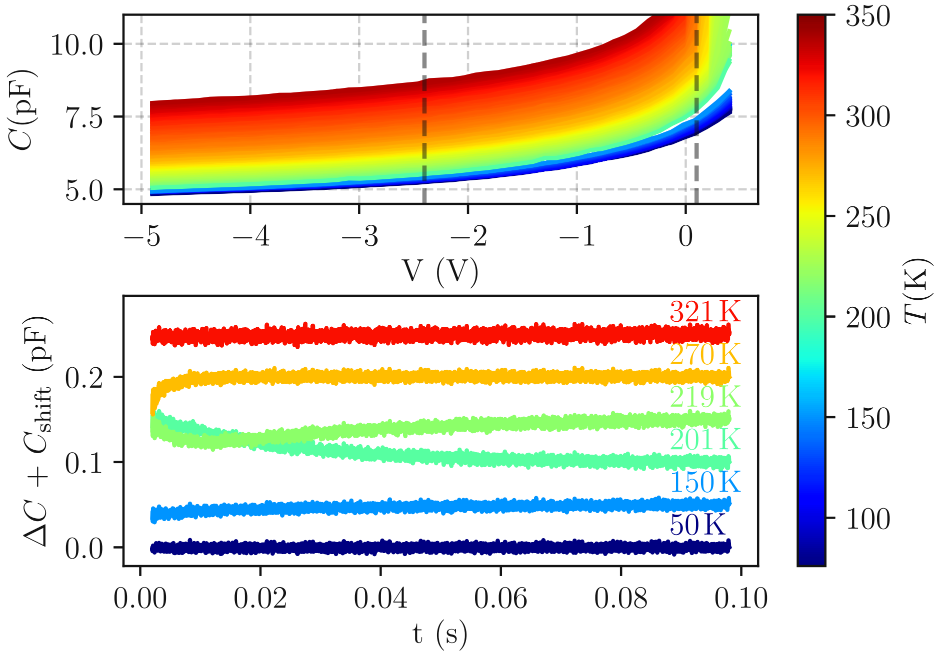

Figure 5.22. DLTS measurement results. **(top)** Measured capacitance-voltage (C-V) characteristics for the DLTS test structure at various temperatures T according to the attached colorbar. The vertical dashed lines (−2.4 V 0.1 V) indicate the applied DLTS voltage levels. **(bottom)** Capacitance C versus time t at a reverse bias of 2.4 V after a 100 ms stress at a forward bias of 0.1 V at specific temperatures with characteristic minority and majority carrier trapping. The curves are arbitrarily shifted for better readability. Originally published in [PSC2].

majority carrier defects (H_1, H_2) and one minority carrier defect (E_1). An additional set of DLTS measurements with varied pulse voltages is performed to distinguish between energetically discretely or continuously distributed traps and the results are shown in the right hand side plots of Fig. 5.23. With different pulse voltages V_p the peak positions of $\Delta C(T)$ for a fixed rate window slightly shift for the traps H_1 and E_1, which indicates

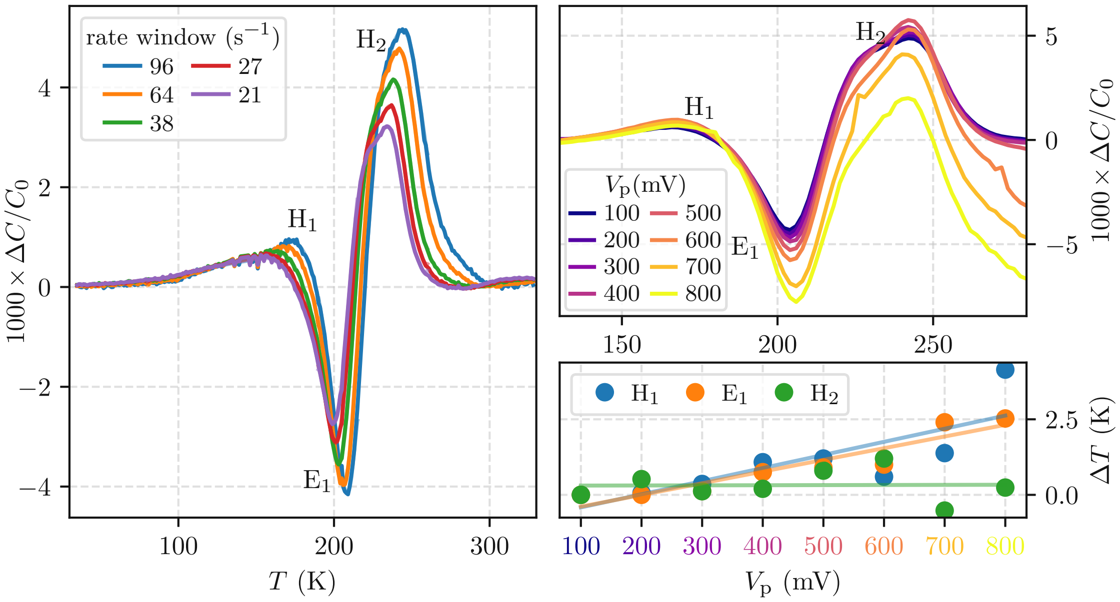

Figure 5.23. DLTS rate window analysis of the DTI test structure. Conventional DLTS plot of the transients shown in Fig. 5.22: **(left)** Normalized capacitance difference $\Delta C/C_0$ versus temperature T. Three traps, labelled H_1, H_2 and E_1 are visible. **(right)** DLTS analysis for a varied pulse voltage V_p. **(right top)** DLTS plots for a fixed rate window of 38 s^{-1} and a varied V_p. **(right bottom)** Temperature shift ΔT of the peak position versus V_p. The linear fits act as guide to the eye and show a slight shift of the peak temperature for the traps H_1 and E_1. Originally published in [PSC2].

that these traps are continuously distributed within the bandgap rather than discrete levels [264].

Laplace Analysis and Trap Identification

As introduced in Section 4.2.1, by applying the Laplacian DLTS analysis each recorded capacitance transient is de-convoluted into its spectrum of exponential functions by means of the inverse Laplace transform. The Lasso regression [265] is utilized to extract the spectra at each temperature, where the extraction is exemplarily shown for the 219 K measurement data in Fig. 5.24 (left hand side plots). As can be seen, the measurement data can be successfully reproduced as a sum of two exponentials with different leading signs corresponding to one active minority and one active majority carrier trap. The full spectra and Arrhenius plot for the LDLTS analysis can be seen in the right hand side plot of Fig. 5.24, where 4 traps were detected. These correspond to the peaks H_1, H_2 and E_1 from the conventional approach in Fig. 5.23. However H_2 can be resolved as two traps (labelled $H_{2,a}$ and $H_{2,b}$) by means of the LDLTS analysis. Note that the ability to resolve traps with similar emission characteristics is one of the main advantages of the LDLTS technique compared to the conventional DLTS analysis. With DLTS, the fingerprints, i.e. the activation energy E_A and capture cross section σ of defects, can be extracted, and the results for this study are summarized in Tab. 5.8.

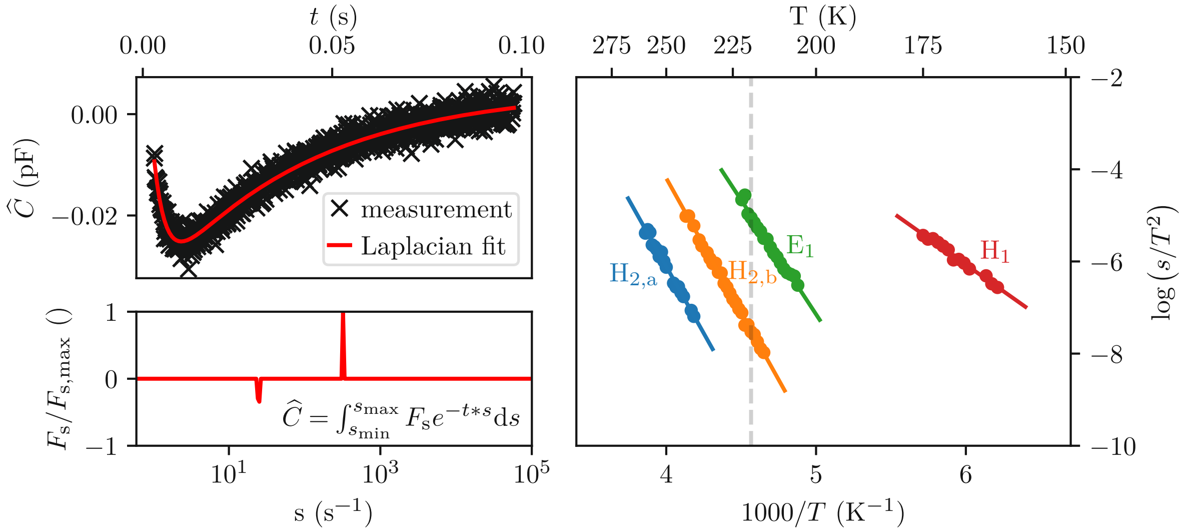

Figure 5.24. Laplacian DLTS analysis of DTI test structures. **(left)** Laplace DLTS extraction at 219 K with simultaneous minority and majority carrier trapping. **(left top)** Normalized capacitance $\widehat{C} = \frac{C(t)-C_0}{C_0}$ versus time t. **(left bottom)** Extracted Laplace coefficients F_s versus emission rates s according to inset formula. **(right)** Arrhenius plot extracted by the LDLTS method. Four traps are detected. The corresponding extracted parameters are presented in Tab. 5.8. The vertical dashed line marks the spectra at 219 K, which is omitted from the left plots. Originally published in [PSC2].

Table 5.8. Extracted DLTS parameter †

	name	E_A (eV)	σ (cm^2)^a
●	H_1	$E_v + 0.20$	4.2×10^{-19}
●	E_1	$E_c - 0.43$	8.4×10^{-15}
●	$H_{2,a}$	$E_v + 0.50$	4.7×10^{-15}
●	$H_{2,b}$	$E_v + 0.50$	3.7×10^{-14}

† Results originally published in [PSC2].

^{a} For the hole traps $\sigma = \sigma_p$ and the activation energy is with reference to the valence band, for the electron trap $\sigma = \sigma_n$ and the activation energy is with reference to the conduction band.

The most important defect for the DTI interface recombination problematic, is defect E_1, since this defect tends to interact with minority carriers, as is investigated in TCAD simulations discussed below. A possible candidate for this defect is the P_b center, where distributions with a peak energy of about $E_c - 0.4$ eV were reported by Dobaczewski et al. [266]. The P_b center is also a candidate for the defect H_1, since it is known that the energetic distribution of this trap state also has a distinct peak at about 0.25 eV above E_v [267]. The low value for the cross section for H_1 stands out among the values extracted for the other defects, however, it is still within the range of values reported in literature for cross sections of the Si-SiO_2 interface [268]. Generally, cross section extracted by DLTS are not unambiguously discussed [269], therefore the main conclusions regarding the DLTS results in this work are based on the extracted activation energy. It should be noted, that the activation energy E_A, as extracted with DLTS, might differ from the trap energy E_T because of a structural relaxation of the defect when changing its charge state. For the P_b center this energy difference may well be 0.05 eV, as is shown in Section 5.2.3. Finally, a direct identification of defect H_2 remains challenging as there are many possible reported candidates for discrete defects at this energy [93, 92].

A Comparison Between the SRH and NMP Model

Typically, trap energies extracted by means of DLTS are considered energies with respect to the corresponding band edges, which is based on the Shockley-Read-Hall (SRH) theory, and hence structural relaxations of the defect depending on its charge state are ignored. A more sophisticated approach to model carrier emission rates from trap states, which considers the structural relaxation of the defect is the nonradiative mulitphonon (NMP) model, as introduced in Section 3.2.3. In the following, these deviations in terms of extracted trap energies comparing the two models are discussed on the example of the Si-SiO$_2$ dangling bond, i.e. the P_b center. For the P_b center the relaxation energy $\mathcal{E}_\mathrm{R}$, as introduced in Section 3.2.3, has been extracted to be around $\approx 0.2\,\mathrm{eV}$ [270, 112]. Considering that the extracted activation energy E_A in Tab. 5.8 corresponds to $\mathcal{E}_{21}^{NMP}$ rather than $E_{21} = -\mathcal{E}_{21}^{SRH}$ the value for E_T with respect to E_c, which considers the structural relaxation, can be calculated by inverting Equation (3.37a). Such a comparison between the two models is shown in Tab. 5.9, showing an energy difference of 0.04 eV.

Table 5.9. Comparison of extracted trap energies[†]

model	Emission barrier[a] $\mathcal{E}_{21}$	Trap energy[b] E_{21}
SRH	0.43 eV	0.43 eV
NMP[c]		0.39 eV

[†] Results originally published in [PSJ1].
[a] Corresponds to the activation energy E_A as extracted by DLTS.
[b] With respect to the conduction band edge.
[c] Assuming linear electron-phonon coupling and $\mathcal{E}_\mathrm{R} = 0.2\,\mathrm{eV}$.

To demonstrate the difference in emission rates of the two models a process simulation of the test structures as shown in Fig. 5.21 is performed. Subsequently, device simulations have been performed, mimicking a DLTS measurements with a single trap at $E_\mathrm{c} - E_\mathrm{T} = 0.39\,\mathrm{eV}$, comparing the SRH and NMP model. The utilized models for process and device simulation are as described in Section 5.2.2. The resulting DLTS plots are shown in Fig. 5.25, where a clear shift in the DLTS plot between the two models can be seen. The extracted parameters, as shown in the inset in the right hand side plot, correspond to those presented in Tab. 5.9 and Tab. 5.8 (cross section of E$_1$), which further validates the extraction procedure. From a modeling perspective, it can be concluded

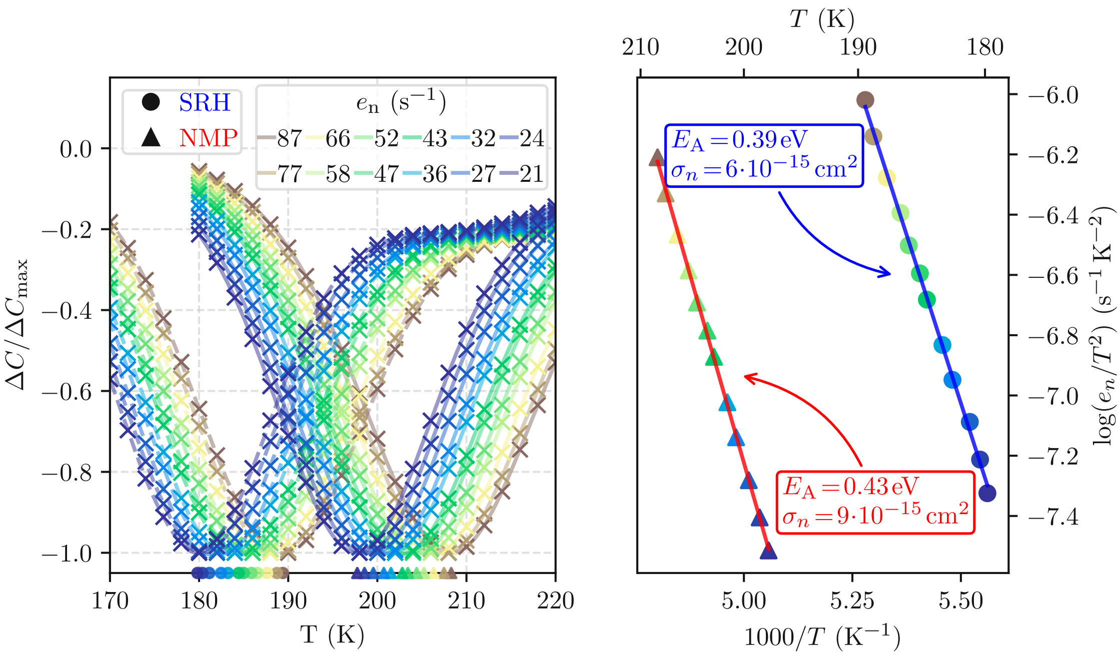

Figure 5.25. TCAD simulated DLTS: a comparison between the SRH and NMP model. **(left)** DLTS plot for different emission rates e_n. **(right)** Arrhenius plot and extracted parameters comparing the SRH and NMP model. Originally published in [PSJ1].

that the physically more accurate NMP model can be effectively modeled with the SRH model and a shift of 0.04 eV in the trap energy as for a DLTS measurement only the emission process is relevant. It should be mentioned, however, that for the opposite process, i.e. carrier capture, the difference between the two models will be even more considerable, since for this process the SRH model does not consider an energetic barrier at all.

Impact on the Performance of Photodiodes

Finally, the parameters of the extracted trap state E_1 according to Tab. 5.8 and Tab. 5.9 are utilized to perform TCAD simulations on DT-terminated photodiodes, where the experimental results as well as simulation details were comprehensively presented in Section 5.2.2. To model interface recombination the NMP model was utilized as described in the previous section. The simulation results are shown in Fig. 5.26, where the detectors radiant flux Φ-dependent responsivity R is compared to experimental results from the DTI-terminated island photodiode. The fixed oxide charge density Q_0 and interface trap density were fitted by minimizing residuals to the experimental results and their values are shown as inset in the plot. The fitted parameters are well within the range of typically reported parameters for the Si-SiO$_2$ interface [235, 252, 254]. As can be seen, by modeling the interface recombination via the trap state E_1, good agreement between measurement and simulation can be achieved. It should be mentioned, that the defect landscape was modeled differently in the two approaches (Fig. 5.17 versus Fig. 5.26). Whilst in the first case, the defect landscape was implemented according to modeling approaches frequently utilized in literature (see Fig. 5.18), in the second procedure a single discrete trap level with energy and cross section according to the DLTS results was used.

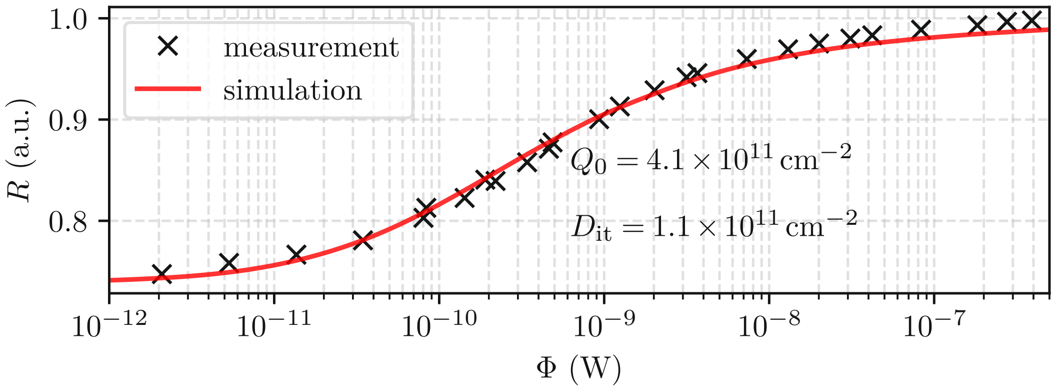

Figure 5.26. Utilizing DLTS results to model measured interface recombination. Simulated and measured responsivity R versus radiant flux Φ. In the simulation trap E_1 (activation energy and cross section) was used to model the DTI to silicon interface recombination. The fixed oxide charge density Q_0 and the trap density D_{it} were adjusted to match the experiments, the extracted values are written in the inset.

5.2.4 Discussion

Interface recombination at DTI terminated photodiodes can strongly impact the quantum efficiency of detectors and hence limit their performance. The injection-dependent SRH interface recombination rate at the DTI sidewalls gets manifested in a radiant-flux dependent responsivity. Thus, a direct comparison of DTI/NWG terminated photodiodes and their impact on the device efficiency is presented. Measurements and simulations over 6 decades of radiant flux (from about 1 pW to 1 µW) confirm, that for the same geometrical constraints, DTI outperforms the NWG in terms of overall responsivity and electrical cross-talk. However, as mentioned several times, the essential drawback of DTI terminated photodiodes is the injection-dependent recombination at the DTI sidewalls. It is shown, that a sufficiently large band-bending towards the interface either achieved by fixed charges ($|Q_0| > 10^{12}\,\mathrm{cm}^{-2}$), by a strong enough trench sidewall doping with peak concentrations $N_{\mathrm{peak}} > 10^{18}\,\mathrm{cm}^{-3}$ or by applying a gate bias to a DTMOSCAP structure, can effectively passivate the sidewall interfaces leading to maximized and linear quantum efficiencies. However, applying these passivation techniques is a challenging task because of the small dimensions and large aspect ratio of the trench. Finally, a DLTS study on dedicated test structures reveals that with DTI processing a large amount of defects are introduced at the DTI oxide to silicon interface, which are responsible for the device degradation. The P_b center is identified as possible candidate for two of the trap states and it is shown that such trap states can lead to non-linear recombination of photo-generated carriers in DTI terminated island photodiodes.

Chapter 6

Summary, Conclusions and Outlook

This chapter provides a comprehensive overview of the key findings and implications of this thesis, as well as a discussion of potential avenues for future research.

6.1 Summary and Conclusions

Photodiodes play an inherent role for the technologies and devices we use in our daily lives. Continuous improvements and advancements over the recent decades in the processing techniques, design as well as understanding of the underlying physics, have led to highly efficient and precise optoelectronic devices. Photodetectors made of silicon, which is the predominant material in the semiconductor-based sensor industry, are so pure, that spurious amounts of contamination or a tiny fractional amount of crystallographic mismatch may cause detrimental effects on the device performance. The fundamental reason for this device degradation is, that electronic states within the band-gap are created, and charge carriers may interact with these states disturbing the nominal operation. Fundamentally, the interaction of charge carriers with these defect states can be described with the Shockley-Read-Hall (SRH) model, where carriers from either the valence band or the conduction band can be captured or emitted from trap states, which is described mathematically by the corresponding rates. These defect-carrier interactions may impact the operational parameters of a photodiode, such as responsivity, response times, noise characteristics or linearity. Therefore, the characterization of defects in photodiodes is essential to understand, identify and eradicate trap-related performance degradation, as well as to design devices that are resilient to charge-trapping effects. Several techniques have emerged to characterize defect states in pn-junctions.

First, the characterization of lifetimes, which are directly related to the underlying trap states considering the SRH theory and constitute an important opto-electronic parameter, was discussed in this work. A variety of methods and literature on this topic has amassed, where three selected approaches to determine lifetimes have been reviewed and utilized. State-of-the-art photodiodes often consist of epitaxial layers grown on a substrate. The width of the grown layer is typically much smaller than the diffusion length of the corresponding minority carriers and hence the interface between the epitaxial layer and the below-laying substrate becomes a critical spot strongly influencing the extracted lifetimes. This has been systematically investigated in this work by means of measurements and simulations. It has been shown, that methods, such as open circuit voltage decay (OCVD) or reverse recovery (RR), are candidates to extract the effective carrier lifetimes, which are impacted by the epitaxial layer to substrate boundary. The smaller the ratio of diffusion length to layer thickness the more pronounced the mismatch between effective and SRH related carrier lifetime. However, other lifetime measurement methods are not influenced by this interface and are hence candidates to extract SRH lifetimes also on epitaxial layers. It has been shown, that with the combined I-V and C-V (cIVCV) method SRH lifetimes corresponding to diffusion lengths much larger than the layer thickness can be extracted, because the main signal investigated by this method originates from the junction depletion zone. Both parameters, effective as well as SRH lifetimes, are of interest and provide important information to engineers designing devices or evaluating processing performance.

Secondly, the influence of defects on photodiodes with deep-trenches (DTs) have been investigated. With combined efforts of measurements and TCAD simulations it has been shown that the DT termination concept is able to outperform other termination concepts like the n-well guard (NWG) in terms of important parameters, such as cross-talk. However, defect-mediated recombination at the DT sidewalls causes an injection-, and thus, radiant flux-dependent responsivity, which is undesired for certain applications. Experimentally, the influence of a DT sidewall implant has been investigated which was extended by simulations to show, that the achieved sidewall peak doping concentrations were not high enough to successfully passivate the interface and mitigate the problem of injection-dependent recombination. To get further insights into the defect landscape a deep-level transient spectroscopy (DLTS) study has been performed on dedicated test structures with maximized influence of DT sidewalls. Four different trap states could be detected by means of a Laplacian analysis of the recorded capacitance transients and one important defect candidate was identified as the silicon dangling bond, also known as P_b center. By inheriting the parameters extracted for this defect, TCAD simulations could be matched to the experiments supporting the theory that this defect is related to the observed phenomena. Furthermore, this defect was exemplarily taken to study the influence of structural relaxation on the transients observed in DLTS measurements by comparing the emission rates related to the SRH and non-radiative multi-phonon (NMP) model.

6.2 Outlook

In this section potential future research directions based on the findings and conclusions of the study are discussed, highlighting opportunities for continued investigations and developments in the field.

Development and Characterization of a DTMOSCAP Device

In Section 5.2 of this work, the problem of injection-dependent interface recombination of DT-terminated photodiodes has been addressed. Despite the advantages in terms of crosstalk and overall responsivity compared to other termination concepts, such a device suffers from non-linearity issues. Different approaches to mitigate the problem have been developed and discussed, where the concept of a deep-trench metal-oxide-semiconductor capacitor (DTMOSCAP) by making electrical contact to the poly-silicon filling the trench appears to be the most feasible and reliable. In this work, the effectiveness of such a structure and its ability to control and passivate the critical interface was demonstrated by means of TCAD simulations. A next step, is to put such a device into real silicon and further prove its applicability. The suggested device is also an interesting candidate to perform further DLTS studies, since with a gate bias the energetic levels of defect and reservoir can be shifted against each other allowing to further explore the defect landscape.

Extending the Defect Study to Novel Materials

Within this work, electrical defect characterization of silicon based opto-electronic devices was discussed, explained and explored by means of measurements and simulations. However, while silicon is the most utilized material for light sensing and harvesting it can not cover and fulfill the requirements for all optoelectronic applications. Therefore, the utilization of novel materials and approaches for certain applications, such as IR sensing, has been established. The methods and framework for electrical defect characterization, as discussed in this work, can be extended to such novel materials, keeping in mind, that a higher amount of defects can be expected because of less-mature processing techniques concerning materials other than silicon. Additionally, the manifestation of defects on the performance of devices relying on other groundlaying physical principles, such as quantum dot-based light detectors, is expected to be different which further motivates defect-related studies on novel or exotic materials and devices.

References

[1] Jose Luis Santos and Faramarz Farahi, eds. *Handbook of optical sensors*. Optical science and engineering. Literaturverzeichnis: Seite 679-683. Boca Raton, 2017. 699 pp. ISBN: 9781439866856.

[2] Edmond Becquerel. “On electric effects under the influence of solar radiation”. In: *Compt. Rend.* 9 (1839), p. 561.

[3] Willoughby Smith. “Effect of light on selenium”. In: *Nature* 7 (1873), p. 303.

[4] A. Einstein. “Über die von der molekularkinetischen Theorie der Waerme geforderte Bewegung von in ruhenden Fluessigkeiten suspendierten Teilchen”. In: *Annalen der Physik* 322.8 (1905), pp. 549–560. DOI: `10.1002/andp.19053220806`.

[5] Joseph Slepian. “Hot Cathode Tube”. United States Patent US1450265A. Mar. 1923.

[6] Byung Jun Park et al. “Deep trench isolation for crosstalk suppression in active pixel sensors with 1.7 µm pixel pitch”. In: *Japanese Journal of Applied Physics* 46.4B (Apr. 2007), pp. 2454–2457. DOI: `10.1143/jjap.46.2454`.

[7] Silvano Donati. *Photodetectors: devices, circuits, and applications*. Vol. 12. 5. May 2001, p. 653. DOI: `10.1088/0957-0233/12/5/703`.

[8] George E. Smith. “The invention and early history of the CCD”. In: *Nuclear Instruments and Methods in Physics Research Section A: Accelerators, Spectrometers, Detectors and Associated Equipment* 607.1 (Aug. 2009), pp. 1–6. DOI: `10.1016/j.nima.2009.03.233`.

[9] E. R. Fossum. “CMOS image sensors: electronic camera-on-a-chip”. In: *IEEE Transactions on Electron Devices* 44.10 (1997), pp. 1689–1698. DOI: `10.1109/16.628824`.

[10] M. Bigas et al. “Review of CMOS image sensors”. In: *Microelectronics Journal* 37.5 (May 2006), pp. 433–451. DOI: `10.1016/j.mejo.2005.07.002`.

[11] Eric R. Fossum. “The Invention and Development of CMOS Image Sensors”. In: *75th Anniversary of the Transistor*. John Wiley & Sons, Ltd, 2023. Chap. 23, pp. 281–291. ISBN: 9781394202478. DOI: `https://doi.org/10.1002/9781394202478.ch23`.

[12] J. C. Campbell et al. "Recent advances in avalanche photodiodes". In: *IEEE Journal of Selected Topics in Quantum Electronics* 10.4 (July 2004), pp. 777–787. DOI: `10.1109/jstqe.2004.833971`.

[13] F. Zappa et al. "Principles and features of single-photon avalanche diode arrays". In: *Sensors and Actuators A: Physical* 140.1 (Oct. 2007), pp. 103–112. DOI: `10.1016/j.sna.2007.06.021`.

[14] K. I. Khomiakova, A. P. Kokhanenko, and A. V. Losev. "Investigation of the parameters of a single photon detector for quantum communication". In: *Journal of Physics: Conference Series* 2140.1 (Dec. 2021), p. 012030. DOI: `10.1088/1742-6596/2140/1/012030`.

[15] M. Yokoyama et al. "Application of Hamamatsu MPPCs to T2K neutrino detectors". In: *Nuclear Instruments and Methods in Physics Research Section A: Accelerators, Spectrometers, Detectors and Associated Equipment* 610.1 (Oct. 2009), pp. 128–130. DOI: `10.1016/j.nima.2009.05.077`.

[16] Wei Shen and H.-. C. Schultz-Coulon. "STIC - A current mode constant fraction discriminator for positron emission tomography using SiPM (MPPC)". In: *2009 IEEE Nuclear Science Symposium Conference Record (NSS/MIC)*. IEEE, Oct. 2009. DOI: `10.1109/nssmic.2009.5401693`.

[17] Adrienne D. Stiff-Roberts. "Quantum-dot infrared photodetectors: a review". In: *Journal of Nanophotonics* 3.1 (2009), p. 031607. DOI: `10.1117/1.3125802`.

[18] Papichaya Chaisakul et al. "Recent progress on Ge/SiGe quantum well optical modulators, detectors, and emitters for optical interconnects". In: *Photonics* 6.1 (Mar. 2019), p. 24. DOI: `10.3390/photonics6010024`.

[19] Cesare Soci et al. "Nanowire photodetectors". In: *Journal of Nanoscience and Nanotechnology* 10.3 (Mar. 2010), pp. 1430–1449. DOI: `10.1166/jnn.2010.2157`.

[20] Alexandre Delga. "Quantum cascade detectors: A review". In: *Mid-infrared Optoelectronics*. Elsevier, 2020, pp. 337–377. DOI: `10.1016/b978-0-08-102709-7.00008-5`.

[21] Fuwei Zhuge et al. "Nanostructured materials and architectures for advanced infrared photodetection". In: *Advanced Materials Technologies* 2.8 (May 2017), p. 1700005. DOI: `10.1002/admt.201700005`.

[22] A. Rogalski. "History of infrared detectors". In: *Opto-Electronics Review* 20.3 (Jan. 2012). DOI: `10.2478/s11772-012-0037-7`.

[23] Liwen Sang, Meiyong Liao, and Masatomo Sumiya. "A comprehensive review of semiconductor ultraviolet photodetectors: from thin film to one-dimensional nanostructures". In: *Sensors* 13.8 (Aug. 2013), pp. 10482–10518. DOI: `10.3390/s130810482`.

[24] Hongyu Chen et al. "New concept ultraviolet photodetectors". In: *Materials Today* 18.9 (Nov. 2015), pp. 493–502. DOI: `10.1016/j.mattod.2015.06.001`.

[25] Massimo Rudan, Rossella Brunetti, and Susanna Reggiani, eds. *Springer handbook of semiconductor devices*. 1st ed. 2023. Springer Handbooks. Cham: Imprint: Springer, 2023. ISBN: 9783030798277.

[26] Hans J. Queisser and Eugene E. Haller. “Defects in semiconductors: some fatal, some vital”. In: *Science* 281.5379 (Aug. 1998), pp. 945–950. DOI: `10.1126/science.281.5379.945`.

[27] S. M. Hu. “Nonequilibrium point defects and diffusion in silicon”. In: *Materials Science and Engineering: R: Reports* 13.3-4 (Oct. 1994), pp. 105–192. DOI: `10.1016/0927-796x(94)90009-4`.

[28] M. Y. L. Jung et al. “Interstitial charge states in boron-implanted silicon”. In: *Journal of Applied Physics* 97.6 (Mar. 2005). DOI: `10.1063/1.1829787`.

[29] Vilius Palenskis and Kestutis Maknys. “Nature of low-frequency noise in homogeneous semiconductors”. In: *Scientific Reports* 5.1 (Dec. 2015). DOI: `10.1038/srep18305`.

[30] K. Takakura et al. “Radiation defects and degradation of Si photodiodes irradiated by neutrons at low temperature”. In: *Physica B: Condensed Matter* 376-377 (Apr. 2006), pp. 403–406. DOI: `10.1016/j.physb.2005.12.104`.

[31] Tibor Grasser. “Stochastic charge trapping in oxides: From random telegraph noise to bias temperature instabilities”. In: *Microelectronics Reliability* 52.1 (Jan. 2012), pp. 39–70. DOI: `10.1016/j.microrel.2011.09.002`.

[32] Michael Waltl et al. “Impact of single-defects on the variability of CMOS inverter circuits”. In: *Microelectronics Reliability* 126 (Nov. 2021), p. 114275. DOI: `10.1016/j.microrel.2021.114275`.

[33] T. Sinno et al. “Defect engineering of Czochralski single-crystal silicon”. In: *Materials Science and Engineering: R: Reports* 28.5-6 (July 2000), pp. 149–198. DOI: `10.1016/s0927-796x(00)00015-2`.

[34] Lin Shao et al. “Boron diffusion in silicon: the anomalies and control by point defect engineering”. In: *Materials Science and Engineering: R: Reports* 42.3-4 (Nov. 2003), pp. 65–114. DOI: `10.1016/j.mser.2003.08.002`.

[35] W. Shockley and W. T. Read. “Statistics of the recombinations of holes and electrons”. In: *Physical Review* 87.5 (5 Sept. 1952), pp. 835–842. ISSN: 0031-899X. DOI: `10.1103/PhysRev.87.835`.

[36] R. N. Hall. “Electron-hole recombination in germanium”. In: *Physical Review* 87.2 (2 July 1952), p. 387. ISSN: 0031-899X. DOI: `10.1103/PhysRev.87.387`.

[37] H. Jafari and S. A. H. Feghhi. “Analytical modeling for gamma radiation damage on silicon photodiodes”. In: *Nuclear Instruments and Methods in Physics Research Section A: Accelerators, Spectrometers, Detectors and Associated Equipment* 816 (Apr. 2016), pp. 62–69. DOI: `10.1016/j.nima.2016.01.079`.

[38] H. Ohyama et al. "Impact of lattice defects on the performance degradation of Si photodiodes by high-temperature gamma and electron irradiation". In: *Physica B: Condensed Matter* 308-310 (Dec. 2001), pp. 1226–1229. DOI: `10.1016/s0921-4526(01)00949-8`.

[39] Lorenzo Colace, Andrea Scacchi, and Gaetano Assanto. "Noise characterization of Ge/Si photodetectors". In: *8th IEEE International Conference on Group IV Photonics*. IEEE, Sept. 2011. DOI: `10.1109/group4.2011.6053793`.

[40] S. D. Brotherton. "Photocurrent deep level transient spectroscopy in silicon". In: *Journal of Applied Physics* 55.10 (May 1984), pp. 3636–3643. DOI: `10.1063/1.332913`.

[41] Rebekka Eberle et al. "Prediction of local temperature-dependent performance of silicon solar cells". In: *Progress in Photovoltaics: Research and Applications* 27.11 (Apr. 2019), pp. 999–1006. DOI: `10.1002/pip.3130`.

[42] Jason J. Ackert et al. "High-speed detection at two micrometres with monolithic silicon photodiodes". In: *Nature Photonics* 9.6 (May 2015), pp. 393–396. DOI: `10.1038/nphoton.2015.81`.

[43] Dylan F. Logan, Paul E. Jessop, and Andrew P. Knights. "Modeling defect enhanced detection at 1550 nm in integrated silicon waveguide photodetectors". In: *Journal of Lightwave Technology* 27.7 (Apr. 2009), pp. 930–937. DOI: `10.1109/jlt.2008.927752`.

[44] Erik Agrell et al. "Roadmap of optical communications". In: *Journal of Optics* 18.6 (May 2016), p. 063002. DOI: `10.1088/2040-8978/18/6/063002`.

[45] W. Shockley. "The theory of p-n junctions in semiconductors and p-n junction transistors". In: *Bell System Technical Journal* 28.3 (July 1949), pp. 435–489. DOI: `10.1002/j.1538-7305.1949.tb03645.x`.

[46] Chih-tang Sah, Robert N. Noyce, and William Shockley. "Carrier generation and recombination in p-n junctions and p-n junction characteristics". In: *Proceedings of the IRE* 45.9 (Sept. 1957), pp. 1228–1243. DOI: `10.1109/JRPROC.1957.278528`.

[47] Gyuho Myeong et al. "Dirac-source diode with sub-unity ideality factor". In: *Nature Communications* 13.1 (July 2022). ISSN: 2041-1723. DOI: `10.1038/s41467-022-31849-5`.

[48] Zhijiang Wang et al. "Cold source diodes with sub-unity ideality factor and giant negative differential resistance". In: *IEEE Electron Device Letters* 43.12 (Dec. 2022), pp. 2184–2187. DOI: `10.1109/led.2022.3212681`.

[49] Jay M. Shah et al. "Experimental analysis and theoretical model for anomalously high ideality factors ($n \gg 2.0$) in AlGaN/GaN p-n junction diodes". In: *Journal of Applied Physics* 94.4 (July 2003), pp. 2627–2630. DOI: `10.1063/1.1593218`.

[50] Gyeong Won Lee, Jong-In Shim, and Dong-Soo Shin. “On the ideality factor of the radiative recombination current in semiconductor light-emitting diodes”. In: *Applied Physics Letters* 109.3 (July 2016). DOI: 10.1063/1.4959081.

[51] W. Budde. “Multidecade linearity measurements on Si photodiodes”. In: *Applied Optics* 18.10 (May 1979), p. 1555. DOI: 10.1364/ao.18.001555.

[52] W. Budde. “Large-flux-ratio linearity measurements on Si photodiodes”. In: *Applied Optics* 21.20 (Oct. 1982), p. 3699. DOI: 10.1364/ao.21.003699.

[53] J. Prasanth Ram, T. Sudhakar Babu, and N. Rajasekar. “A comprehensive review on solar PV maximum power point tracking techniques”. In: *Renewable and Sustainable Energy Reviews* 67 (Jan. 2017), pp. 826–847. DOI: 10.1016/j.rser.2016.09.076.

[54] M. Singh Tyagi. “Zener and avalanche breakdown in silicon alloyed p-n junctions-I: analysis of reverse characteristics”. In: *Solid-State Electronics* 11.1 (Jan. 1968), pp. 99–115. DOI: 10.1016/0038-1101(68)90141-x.

[55] M. Singh Tyagi. “Zener and avalanche breakdown in silicon alloyed p-n junctions-II: effect of temperature on the reverse characteristics and criteria for distinguishing between the two breakdown mechanisms”. In: *Solid-State Electronics* 11.1 (Jan. 1968), pp. 117–128. DOI: 10.1016/0038-1101(68)90142-1.

[56] S. Cova et al. “Avalanche photodiodes and quenching circuits for single-photon detection”. In: *Applied Optics* 35.12 (Apr. 1996), pp. 1956–1976. DOI: 10.1364/AO.35.001956.

[57] M. Jamal Deen. *Silicon photonics. Fundamentals and devices*. Ed. by P. K. Basu. Wiley series in materials for electronic and optoelectronic applications. Includes bibliographical references and index. - Description based on print version record. Chichester, West Sussex, UK ; Wiley, 2012. 11 pp. ISBN: 1119940907.

[58] P. Dirac. “The quantum theory of the emission and absorption of radiation”. In: *Proceedings of the Royal Society of London. Series A, Containing Papers of a Mathematical and Physical Character* 114.767 (Mar. 1927), pp. 243–265. DOI: 10.1098/rspa.1927.0039.

[59] S. S. Sheinin and C. D. Cann. “A perturbation method for calculating absorption coefficients of degenerate bloch waves in the dynamical theory of electron diffraction”. In: *Physica Status Solidi (b)* 57.1 (May 1973), pp. 315–320. DOI: 10.1002/pssb.2220570131.

[60] B. Jensen. “The quantum mechanical extension of the Boltzmann transport equation and optical absorption in semiconductors”. In: *Annals of Physics* 95.2 (Dec. 1975), pp. 229–266. DOI: 10.1016/0003-4916(75)90056-1.

[61] Chin-Yi Tsai. “Absorption coefficients of silicon: A theoretical treatment”. In: *Journal of Applied Physics* 123.18 (May 2018). DOI: 10.1063/1.5028053.

[62] Chin-Yi Tsai. “Theoretical model for the optical gain coefficient of indirect-band-gap semiconductors”. In: *Journal of Applied Physics* 99.5 (Mar. 2006). DOI: 10.1063/1.2177386.

[63] Christophe Ballif et al. “Status and perspectives of crystalline silicon photovoltaics in research and industry”. In: *Nature Reviews Materials* 7.8 (Mar. 2022), pp. 597–616. DOI: 10.1038/s41578-022-00423-2.

[64] Martin A. Green. “Self-consistent optical parameters of intrinsic silicon at 300K including temperature coefficients”. In: *Solar Energy Materials and Solar Cells* 92.11 (Nov. 2008), pp. 1305–1310. DOI: 10.1016/j.solmat.2008.06.009.

[65] Timothy Nathan Nunley et al. “Optical constants of germanium and thermally grown germanium dioxide from 0.5 to 6.6 eV via a multisample ellipsometry investigation”. In: *Journal of Vacuum Science & Technology B* 34.6 (Sept. 2016). DOI: 10.1116/1.4963075.

[66] Edward D. Palik, ed. *Handbook of optical constants of solids*. Includes bibliographical references. San Diego: Academic Press, 1998. 1804 pp.

[67] R. E. Treharne et al. “Optical design and fabrication of fully sputtered CdTe/CdS solar cells”. In: *Journal of Physics: Conference Series* 286 (Mar. 2011). DOI: 10.1088/1742-6596/286/1/012038.

[68] Konstantinos Papatryfonos et al. “Refractive indices of MBE-grown $\mathrm{Al_xGa_{1-x}As}$ ternary alloys in the transparent wavelength region”. In: *AIP Advances* 11.2 (Feb. 2021). DOI: 10.1063/5.0039631.

[69] Sten Seifert and Patrick Runge. “Revised refractive index and absorption of $\mathrm{In_{1-x}Ga_xAs_yP_{1-y}}$ lattice-matched to InP in transparent and absorption IR-region”. In: *Optical Materials Express* 6.2 (Jan. 2016), p. 629. DOI: 10.1364/ome.6.000629.

[70] C. Tanguy. “Refractive index of direct bandgap semiconductors near the absorption threshold: influence of excitonic effects”. In: *IEEE Journal of Quantum Electronics* 32.10 (1996), pp. 1746–1751. DOI: 10.1109/3.538780.

[71] Adolf Goetzberger, Christopher Hebling, and Hans-Werner Schock. “Photovoltaic materials, history, status and outlook”. In: *Materials Science and Engineering: R: Reports* 40.1 (Jan. 2003), pp. 1–46. DOI: 10.1016/s0927-796x(02)00092-x.

[72] F. Scholze et al. “Determination of the electron–hole pair creation energy for semiconductors from the spectral responsivity of photodiodes”. In: *Nuclear Instruments and Methods in Physics Research Section A: Accelerators, Spectrometers, Detectors and Associated Equipment* 439.2-3 (Jan. 2000), pp. 208–215. DOI: 10.1016/s0168-9002(99)00937-7.

[73] Emil Antoncik. “On the theory of the spectral dependence of the quantum efficiency of homopolar crystals”. In: *Czechoslovak Journal of Physics* 7.6 (Nov. 1957), pp. 674–689. DOI: 10.1007/bf01946591.

[74] Ove Christensen. “Quantum efficiency of the internal photoelectric effect in silicon and germanium”. In: *Journal of Applied Physics* 47.2 (Feb. 1976), pp. 689–695. DOI: 10.1063/1.322635.

[75] M. Garin et al. “Black-silicon ultraviolet photodiodes achieve external quantum efficiency above 130 %”. In: *Physical Review Letters* 125.11 (Sept. 2020), p. 117702. DOI: 10.1103/physrevlett.125.117702.

[76] Kexun Chen et al. “Harnessing carrier multiplication in silicon solar cells using UV photons”. In: *IEEE Photonics Technology Letters* 33.24 (Dec. 2021), pp. 1415–1418. DOI: 10.1109/lpt.2021.3124307.

[77] Krzysztof B. Beć and Christian W. Huck. “Breakthrough potential in near-infrared spectroscopy: spectra simulation. a review of recent developments”. In: *Frontiers in Chemistry* 7 (Feb. 2019). DOI: 10.3389/fchem.2019.00048.

[78] Lei Shi and Stoyan Nihtianov. “Comparative study of silicon-based ultraviolet photodetectors”. In: *IEEE Sensors Journal* 12.7 (July 2012), pp. 2453–2459. DOI: 10.1109/jsen.2012.2192103.

[79] Michael A. Kinch. “The future of infrared; III-Vs or HgCdTe?” In: *Journal of Electronic Materials* 44.9 (Mar. 2015), pp. 2969–2976. DOI: 10.1007/s11664-015-3717-5.

[80] D. Alonso-Alvarez et al. “Solcore: a multi-scale, Python-based library for modelling solar cells and semiconductor materials”. In: *Journal of Computational Electronics* 17.3 (Apr. 2018), pp. 1099–1123. DOI: 10.1007/s10825-018-1171-3.

[81] William Shockley and Hans J. Queisser. “Detailed balance limit of efficiency of p-n junction solar cells”. In: *Journal of Applied Physics* 32.3 (Mar. 1961), pp. 510–519. DOI: 10.1063/1.1736034.

[82] John P. Dakin. *Handbook of optoelectronics. Concepts, Devices, and Techniques (Volume One)*. Ed. by Robert Brown. 2nd ed. Series in Optics and Optoelectronics. Boca Raton, FL: CRC Press, 2017. 1 p. ISBN: 1482241781.

[83] Alexander O. Goushcha and Bernd Tabbert. “On response time of semiconductor photodiodes”. In: *Optical Engineering* 56.09 (Sept. 2017), p. 1. DOI: 10.1117/1.oe.56.9.097101.

[84] Jasprit Singh. *Semiconductor optoelectronics. Physics and technology*. McGraw Hill series in electrical and computing engineering. Literaturangaben. New York, NY [u.a.]: McGraw-Hill, 1995. 725 pp. ISBN: 0070576378.

[85] F. N. Hooge. “1/f noise sources”. In: *IEEE Transactions on Electron Devices* 41.11 (1994), pp. 1926–1935. DOI: 10.1109/16.333808.

[86] R. Clark Jones. “Proposal of the detectivity D* for detectors limited by radiation noise”. In: *Journal of the Optical Society of America* 50.11 (Nov. 1960), p. 1058. DOI: 10.1364/josa.50.001058.

[87] Behrooz Nakhkoob, Sagar Ray, and Mona M. Hella. "High speed photodiodes in standard nanometer scale CMOS technology: a comparative study". In: *Optics Express* 20.10 (May 2012), p. 11256. DOI: 10.1364/oe.20.011256.

[88] Werner Bergholz. "Defect engineering in silicon materials". In: *Defects and Impurities in Silicon Materials*. Springer Japan, 2015, pp. 431–487. DOI: 10.1007/978-4-431-55800-2_9.

[89] Koichi Momma and Fujio Izumi. "VESTA 3 for three-dimensional visualization of crystal, volumetric and morphology data". In: *Journal of Applied Crystallography* 44.6 (Oct. 2011), pp. 1272–1276. DOI: 10.1107/s0021889811038970.

[90] Charles Kittel. *Introduction to solid state physics*. 8. ed., [repr.] Hoboken, NJ: Wiley, 2013. 680 pp. ISBN: 9780471415268.

[91] J. Frenkel. "Über die Wärmebewegung in festen und flüssigen Körpern". In: *Zeitschrift für Physik* 35.8-9 (Aug. 1926), pp. 652–669. DOI: 10.1007/bf01379812.

[92] J. L. Benton and L. C. Kimerling. "Capacitance transient spectroscopy of trace contamination in silicon". In: *Journal of The Electrochemical Society* 129.9 (Sept. 1982), pp. 2098–2102. DOI: 10.1149/1.2124387.

[93] Klaus Graff. *Metal impurities in silicon-device fabrication*. Second, revised edition. Springer Series in Materials Science 24. Includes bibliographical references and index. Description based on print version record. Berlin, [Germany] ; Springer, 2000. 1284 pp. ISBN: 9783642571213.

[94] Eddy Simoen Claeys Cor. *Metal impurities in silicon- and germanium-based technologies. Origin, Characterization, Control, and Device Impact*. Springer Series in Materials Science Ser. v.270. Description based on publisher supplied metadata and other sources. Cham: Springer International Publishing AG, 2018. 1464 pp. ISBN: 9783319939254.

[95] V. V. Lukjanitsa. "Energy levels of vacancies and interstitial atoms in the band gap of silicon". In: *Semiconductors* 37.4 (Apr. 2003), pp. 404–413. DOI: 10.1134/1.1568459.

[96] Michael Sluydts et al. "High-throughput screening of extrinsic point defect properties in Si and Ge: database and applications". In: *Chemistry of Materials* 29.3 (Dec. 2016), pp. 975–984. DOI: 10.1021/acs.chemmater.6b03368.

[97] Danny Broberg et al. "High-throughput calculations of charged point defect properties with semi-local density functional theory-performance benchmarks for materials screening applications". In: *npj Computational Materials* 9.1 (May 2023). DOI: 10.1038/s41524-023-01015-6.

[98] W.-K. Leung et al. "Calculations of silicon self-interstitial defects". In: *Physical Review Letters* 83.12 (Sept. 1999), pp. 2351–2354. DOI: 10.1103/physrevlett.83.2351.

[99] Martin Kittler and Manfred Reiche. *Structure and properties of dislocations in silicon*. InTech, July 2011. DOI: 10.5772/22902.

[100] W. T. Read. “XVI. Scattering of electrons by charged dislocations in semiconductors”. In: *The London, Edinburgh, and Dublin Philosophical Magazine and Journal of Science* 46.373 (Feb. 1955), pp. 111–131. DOI: `10.1080/14786440208520556`.

[101] L. C. Kimerling and J. R. Patel. “Defect states associated with dislocations in silicon”. In: *Applied Physics Letters* 34.1 (Jan. 1979), pp. 73–75. DOI: `10.1063/1.90563`.

[102] T. Uchino, M. Takahashi, and T. Yoko. “E' centers in amorphous SiO_2 revisited: a new look at an old problem”. In: *Physical Review Letters* 86.24 (June 2001), pp. 5522–5525. DOI: `10.1103/physrevlett.86.5522`.

[103] Benedikt Ziebarth et al. “Interstitial iron impurities at cores of dissociated dislocations in silicon”. In: *Physical Review B* 92.19 (Nov. 2015), p. 195308. DOI: `10.1103/physrevb.92.195308`.

[104] Ichiro Yonenaga. *Defects in crystalline silicon: dislocations*. Springer Berlin Heidelberg, 2019, pp. 541–588. DOI: `10.1007/978-3-662-56472-1_24`.

[105] F. J. Grunthaner and P. J. Grunthaner. “Chemical and electronic structure of the SiO_2/Si interface”. In: *Materials Science Reports* 1.2 (Jan. 1986), pp. 65–160. DOI: `10.1016/s0920-2307(86)80001-9`.

[106] W. Füssel et al. “Defects at the Si/SiO_2 interface: their nature and behaviour in technological processes and stress”. In: *Nuclear Instruments and Methods in Physics Research Section A: Accelerators, Spectrometers, Detectors and Associated Equipment* 377.2-3 (Aug. 1996), pp. 177–183. DOI: `10.1016/0168-9002(96)00205-7`.

[107] Arthur H. Edwards. “Interaction of H and H_2 with the silicon dangling orbital at the $\langle 1\,1\,1 \rangle$ Si/SiO_2 interface”. In: *Physical Review B* 44.4 (July 1991), pp. 1832–1838. DOI: `10.1103/physrevb.44.1832`.

[108] P. Ugliengo et al. “Realistic models of hydroxylated amorphous silica surfaces and MCM-41 mesoporous material simulated by large-scale periodic b3lyp calculations”. In: *Advanced Materials* 20.23 (Dec. 2008), pp. 4579–4583. DOI: `10.1002/adma.200801489`.

[109] W. Goes et al. “Charging and discharging of oxide defects in reliability issues”. In: *IEEE Transactions on Device and Materials Reliability* 8.3 (Sept. 2008), pp. 491–500. DOI: `10.1109/tdmr.2008.2005247`.

[110] Pei Li, Yu Song, and Xu Zuo. “Computational Study on Interfaces and Interface Defects of Amorphous Silica and Silicon”. In: *physica status solidi (RRL) - Rapid Research Letters* 13.3 (Jan. 2019). DOI: `10.1002/pssr.201800547`.

[111] Stanislav Tyaginov and Tibor Grasser. “Modeling of hot-carrier degradation: Physics and controversial issues”. In: *2012 IEEE International Integrated Reliability Workshop*. IEEE, Oct. 2012. DOI: `10.1109/iirw.2012.6468962`.

[112] Markus Jech et al. “Ab initio treatment of silicon-hydrogen bond rupture at Si / SiO_2 interfaces”. In: *Physical Review B* 100.19 (Nov. 2019), p. 195302. DOI: `10.1103/physrevb.100.195302`.

[113] Alexander Shluger. “Defects in oxides in electronic devices”. In: *Handbook of Materials Modeling*. Springer International Publishing, Oct. 2018, pp. 1–22. DOI: `10.1007/978-3-319-50257-1_79-1`.

[114] Chih-Tang Sah. *Fundamentals of solid-state electronics*. 1st ed. Singapore: World Scientific, 2006. 1010 pp. ISBN: 9810206372.

[115] K. Xerxes Steirer et al. “Defect tolerance in methylammonium lead triiodide perovskite”. In: *ACS Energy Letters* 1.2 (July 2016), pp. 360–366. DOI: `10.1021/acsenergylett.6b00196`.

[116] Helmut Feichtinger. “Deep centers in semiconductors”. In: *Handbook of Semiconductor Technology*. John Wiley & Sons, Ltd, 2000. Chap. 4, pp. 167–229. ISBN: 9783527621842. DOI: `10.1002/9783527621842.ch4`.

[117] H. G. Grimmeiss. “Deep level impurities in semiconductors”. In: *Annual Review of Materials Science* 7.1 (Aug. 1977), pp. 341–376. DOI: `10.1146/annurev.ms.07.080177.002013`.

[118] Yong Zhang. “Electronic structures of impurities and point defects in semiconductors”. In: *Chinese Physics B* 27.11 (Nov. 2018), p. 117103. DOI: `10.1088/1674-1056/27/11/117103`.

[119] C. H. Henry and D. V. Lang. “Nonradiative capture and recombination by multiphonon emission in GaAs and GaP”. In: *Physical Review B* 15.2 (Jan. 1977), pp. 989–1016. DOI: `10.1103/physrevb.15.989`.

[120] J. W. Chen and A. G. Milnes. “Energy levels in silicon”. In: *Annual Review of Materials Science* 10.1 (Aug. 1980), pp. 157–228. DOI: `10.1146/annurev.ms.10.080180.001105`.

[121] Audrius Alkauskas, Qimin Yan, and Chris G. Van de Walle. “First-principles theory of nonradiative carrier capture via multiphonon emission”. In: *Physical Review B* 90.7 (Aug. 2014), p. 075202. DOI: `10.1103/physrevb.90.075202`.

[122] J. G. Simmons and G. W. Taylor. “Nonequilibrium Steady-State Statistics and Associated Effects for Insulators and Semiconductors Containing an Arbitrary Distribution of Traps”. In: *Physical Review B* 4.2 (July 1971), pp. 502–511. DOI: `10.1103/physrevb.4.502`.

[123] Alessandro Inglese et al. “Recombination activity of light-activated copper defects in p-type silicon studied by injection- and temperature-dependent lifetime spectroscopy”. In: *Journal of Applied Physics* 120.12 (Sept. 2016). DOI: `10.1063/1.4963121`.

[124] Armin G. Aberle. *Crystalline silicon solar cells: Advanced surface passivation and analysis*. Reprinted. Sydney: Centre for Photovoltaic Enginering, Univ. of NSW, 2004. ISBN: 9780733406454.

[125] P. Spirito and A. Sanseverino. "Determination of energy levels of recombination centers in low-doped Si layers by temperature dependence of recombination lifetime". In: *Solid-State Electronics* 37.7 (July 1994), pp. 1429–1436. DOI: 10.1016/0038-1101(94)90202-x.

[126] Ken Yamaguchi, Takuhito Kuwabara, and Tsuyoshi Uda. "A generation/recombination model assisted with two trap centers in wide band-gap semiconductors". In: *Journal of Applied Physics* 113.10 (Mar. 2013). DOI: 10.1063/1.4795114.

[127] Donald T. Stevenson and Robert J. Keyes. "Measurements of the recombination velocity at germanium surfaces". In: *Physica* 20.7-12 (Jan. 1954), pp. 1041–1046. DOI: 10.1016/s0031-8914(54)80229-1.

[128] Walter H. Brattain and John Bardeen. "Surface Properties of Germanium". In: *Bell System Technical Journal* 32.1 (Jan. 1953), pp. 1–41. DOI: 10.1002/j.1538-7305.1953.tb01420.x.

[129] Armin G. Aberle. "Surface passivation of crystalline silicon solar cells: a review". In: *Progress in Photovoltaics: Research and Applications* 8.5 (2000), pp. 473–487. ISSN: 1099-159X. DOI: 10.1002/1099-159x(200009/10)8:5<473::aid-pip337>3.0.co;2-d.

[130] G. J. Rees. "Surface recombination velocity- A useful concept?" In: *Solid-State Electronics* 28.5 (May 1985), pp. 517–519. ISSN: 0038-1101. DOI: 10.1016/0038-1101(85)90116-9.

[131] Keith R. McIntosh and Lachlan E. Black. "On effective surface recombination parameters". In: *Journal of Applied Physics* 116.1 (July 2014). ISSN: 1089-7550. DOI: 10.1063/1.4886595.

[132] Kun Huang and Avril Rhys. "Theory of light absorption and non-radiative transitions in F-centres". In: *Proceedings of the Royal Society of London. Series A, Mathematical and Physical Sciences* 204.1078 (1950), pp. 406–423. ISSN: 00804630.

[133] Hermann Gummel and Melvin Lax. "Thermal capture of electrons in silicon". In: *Annals of Physics* 2.1 (July 1957), pp. 28–56. ISSN: 0003-4916. DOI: 10.1016/0003-4916(57)90034-9.

[134] M. Schulz and N. M. Johnson. "Evidence for multiphonon emission from interface states in MOS structures". In: *Solid State Communications* 25.7 (Feb. 1978), pp. 481–484. ISSN: 0038-1098. DOI: 10.1016/0038-1098(78)90162-x.

[135] Michael Waltl. "Reliability of miniaturized transistors from the perspective of single-defects". In: *Micromachines* 11.8 (July 2020), p. 736. ISSN: 2072-666X. DOI: 10.3390/mi11080736.

[136] Dominic Waldhoer et al. "Comphy v3.0-A compact-physics framework for modeling charge trapping related reliability phenomena in MOS devices". In: *Microelectronics Reliability* 146 (July 2023), p. 115004. ISSN: 0026-2714. DOI: 10.1016/j.microrel.2023.115004.

[137] M. Born and R. Oppenheimer. “Zur Quantentheorie der Molekeln”. In: *Annalen der Physik* 389.20 (Jan. 1927), pp. 457–484. ISSN: 1521-3889. DOI: `10.1002/andp.19273892002`.

[138] S. M. Sze. *Physics of semiconductor devices*. Ed. by Yiming Li and Kwok Kwok Ng. Fourth edition. Hoboken, NJ: Wiley, 2021. ISBN: 9781119429111.

[139] Donald L. Chubb. *Fundamentals of thermophotovoltaic energy conversion*. Description based on publisher supplied metadata and other sources. Oxford: Elsevier Science & Technology, 2007. 1532 pp. ISBN: 9780080560687.

[140] McColgin et al. “Dark current quantization in CCD image sensors”. In: *International Technical Digest on Electron Devices Meeting*. IEEE, 1992. DOI: `10.1109/iedm.1992.307321`.

[141] Wolfram Research Inc. *Mathematica, Version 13.0*. Champaign, IL, 2023.

[142] Gian Franco Dalla Betta. *Advances in photodiodes*. Rijeka: IntechOpen, Mar. 2011. ISBN: 9789533071633. DOI: `10.5772/588`.

[143] A. Van Der Ziel. “On the noise spectra of semi-conductor noise and of flicker effect”. In: *Physica* 16.4 (Apr. 1950), pp. 359–372. ISSN: 0031-8914. DOI: `10.1016/0031-8914(50)90078-4`.

[144] N. Mainzer, E. Lakin, and E. Zolotoyabko. “Point-defect influence on 1/f noise in HgCdTe photodiodes”. In: *Applied Physics Letters* 81.4 (July 2002), pp. 763–765. ISSN: 1077-3118. DOI: `10.1063/1.1494118`.

[145] R. E. Burgess. “The statistics of charge carrier fluctuations in semiconductors”. In: *Proceedings of the Physical Society. Section B* 69.10 (Oct. 1956), pp. 1020–1027. ISSN: 0370-1301. DOI: `10.1088/0370-1301/69/10/308`.

[146] T. G. M. Kleinpenning. “Noise in p-n diodes”. In: *Physica B+C* 98.4 (Mar. 1980), pp. 289–299. ISSN: 0378-4363. DOI: `10.1016/0378-4363(80)90045-5`.

[147] Xinyang Wang et al. “A CMOS image sensor with a buried-channel source follower”. In: *2008 IEEE International Solid-State Circuits Conference - Digest of Technical Papers*. IEEE, Feb. 2008. DOI: `10.1109/isscc.2008.4523057`.

[148] Bernhard Stampfer et al. “Semi-automated extraction of the distribution of single defects for NMOS transistors”. In: *Micromachines* 11.4 (Apr. 2020), p. 446. ISSN: 2072-666X. DOI: `10.3390/mi11040446`.

[149] A. Schenk. “A model for the field and temperature dependence of Shockley-Read-Hall lifetimes in silicon”. In: *Solid-State Electronics* 35.11 (Nov. 1992), pp. 1585–1596. DOI: `10.1016/0038-1101(92)90184-e`.

[150] D. V. Lang. “Deep-level transient spectroscopy: A new method to characterize traps in semiconductors”. In: *Journal of Applied Physics* 45.7 (July 1974), pp. 3023–3032. DOI: `10.1063/1.1663719`.

[151] Jan Schmidt. "Temperature- and injection-dependent lifetime spectroscopy for the characterization of defect centers in semiconductors". In: *Applied Physics Letters* 82.13 (Mar. 2003), pp. 2178–2180. ISSN: 1077-3118. DOI: 10.1063/1.1563830.

[152] Jon Geist. "Silicon photodiode front region collection efficiency models". In: *Journal of Applied Physics* 51.7 (July 1980), pp. 3993–3995. DOI: 10.1063/1.328186.

[153] A. Augusto et al. "Exploring the practical efficiency limit of silicon solar cells using thin solar-grade substrates". In: *Journal of Materials Chemistry A* 8.32 (2020), pp. 16599–16608. DOI: 10.1039/d0ta04575f.

[154] D. K. Schroder. "Carrier lifetimes in silicon". In: *IEEE Transactions on Electron Devices* 44.1 (Jan. 1997), pp. 160–170. ISSN: 0018-9383. DOI: 10.1109/16.554806.

[155] Dieter K. Schroder. *Semiconductor material and device characterization*. Third edition. [Piscataway, NJ]: IEEE Press, 2006. 1779 pp. ISBN: 9780471749097.

[156] D. K. Schroder. "The concept of generation and recombination lifetimes in semiconductors". In: *IEEE Transactions on Electron Devices* 29.8 (Aug. 1982), pp. 1336–1338. ISSN: 0018-9383. DOI: 10.1109/T-ED.1982.20879.

[157] A. Lemaire et al. "Open-circuit voltage decay simulations on silicon and gallium arsenide p-n homojunctions: design influences on bulk lifetime extraction". In: *Microelectronics Journal* 101 (July 2020), p. 104735. DOI: 10.1016/j.mejo.2020.104735.

[158] Yan Zhu and Ziv Hameiri. "Review of injection dependent charge carrier lifetime spectroscopy". In: *Progress in Energy* 3.1 (Jan. 2021), p. 012001. ISSN: 2516-1083. DOI: 10.1088/2516-1083/abd488.

[159] H. Schlangenotto, H. Maeder, and W. Gerlach. "Temperature dependence of the radiative recombination coefficient in silicon". In: *Physica Status Solidi (a)* 21.1 (Jan. 1974), pp. 357–367. ISSN: 1521-396X. DOI: 10.1002/pssa.2210210140.

[160] J. Dziewior and W. Schmid. "Auger coefficients for highly doped and highly excited silicon". In: *Applied Physics Letters* 31.5 (Sept. 1977), pp. 346–348. ISSN: 0003-6951. DOI: 10.1063/1.89694.

[161] Sheng S. Li. *Semiconductor physical electronics*. 2nd ed. Description based on publisher supplied metadata and other sources. New York, NY: Springer New York, 2006. 1708 pp. ISBN: 9780387377667.

[162] Emmanouil Kioupakis et al. "Temperature and carrier-density dependence of Auger and radiative recombination in nitride optoelectronic devices". In: *New Journal of Physics* 15.12 (Dec. 2013), p. 125006. ISSN: 1367-2630. DOI: 10.1088/1367-2630/15/12/125006.

[163] P. T. Landsberg. "Trap-Auger recombination in silicon of low carrier densities". In: *Applied Physics Letters* 50.12 (Mar. 1987), pp. 745–747. ISSN: 1077-3118. DOI: 10.1063/1.98086.

[164] A. Hangleiter and R. Häcker. “Enhancement of band-to-band Auger recombination by electron-hole correlations”. In: *Physical Review Letters* 65.2 (July 1990), pp. 215–218. ISSN: 0031-9007. DOI: `10.1103/physrevlett.65.215`.

[165] Armin Richter et al. “Improved quantitative description of Auger recombination in crystalline silicon”. In: *Physical Review B* 86.16 (Oct. 2012), p. 165202. DOI: `10.1103/physrevb.86.165202`.

[166] T. Trupke et al. “Temperature dependence of the radiative recombination coefficient of intrinsic crystalline silicon”. In: *Journal of Applied Physics* 94.8 (Sept. 2003), p. 4930. ISSN: 0021-8979. DOI: `10.1063/1.1610231`.

[167] J. E. Park et al. “Silicon epitaxial layer lifetime characterization”. In: *Journal of The Electrochemical Society* 148.8 (2001), G411. DOI: `10.1149/1.1380257`.

[168] D. K. Schroder et al. “Silicon epitaxial layer recombination and generation lifetime characterization”. In: *IEEE Transactions on Electron Devices* 50.4 (Apr. 2003), pp. 906–912. ISSN: 0018-9383. DOI: `10.1109/TED.2003.812488`.

[169] John P. MacKelvey. *Solid state and semiconductor physics*. Repr. Ed. , 6. Dr. Malabar, Florida: Robert E. Krieger, 1986. 512 pp. ISBN: 0898743966.

[170] Keung L. Luke and Li-Jen Cheng. “Analysis of the interaction of a laser pulse with a silicon wafer: Determination of bulk lifetime and surface recombination velocity”. In: *Journal of Applied Physics* 61.6 (Mar. 1987), pp. 2282–2293. ISSN: 1089-7550. DOI: `10.1063/1.337938`.

[171] Yoh-Ichiro Ogita. “Bulk lifetime and surface recombination velocity measurement method in semiconductor wafers”. In: *Journal of Applied Physics* 79.9 (May 1996), pp. 6954–6960. DOI: `10.1063/1.361459`.

[172] Johannes Giesecke. *Quantitative recombination and transport properties in silicon from dynamic luminescence*. 1st ed. Springer Theses Ser. Description based on publisher supplied metadata and other sources. Cham: Springer International Publishing AG, 2014. 1296 pp. ISBN: 9783319061573.

[173] Robert Kingston. “Switching time in junction diodes and junction transistors”. In: *Proceedings of the IRE* 42.5 (May 1954), pp. 829–834. DOI: `10.1109/jrproc.1954.274521`.

[174] E. M. Pell. “Recombination rate in germanium by observation of pulsed reverse characteristic”. In: *Physical Review* 90.2 (Apr. 1953), pp. 278–279. DOI: `10.1103/physrev.90.278`.

[175] Benjamin Lax and S. F. Neustadter. “Transient response of a p-n junction”. In: *Journal of Applied Physics* 25.9 (Sept. 1954), pp. 1148–1154. DOI: `10.1063/1.1721830`.

[176] B. R. Gossick. “On the transient behavior of semiconductor rectifiers”. In: *Journal of Applied Physics* 26.11 (Nov. 1955), pp. 1356–1365. ISSN: 0021-8979. DOI: `10.1063/1.1721908`.

[177] S. Lederhandler and L. Giacoletto. “Measurement of minority carrier lifetime and surface effects in junction devices”. In: *Proceedings of the IRE* 43.4 (1955), pp. 477–483. DOI: 10.1109/jrproc.1955.277857.

[178] J. Mueller and B. Schiek. “Transient responses of a pulsed MIS-capacitor”. In: *Solid-State Electronics* 13.10 (Oct. 1970), pp. 1319–1332. DOI: 10.1016/0038-1101(70)90166-8.

[179] F. P. Heiman. “On the determination of minority carrier lifetime from the transient response of an MOS capacitor”. In: *IEEE Transactions on Electron Devices* 14.11 (1967), pp. 781–784. ISSN: 0018-9383. DOI: 10.1109/T-ED.1967.16107.

[180] D. K. Schroder, J. D. Whitfield, and C. J. Varker. “Recombination lifetime using the pulsed MOS capacitor”. In: *IEEE Transactions on Electron Devices* 31.4 (1984), pp. 462–467. ISSN: 0018-9383. DOI: 10.1109/T-ED.1984.21551.

[181] Donald T. Stevenson and Robert J. Keyes. “Measurement of carrier lifetimes in germanium and silicon”. In: *Journal of Applied Physics* 26.2 (Feb. 1955), pp. 190–195. DOI: 10.1063/1.1721958.

[182] A. Poyai et al. “Extraction of the carrier generation and recombination lifetime from the forward characteristics of advanced diodes”. In: *Materials Science and Engineering: B* 102.1-3 (Sept. 2003), pp. 189–192. DOI: 10.1016/s0921-5107(02)00654-2.

[183] Yoshio Murakami, Hidenobu Abe, and Takayuki Shingyouji Takayuki Shingyouji. “Calculation of diffusion component of leakage current in pn junctions formed in various types of silicon wafers (intrinsic gettering, epitaxial, silicon on insulator)”. In: *Japanese Journal of Applied Physics* 34.3R (Mar. 1995), p. 1477. DOI: 10.1143/jjap.34.1477.

[184] C. Y. Kwok. “Space charge and injection capacitances of p-n junctions from small signal numerical solutions”. In: *Journal of Physics D: Applied Physics* 16.12 (Dec. 1983), pp. L263–L267. DOI: 10.1088/0022-3727/16/12/005.

[185] Yoshio Murakami and Takayuki Shingyouji. “Separation and analysis of diffusion and generation components of pn junction leakage current in various silicon wafers”. In: *Journal of Applied Physics* 75.7 (Apr. 1994), pp. 3548–3552. ISSN: 0021-8979. DOI: 10.1063/1.356091.

[186] E. Simoen et al. “Accurate extraction of the diffusion current in silicon p-n junction diodes”. In: *Applied Physics Letters* 72.9 (1998), pp. 1054–1056. ISSN: 0003-6951. DOI: 10.1063/1.120962.

[187] P. U. Calzolari and S. Graffi. “A theoretical investigation on the generation current in silicon p-n junctions under reverse bias”. In: *Solid-State Electronics* 15.9 (Sept. 1972), pp. 1003–1011. DOI: 10.1016/0038-1101(72)90143-8.

[188] C. Cane et al. “An easy technique for determining diffusion and generation-recombination components of the current of pn junctions for better modelling”. In: *ICMTS 93 Proceedings of the 1993 International Conference on Microelectronic Test Structures*. 1993, pp. 167–170. DOI: `10.1109/ICMTS.1993.292926`.

[189] A. Czerwinski et al. “Impact of the generation width on the lifetime extraction in Cz silicon p-n junctions”. In: *Proceedings of the 3rd International Symposium on Defects in Silicon* 99.1 (1999), pp. 88–99. ISSN: 1-56677-223-0.

[190] Donald A. Neamen. *Semiconductor physics and devices: basic principles*. Third. New York: McGraw-Hill, 2003. Chap. 8, pp. 297–305. ISBN: 0-07-232107-5.

[191] Takuya Maeda et al. “Shockley–Read–Hall lifetime in homoepitaxial p-GaN extracted from recombination current in GaN p-n+ junction diodes”. In: *Japanese Journal of Applied Physics* 58.SC (May 2019). DOI: `10.7567/1347-4065/ab07ad`.

[192] S. C. Choo. “On space-charge recombination in pn junctions”. In: *Solid-State Electronics* 39.2 (Feb. 1996), pp. 308–310. DOI: `10.1016/0038-1101(95)00139-5`.

[193] Richard Corkish and Martin A. Green. “Junction recombination current in abrupt junction diodes under forward bias”. In: *Journal of Applied Physics* 80.5 (Sept. 1996), pp. 3083–3090. DOI: `10.1063/1.363168`.

[194] J. Vanhellemont, E. Simoen, and C. Claeys. “Extraction of the minority carrier recombination lifetime from forward diode characteristics”. In: *Applied Physics Letters* 66.21 (1995), pp. 2894–2896. ISSN: 0003-6951. DOI: `10.1063/1.113465`.

[195] Mario El-Tahchi et al. “Degradation of the diode ideality factor of silicon n-p junctions”. In: *Solar Energy Materials and Solar Cells* 62.4 (June 2000), pp. 393–398. DOI: `10.1016/S0927-0248(99)00171-3`.

[196] Yurii Nosov. *Switching in semiconductor diodes*. First. Vol. 13. Boston, MA: Springer US, 1995. Chap. Planar Diode with a Thin Base, pp. 125–127. ISBN: 978-1-4684-8193-8. DOI: `10.1007/978-1-4684-8193-8`.

[197] Martin A. Green. “Minority carrier lifetimes using compensated differental open circuit voltage decay”. In: *Solid-State Electronics* 26.11 (Nov. 1983), pp. 1117–1122. DOI: `10.1016/0038-1101(83)90011-4`.

[198] Salvatore Bellone et al. “An analytical model of an OCVD-based measurement technique of the local carrier lifetime”. In: *IEEE Transactions on Electron Devices* 54.11 (Nov. 2007), pp. 2998–3006. DOI: `10.1109/ted.2007.907162`.

[199] H. J. Kuno. “Analysis and characterization of P-N junction diode switching”. In: *IEEE Transactions on Electron Devices* 11.1 (Jan. 1964), pp. 8–14. DOI: `10.1109/ted.1964.15272`.

[200] J. Moll, S. Krakauer, and R. Shen. “P-N junction charge-storage diodes”. In: *Proceedings of the IRE* 50.1 (Jan. 1962), pp. 43–53. DOI: `10.1109/jrproc.1962.288273`.

[201] David V. Lang. “Recalling the origins of DLTS”. In: *Physica B: Condensed Matter* 401–402 (Dec. 2007), pp. 7–9. ISSN: 0921-4526. DOI: 10.1016/j.physb.2007.08.102.

[202] A. A. Istratov. “The resolution limit of traditional correlation functions for deep level transient spectroscopy”. In: *Review of Scientific Instruments* 68.10 (Oct. 1997), pp. 3861–3865. ISSN: 1089-7623. DOI: 10.1063/1.1148038.

[203] L. Dobaczewski, A. R. Peaker, and K. Bonde Nielsen. “Laplace-transform deep-level spectroscopy: The technique and its applications to the study of point defects in semiconductors”. In: *Journal of Applied Physics* 96.9 (Oct. 2004), pp. 4689–4728. ISSN: 1089-7550. DOI: 10.1063/1.1794897.

[204] A. R. Peaker, V. P. Markevich, and J. Coutinho. “Tutorial: Junction spectroscopy techniques and deep-level defects in semiconductors”. In: *Journal of Applied Physics* 123.16 (Jan. 2018). ISSN: 1089-7550. DOI: 10.1063/1.5011327.

[205] J. A. Nelder and R. Mead. “A Simplex Method for Function Minimization”. In: *The Computer Journal* 7.4 (Jan. 1965), pp. 308–313. ISSN: 0010-4620. DOI: 10.1093/comjnl/7.4.308.

[206] S. Rein et al. “Lifetime spectroscopy for defect characterization: Systematic analysis of the possibilities and restrictions”. In: *Journal of Applied Physics* 91.4 (Feb. 2002), pp. 2059–2070. ISSN: 1089-7550. DOI: 10.1063/1.1428095.

[207] Jan Schmidt and Andrés Cuevas. “Electronic properties of light-induced recombination centers in boron-doped Czochralski silicon”. In: *Journal of Applied Physics* 86.6 (Sept. 1999), pp. 3175–3180. ISSN: 1089-7550. DOI: 10.1063/1.371186.

[208] Daniel Macdonald, Andrés Cuevas, and Jennifer Wong-Leung. “Capture cross sections of the acceptor level of iron–boron pairs in p-type silicon by injection-level dependent lifetime measurements”. In: *Journal of Applied Physics* 89.12 (June 2001), pp. 7932–7939. ISSN: 1089-7550. DOI: 10.1063/1.1372156.

[209] Pietro P. Altermatt. “Models for numerical device simulations of crystalline silicon solar cells—a review”. In: *Journal of Computational Electronics* 10.3 (July 2011), pp. 314–330. DOI: 10.1007/s10825-011-0367-6.

[210] Andreas Schenk. “Finite-temperature full random-phase approximation model of band gap narrowing for silicon device simulation”. In: *Journal of Applied Physics* 84.7 (Oct. 1998), pp. 3684–3695. DOI: 10.1063/1.368545.

[211] D. B. M. Klaassen. “A unified mobility model for device simulation-I. Model equations and concentration dependence”. In: *Solid-State Electronics* 35.7 (July 1992), pp. 953–959. DOI: 10.1016/0038-1101(92)90325-7.

[212] A. Cuevas et al. “Extraction of the surface recombination velocity of passivated phosphorus-doped silicon emitters”. In: 2 (1994), 1446–1449 vol.2. DOI: 10.1109/WCPEC.1994.520221.

[213] A. G. Aberle et al. "High-efficiency silicon solar cells: Si/SiO, interface parameters and their impact on device performance". In: *Progress in Photovoltaics: Research and Applications* 2.4 (Oct. 1994), pp. 265–273. DOI: 10.1002/pip.4670020402.

[214] Vun Jack Chin, Zainal Salam, and Kashif Ishaque. "An accurate modelling of the two-diode model of PV module using a hybrid solution based on differential evolution". In: *Energy Conversion and Management* 124 (Sept. 2016), pp. 42–50. DOI: 10.1016/j.enconman.2016.06.076.

[215] Vun Jack Chin, Zainal Salam, and Kashif Ishaque. "An accurate and fast computational algorithm for the two-diode model of PV module based on a hybrid method". In: *IEEE Transactions on Industrial Electronics* 64.8 (Aug. 2017), pp. 6212–6222. DOI: 10.1109/tie.2017.2682023.

[216] Shu-xian Lun et al. "A new explicit double-diode modeling method based on Lambert W-function for photovoltaic arrays". In: *Solar Energy* 116 (June 2015), pp. 69–82. DOI: 10.1016/j.solener.2015.03.043.

[217] Hussein Mohammed Ridha. "Parameters extraction of single and double diodes photovoltaic models using marine predators algorithm and Lambert w function". In: *Solar Energy* 209 (Oct. 2020), pp. 674–693. DOI: 10.1016/j.solener.2020.09.047.

[218] Yujie Chen, Yize Sun, and Zhuo Meng. "An improved explicit double-diode model of solar cells: Fitness verification and parameter extraction". In: *Energy Conversion and Management* 169 (Aug. 2018), pp. 345–358. DOI: 10.1016/j.enconman.2018.05.035.

[219] Suresh C. Jain and Roger J. Van Overstraeten. "Discussion of the validity of Kuno's relation to determine the base lifetime from a reverse recovery experiment". In: *Journal of Applied Physics* 55.2 (Jan. 1984), pp. 604–606. DOI: 10.1063/1.333074.

[220] A. B. Sproul. "Dimensionless solution of the equation describing the effect of surface recombination on carrier decay in semiconductors". In: *Journal of Applied Physics* 76.5 (Sept. 1994), pp. 2851–2854. DOI: 10.1063/1.357521.

[221] K. Joardar, R. C. Dondero, and D. K. Schroder. "A critical analysis of the small-signal voltage-decay technique for minority-carrier lifetime measurement in solar cells". In: *Solid-State Electronics* 32.6 (June 1989), pp. 479–483. ISSN: 0038-1101. DOI: 10.1016/0038-1101(89)90030-0.

[222] K. Joardar and D. K. Schroder. "Analysis of the small-signal voltage decay technique in the characterization of Si concentrator solar cells". In: *IEEE Transactions on Electron Devices* 39.7 (July 1992), pp. 1622–1632. ISSN: 0018-9383. DOI: 10.1109/16.141227.

[223] Helmut Mäckel and Kenneth Varner. "On the determination of the emitter saturation current density from lifetime measurements of silicon devices". In: *Progress in Photovoltaics: Research and Applications* 21.5 (2013), pp. 850–866. DOI: `10.1002/pip.2167`.

[224] Hidenori Takahashi and Takao Maekawa. "Evaluations of carrier lifetime in silicon epitaxial layers grown on lightly doped substrates". In: *Japanese Journal of Applied Physics* 39.Part 1, No. 7A (July 2000), pp. 3854–3859. ISSN: 0021-4922. DOI: `10.1143/JJAP.39.3854`.

[225] G. V. Ram and M. S. Tyagi. "Effective recombination velocity at the NN+ interface". In: *Solid-State Electronics* 24.8 (Aug. 1981), pp. 753–761. DOI: `10.1016/0038-1101(81)90057-5`.

[226] Hidenori Takahashi and Takao Maekawa. "Evaluation of effective recombination velocity related to the potential barrier in N/N+ silicon epitaxial wafers". In: *Japanese Journal of Applied Physics* 41.3R (Mar. 2002), p. 1214. DOI: `10.1143/JJAP.41.1214`.

[227] J. Vobeckỳ, P. Hazdra, and V. Záhlava. "Open circuit voltage decay lifetime of ion irradiated devices". In: *Microelectronics Journal* 30.6 (June 1999), pp. 513–520. DOI: `10.1016/S0026-2692(98)00173-6`.

[228] A. Zemel and M. Gallant. "Carrier lifetime in InP/InGaAs/InP by open-circuit voltage and photoluminescence decay". In: *Journal of Applied Physics* 78.2 (July 1995), pp. 1094–1100. DOI: `10.1063/1.360342`.

[229] A. Rohatgi and P. Rai-Choudhury. "Design, fabrication, and analysis of 17-18-percent efficient surface-passivated silicon solar cells". In: *IEEE Transactions on Electron Devices* 31.5 (May 1984), pp. 596–601. DOI: `10.1109/t-ed.1984.21574`.

[230] Donghyuk Park et al. "A 0.8 µm smart dual conversion gain pixel for 64 megapixels CMOS image sensor with 12k e- full-well capacitance and low dark noise". In: *2019 IEEE International Electron Devices Meeting (IEDM)*. IEEE, Dec. 2019. DOI: `10.1109/iedm19573.2019.8993487`.

[231] Sungbong Park et al. "A 64Mpixel CMOS image sensor with 0.56 µm unit pixels separated by front deep-trench isolation". In: *2022 IEEE International Solid- State Circuits Conference (ISSCC)*. IEEE, Feb. 2022. DOI: `10.1109/isscc42614.2022.9731750`.

[232] Mehdi Khabir and Mohammad Azim Karami. "Characterization and analysis of electrical crosstalk in a linear array of CMOS image sensors". In: *Applied Optics* 61.33 (Nov. 2022), p. 9851. ISSN: 2155-3165. DOI: `10.1364/ao.474633`.

[233] HyunChul Kim et al. "5.6 A 1/2.65 in 44 Mpixel CMOS image sensor with 0.7 µm pixels fabricated in advanced full-depth deep-trench isolation technology". In: *2020 IEEE International Solid- State Circuits Conference - (ISSCC)*. IEEE, Feb. 2020. DOI: `10.1109/isscc19947.2020.9062924`.

[234] A. Tournier et al. “Pixel-to-pixel isolation by deep trench technology: Application to CMOS image sensor”. In: *Proc. Int. Image Sensor Workshop*. 2011, pp. 12–15.

[235] Armin G. Aberle, Stefan Glunz, and Wilhelm Warta. “Impact of illumination level and oxide parameters on Shockley–Read–Hall recombination at the Si-SiO_2 interface”. In: *Journal of Applied Physics* 71.9 (May 1992), pp. 4422–4431. ISSN: 1089-7550. DOI: 10.1063/1.350782.

[236] R. B. M. Girisch, R. P. Mertens, and R. F. De Keersmaecker. “Determination of Si-SiO_2 interface recombination parameters using a gate-controlled point-junction diode under illumination”. In: *IEEE Transactions on Electron Devices* 35.2 (1988), pp. 203–222. ISSN: 0018-9383. DOI: 10.1109/16.2441.

[237] T. Binder et al. *MINIMOS-NT user guide*. 1998.

[238] Susan C. Vitkavage, Eugene A. Irene, and Hisham Z. Massoud. “An investigation of Si-SiO_2 interface charges in thermally oxidized (100), (110), (111), and (511) silicon”. In: *Journal of Applied Physics* 68.10 (Nov. 1990), pp. 5262–5272. ISSN: 1089-7550. DOI: 10.1063/1.347042.

[239] Yannis Tsividis and Colin McAndrew. *Operation and modeling of the MOS transistor*. Third. Includes index. New York [u.a.]: Oxford Univ. Press, 2011. ISBN: 9780195170153.

[240] Jan Schmidt, Robby Peibst, and Rolf Brendel. “Surface passivation of crystalline silicon solar cells: present and future”. In: *Solar Energy Materials and Solar Cells* 187 (Dec. 2018), pp. 39–54. ISSN: 0927-0248. DOI: 10.1016/j.solmat.2018.06.047.

[241] Ruy S. Bonilla and Peter R. Wilshaw. “On the c-Si/SiO_2 interface recombination parameters from photo-conductance decay measurements”. In: *Journal of Applied Physics* 121.13 (Apr. 2017). ISSN: 1089-7550. DOI: 10.1063/1.4979722.

[242] Chun-Min Zhang et al. “A generalized EKV charge-based MOSFET model including oxide and interface traps”. In: *Solid-State Electronics* 177 (Mar. 2021), p. 107951. ISSN: 0038-1101. DOI: 10.1016/j.sse.2020.107951.

[243] Laermer Franz and Schilck Andrea. “Verfahren zum anisotropen Ätzen von Silicium”. 4241045C1. May 1995.

[244] R. Kakoschke et al. “Trench sidewall implantation with a parallel scanned ion beam”. In: *IEEE Transactions on Electron Devices* 37.4 (Apr. 1990), pp. 1052–1056. ISSN: 0018-9383. DOI: 10.1109/16.52441.

[245] S. E. Berberich et al. “Trench sidewall doping for lateral power devices [ion implantation]”. In: *ESSDERC '03. 33rd Conference on European Solid-State Device Research, 2003*. IEEE, 2003. DOI: 10.1109/essderc.2003.1256893.

[246] Dong Gan et al. “n-p-n array yield improvement in a 0.18 µm deep trench SiGe BiCMOS process”. In: *IEEE Transactions on Electron Devices* 59.3 (Mar. 2012), pp. 590–595. ISSN: 1557-9646. DOI: 10.1109/ted.2011.2179806.

[247] S. R. Wilson and Han-Bin K. Liang. "The characterization of TEOS oxides used in the isolation module of high-speed bipolar and BiCMOS circuits". In: *Thin Solid Films* 220.1–2 (Nov. 1992), pp. 59–65. ISSN: 0040-6090. DOI: `10.1016/0040-6090(92)90549-q`.

[248] A. Inberg. "Theoretical model and experimental studies of infrared radiation propagation in hollow plastic and glass waveguides". In: *Optical Engineering* 39.5 (May 2000), p. 1316. ISSN: 0091-3286. DOI: `10.1117/1.602505`.

[249] John Gowar. *Optical communication systems*. 2. ed., [Nachdr.] Prentice Hall international series in optoelectronics. Literaturangaben. New York [u.a.]: Prentice Hall, 1997. 696 pp. ISBN: 0136387276.

[250] *TCAD Sentaurus User Manual: Sentaurus Device User Guide Version P-2019.03*. Synopsys. Mountain View, CA, USA, Mar. 2019.

[251] D. J. Roulston, N. D. Arora, and S. G. Chamberlain. "Modeling and measurement of minority-carrier lifetime versus doping in diffused layers of n+-p silicon diodes". In: *IEEE Transactions on Electron Devices* 29.2 (Feb. 1982), pp. 284–291. ISSN: 0018-9383. DOI: `10.1109/t-ed.1982.20697`.

[252] Shuai Nie, Ruy Sebastian Bonilla, and Ziv Hameiri. "Unravelling the silicon-silicon dioxide interface under different operating conditions". In: *Solar Energy Materials and Solar Cells* 224 (June 2021), p. 111021. ISSN: 0927-0248. DOI: `10.1016/j.solmat.2021.111021`.

[253] Ruy S. Bonilla, Frederick Woodcock, and Peter R. Wilshaw. "Very low surface recombination velocity in n-type c-Si using extrinsic field effect passivation". In: *Journal of Applied Physics* 116.5 (Aug. 2014). ISSN: 1089-7550. DOI: `10.1063/1.4892099`.

[254] Halvard Haug et al. "Modulating the field-effect passivation at the SiO_2/c-Si interface: Analysis and verification of the photoluminescence imaging under applied bias method". In: *Journal of Applied Physics* 114.17 (Nov. 2013). ISSN: 1089-7550. DOI: `10.1063/1.4827417`.

[255] Sungjin Choi et al. "Interface analysis of ultrathin SiO_2 layers between c-Si substrates and phosphorus-doped poly-Si by theoretical surface potential analysis using the injection-dependent lifetime". In: *Progress in Photovoltaics: Research and Applications* 29.1 (Nov. 2020), pp. 32–46. ISSN: 1099-159X. DOI: `10.1002/pip.3338`.

[256] Mingzhe Yu et al. "Extracting band-tail interface state densities from measurements and modelling of space charge layer resistance". In: *Solar Energy Materials and Solar Cells* 231 (Oct. 2021), p. 111307. ISSN: 0927-0248. DOI: `10.1016/j.solmat.2021.111307`.

[257] H. Deuling, E. Klausmann, and A. Goetzberger. "Interface states in Si/SiO_2 interfaces". In: *Solid-State Electronics* 15.5 (May 1972), pp. 559–571. ISSN: 0038-1101. DOI: `10.1016/0038-1101(72)90157-8`.

[258] A. J. Learn and D. W. Hess. "Effects of ion implantation on charges in the silicon–silicon dioxide system". In: *Journal of Applied Physics* 48.1 (Jan. 1977), pp. 308–312. ISSN: 1089-7550. DOI: 10.1063/1.323378.

[259] J. Snel. "The doped Si/SiO_2 interface". In: *Solid-State Electronics* 24.2 (Feb. 1981), pp. 135–139. ISSN: 0038-1101. DOI: 10.1016/0038-1101(81)90008-3.

[260] Pierre Saint-Cast et al. "Very low surface recombination velocity on p-type c-Si by high-rate plasma-deposited aluminum oxide". In: *Applied Physics Letters* 95.15 (Oct. 2009). ISSN: 1077-3118. DOI: 10.1063/1.3250157.

[261] Deven Raj et al. "Plasma doping of high aspect ratio structures". In: *2014 20th International Conference on Ion Implantation Technology (IIT)*. IEEE, June 2014. DOI: 10.1109/iit.2014.6940003.

[262] N. Ahmed et al. "MOS capacitor deep trench isolation for CMOS image sensors". In: *2014 IEEE International Electron Devices Meeting*. IEEE, Dec. 2014. DOI: 10.1109/iedm.2014.7046979.

[263] Michael Waltl. "Ultra-low noise defect probing instrument for defect spectroscopy of MOS transistors". In: *IEEE Transactions on Device and Materials Reliability* 20.2 (Apr. 2020), pp. 242–250. DOI: 10.1109/TDMR.2020.2988650.

[264] A. V. P. Coelho, M. C. Adam, and H. Boudinov. "Distinguishing bulk traps and interface states in deep-level transient spectroscopy". In: *Journal of Physics D: Applied Physics* 44.30 (July 2011), p. 305303. ISSN: 1361-6463. DOI: 10.1088/0022-3727/44/30/305303.

[265] Robert Tibshirani. "Regression shrinkage and selection via the Lasso". In: *Journal of the Royal Statistical Society: Series B (Methodological)* 58.1 (Jan. 1996), pp. 267–288. ISSN: 2517-6161. DOI: 10.1111/j.2517-6161.1996.tb02080.x.

[266] L. Dobaczewski et al. "Energy state distributions of the P_b centers at the (1 0 0), (1 1 0), and (1 1 1) Si/SiO_2 interfaces investigated by Laplace deep level transient spectroscopy". In: *Applied Physics Letters* 92.24 (June 2008). ISSN: 1077-3118. DOI: 10.1063/1.2939001.

[267] Lars-Åke Ragnarsson and Per Lundgren. "Electrical characterization of Pb centers in (1 0 0) Si–SiO_2 structures: The influence of surface potential on passivation during post metallization anneal". In: *Journal of Applied Physics* 88.2 (July 2000), pp. 938–942. ISSN: 1089-7550. DOI: 10.1063/1.373759.

[268] J. T. Ryan et al. "Interface-state capture cross section-Why does it vary so much?" In: *Applied Physics Letters* 106.16 (Apr. 2015). ISSN: 1077-3118. DOI: 10.1063/1.4919100.

[269] Fiacre E. Rougieux, Chang Sun, and Daniel Macdonald. "Determining the charge states and capture mechanisms of defects in silicon through accurate recombination analyses: A review". In: *Solar Energy Materials and Solar Cells* 187 (Dec. 2018), pp. 263–272. ISSN: 0927-0248. DOI: 10.1016/j.solmat.2018.07.029.

[270] Bernhard Ruch et al. “Applicability of Shockley-Read-Hall theory for interface states”. In: *IEEE Transactions on Electron Devices* 68.4 (Apr. 2021), pp. 2092–2097. DOI: `10.1109/ted.2021.3049760`.

List of Publications

Scientific Journals

[PSJ1] **Paul Stampfer**, Frederic Roger, Lukas Cvitkovich, Tibor Grasser, and Michael Waltl. “A DLTS Study on Deep Trench Processing Induced Trap States in Silicon Photodiodes”. In: *IEEE Transactions on Device and Materials Reliability* (2024), accepted. DOI: 10.1109/TDMR.2024.3382396.

[PSJ2] **Paul Stampfer**, Bernhard Stampfer, Tibor Grasser, and Michael Waltl. “Accurate extraction of minority carrier lifetimes-Part I: Transient methods”. In: *IEEE Transactions on Electron Devices* 70.8 (2023), pp. 4320–4325. DOI: 10.1109/TED.2023.3286798.

[PSJ3] **Paul Stampfer**, Bernhard Stampfer, Tibor Grasser, and Michael Waltl. “Accurate extraction of minority carrier lifetimes-Part II: Combined I–V C–V methods”. In: *IEEE Transactions on Electron Devices* 70.8 (2023), pp. 4326–4331. DOI: 10.1109/TED.2023.3286792.

[PSJ4] **Paul Stampfer**, Frederic Roger, Tibor Grasser, and Michael Waltl. “Impact of trap states at deep trench sidewalls on the responsivity of island photodiodes”. In: *IEEE Transactions on Electron Devices* 70.11 (Nov. 2023), pp. 5738–5744. DOI: 10.1109/TED.2023.3315225.

Conference Proceedings

[PSC1] **Paul Stampfer**, Gerald Meinhardt, Tibor Grasser, and Michael Waltl. “Simulating and modeling the influence of deep trench interface recombination on Si photodiodes”. In: *2022 IEEE International Integrated Reliability Workshop (IIRW)*. 2022, pp. 1–5. DOI: 10.1109/IIRW56459.2022.10032736.

[PSC2] **Paul Stampfer**, Bernhard Stampfer, Frederic Roger, Rainer Minixhofer, Tibor Grasser, and Michael Waltl. “A DLTS study on deep trench processing induced trap states in silicon photodiodes”. In: *2023 IEEE International Integrated Reliability Workshop (IIRW)*. 2023, pp. 1–4. DOI: 10.1109/IIRW59383.2023.10477712.